

**Numerical Parametric Study of Wind-Driven Rain and Overhang Effectiveness on
a Mid-Rise Building**

Ali Khalilzadeh

A Thesis

in

The Department

of

Mechanical, Industrial & Aerospace Engineering

Presented in Partial Fulfillment of the Requirements

For the Degree of Master of Applied Science (Mechanical Engineering) at

Concordia University

Montreal, Quebec, Canada

August 2017

© Ali Khalilzadeh, 2017

CONCORDIA UNIVERSITY
School of Graduate Studies

This is to certify that the thesis prepared

By: Ali Khalilzadeh

Entitled: “Numerical Parametric Study of Wind-Driven Rain and Overhang Effectiveness on
 a Mid-Rise Building”

and submitted in partial fulfillment of the requirements for the degree of

Master of Applied Science (Mechanical Engineering)

complies with the regulations of the University and meets the accepted standards with respect to originality and quality.

Signed by the final Examining Committee:

_____	Chair
<i>Dr. Tsz Ho Kwok</i>	
_____	Examiner
<i>Dr. Ted Stathopoulos</i>	
_____	Examiner
<i>Dr. Charles Basenga Kiyanda</i>	
_____	Supervisor
<i>Dr. Hua Ge</i>	
_____	Supervisor
<i>Dr. Hoi Dick Ng</i>	

Approved by _____
Dr. Martin D. Pugh
Chair of Department or Graduate Program Director

_____ *Dr. Amir Asif*
Dean of Faculty of Engineering and Computer Science

Date

July 27, 2017

Abstract

Numerical Parametric Study of Wind-Driven Rain and Overhang Effectiveness on a Mid-Rise Building

Ali Khalilzadeh

The question of how wind and wind-accompanied rain are properly predicted, regardless of the method, whether experimental, semi-empirical or numerical is to this day unsettled. Moreover, parametric study of the Wind-Driven Rain (WDR), and consequently its wetting building façades is rather insufficiently dealt with. Due to the destructive repercussions of moisture penetration induced by WDR, façade protection in form of an overhang, which is considered as the most effective means to address the issue with, in regions with high levels of liquid precipitation, is the necessity of this study. Suitable numerical solution, alongside delving into the effect of numerous parameters governing the natural phenomenon, including wind direction and speed, rainfall intensity, and overhang size and shape, is the target of this work. To reach this goal, a MATLAB code controls raindrop injection into pre-solved domain of external flow on stand-alone and surrounded building. Wind flow solution of multiple turbulence schemes is bestowed upon ANSYS Fluent software package. Drag simulation and inlet velocity profiles, are hooked to the solver using User-Defined Functions (UDFs). Validation of wind simulation is done by comparing the predictions to wind-tunnel measurements. Validation of rain simulation on the other hand is performed by comparing the results to real-life conditions on a medium-rise building. Results of validation are rather promising for the upper-half of the windward façade. Proper technique of simulation of wind with conventional two-equation turbulence models, alongside the inlet velocity profiles is found to be boundary-treated Standard $k-\omega$, wind log-law. Overhang presence and its shape and size are vastly studied and parametrized to find the effect of those parameters on the effectiveness of the overhang. This study shows that although rainfall intensity is faintly influential, the wind speed and direction, alongside overhang size and shape, considerably influence catch ratio and effectiveness of the overhang. The effectiveness decreases by an increase in wind speed and increases for oblique winds.

Façade effectiveness of the overhang decreases with an increase in rainfall intensity; although this parameter's influence on point effectiveness is dependent upon the location of point on the façade. Finally, the wider the overhang, the more effective it is in protecting the façade, as a whole, from rain.

Acknowledgements

Not a second passed and I did not think I am being championed by my caring supervisors. This would not have happened without the inspiration and counsel of Dr. H. Ge and Dr. H. D. Ng.

I shall state my recognition of the financial support received from NSERC Strategic Research Network for Engineered Wood-Based Building Systems (NEWBuildS), and the Homeowner Protection Office Branch of British Columbia Housing; alongside the Faculty of Engineering and Computer Science of Concordia University and Power Corporation of Canada.

Dedication

Whatever I have accomplished is the result of my family paving the way and being there for me no matter what. I dedicate this work to my parents and my siblings.

Table of Contents

List of Tables	ix
List of Figures	x
Nomenclature	xvi
Roman Symbols	xvi
Greek Symbols	xvii
Acronyms	xviii
Chapter 1 Introduction	1
1.1 Wind.....	2
1.1.1 Literature Review	4
1.2 Wind-Driven Rain.....	16
1.2.1 Experimental Methods.....	17
1.2.2 Semi-Empirical Methods	17
1.2.3 Numerical Methods	17
1.2.4 Literature Review	17
1.3 Overhang.....	26
1.3.1 Effectiveness of Overhang.....	26
1.4 Summary of Literature Review.....	27
1.5 Scope.....	28
1.6 Aim and Methodology	28
1.7 Thesis Outline	29
Chapter 2 Numerical Simulation and Model Verification	31
2.1 Governing Equations	31
2.2 Turbulence Modeling.....	32
2.2.1 Realizable k- ϵ Model.....	32
2.2.2 Standard k- ω Model.....	32
2.2.3 Shear-Stress Transport (SST) k- ω Model.....	32
2.2.4 Standard Wall Functions	33
2.2.5 Matching the Wall-Function-Modified-for-Roughness and ABL Flow.....	34
2.3 Wind-Driven Rain.....	36
2.3.1 Numerical Solution to Wind and WDR.....	36

2.3.1.1	Building Geometry, Computational Domain, and Grid Study.....	37
2.3.1.2	Blocking of the Mesh of the Domain.....	38
2.3.1.3	Boundary Conditions.....	41
2.3.1.4	Near-Wall-Cell Center-Point Distance to the Wall.....	41
2.3.1.5	Numerical Solution to Rain Phase	45
2.3.1.6	Rain Event Selection Procedure.....	48
2.3.1.7	Effect of 10° Difference in Angle of Wind Blowing on the Façade on Catch Ratio Calculation.....	49
2.3.2	Experimental Solution to Wind and WDR.....	51
2.3.2.1	Wind Tunnel Measurements	51
2.3.2.2	Field Measurements	54
2.3.3	Sources of Wind Simulation Error	55
2.3.4	Sources of WDR Simulation Error.....	56
2.3.5	Overhang Effectiveness.....	58
Chapter 3 Validation, Results, and Discussion.....		60
3.1	Wind Simulation	60
3.1.1	Validation of Simulation on Stand-Alone Building.....	60
3.1.1.1	Normal Wind to the East Façade.....	60
3.1.1.2	Oblique Wind on the East and South Façades	65
3.1.2	Validation of Simulations on Surrounded Building.....	67
3.1.2.1	Normal Wind to the East Façade.....	67
3.1.2.2	Oblique Wind on the East and South Façades	70
3.1.2.3	Oblique Wind on the East and North Façades	72
3.1.3	Comparison amongst Turbulence Models.....	74
3.1.4	Oblique Wind Parametric Study.....	81
3.1.5	Wind Simulation Summary	83
3.2	Rain Simulation	83
3.2.1	Validation and Model Comparison of Simulation on Stand-Alone Building	84
3.2.2	Validation and Model Comparison of Simulation on Surrounded Building with Unprotected Façade.....	88
3.2.3	Validation and Model Comparison of Simulation on Surrounded Building with Protected Façade	93
3.2.3.1	2' On-Site Overhang	93

3.2.3.2	4' On-Site Overhang	97
3.2.4	Rain Parametric Study with Oblique Wind Direction on Unprotected Façade	99
3.2.5	Rain Parametric Study with Oblique Wind Direction on Protected Façade.....	101
3.2.6	Rain Simulation Summary.....	103
Chapter 4	Overhang Effectiveness Parametric Study	104
4.1	Façade Covering Overhang.....	104
4.1.1	Effectiveness Index.....	107
4.2	On-Site Overhang	110
4.3	Wind Speed Effect on Overhang Effectiveness.....	116
4.4	Wind Direction Effect on Overhang Effectiveness	129
Chapter 5	Conclusions and Recommendations.....	134
5.1	Conclusions.....	134
5.1.1	Modeling and Validation	135
5.1.2	Parametric Study.....	137
5.1.3	Summary.....	138
5.2	Recommendations.....	138
References	140
Appendices	149
Appendix A -	Discretization Error Formulation.....	149
Appendix B -	Error Percentage Plots	151
Appendix C -	Catch Ratio Validation Charts	157
Appendix D -	Velocity Contours.....	158
Appendix E -	Catch Ratio Parametric Study.....	159
Appendix F -	Effectiveness Charts	168

List of Tables

Table 1.1.1 - Atmospheric boundary layer flow fitted function parameters for terrain with different surface roughness (Aynsley, et al., 1977) and (Wang, 2005)	4
Table 2.2.1 - Standard wall function parameters and constants	33
Table 2.2.2 - Modified inlet turbulence parameters for the velocity profiles used in this study ..	35
Table 2.3.1 - Computational domain size and discretization.....	38
Table 2.3.2 - Summary of boundary conditions	41
Table 2.3.3 - WDR event parameters used to study the effect small change in wind direction on catch ratio.....	51
Table 2.3.4 - Calculations of discretization error	56
Table 3.2.1 - WDR event parameters for stand-alone building validation	84
Table 3.2.2 - Wind and WDR parameters of the rain events created to validate simulations on surrounded unprotected building, exposed to normal wind on the east façade	89
Table 3.2.3 - Computational domain size and discretization for surrounded building, exposed to normal wind on the east façade.....	89
Table 3.2.4 - Wind and WDR parameters of the rain events created to validate simulations on surrounded protected building, exposed to normal wind on the east façade	93
Table 3.2.5 - Computational domain size and discretization for surrounded building, exposed to normal wind on the east façade.....	93
Table 3.2.6 - Wind and WDR parameters of the rain events created to validate simulations on surrounded protected building, exposed to normal wind on the east façade	97
Table 3.2.7 - Computational domain size and discretization for surrounded building, exposed to normal wind on the east façade.....	97

List of Figures

Figure 1.1.1 - Wind profile development for different terrain roughness (Gaetani, 2013)	2
Figure 1.1.2 - Streamlines in the plane of symmetry, surface mounted cube for wind tunnel, non-linear turbulence model proposed and Standard k- ϵ (Ehrhard & Moussiopoulos, 2000)...	5
Figure 1.1.3 - Comparison of CFD results and wind tunnel measurements of wind speed ratio for the isolated building by Yoshie et al. (Yoshie, et al., 2007) for steady RANS with Standard k- ϵ model, steady RANS with LK k- ϵ model, and steady RANS with RNG k- ϵ models.	10
Figure 1.1.4 - Flow patterns around building models obtained with smoke-wire technique, Realizable k- ϵ turbulence model and Standard k- ω turbulence model (a,d,g) roof pitch of 15°, (b,e,h) roof pitch of 30°, (c,f,i) roof pitch of 45° (Ozmen, et al., 2016).....	15
Figure 1.2.1 - Raindrop-size distribution in an air volume with the rainfall intensity as a parameter (Best, 1950).....	18
Figure 1.2.2 - Catch ratio η as a function of reference wind speed U_{10} and horizontal rainfall intensity R_h for (a) position 1 and (b) position 3 (Blocken, 2004).....	19
Figure 1.2.3 - Spatial distribution of the catch ratio on the monumental tower. The experimental results at the locations of the wind-driven rain gauges are shown on the left, the numerical results are shown on the right (Briggen, et al., 2009).....	21
Figure 1.2.4 - Catch ratio distribution on façades and roofs of all cubes for the reference wind speed $U = 5$ m/s and the reference rainfall intensity $R_h = 1$ mm/h for wind from a) west and b) southwest. (Kubilay, et al., 2014)	23
Figure 1.2.5 - Streamlines and contour plot of the wind flow in the a) vertical center-plane for wind from west, b) horizontal plane at $y = 1$ m height for wind from west, c) horizontal plane at $y = 1$ m height for wind from southwest. Streamlines in b) and c) are projected on the horizontal plane and hence have no out-of-plane component (Kubilay, et al., 2014)	24
Figure 2.3.1 - Aerial view of the building site (Google Maps, 2017).....	37
Figure 2.3.2 - Test building and its surrounding in the terrain	38
Figure 2.3.3 - Computational schematics with boundary conditions.....	39
Figure 2.3.4 - Blocking scheme of the computation domain.....	39
Figure 2.3.5 - Inlet - Outlet comparison of velocity profiles, and turbulence parameters for different y_p values	42
Figure 2.3.6 - (a) Turbulent dissipation rate (ϵ), and (b) specific dissipation rate (ω) versus vertical distance from the ground for different y_0 values, at the inlet.....	43

Figure 2.3.7 - (a) Turbulent dissipation rate (ϵ), and (b) specific dissipation rate (ω), versus vertical distance from the ground for different y_p values, at the inlet.....	43
Figure 2.3.8 - y^+ value for ground boundary, with wind normal to the east façade, at $y_p = 0.25$ m	45
Figure 2.3.9 - Reference and vertical wetted areas that appear in the definition of catch ratio (Blocken, 2004).....	47
Figure 2.3.10 - Catch ratio contours - error percentage on each measurement gauge, with wind on the east façade (and north in case of oblique wind), Standard $k-\omega$ with log-law inlet velocity profile. Black dots are error percentage compared to field measurement. Bottom white areas show zero catch ratio.	50
Figure 2.3.11 - The test building and surrounding buildings within a 200-m radius placed in ABL wind tunnel (Chiu, 2016).	52
Figure 2.3.12 - Normalized mean velocity and turbulence intensity for a suburban exposure measured in the boundary layer wind tunnel (Chiu, 2016).....	52
Figure 2.3.13 - Location of wind velocity measurements around the test building, N, S, E, W stand for north, south, east, and west	54
Figure 2.3.14 - Schematics of the building and the mechanical room with the wind monitor mounted on top of it (Chiu, 2016)	55
Figure 2.3.15 - Effectiveness index calculation portions on windward façade of the test building	58
Figure 3.1.1 - x -velocity on a horizontal profile, alongside value comparison, on stand-alone building exposed at normal wind on the east façade	61
Figure 3.1.2 - x -velocity on vertical profile, with value comparison to wind tunnel measurement, on stand-alone building exposed to normal wind on the east façade.....	63
Figure 3.1.3 - x -velocity value comparison on a vertical profile, with stand-alone building exposed at 45° wind on the east and south façades.....	66
Figure 3.1.4 - Velocity contour (plan view) and streamlines at 5 m above the ground, alongside the location of stagnation point, around surrounded test building, exposed to normal wind on the east façade, Standard $k-\omega$ with $U_{10} = 6.7$ m/s, left pointing arrow shows inlet wind direction	68
Figure 3.1.5 - x -velocity value comparison on vertical profile, with the surrounded building exposed to normal wind on the east façade	69
Figure 3.1.6 - x -velocity value comparison on vertical profile, with surrounded building exposed to 45° wind on the east and south façades.....	71
Figure 3.1.7 - x -velocity value comparison on vertical profile, with surrounded building exposed to 45° wind on the east and north façades.....	73

Figure 3.1.8 - Contours of velocity and field of velocity at $z = 0$ plane, around surrounded test building exposed to normal wind to the east façade, for $U_{10} = 6.7$ m/s, arrow shows inlet wind direction	76
Figure 3.1.9 - Contour of velocity magnitude at 3.6 m upstream of the east façade, around surrounded test building exposed to normal wind on the east façade at $U_{10} = 6.7$ m/s	78
Figure 3.1.10 - Streamlines of the wind velocity with turbulent kinetic energy at mid z -plane, around surrounded test building exposed to normal wind to the east façade at $U_{10} = 6.7$ m/s, arrow shows inlet wind direction.....	79
Figure 3.1.11 - Velocity contour (top view) and streamlines at 19.45 m above the ground (at the level of ES1 and EN1 gauges, Figure 2.3.13b), around surrounded test building exposed to normal wind to the east façade, at $U_{10} = 6.7$ m/s, arrow shows inlet wind direction....	80
Figure 3.1.12 - Velocity contour (top view) and streamlines at 15.23 m above the ground (at the level of ES3 and EN3 gauges, Figure 2.3.13b), around surrounded test building exposed to normal wind to the east façade, at $U_{10} = 6.7$ m/s, arrow shows inlet wind direction....	81
Figure 3.1.13 - Velocity magnitude contour (plan view) and streamlines at 5 m above the ground, around surrounded test building, exposed to normal wind on the east façade, Standard $k-\omega$ with $U_{10} = 6.7$ m/s	82
Figure 3.2.1 - $U_{10} = 6.7$ m/s raindrop trajectories for $d = 0.6$ mm, around surrounded test building exposed to normal wind on the east façade	83
Figure 3.2.2 - Catch ratio CFD prediction comparison to field measurements, for Event 1 (Table 3.2.1) simulation of WDR, stand-alone building exposed to normal wind on the east façade. Black dots are field measurement catch ratio values. Bottom white areas show zero catch ratio.....	85
Figure 3.2.3 - Raindrop impingement for 0.6 mm and 1.2 mm raindrop sizes, with wind normal to the east façade, Event 2 on Table 3.2.1	87
Figure 3.2.4 - WDR simulation validation of surrounded unprotected building domain, at various locations, with east façade exposed at normal wind onto the east façade, multiple rain events	90
Figure 3.2.5 - Raindrop impingement for 0.5 mm and 1.0 mm raindrop sizes, with wind normal to the east façade, Event 2 on Table 3.2.2	91
Figure 3.2.6 - Catch ratio CFD prediction error percentage, for Event 1 (Table 3.2.1). Black dots are field measurement catch ratio. Bottom white areas show zero catch ratio.	92
Figure 3.2.7 - WDR simulation validation of surrounded protected building with 2' overhang, at various locations, with the east façade exposed at normal wind onto the east façade, multiple rain events.....	94
Figure 3.2.8 - Raindrop impingement on the east façade of the test building, equipped with 2' overhang, for different raindrop diameters, around surrounded building exposed to	

normal wind on the east façade, Event 2 in Table 3.2.4, with Standard k- ω and log-law inlet velocity profile	94
Figure 3.2.9 - Regions of protected façade with non-covering overhang, Figure 3.2.8c, region 2 is protected, 1 is unprotected	95
Figure 3.2.10 - Catch ratio comparison of CFD with field measurements for the east façade of the surrounded test building equipped with 2' overhang, exposed to normal wind, with Standard k- ω on log-law inlet velocity. Black dots are field measurement catch ratio. Bottom white areas show zero catch ratio.	96
Figure 3.2.11 - WDR simulation validation of surrounded protected building with 4' overhang, at various locations, with the east façade exposed at normal wind onto the east façade, multiple rain events.....	97
Figure 3.2.12 - Raindrop impingement on the east façade of the test building, equipped with 4' overhang, for different raindrop diameters, around surrounded building exposed to normal wind on the east façade, Event 1 in Table 3.2.6, with Standard k- ω and log-law inlet velocity profile	98
Figure 3.2.13 - Catch ratio comparison of CFD with field measurements for the east façade of the surrounded test building equipped with 4' overhang, exposed to normal wind, with Standard k- ω and log-law inlet velocity profile. Black dots are field measurement catch ratio. Bottom white areas show zero catch ratio.	99
Figure 3.2.14 - Set of oblique wind directions studied.....	99
Figure 3.2.15 - Raindrop impingement for 0.6 mm and 1.0 mm raindrop sizes, Standard k- ω , log-law velocity profile, $U_{10} = 6.7$ m/s, and $R_h = 4$ mm/hr, oblique wind direction, unprotected façade	100
Figure 3.2.16 - Catch ratio comparison of normal and oblique wind on the unprotected east façade of the surrounded test building, with Standard k- ω on log-law inlet velocity, $U_{10} = 6.7$ m/s and $R_h = 4$ mm/hr. White areas show zero catch ratio.	101
Figure 3.2.17 - Raindrop impingement for 0.6 mm and 1.0 mm raindrop sizes, Standard k- ω , log-law velocity profile, $U_{10} = 6.7$ m/s and $R_h = 4$ mm/hr, oblique wind direction, protected façade	102
Figure 3.2.18 - Catch ratio comparison of normal and oblique wind on the protected east façade with 3' overhang, of the surrounded test building, with Standard k- ω on log-law inlet velocity, $U_{10} = 6.7$ m/s and $R_h = 4$ mm/hr. White areas show zero catch ratio.	103
Figure 4.1.1 - Catch ratio contour of smoothed data on the east façade with surrounded building unprotected and protected with façade covering overhang, $U_{10} = 3.0$ m/s, $R_h = 4.16$ mm/hr. White areas show zero catch ratio.	105
Figure 4.1.2 - Contour of x-velocity on a plane 0.5 m upstream of the east façade, with surrounded building unprotected and protected with façade covering overhang, $U_{10} = 6.7$ m/s, $R_h = 4.0$ mm/hr.....	106

Figure 4.1.3 - Effectiveness index of the overhang over different overhang sizes under different rainfall intensities.....	108
Figure 4.1.4 - Effectiveness index of the overhang over different rainfall intensities under different façade division groups.....	109
Figure 4.2.1 - The east façade at normal wind, surrounded by upwind buildings equipped with 4' on-site overhang.....	110
Figure 4.2.2 - Catch ratio contour of raw data on the east façade, with surrounding buildings, on-site overhang. White areas show zero catch ratio.	112
Figure 4.2.3 - Contour comparison 0.5 m upstream of the east façade, with surrounding buildings, on-site overhang.....	113
Figure 4.2.4 - Effectiveness index of the overhang over different overhang sizes under different rainfall intensities, full façade calculation	114
Figure 4.2.5 - Effectiveness of the overhang over different overhang sizes under different rainfall intensities, protected portion calculation	115
Figure 4.2.6 - Effectiveness of the overhang over different rainfall intensities under different façade division groups, protected portion calculation	116
Figure 4.3.1 - x -velocity at various points on the east façade, on corresponding vertical base, Figure 2.3.13b, versus U_{10} value.....	118
Figure 4.3.2 - Catch ratio parametric study for protected and unprotected windward façade, the east façade, exposed to normal wind at different rates, at ES1 and EN1	119
Figure 4.3.3 - Catch ratio parametric study for protected and unprotected windward façade, the east façade, exposed to normal wind at different rates, at EC2 and EN9.....	121
Figure 4.3.4 - Catch ratio at various measurement gauges on the east façade, Figure 2.3.13b, versus U_{10} value	122
Figure 4.3.5 - Effectiveness of overhang (in percent) on windward façade, exposed to normal wind at different rates, and rain in different intensities, at A1 (100% of the façade).....	123
Figure 4.3.6 - Point effectiveness (in percent) parametric study for protected windward façade, the east façade, exposed to normal wind at different rates	125
Figure 4.3.7 - Effectiveness contour on the east façade, with surrounding buildings, façade-covering overhang.....	127
Figure 4.3.8 - Effectiveness contour on the east façade, with surrounding buildings, on-site overhang. White spots show zero effectiveness.	128
Figure 4.4.1 - Catch ratio parametric study for protected and unprotected windward façade, oblique wind on the east and north façades, at ES1, EC1, and EN1, Figure 2.3.13b, Standard k - ω with log-law inlet velocity profile, $U_{10} = 6.7$ m/s and $R_h = 4$ mm/hr.....	129

Figure 4.4.2 - Catch ratio parametric study for protected and unprotected windward façade, oblique wind on the east and north façades, at EC2, EN9, and ES7, Figure 2.3.13b, Standard k- ω with log-law inlet velocity profile, $U_{10} = 6.7$ m/s and $R_h = 4$ mm/hr.....	130
Figure 4.4.3 - Point effectiveness (in percent) parametric study for protected windward façade, the east façade, exposed to oblique wind on the east and north façades, Standard k- ω with log-law inlet velocity profile, $U_{10} = 6.7$ m/s and $R_h = 4$ mm/hr	131
Figure 4.4.4 - Effectiveness of overhang (in percent) on the east façade, exposed to oblique wind at angles on the east and north façades, and rain in different intensities, Standard k- ω with log-law inlet velocity profile, $U_{10} = 6.7$ m/s and $R_h = 4$ mm/hr	132
Figure 4.4.5 - Effectiveness contour on the east façade, with surrounding buildings, 3' façade-covering overhang, oblique wind. White spots show zero effectiveness.	133
Figure B.1 - x -velocity error percentage on a horizontal profile, normal to the north façade at different locations, with the stand-alone building exposed to normal wind on the east façade	151
Figure B.2 - x -velocity error percentage on vertical profile, with value comparison to wind tunnel measurement, on stand-alone building exposed to normal wind on the east façade	152
Figure B.3 - x -velocity error percentage on vertical profile, with stand-alone building exposed at 45° wind on the east and south façades.....	153
Figure B.4 - x -velocity error percentage on vertical profile, with surrounded building exposed to normal wind on the east façade.....	154
Figure B.5 - x -velocity error percentage on vertical profile, with surrounded building exposed to 45° wind on the east and south façades.....	155
Figure B.6 - x -velocity error percentage on vertical profile, with surrounded building exposed to 45° wind on the east and north façades.....	156
Figure C.1 - WDR simulation validation of surrounded unprotected building domain, at various locations, with the east façade exposed at normal wind onto the east façade, multiple rain events	157
Figure D.1 - Contour of velocity magnitude on a plane 0.5 m upstream of the east façade, with surrounded building unprotected and protected with façade covering overhang	158
Figure E.1 - Catch ratio parametric study for protected and unprotected windward façade, the east façade, exposed to normal wind at different rates, at ES1 and EN1	167
Figure F.1 - Effectiveness of overhang on windward façade, exposed to normal wind at different rates, and rain in different intensities.....	168

Nomenclature

Roman Symbols

A_{df}	Frontal area of droplet	[m ²]
A_f	Wetted area	[m ²]
A_h	Area of a reference horizontal surface	[m ²]
C_D	Drag coefficient	-
C_{Ks}	Roughness constant	-
C_μ	Constant from the k- ϵ model (usually taken to be 0.09)	-
d	Diameter	[m]
E	Empirical constant (= 9.793)	-
\vec{F}_D	Drag force	[N]
\vec{g}	Gravitational acceleration	[m/s ²]
h	Equilibrium boundary layer height	[m]
I_u	Turbulence intensity	[%]
k	Kinetic turbulence energy	[m ² /s ²]
k_p	Turbulent kinetic energy at point p	[m ² /s ²]
K_s	Roughness height	[m]
p	Pressure	[Pa]
\vec{r}	Position vector of droplet	[m]
Re	Reynolds number	-
R_h	Horizontal rainfall intensity	[mm/hr]
R_{wdr}	WDR rainfall intensity	[mm/hr]

S	Momentum source term	[Pa/m]
t	time	[s]
U	Mean horizontal wind speed	[m/s]
U_{ref}	Mean wind speed at reference point of designation	[m/s]
U^*	Dimensionless velocity	-
\mathbf{u}	Velocity vector	[m/s]
u^*_{ABL}	Friction velocity	[m/s]
y_0	Aerodynamic roughness length	[m]
y_p	Distance from the centroid of the wall-adjacent cell to the wall, p	[m]
y_{ref}	Height of reference point of designation	[m]
y^*	Dimensionless distance from the wall	[m]

Greek Symbols

α	Dimensionless exponent of power-law profile	
δ	Kronecker delta	
δ_f	Overhang façade effectiveness	
δ_p	Overhang point effectiveness	
ε	Turbulent kinetic energy dissipation	[m ² /s ³]
η	Catch ratio	
η_d	Specific catch ratio	
κ	von Karman constant	
λ	Step length factor	

μ	Dynamic viscosity	[N.s/m ²]
ν	Kinematic viscosity	[m ² /s]
ρ	Air density	[kg/m ³]
ρ_w	Water density	[kg/m ³]
τ	Shear stress tensor	[N/m ²]
τ_w	Wall friction (shear stress)	[N/m ²]
ω	Turbulent specific dissipation rate	[1/s]

Acronyms

ABL	Atmospheric Boundary Layer
CFD	Computational Fluid Dynamics
CV	Control Volume
DPM	Discrete Phase Model
EM	Eulerian Multiphase Modeling
OH	Overhang
PDE	Partial Differential Equation
RANS	Reynolds Averaged Navier-Stokes
R-HVAC	Refrigeration-Heat, Ventilation, Air Conditioning
SST	Shear-Stress Transport
SIMPLE	Semi-Implicit Method for Pressure Linked Equations
UDF	User-Defined Function
WDR	Wind-Driven Rain

Chapter 1 INTRODUCTION

The necessity of knowing the mechanism of wind flow and raindrop motion has been a prominent motive to various studies on atmospheric and meteorological phenomena. Aside from the fact that by industrialization and growth of population, excess amount of pollutants can be carried around by wind and precipitated down by raindrops, driving rain and moisture penetration has momentous impact on soil, bodies of water, target habitats and the subject of this study, building envelopes. Various reports from across the globe have been on residential and commercial buildings take noticeable damage due to heavy wind and rain, incidences of which will be discussed later throughout this chapter. With global warming and melting of Earth's ice storage on both poles, the effects of such phenomenon is most likely accentuated.

Wind around a building has direct repercussions on Refrigeration-Heat, Ventilation, Air Conditioning (R-HVAC) systems and mechanical properties of the envelope as well as the structure of the building. The effect on R-HVAC is because outdoor pressure and stream are boundary conditions of these systems. Aside from those effects, wind's co-occurrence with rain results in what called Wind-Driven Rain which is one of the main sources of moisture that causes façade failure (Hershfield, 1996) and (Hazleden & Morris, 1999). Lourenco et al. in a case study of a historical center in Northern Portugal performed a survey of defects in the envelope (Lourenço, et al., 2006). They find water-related problems to be the single most important defect. The authors claim that infiltrations of water through the roof or the façade are responsible for most of pathological manifestations. A crucial part of finding how wind-driven rain wets a building façade, is the correct and accurate solution to the wind in the domain. As the coupling between many phases involved in a wind-driven rain is one way, (Elghobashi, 1994) and (Csanady, 1963), in such a way that the raindrops' effect on wind dynamics is negligible, current study goes beyond the field of multiphase flow and expands to proper solution of wind around buildings as a pivotal role. Numerous studies have targeted the accuracy and validation of wind around buildings. These include very detailed problems such as urban canopy, interunit dispersion and so many other aspects of Atmospheric Boundary Layer (ABL) flow over single or multiple building units.

One of the most effective means of protecting the façade against WDR is by deflecting the incoming water onto it (Hazleden & Morris, 1999). Overhangs are found to be the most

important and effective means for the job. Current thesis deploys the proper method of solution to WDR for unprotected façade to predict the intensity of vertical rain on protected façade and subsequently goes beyond to validate and parameterize the use of overhangs for various wind and rain conditions.

Current chapter reviews critical papers and studies regarding prediction of wind in urban or suburban terrain, as well as WDR related literature. Important concepts are introduced briefly followed by scope, aim and methodology of the work.

1.1 Wind

On an empty terrain, within negligible spans relative to the radius of Earth, wind can be characterized by a two-dimensional horizontal vector field. In climatology, wind is defined as the movement of air relative to the surface of the earth. Atmospheric pressure gradients induced by dramatic change in regional temperature due to the spectrum of solar radiation from either pole to the equator result in wind. Current study focuses on quantifying the motion of wind near the surface of Earth. Due to non-slip surface, and fluid viscosity, wind takes a certain shape of profile, which is altered by wind speed and terrain characteristics, shown in Figure 1.1.1.

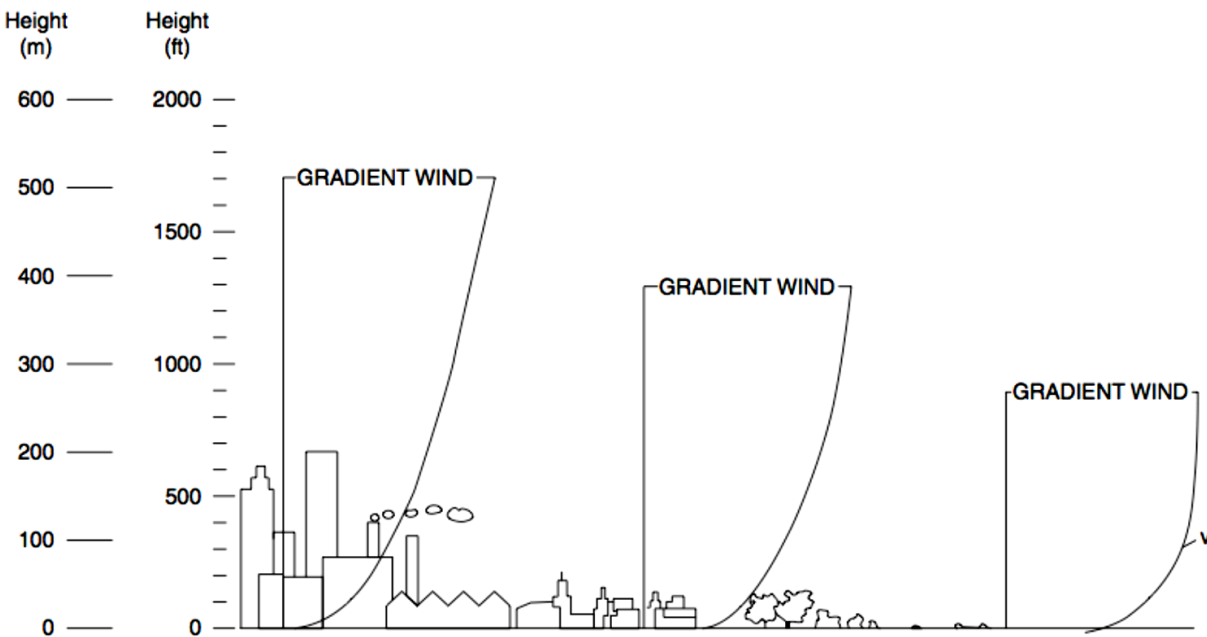


Figure 1.1.1 - Wind profile development for different terrain roughness (Gaetani, 2013)

Three major profiles that fit to such shapes are

1. Power-law (Davenport, 1960)¹

$$U(y) = U_{\text{ref}} \left(\frac{y}{y_{\text{ref}}} \right)^{\alpha} \quad (1.1.1)$$

in which U_{ref} is the mean wind speed at reference point of designation, y_{ref} and α is the dimensionless exponent of the function, which varies with the terrain under study.

2. Log-law, based on existing boundary-layer theory (Oke, 1987)²

$$U(y) = \frac{u_{\text{ABL}}^*}{\kappa} \ln \left(\frac{y + y_0}{y_0} \right) \quad (1.1.2)$$

in which u_{ABL}^* is the friction velocity, κ is the von Karman constant and y_0 , the aerodynamic roughness length. Roughness length in the log-law profile is equivalent to the height at which the wind speed theoretically becomes zero. And finally

3. Deaves and Harris (D&H) model (Cook, 1997)

$$U(y) = \frac{u_{\text{ABL}}^*}{\kappa} \left[\ln \frac{y}{y_0} + 5.75 \left(\frac{y}{h} \right) - 1.88 \left(\frac{y}{h} \right)^2 - 1.33 \left(\frac{y}{h} \right)^3 + 0.25 \left(\frac{y}{h} \right)^4 \right] \quad (1.1.3)$$

in which h is the equilibrium boundary layer height.

The parameters for the models stated are listed in Table 1.1.1. Roughness of the terrain under study in this thesis is at $\alpha = 0.22$ which by interpolating data on Table 1.1.1, gives $y_0 = 0.152$. This is considered to be in suburban category.

Wind modeling is possible with life-size measurement tools in the field, wind-tunnel measurements and, the focus of this thesis, numerical methods. Although a brief review of experimental and semi-empirical methods presented, review of numerical methods which is based on CFD, is delved into in the succeeding section.

¹ Also (Davenport, 1961)

² Derivation given in Appendix A of (Blocken, 2004)

Table 1.1.1 - Atmospheric boundary layer flow fitted function parameters for terrain with different surface roughness (Aynsley, et al., 1977) and (Wang, 2005)

	y_0 [m]	α
Sea	0.0002	0.09
Smooth	0.005	0.125
Open Country with low scrub or scattered trees	0.03	0.15 – 0.17
Roughly open	0.1	0.2
Suburban (rough)	0.25	0.25
Very rough	0.5	0.3
Urban (closed)	1	0.33

1.1.1 Literature Review

This section cites important and related works and studies to this thesis' scope. The works reviewed in this section target a variety of aspects of wind study. Notable aspects are turbulence modeling, validation with wind tunnel or field measurements, different building configuration in the domain, and building size and details. Other less-dealt-with aspects include presenting a state-of-the-art, comparison between turbulence models, discussion on the solver used, different wind parameters and wall treatments.

Murakami presents the state-of-the-art of utilizing turbulence models in wind simulation (Murakami, 1998). This paper presents three types of flow analysis methods, which are direct numerical solution (DNS), Large Eddy Simulation (LES) and Reynolds-Averaged Navier-Stokes (RANS). (Murakami, 1998) cites new models and new techniques of LES. It describes modified versions of Standard k- ϵ model for adopting the bluff body aerodynamics. Between LES, Reynolds Stress Model (RSM) and the Standard k- ϵ , best performance is shown by LES and the latter two are the worst in predicting the reverse flow region of flow field around a square cylinder. Major computational expense of DNS is described in detail for a flow field with Reynolds number (Re) of 10^6 .

Kim and Boysan in (Kim & Boysan, 1999) also investigate the application of Computational Fluid Dynamics (CFD) to environmental flows with considering major issues primarily about meshing and turbulence modeling of CFD.

Ehrhard and Moussiopoulos proposed a non-linear turbulence model to overcome the deficiencies of the Standard $k-\epsilon$ turbulence model and not indulge high computational demand of DNS and LES (Ehrhard & Moussiopoulos, 2000). This study suggests that although there are other linear two-equation turbulence models that have been proposed, none show a significant improvement in simulation accuracy over Standard $k-\epsilon$ in the field of wind engineering. (Ehrhard & Moussiopoulos, 2000) proposes a non-linear turbulence model, which leads to improved results compared to a conventional eddy-viscosity scheme. For validation, simple shear, and boundary layer flows as well as flow around arrays of cubic obstacles were used. And to find out about the accuracy, wind-tunnel measurements are performed. The streamlines around a surface mounted cube under the simulations done in the article are depicted in Figure 1.1.2. Streamlines in Figure 1.1.2 show that the height of the separation bubble on top of the cube is underestimated by the Standard $k-\epsilon$ model. The reason for that, as the authors claim is the well-known overproduction of turbulent kinetic energy, which leads to the flow approaching the stagnation point. Overprediction of turbulent kinetic energy would lead to an increased turbulent exchange downstream of the stagnation region which subtends separation. Having said that, streamlines on the lee in Figure 1.1.2 show that the length of recirculation region is highly overpredicted by Standard $k-\epsilon$.

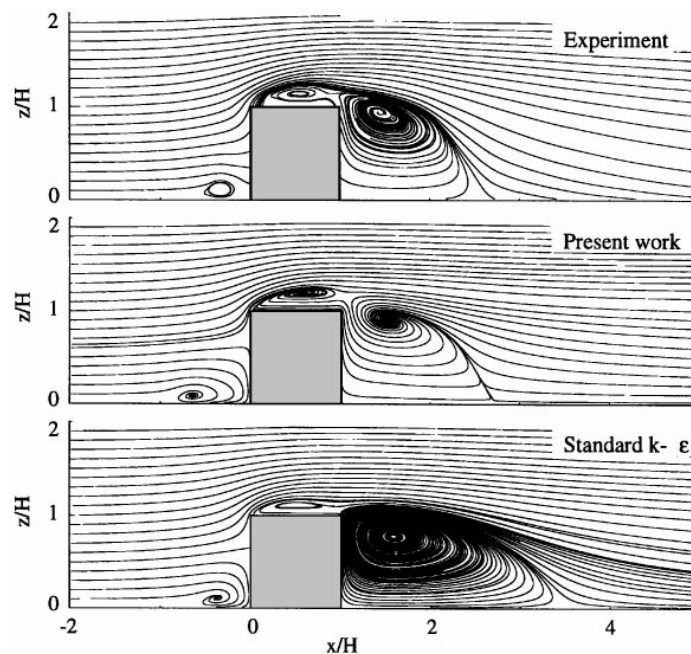


Figure 1.1.2 - Streamlines in the plane of symmetry, surface mounted cube for wind tunnel, non-linear turbulence model proposed and Standard $k-\epsilon$ (Ehrhard & Moussiopoulos, 2000)

This shows a low level of turbulence, which indicated that Standard k- ϵ model incorrectly predicts the production of turbulent kinetic energy in wake regions.

Hanna et al. propose a numerical code with unstructured tetrahedral grids on finite element flow solver (FEFLO) that is used to simulate flow within obstacle array configurations consisting of simple cubical elements (Hanna, et al., 2002). This study shows that the numerical simulations could capture the general flow and turbulence within 40% margin of error on average.

Wright and Easom present a comparison of CFD against full-scale results over a building. A non-linear k- ϵ model is implemented for this study (Wright & Easom, 2003). The authors claim that the non-linear k- ϵ model will result in a better account for the production of turbulent kinetic energy and the anisotropic nature of the turbulence. For the simulations, commercial CFX software is used on a 6-m cubic building. The cube is exposed at 0° and 45° to the wind. The roughness length is set to 0.01 m to represent country open space and the cube walls were given a roughness length equal to 0.005 m. Velocity at building height is set to 10 m/s at the inlet. Four turbulence models including a k- ϵ based model, developed by Murakami, Mochida and Kondo (k- ϵ MMK), Re-Normalization Group (RNG) and the Standard k- ϵ model and the Differential Stress Model (DSM) were tested for both wind directions on the cube. The non-linear expansion of the Boussinesq hypothesis used in (Wright & Easom, 2003) incorporates the best features of both the DSM and the Standard k- ϵ model. The features are listed as numerical stability of Standard k- ϵ and the ability of modeling anisotropic turbulence, as in DSM. The authors conclude that despite the improvements the non-linear k- ϵ model offers to the wind simulation, significant errors were found in the prediction of the pressure distribution.

Zhang et al. provide a numerical model with the RNG k- ϵ turbulence closure to examine three different building configuration effects on wind flow (Zhang, et al., 2005). The results are compared to experimental data, 1:150 scale models tested in low speed wind tunnels were chosen. They suggest that changing wind direction from perpendicular to the building façades to 45°-incidence angle has a significant effect on the flow field for different configurations.

Boundary conditions used in (Zhang, et al., 2005) are

$$u^+ = \frac{u_\tau}{\kappa} \ln(Ey_w^+) \quad (1.1.4)$$

$$k_w = \frac{u_\tau^2}{\sqrt{C_\mu}} \quad (1.1.5)$$

$$\epsilon = \frac{C_\mu^{\frac{3}{4}} k_w^{\frac{3}{2}}}{\kappa y_w} \quad (1.1.6)$$

$$\tau_w = \kappa \rho C_\mu^{\frac{1}{4}} k_w^{\frac{1}{2}} / \ln(Ey_w^+) \quad (1.1.7)$$

in which y_w^+ , κ and E are the wall coordinates, the von Karman constant and a constant respectively. The wall coordinate y_w^+ is defined as $y_w^+ = \rho u_\tau y_w / \mu$ and $u_\tau = \sqrt{\tau_w / \rho}$.

(Zhang, et al., 2005) concludes that for the locations experimentally tested, computational results are generally in good agreement with the wind tunnel results. Moreover, CFD results are faster and more economical to solve wind flow. Building layout strongly affects the wind flow. The authors suggest the use of such study in the design phase of the process to obtain the improved building arrangement.

Blocken, et al. study the CFD simulation of ABL flow, focusing on wall function roughness modifications based on experimental data for sand-grain roughened pipes and channels that are applied at the bottom of the computational domain (Blocken, et al., 2007). The authors investigate the problem of accurate CFD simulation of ABL flow. The modifications proposed are applied to commercial CFD codes including Fluent 6.2 and ANSYS CFX 10.0. (Blocken, et al., 2007) argues that the problem with ABL flow simulation with such commercial software packages is the unintended stream-wise gradients in the vertical mean wind speed and turbulence profiles as they travel through the computational domain. That is the acceleration of horizontal wind speed near the ground as wind passes through the domain. This issue can be partially responsible for the discrepancies that are found further into the domain.

Wind speed conditions in passages between parallel buildings and effect of wall function roughness modifications for the atmospheric boundary layer flow using CFD are done in another study by Blocken et al. (Blocken, et al., 2007). Authors validate the predictions by comparing the

results to wind tunnel measurements. (Blocken, et al., 2007) also studies the effect of well-known physical and fluid dynamics phenomena in urban terrain such as Venturi effect.

Huang et al. present a numerical study of wind effects on standard tall building. They deploy LES, RANS model, etc. to solve wind field around the building and comparison to experimental data gathered in the wind tunnel is the follow up (Huang, et al., 2007). The main objective of (Huang, et al., 2007) is to find an effective and reliable approach for evaluation of wind effects on tall buildings by CFD techniques. Seven different wind tunnels were used to find extensive experimental data to validate and compare the CFD results with. The authors claim that the LES with a dynamic subgrid-scale (SGS) model can give satisfactory predictions for mean and dynamic wind loads on the tall building, while the RANS with modifications can yield encouraging results in most cases and has the advantage of providing rapid solutions. Features of the flow field around such buildings can numerically be captured. It is necessary to correctly simulate both the incident wind velocity profile and turbulence intensity profile in CFD computations to accurately predict wind effects on tall buildings. (Huang, et al., 2007) makes recommendations on CFD technique and associated numerical treatments for designers to access wind effects on a tall building and for detailed wind tunnel test. Fluent software package is used for the simulations in this study. Four typical turbulence models are used for (Huang, et al., 2007), which are: Standard k- ϵ , k- ϵ with Launder and Kato (LK) modification, k- ϵ with MMK modification and LES. MMK is not provided in Fluent and therefore the authors added this to Fluent through a User Defined Function (UDF). Reynolds number of the flow is shown to be high ($>10^5$). One noticeable thing about the simulations in (Huang, et al., 2007) is that they use a power-law function to follow inlet velocity profile of ABL flow.

Kinetic energy of turbulence and its dissipation rate at the inlet section are calculated per the following equations:

$$k = \frac{3}{2} (U_{\text{avg}} I)^2 \quad (1.1.8)$$

$$\epsilon = C_{\mu}^{3/4} \frac{k^{3/2}}{l} \quad (1.1.9)$$

in which U_{avg} is the mean velocity at inlet, I is the turbulence intensity and l is the turbulence integral length scale, which is measured to be 0.58 at the model height, in two wind tunnel tests.

(Huang, et al., 2007) recommends choosing the height of the first boundary layer to be $D_y/4000$ (D_y is the width of the building) and this will ensure the wall unit $y^+ < 5$.¹ A grid dependency study was performed for the simulations as well for meshes with $1.2 \times 10^6 \sim 3.5 \times 10^6$ grid number for the computations by the RANS and the LES. This study concludes that Standard k- ϵ model under-predicts the drag force coefficient C_D by about 20%. Moreover, it finds the wind flow predicted is in steady state, even though it is solved in transient mode, which clearly is incorrect with the Reynolds number range of larger than 10^5 . k- ϵ model with LK modification improves the results of C_D prediction to an error level of less than 5%. MMK model even gives better results than LK and finally LES gives the correct answer for drag coefficient. On turbulence, Standard k- ϵ model excessively over-predicts it with an unrealizable turbulence ratio calculated in the impinging region and wake region. Small separation bubble but large and downstream arch vortex prediction is the result of over-predicted turbulent viscosity (Murakami, 1998). LK model reduces the over-prediction, though it is still there, in the wake region, and MMK performs better than the other two. The authors conclude that although results obtained by CFD are encouraging, wind tunnel measurements are indispensable for the wind effects on buildings and structures.

The comparison between select RANS models are presented for multiple cases from (Yoshie, et al., 2007) in Figure 1.1.3. The RANS models used in (Yoshie, et al., 2007) are Standard k- ϵ , Launder-Kato (LK) k- ϵ and Renormalization Group (RNG) k- ϵ . These figures compare the RANS to experimental scalar wind velocity. The wind speed is normalized according to the wind speed at the same height when there is no building (i.e., wind speed increase ratio).

For regions where there is high wind speed increase ratio, 1.0 or more, which the pedestrian wind environment prediction is of interest, the error margin is within 10%. However, in weak wind regions, this error margin increases. In these regions, the wind speed is found to be less than what experiment shows. Moreover, in comparison between modified k- ϵ models to Standard k- ϵ , in strong wind speed the modified ones perform slightly better. Though in low wind speed regions, Standard k- ϵ is the better model to be used. As far as the reattachment length behind the

¹ y^+ is a non-dimensional distance.

building is concerned, modified k- ϵ models find it longer than the Standard k- ϵ . Wind tunnel experiments are conducted to validate the CFD predictions.

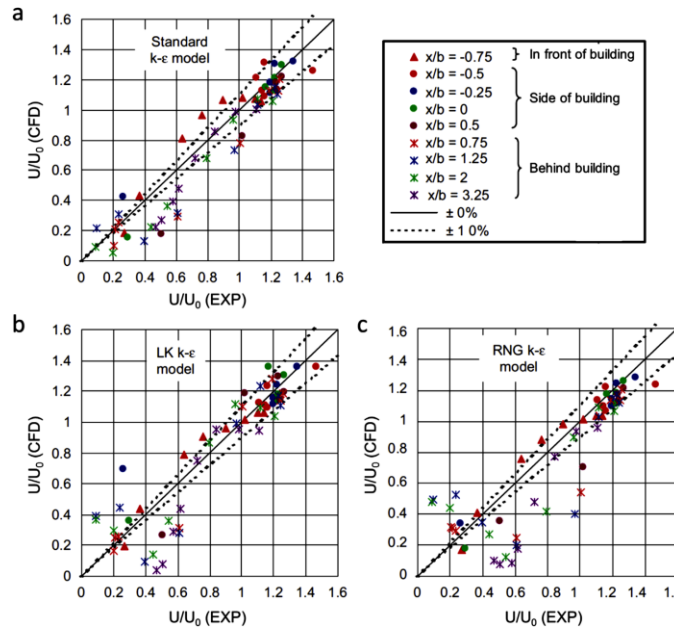


Figure 1.1.3 - Comparison of CFD results and wind tunnel measurements of wind speed ratio for the isolated building by Yoshie et al. (Yoshie, et al., 2007) for steady RANS with Standard k- ϵ model, steady RANS with LK k- ϵ model, and steady RANS with RNG k- ϵ models.

Zhang and Gu present numerical and experimental study of wind-induced interference effects on pressure distributions on a building adjacent to another one in staggered arrangement (Zhang & Gu, 2008). RANS using renormalization group (RNG) k- ϵ turbulence model is used and compared to wind tunnel low-speed boundary layer wind. They report a general good agreement of pressure, base force, and base moment coefficients in different wind directions.

Various studies on effect of turbulence modeling techniques on predicting wind flow around a high-rise building have been conducted. Such as the work of Tominaga, et al., (Tominaga, et al., 2008), that compares CFD results with various revised models of k- ϵ and LES and applied to predict the flow around a high-rise building. Amongst the models used, which are LK model, MMK and Durbin's revised k- ϵ . (Tominaga, et al., 2008) suggests Durbin's revised k- ϵ model performs the best, compared to experimental data. The study suggests that the reason for the good performance of the Durbin's model is based on realizability of the predicted results. More

on that, LES is also deployed to such flow simulation, with and without inflow turbulence. The results are compared to Durbin's model and experiment which show generally good agreement in terms of the distributions of velocity and turbulence energy. LES produces the flow behind the building better due to the fact that the periodic velocity fluctuation behind the building is better reproduced (Tominaga, et al., 2008).

Tominaga et al. in (Tominaga, et al., 2008) give Architectural Institute of Japan (AIJ) guidelines for practical applications of CFD to pedestrian wind environment around buildings. These guidelines are the summary of important points in using the CFD techniques. They are based upon cross-comparison between CFD predictions, wind tunnel test results and field measurements for seven test cases.

The validation process for CFD simulations of wind around a building with large number of simulations, investigating wind comfort at the pedestrian level is carried out by Reiter (Reiter, 2008). The simulation and validations are carried out using ANSYS Fluent and the comparison is made between simulated results and wind tunnel tests. Reiter takes single stand-alone building, two buildings in the domain to find the interaction between the two and urban simulations. This study also tried to optimize the choice of various modeling parameters such as grid resolution and turbulence model used for simulations. At the end, it gives guidelines for numerical wind modeling to quantify wind discomfort levels.

One thing to be noticed is the computational domain size, which must be large enough. (Franke, et al., 2010) gives a practice guideline for the CFD simulation of fluids in an urban environment. (Franke, et al., 2010) uses several turbulence models including Standard k - ϵ , Realizable k - ϵ , renormalization group k - ϵ model for pressure on buildings and Reynolds stress model (RSM) with and without wall damping. The problem with low-Re k - ϵ model is that it predicts the wrong behavior for k and ϵ near the solid wall boundary. And therefore, the k and ϵ equations are modified using algebraic functions to damp certain terms. Classic model of such functions is Launder and Sharma model which is as follows,

$$f_1 = 1, f_2 = 1 - 0.3e^{-Re_T^2}, f_\mu = e^{-\frac{3.4}{(1+0.02Re_T)^2}} \quad (1.1.10)$$

in which

$$\text{Re}_T = \frac{\rho k^2}{\mu \epsilon} \quad (1.1.11)$$

As far as the domain size is concerned, if the height and width are not too different (Hall, 1997) gives recommendations for single buildings. Otherwise they use a domain height of $6H_{\max}$ and the span-wise extent is determined by applying the aspect ratio of the building to the domain (Blocken, et al., 2004).

In front of the building they use a minimum $5H_{\max}$ and behind the building $15H_{\max}$. For multiple buildings, (Blocken, et al., 2004) proposes the wind tunnel dimensions that the experiments done for validation are performed in.

Von Hooff et al. investigate 3D simulation of wind flow and WDR shelter in sports stadia and the influence the stadium geometry has on such flow. These simulations include simulation of 12 generic stadium configurations for both wind flow and wind-driven rain. The WDR is carried out using Lagrangian multiphase flow. Alongside of influence of stadium geometry, roof slope effect is studied. This study also gives guidelines to such simulations (von Hooff, et al., 2011).

An et al. investigate sensitivity study of inflow turbulence profiles on downstream wind velocity and turbulent kinetic energy profiles (An, et al., 2013). This study uses Realizable k- ϵ turbulence model and is validated by wind tunnel measurements. This is done within the street arrays of urban environments. The results of the study show that turbulence is internally generated by the upwind building obstacles. Moreover, the shape and magnitude of downwind velocity and turbulence profiles are not greatly affected by different input turbulence profiles deviating from the baseline turbulence profile. This study finds that even with a significant deviation (50%) in magnitude from the inflow turbulent kinetic energy profile, there is less than 15% difference in the wind speed and turbulent kinetic energy in the downwind region of the urban area.

3D steady RANS CFD for predicting mean wind pressure distributions on windward and leeward surfaces of a mid-rise building with and without balconies is done by (Montazeri & Blocken, 2013). This study shows that RANS can accurately reproduce the mean wind pressure distribution across the windward façade of the building, despite its limitations. Major factors influencing wind-induced pressure distribution are identified to be approach-flow conditions, urban surroundings and building geometry. More on that, the focus of (Montazeri & Blocken, 2013) is on the façade details and how balconies as a major game changing detail can influence

flow pattern and the overall pressure distribution on the façade. For that, medium-rise building with and without balconies are studied. Wind tunnel measurements are used as well as grid sensitivity analysis to validate the results. Since building balconies can introduce multiple areas of flow separation and recirculation across the façade, they can lead to very strong changes in wind pressure distribution. (Montazeri & Blocken, 2013) reports the average deviation from the wind-tunnel measurements are 12% and 10% for the building with and without balconies, respectively. The authors use commercial CFD code Fluent 6.3.26 to perform the simulations. 3D steady RANS equations are solved with Realizable k- ϵ model by Shih et al. (Shih, et al., 1995).

Simulation of wind flow around an isolated building using various types of RANS turbulence models is done by (Toja-Silva, et al., 2015). The authors claim that due to temporal and computational ease of use associated with RANS, they are widely used, though they are highly sensitive to turbulence parametrization chosen and the results can vary according to the application. This article uses OpenFOAM to simulate the wind flow around a stand-alone building and compares the results with benchmark experimental data. It performs a grid dependency analysis to confirm the numerical accuracy of the simulations. What is noteworthy in the study is that amongst all, the cases and models that successfully pass a validation criterion, are analyzed at different regions of the building roof, and the most accurate RANS models for the modelling of the flow at each region are identified. The models used are Standard k- ϵ , Durbin k- ϵ (Durbin, 1996), Durbin-Tominaga k- ϵ (Tominaga, et al., 2008), Durbin-New k- ϵ , Murakami-Mochida-Kondo (MMK) k- ϵ (Tsuchiya, et al., 1997), k- ϵ RNG (Yakhot & Smith, 1992), linear k- ϵ by Yap (Yap, 1987), Non-linear k- ϵ (Shih, et al., 1993) and k- ω SST. On top of that, three source-coefficient sets for the linear k- ϵ models are chosen.

Kim et al. study wind-induced interference effects on wind-loads on a couple of buildings in a series of wind tunnel tests (Kim, et al., 2015). This study is done on typical tall building models using a pressure measurement technique. The authors, consider five types of adjacent building models, with height ratio ($H_r = 0.5, 0.7, 1, 1.5$ and 2) in different wind angles, 0° to 355° in 5° steps. What is discussed in (Kim, et al., 2015) is aerodynamic interference effects on base moments and local wind forces along nine height levels of the principal building.

Joubert et al. simulate the turbulent flow around a surface mounted rectangular prism computationally (Joubert, et al., 2015). The authors use Spalart-Allmaras improved delayed detached eddy simulation (IDDES) turbulence model to solve the flow. What is noticeable is that All- y^+ treatment is used to numerically reproduce the flow features around a rectangular cross-sectional beam. Wind tunnel comparison is used to validate the results.

Cui et al. in (Cui, et al., 2016) investigate inter-unit pollutant dispersion around a multi-story building in two wind directions (zero and 45 degrees) using CFD and validates the results against experimental data with presence of an upstream building in different heights. (Cui, et al., 2016) claims that previous studies on inter-unit dispersion are limited to isolated buildings. The results of this study show that the presence of an upstream building significantly changes the path lines around the downstream target building and the pollutant transportation routes around it. It also claims that the presence of a low upstream building also greatly increases the average air exchange rate (ACH) values and the pollutant re-entry ratios (R_k) on the leeward side of the downstream building for oblique wind incidence.

(Mooneghi & Kargarmoakhar, 2016) presents a study on aerodynamic mitigation techniques applicable to low-rise and high-rise buildings and aerodynamic shape optimization techniques for reducing wind loads on tall buildings are presented using CFD. This article cites past and recent work on various aerodynamic mitigation techniques developed for reducing wind loads on buildings by modifying their shapes and/or adding simple architectural elements. More on that, (Mooneghi & Kargarmoakhar, 2016) uses $k-\omega$ SST turbulence model for all the cases that are run transiently with 20 m/s uniform inlet velocity. The reason is claimed to be its proved ability for modeling detached flows with periodic vortex shedding (Catalano & Amato, 2003).

Blocken et al. review the wind tunnel and CFD techniques and their accuracy to determine pedestrian-level wind speeds around buildings (Blocken, et al., 2016). Per this study, generally, pedestrian-level wind (PLW) simulation is done using methods such as hot-wire or hot-film anemometers, Irwin probes or sand erosion which are low-cost. Keeping in mind that the use of Laser-Dropper Anemometry (LDA) and Particle-Image Velocimetry (PIV) is less often because they are more expensive. Same for CFD modeling, with low-cost RANS being widely used and Large-Eddy Simulations (LES) left untouched due to larger complexity and cost. With amplification factor defined as the ratio of local mean wind speed to mean wind speed at the

same position without buildings present, (Blocken, et al., 2016) claims that there are studies that show the low-cost wind tunnel techniques and steady RANS simulations can provide results within 10% margin of error for high amplification factors (>1) and low accuracy for low amplification factors.

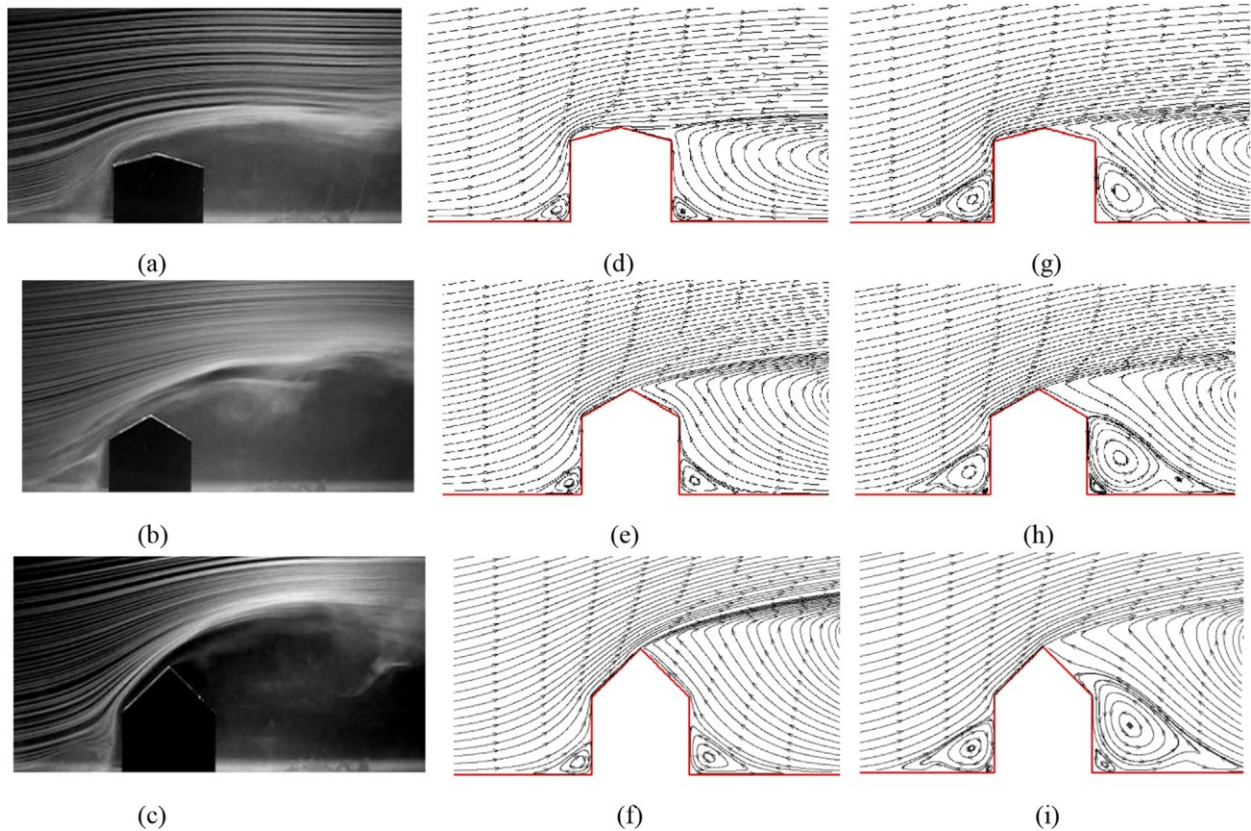


Figure 1.1.4 - Flow patterns around building models obtained with smoke-wire technique, Realizable $k-\epsilon$ turbulence model and Standard $k-\omega$ turbulence model (a,d,g) roof pitch of 15° , (b,e,h) roof pitch of 30° , (c,f,i) roof pitch of 45° (Ozmen, et al., 2016).

Ozmen, et al. investigate the turbulent flow fields on the low-rise building models with gabled roofs having different pitch angles immersed in atmospheric boundary layer experimentally and numerically (Ozmen, et al., 2016). They claim that the mean velocity and turbulence kinetic energy profiles are influenced by the roof pitch. Recirculation regions occur on the leeward part of roofs and at the back of the model, due to flow separation. 15° roof pitch causes more critical suction on the roofs than those of the 30° and 45° roof pitches, Figure 1.1.4.

The authors claim that Realizable k - ϵ turbulence model used in this study exhibits a better agreement at the prediction of mean velocity and turbulence kinetic energy. Standard k - ω turbulence models exhibit better agreement at the prediction of mean pressure coefficients. Models of the Belgian Building Research Institute test building with a scale of 1:100 were studied with 15°, 30° and 45° roof pitches for the wind direction of 90°. Flow visualization, measurements of velocity and surface pressure around the models placed in wind tunnel were made. Largest values of turbulence kinetic energy in this study for entire flow field are found to be at height of the roof level and they prove the presence of the mixing layer between the free stream flow and reverse flow region.

As mentioned at the beginning of this section, less-dealt-with aspects in the literature include presenting a state-of-the-art, comparison between turbulence models, discussion on the solver used, different wind parameters and wall treatments. This thesis targets all those except for a complete state-of-the-art, nor does it include a discussion on the solver used for the simulations.

1.2 Wind-Driven Rain

Rain can be defined as particulate liquid water formed in a cloud heading down to the surface of Earth (Blocken, 2004). If wind and rain happen at the same time, the trajectory of the raindrops deviate from the vertical fall in midair and develop a horizontal component which is wind-driven rain. On the importance of such study, it should be mentioned that WDR is one of the major causes for moisture damages to building façade in urban and sub-urban areas with high amount of precipitation. The accurate quantification of WDR loads on building façades is important for establishing designs that minimize moisture related issues. This, in particular, is accentuated in coastal climates, such as that of British Columbia, Canada. Multiple issues to be named are moisture induced salt migration, structural cracking due to moisture concentration, etc. which are results of porous material build-up and water runoff which is due to WDR itself. Moisture damage to porous materials are freeze/thaw damage, staining, etc. Wood frame construction will suffer from moisture damages, in forms of decay and mold growth to name a few.

There are three major categories to the quantification of WDR, which are numerical methods that are based on CFD, on-site measurements, and semi-empirical methods. There are advantages and disadvantages to each of the mentioned evaluation categories. The focus of this study is the

former, and the results are validated against wind tunnel measurement and on-site WDR measurements, for a building located in Vancouver, British Columbia.

1.2.1 Experimental Methods

Blocken and Carmeliet suggest that due to possible large margins of error, high levels of time consumption as well as costliness, this method is not viable all the time (Blocken & Carmeliet, 2007). Aside from what discussed, the fact that the application of limited measured cases to other cases is most of the time not feasible, is another reason to reconsider the use of on-site measurements.

1.2.2 Semi-Empirical Methods

For the mentioned facts about experimental methods, semi-empirical methods started to be developed. Ease of use and generic data provided by them are the advantage and disadvantage of these methods, respectively. These methods are based mostly on climate conditions, partially addressing the shape, and details of the building and target façade, not to mention the building surrounding buildings in a limited fashion, through “obstruction factor”. For instance, ISO, as a standard, provide calculation procedures for six different simplified building geometries. The semi-empirical model by Straube and Burnett (SB) is another example of such methods.

1.2.3 Numerical Methods

These methods solve the multi-phase governing equations of the wind and rain occurring together. By choosing Lagrangian frame of calculation or Eulerian, numerical solutions to governing Navier-Stokes equations using Computational Fluid Dynamics is divided into two main categories. In the former, predominantly the wind is solved beforehand and raindrops in different sizes are injected into the flow in planes that downstream cover the target façade. And the latter takes every raindrop size on top of the wind to be a distinct phase and solves the whole multiphase flow simultaneously. Several studies have validated both the traditional Lagrangian method of simulation and the relatively new form of solution of WDR, Eulerian.

1.2.4 Literature Review

This section reviews noteworthy works related to WDR simulation. From rain parameters, different numerical methods to solve for WDR motion and deposition and multiple measurement

techniques, to building and surrounding characteristics, this section cites works related to current thesis and shows the areas that lack adequate study.

Blocken and Carmeliet conduct a review of WDR research in building science (Blocken & Carmeliet, 2004) which also describes the principles of each method of quantifying WDR. The authors in a different study, (Blocken & Carmeliet, 2002), present a numerical method to determine spatial and temporal distribution of driving rain on buildings. This method is based on a four-step steady-state simulation technique by Choi (Choi & CSIRO. Division of Building, Construction and Eng., 1991) which is as follows. For the calculation of WDR, the authors suggest to first solve the steady-state wind flow around the building using a CFD code. After that, raindrop trajectories are to be obtained by injecting raindrops of different sizes in the calculated wind flow pattern and solving their equations of motion. Then comes the calculation of specific catch ratio followed by catch ratio calculation from the specific catch ratio and size distribution of raindrops. Best, by using empirical formula, calculates raindrop-size distribution in an air volume with the rainfall intensity as a parameter (Best, 1950), shown in Figure 1.2.1.

The method developed in (Blocken & Carmeliet, 2002) takes building geometry and climatic data at the building site as input. (Blocken & Carmeliet, 2002) identifies three major reasons for the patterns of WDR wetting the building façade which are sweeping of raindrops towards the vertical and top edges of the façade and shelter effect by roof overhangs and means of protection. The article applies the same method to transient rain events, through breaking the transient time interval into a number of equidistant time steps, and takes each of them to be steady-state. This way to each of these subevents, a measured value of wind speed and horizontal rainfall intensity is attributed.

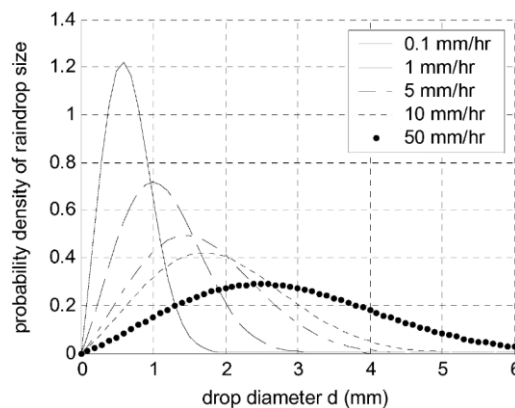


Figure 1.2.1 - Raindrop-size distribution in an air volume with the rainfall intensity as a parameter (Best, 1950)

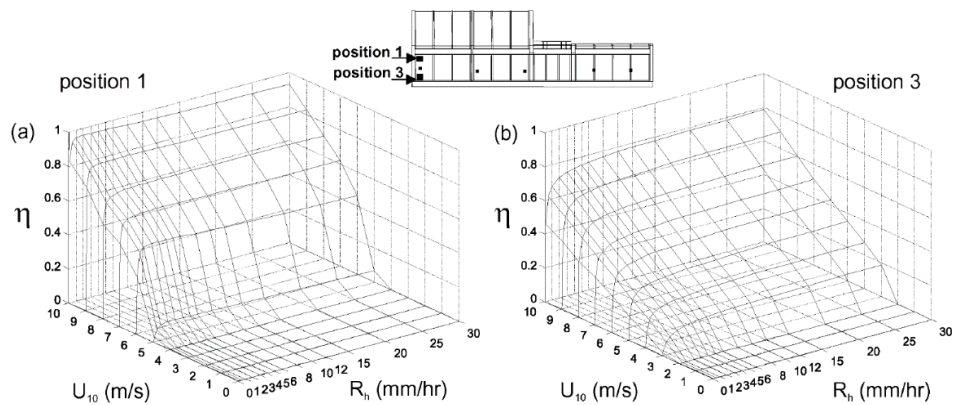


Figure 1.2.2 - Catch ratio η as a function of reference wind speed U_{10} and horizontal rainfall intensity R_h for (a) position 1 and (b) position 3 (Blocken, 2004).

The steady-state calculation is only done for limited number of wind speed and horizontal rainfall intensity couples, shown in Figure 1.2.2. (Blocken & Carmeliet, 2002) also suggests a linear interpolation for the calculation of unknown catch ratio of an unknown couple of wind speed and horizontal rainfall intensity, at a certain time step. Catch ratio of the unknown time step is found from the catch ratio for each of the experimental time steps that are comprised in the set time step. The numerical results in (Blocken & Carmeliet, 2002) are validated against full-scale measurements.

A few years after, Blocken and Carmeliet publish an article to study the effect of wind-blocking effect by a building on its façade's exposure to WDR (Blocken & Carmeliet, 2006). The term "wind-blocking effect" refers to change in wind-flow patterns due to the perpendicular wall boundary, the building, corresponding drop in windward velocity field within certain proximity to the building. (Blocken & Carmeliet, 2006) shows that the wind-blocking effect is one of the main factors that govern the WDR distribution pattern and consequently, concluding that high-rise buildings do not necessarily catch more WDR than low-rise buildings. This study deploys high-resolution experimental WDR database of a low-rise test building in Katholieke Universiteit Leuven. Power-law exponent for the terrain under study is found to be $\alpha = 0.176$. The data is gathered at a 1-min basis rate, which is needed for high quality of experimental data, to achieve accuracy and reliability. The authors conclude that WDR intensity on the building

façade is lower than same intensity at the same location in the space with the presence of the building. They attribute this to the blocking effect of the building. They claim that blocking effect increases when both height and width of the building increase.

(Nore, et al., 2007) gives a dataset of WDR measurements on a low-rise test building in Norway. The authors come up with a model development and model validation using enough information on database (ample size of database). The content includes detailed description of the building, its surroundings, and the meteorological station. WDR measurements are done in free field conditions, which include wind speed, wind direction, horizontal rainfall intensity, temperature, relative humidity, and error estimation for the WDR measurements.

Briggen et al. study the numerical simulation and sensitivity analysis of WDR on the façade of a monumental tower (Briggen, et al., 2009). The focus of the article is rather on the validation of numerical results and the sensitivity of them to the level of geometrical detailing of the computational building model and the upstream terrain aerodynamic roughness length. On-site WDR measurement dataset is used to validate the numerical simulation by CFD. (Briggen, et al., 2009) shows that local effects of geometrical façade details can make differences up to 40%, at lower positions, while leaving negligible at the upper parts of the façade. Log-law is chosen for inlet velocity profile. Realizable k-ε model alongside standard wall functions by Launder and Spalding (Launder & Spalding, 1974) is used in (Briggen, et al., 2009). The height of the wall-adjacent cell is taken to be 6 m for tetrahedral cells, corresponding to a minimum y_p -value of 1.5 m. (Briggen, et al., 2009) studies the sensitivity of the results to aerodynamic roughness length y_0 . Commercial CFD software package Fluent 6.3 is used to solve the RANS equations. For the boundary conditions, the following are taken for inlet turbulence parameters:

$$k(y) = \frac{1}{2} (I_u \cdot U(y))^2 \quad (1.2.1)$$

$$\epsilon(y) = \frac{u_{ABL}^{*3}}{\kappa(y + y_0)} \quad (1.2.2)$$

in which I_u is the turbulence intensity and $U(y)$ is the inlet velocity profile. A comparison of numerical and experimental data is shown in Figure 1.2.3.

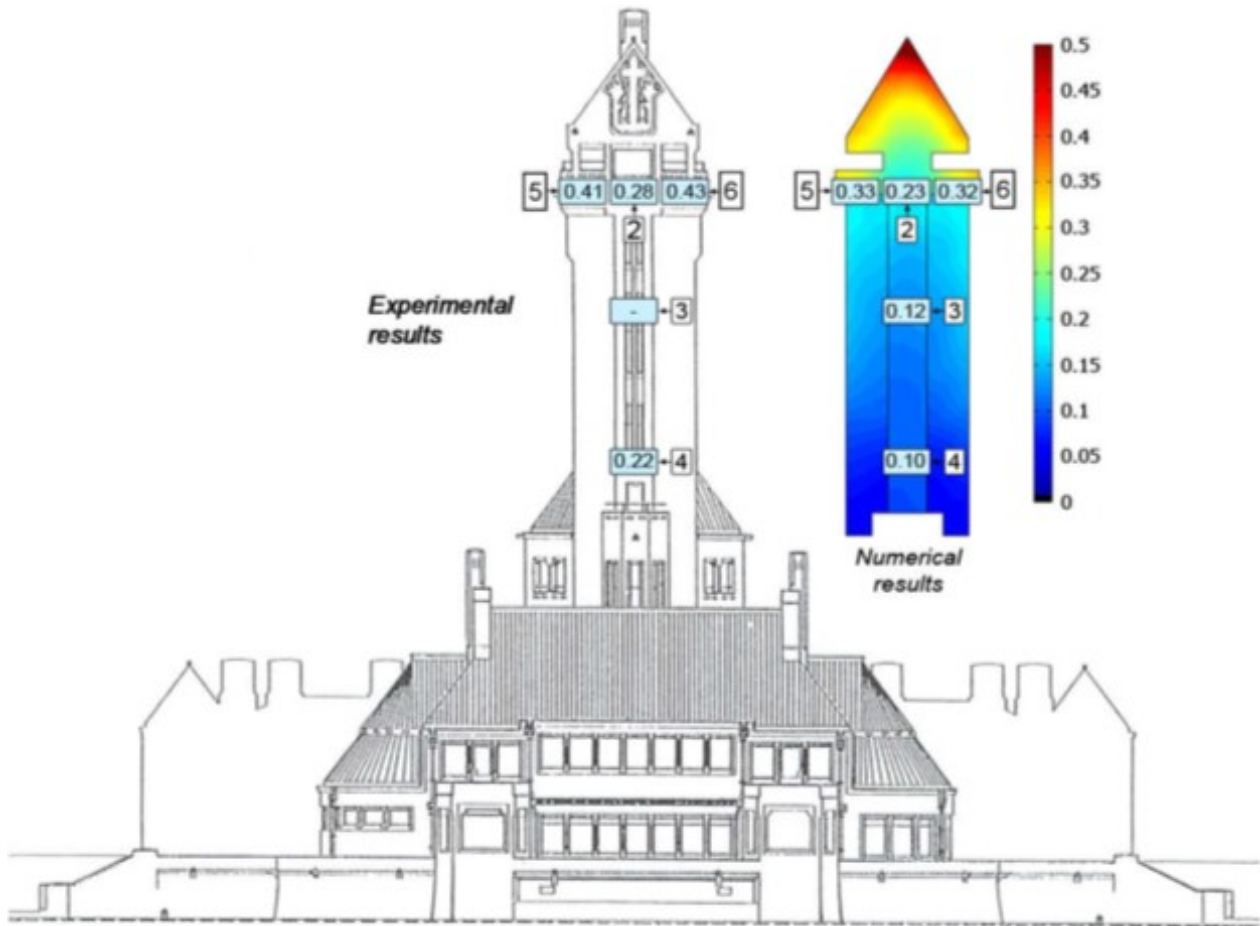


Figure 1.2.3 - Spatial distribution of the catch ratio on the monumental tower. The experimental results at the locations of the wind-driven rain gauges are shown on the left, the numerical results are shown on the right (Briggen, et al., 2009).

The authors report a range of 14% to 30% for the upper part of the tower façade, and consider it a fair agreement, even though simulation underestimates the amount of WDR by more than 50% for lower parts. The underestimation is attributed to exclusion of turbulence dispersion of the raindrops from the simulations, especially for the lower part of the façades of high buildings. Inclusion of façade details for measurement points close to the details have resulted in up to 14% improvement in the results. WDR is reported to be quite insensitive, with differences less than 10% to changes in upstream aerodynamic terrain roughness length y_0 , ranging from 0.5 m to 1 m and 2 m. That is when different inlet mean wind speed profiles are matched at the height of interest, the height of measurement point. Otherwise, authors claim that changes will probably be significant and a correct estimate of y_0 is important.

Blocken and Carmeliet outline and review three state-of-the-art wind-driven rain assessment models and compare them based on model theory (Blocken & Carmeliet, 2010). Semi-empirical model in the ISO standard for WDR (ISO), the semi-empirical model by Straube and Burnett (SB) and the CFD model by Choi, extended by Blocken and Carmeliet. A detailed overview of the three models, including new insights in similarities between these models and relations with recent research results are presented in (Blocken & Carmeliet, 2010). This article shows that influencing parameters of WDR implementation is most highlighted for the CFD model, less for ISO model and the least for SB. The authors claim that the overview and the comparison in (Blocken & Carmeliet, 2010) provide the basis for future comparison studies and future improvements of the semi-empirical models.

Blocken et al. make a comparison between calculation models for WDR deposition on building façades (Blocken, et al., 2010). The models compared are the same as ones studied in (Blocken & Carmeliet, 2010). Authors of this study apply models, such as ISO, SB and CFD, to simulate wind and rain on four identical buildings under steady-state condition.

Blocken, et al., investigate the application of CFD in building performance simulation for the outdoor environment (Blocken, et al., 2011). This study involves background, need for CFD, overview of some past CFD studies. It also includes a discussion about accuracy and some perspectives about practical application on various phenomenon including pedestrian wind environment around buildings. As well, it features WDR on building façades, convective heat transfer coefficient at exterior building façades and air pollutant dispersion around buildings. On top of all that, (Blocken, et al., 2011) discusses the advantages and disadvantages of CFD.

Pérez-Bella et al. combine the use of WDR and wind pressure to define water penetration risk into building façades (Pérez-Bella, et al., 2013). This study is done for a case in Spain. New index is defined to measure the penetration risk. (Pérez-Bella, et al., 2013) combines two atmospheric exposures that are WDR and the action of wind pressure simultaneous with precipitation or driving rain wind pressure (DRWP). Moreover, it presents a risk index map. Ultimate objective of (Pérez-Bella, et al., 2013) is improvement on the current Spanish building regulations governing the design of façades against the penetration of atmospheric water.

Huang and Li perform numerical simulations of wind-driven rain on building envelopes based on Eulerian multiphase model (EM) (Huang & Li, 2010). This study uses the Eulerian multiphase

model which unlike Lagrange-frame based models, simplifies the evaluation of WDR parameters, as well as the boundary condition treatments. It also offers a higher efficiency in transient state of WDR prediction. Using a numerical example, (Huang & Li, 2010) validates the prediction of EM with experimental and numerical data.

Kubilay, et al. simulate and validate WDR on a building façade with a Eulerian multiphase model (Kubilay, et al., 2013). The validation is done for a tower building. The authors attribute the deviation between the field measurements and the model results to low rainfall intensity and wind speed to absence of turbulent dispersion. Eulerian multiphase modeling (EM) advantages are presented in (Kubilay, et al., 2013) as well.

In another study, Kubilay et al. use the same model as in (Kubilay, et al., 2013) and addresses the lack of numerical studies on the WDR intensity in generic and idealized multi-building configurations (Kubilay, et al., 2014). This article solves WDR on an array of 9 low-rise cubic building models for three different wind directions. Aside from the use of EM modeling, turbulent dispersion of raindrops is counted in. For the validation of the simulations, data from field measurements in Dübendorf, Switzerland are deployed after two rain events with different characteristics. (Kubilay, et al., 2013) finds the influence of turbulence dispersion for raindrops to be lower than 3% for both rain events. It also sees that even though the maximum WDR intensity is lower on the façades, the whole building is exposed to up to 57% more WDR.

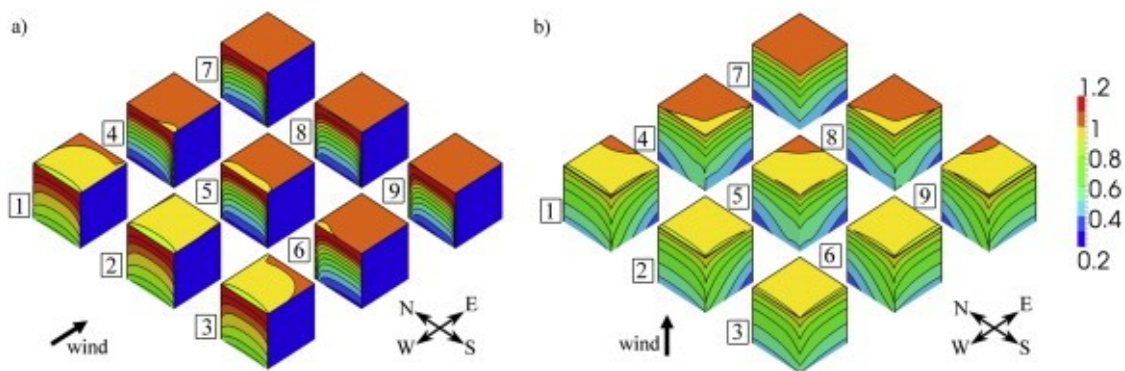


Figure 1.2.4 - Catch ratio distribution on façades and roofs of all cubes for the reference wind speed $U = 5$ m/s and the reference rainfall intensity $R_h = 1$ mm/h for wind from a) west and b) southwest. (Kubilay, et al., 2014)

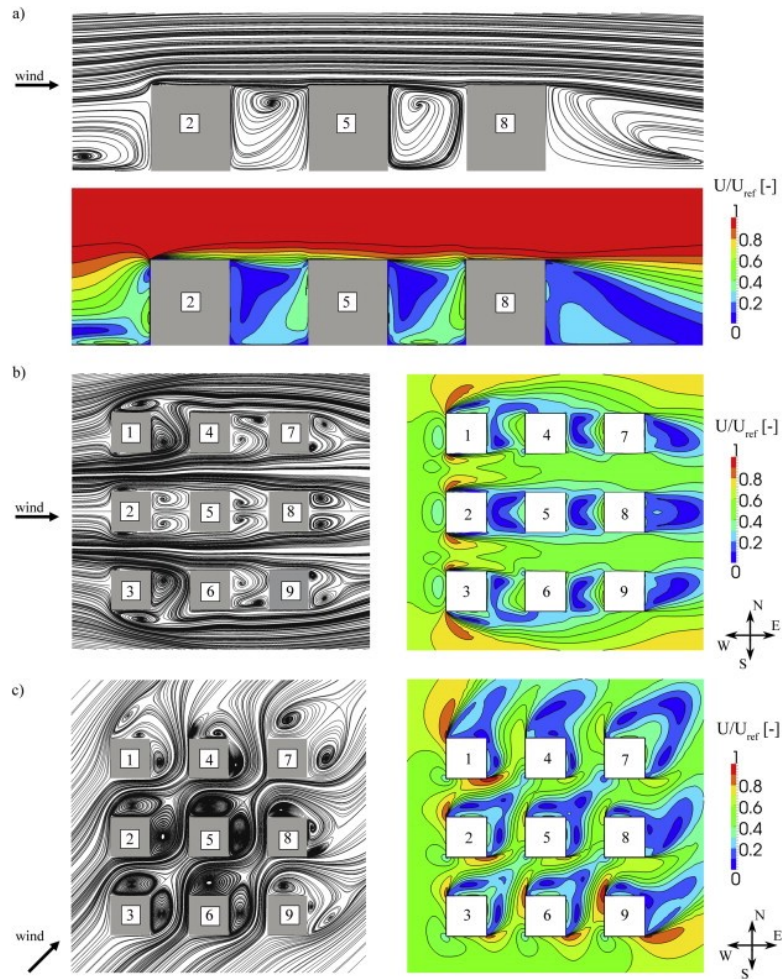


Figure 1.2.5 - Streamlines and contour plot of the wind flow in the a) vertical center-plane for wind from west, b) horizontal plane at $y = 1$ m height for wind from west, c) horizontal plane at $y = 1$ m height for wind from southwest. Streamlines in b) and c) are projected on the horizontal plane and hence have no out-of-plane component (Kubilay, et al., 2014)

Mohaddes Foroushani et al. study the effect of roof overhangs on wind-driven rain wetting of a low-rise cubic building (Mohaddes Foroushani, et al., 2014). This study focuses on the numerical side of the investigation. The effect of various sizes of overhang on the wind-driven rain wetting of a low-rise building for various wind and rain conditions is studied. Validation of the results is done against experimental and numerical data provided in the literature. (Mohaddes Foroushani, et al., 2014) introduces a new global measure to quantify the effectiveness of overhangs in protecting façades from WDR. The authors use Commercial CFD code Fluent to find the steady state solution to RANS equations governing the wind and introduce raindrops later to the domain and track the trajectories. Power-law inlet velocity profile alongside Realizable $k-\epsilon$ with standard

wall functions is deployed for the simulations. Lagrangian particle tracking of raindrops are performed with a fourth-order Runge-Kutta integration scheme, alongside a fourth-order curve fit to the drag coefficients for falling raindrops which is as follows (Gunn & Kinzer, 1949)

$$\log(C_D) = 0.0358 z^4 - 0.2255 z^3 + 0.5731 z^2 - 1.2462 z + 1.4633 \quad (1.2.3)$$

in which $z = \log(\text{Re}_d)$. These parameters and functions used for Lagrangian particle tracking are deployed in current study as well. The authors choose the following inlet turbulence kinetic energy parameters for the simulations, proposed by (Blocken, 2004)

$$k = \frac{(u_{ABL}^*)^2}{\sqrt{C_\mu}} \quad (1.2.4)$$

$$\epsilon(y) = \frac{(u_{ABL}^*)^3}{\kappa(y + y_0)} \quad (1.2.5)$$

Ge et al. use a six-story building to quantify the effectiveness of overhang on the reduction of WDR (Ge, et al., 2017). This mid-rise building is subjected to field measurements. The effectiveness of overhang is evaluated using similarity and symmetry approaches which shows good agreement. This study investigates the spatial distribution of WDR on building façade with and without overhang. In addition, the effectiveness of the overhang is studied with respect to wind speed, wind direction and rainfall intensity. The measurements done suggest that larger overhang provides greater protection, i.e. higher effectiveness. Moreover, from the side edge to the center of the façade, the effectiveness increases. Another observation made from the measurements in (Ge, et al., 2017) is that with the distance from the roofline, overhang effectiveness decreases with a smaller gradient for the larger overhang. Also, the effectiveness increases for oblique winds, though it decreases with an increase in wind speed. This study concludes that overhang provides a shelter which decreases as wind speed increases. The reason for that is stated to be that the trajectory of raindrops become more inclined and the sweeping effect becomes more significant.

As discussed, simulation of WDR on a medium-rise building is rather scarce in the literature. A detailed study of how different schemes including the choice of inlet velocity profile, choice of turbulence model and effect of surroundings on the simulations, alongside the discussion on how each of those choices will affect the predictions in each region of the windward façade of the

medium-rise building is lacking. WDR is parameterized in various regions of the façade with variation of wind speed, rainfall intensity and wind direction.

1.3 Overhang

There are multiple architecture phenomena that will alter the wind flow and consequently the deposition of rain on the building façade, compared to a generic cubic flat building. Cornices, gabled and pitched roof, inset corners, and balconies are some of many. Amongst all, one that is predominantly dedicated to façade protection in coastal regions is overhang. Deflection, drainage, drying and decay resistance are identified by Hazleden and Morris as the four D's of wall design (Hazleden & Morris, 1999). The authors claim that deflection is the first line of defense for the wall system and roof overhang is the primary rain deflection apparatus.

1.3.1 Effectiveness of Overhang

In Southern British Columbia, a field survey on building envelope failure shows that walls protected with wider overhangs have less destructive issues (Hershfield, 1996). Ge and Krpan show that the analysis of WDR data indicates that the WDR exposure of a building site is significantly influenced by the local topography and surrounding buildings and objects (Ge & Krpan, 2009). Moreover, equipping a façade of a low-rise building with 0.3-0.6 m overhang can reduce the impingement of WDR by about 4 times and one and a half times for high-rise buildings, for a small overhang. The authors claim that since the higher amount of driving rain received by high-rise buildings is due to the high rain deposition at the upper part of the building, an overhang may be effective for high-rise buildings in coastal climates.

Blocken and Carmeliet conclude that the shelter effect of the roof overhang increases as the overhang length increases (Blocken & Carmeliet, 2002). Using CFD as discussed before, they claim that near the vertical edges of the sloped roof module, the sweeping effect of drops, both sideward and upwards, diminishes the shelter effect and the line separating sheltered and non-sheltered area (shelter line) shows an upward curvature. Also, at the roof edge of the façade, not employing protection would give rise to high specific catch ratio values. The occurring of the highest values of catch ratio are said to be at the top and side edges; and with the presence of a roof overhang, just below the abrupt transition of from sheltered to non-sheltered area. (Blocken & Carmeliet, 2002) claims that the shelter provided by roof overhang decreases as wind speed

increases, as the trajectories are more inclined and the sweeping effect becomes more important. It also claims that shelter decreases as the raindrop diameter decreases, although this is less pronounced than the influence of wind speed. Although, as discussed previously, overhang is not the objective of (Blocken & Carmeliet, 2002) and the main conclusions. Moreover, dependency of the shelter effect of the overhang to rainfall intensity is not presented in the study. Above all, overhang is not parameterized to be studied and it is a part of the architecture of the test building. In the experimental methods of finding WDR, the work of validation of CFD simulation of WDR on low-rise building, by Blocken and Carmeliet examines the CFD simulations to determine the spatial and temporal distribution of WDR on the façade of a low-rise building. This study incorporates façade details, such as overhang in different sizes, pitched and flat roof simulations. Though the overhang on the test building used in (Blocken & Carmeliet, 2002) is a part of the building and not a target of the study.

Abuku et al. perform a CFD simulation of WDR for a rectangular low-rise test building (Abuku, et al., 2009). They use three different rain events with oblique wind directions. Full-scale measurements were used to validate the predictions. They find the results to be quite satisfactory with significant discrepancies near the roof overhang and near the downwind edge of the façade. The authors attribute the differences downwind to the difficulty of accurately predicting the raindrop impact position at this location for oblique wind. Moreover, they find turbulent dispersion being partially responsible for the differences.

A few other studies such as (Mohaddes Foroushani, et al., 2014), as discussed before, investigate the effectiveness of the overhang more in depth, numerically, and experimentally (Ge, et al., 2017). Lack of proper boundary treatment in the former and the experimental nature of the latter results in the necessity of the current thesis' focus partially on the subject matter.

1.4 Summary of Literature Review

Various papers and studies target different turbulence modeling techniques in variety. Point left out in a lot of those studies is the comparison between set techniques, on wind and WDR simulation. Specifically, as different models predominantly perform differently in different regions of a domain of a ABL flow, the discussion on which of those modeling techniques is a better fit is missed.

In high precipitation areas, field measurements are done in abundance. Even though the missing parts on that are shortage of parametric study on catch ratio. Predominantly, the effectiveness of overhang is rather missed in the literature. Same issue is found with the effect of façade details on catch ratio.

Current thesis addresses the lack of proper parametric study of effectiveness of overhang for a medium-rise building suburban area. The parameters under study are overhang length and shape, wind speed, rainfall intensity and wind direction at various regions of the façade under study. To address the lack of adequate comparison between the performance of turbulence models, in specific regions and the façade in whole, detailed study also targets the subject matter in this thesis.

1.5 Scope

This research is part of the Natural Science and Engineering Research Council of Canada's NEWBuildS network. NEWBuildS is a multi-disciplinary NSERC strategic research network for Engineered Wood-based Building Systems. NEWBuildS focus is on projects related to the use of wood-based products in medium-rise and non-residential construction. Projects of such cover a wide range of building performance issues including: fire, durability, structural, energy and serviceability. The current study is categorized under the theme "Durability and Energy".

Due to inadequate investigation in the effect of multiple parameters governing an overhang protection of a building façade, this thesis focuses on parameterizing catch ratio prediction and effectiveness of an overhang, on a medium-rise building. In addition, current work investigates the suitable choice in wind and WDR modeling technique.

1.6 Aim and Methodology

Primary goal of this study is studying and quantifying the effectiveness of the overhang, in various shapes and sizes, parametrically, under different WDR conditions using CFD. This is due to the need for a better understanding of the façade protection against WDR. The developed CFD model is validated by collected field measurements and wind tunnel collected data. While making recommendations on proper simulation technique, the choice between certain wind modeling schemes and its effect on WDR results obtained, the final checkpoint of this study will

be providing building design teams and architects a robust tool to fetch for a protection for vulnerable façade envelopes from WDR deposition using different overhang size and shapes.

Secondarily, as this work is majorly numerically themed, proper modeling, verification, and validation of numerical solution to RANS and consequently, WDR simulation is one of the objectives.

The latter, comprises of reaching multiple checkpoints. Main obstacle on the way is the meshing of the domain. Dealing with conventional two-equation turbulence models, alongside Standard wall function to address the boundary, the inadequately-dealt-with questions are the method of meshing, proper choice of boundary parameters and wall treatment. This study addresses such issues with attending multiple points of view, including consistency of proper simulation of the atmospheric boundary layer (ABL) flow with respect to meshing and boundary treatment methods and parameters. Proper modeling involves the choice of turbulence model as well as inlet velocity profile fit to ABL, on both stand-alone and surrounded building.

The test building is in suburban terrain in Vancouver, British Columbia. It is a mid-rise six-story flat roof building with a mechanical room mounted on top of it. For validation of the wind modeling, extensive wind-tunnel measurements are used to validate CFD results of the wind simulation, for both stand-alone and surrounded building exposed to different wind directions, at various locations around the test building, including vertical profiles upstream, near façade and on top of the roof and horizontally on its side. This comparison between wind tunnel and CFD is then justified for different regions separately.

A method of making different viable rain events is introduced as the hourly field measurement data gathered is unreliable for a short period, unless the rainfall intensity is considerably high, which happens rarely in the data collected for validation of WDR part of this study. Multiple constructed rain events are then used to validate numerically predicted WDR for surrounded and stand-alone building. This is done for unprotected and protected façade with different sized on-site overhangs. The validity of the simulation on different façade regions is also discussed.

1.7 Thesis Outline

Current chapter of the thesis addresses the necessity of such study, brief presentation of the methods deployed, and detailed literature review of the subject matter. Chapter 2 presents a

detailed description of the methods used for simulation alongside model verification. Chapter 3 is dedicated to validation of the wind and rain modeling, and the overhang protected rain simulation and the results, as well as the necessary discussions. Chapter 4 studies the effectiveness of the overhang, in an extensive parametric fashion. Final chapter is the conclusions and recommendations made by the author.

Chapter 2 NUMERICAL SIMULATION AND MODEL VERIFICATION

Numerical solution to fluid simulation comprises of various checkpoints to be able to depend upon. From the meshing to actual model attributed to fluid motion, to post processing and validation, all are to be properly addressed in current study. In WDR case specifically, as it deals with a multiphase flow simulation, which is categorized in two major phases, air (wind) and water (rain), all those steps are to be followed for each, separately and hierarchically.

2.1 Governing Equations

The flow of air through the atmosphere of Earth, near the ground is considered as wind. For that matter equations governing such flow are mass conservation, and continuity as well as heat equations. Adding rain should be considered as another phase. This results in the necessity to consider WDR a multiphase flow. Contribution of rain phase to space occupation and momentum of the flow, and momentum of the air phase should in theory be considered. Though, conventionally, this contribution is neglected since it is very small compared to the flow in general. This would suggest the use of “one-way” coupling (Elghobashi, 1994). The reason for this is the small value that “phasic volume fraction” of rain in such flow, WDR. Wind governing equations are continuity:

$$\frac{\partial \rho}{\partial t} + \nabla \cdot (\rho \mathbf{u}) = 0 \quad (2.1.1)$$

and Navier-Stokes equations:

$$\frac{\partial(\rho u_i)}{\partial t} + \frac{\partial(\rho u_i u_j)}{\partial x_j} = -\frac{\partial p}{\partial x_i} + \frac{\partial(\tau_{ij})}{\partial x_j} + S_i \quad (2.1.2)$$

in which

$$\tau = \mu \left(\nabla \mathbf{u} + (\nabla \mathbf{u})^T - \frac{2}{3} \delta \nabla \cdot \mathbf{u} \right) \quad (2.1.3)$$

and δ is Kronecker delta. ρ is the density, and \mathbf{u} is the velocity vector. p is pressure, S_i is the momentum source term and τ_{ij} is the shear stress tensor. Time averaged continuity and Navier-Stokes equations are as follows. These equations are obtained using the definition of time average on the corresponding equations:

$$\frac{\partial \rho}{\partial t} + \frac{\partial}{\partial x_j} (\rho U_j) = 0 \quad (2.1.4)$$

$$\frac{\partial \rho U_i}{\partial t} + \frac{\partial}{\partial x_j} (\rho U_i U_j) = -\frac{\partial p}{\partial x_i} + \frac{\partial}{\partial x_j} (\tau_{ij} - \overline{\rho u'_i u'_j}) + S_M \quad (2.1.5)$$

where τ is the molecular stress tensor (including both normal and shear components of the stress). The problem of turbulent flow modeling is revealed here in the Reynolds Average Navier-Stokes equations (RANS) and that is the term $-\overline{\rho u'_i u'_j}$. This term is known as the Reynolds-stress tensor. In a three-dimensional (3D) simulation, this term produces six unknowns that are to be calculated and because there is no additional equation for these six unknowns, the problem is not closed (Wilcox, 2006). To close the equation set, multiple two-equation models are proposed. Three of those models are employed in simulation in this study.

2.2 Turbulence Modeling

2.2.1 Realizable k- ϵ Model

The term "realizability" means that "all physically positive-definite turbulence properties be computationally positive-definite and that all computed correlation coefficients lie between ± 1 "¹. This means that the model mathematical and physical constraints posed on Reynolds stresses, are found to be consistent with the physics of the flow.

2.2.2 Standard k- ω Model

Kolmogorov proposed the second parameter for a two-equation model of turbulence to be the dissipation per unit turbulence kinetic energy, ω (Kolmogorov, 1942). In this model, ω satisfies a differential equation similar to the equation for kinetic turbulence energy, k (Wilcox, 2006). One problem with this model which is based on Wilcox model is that the solution is sensitive to values of k and ω outside the shear layer (which is called freestream sensitivity).

2.2.3 Shear-Stress Transport (SST) k- ω Model

This model accounts for the transport of the turbulent shear stress. That is why it predicts the eddy-viscosity more accurately. That is why this model is more accurate and reliable for a wider class of flows (Menter, 1993).

¹ (Wilcox, 2006) Section 6.3: Second-Order Closure Models

2.2.4 Standard Wall Functions

Based on the work of Launder and Spalding (Launder & Spalding, 1974), ANSYS Fluent presents the standard wall functions. These are used in this work for Realizable k-ε turbulent models. For the mean velocity, we have:

$$U^* = \frac{1}{\kappa} \ln(Ey^*) \quad (2.2.1)$$

in which the dimensionless velocity is:

$$U^* = \frac{U_p C_\mu^{\frac{1}{4}} k_p^{\frac{1}{2}}}{\frac{\tau_w}{\rho}} \quad (2.2.2)$$

and the dimensionless distance from the wall is:

$$y^* = \frac{\rho C_\mu^{\frac{1}{4}} k_p^{\frac{1}{2}} y_p}{\mu} \quad (2.2.3)$$

and the constants are listed in Table 2.2.1.

Table 2.2.1 - Standard wall function parameters and constants

Constant	Description
κ	von Kármán constant (= 0.4187)
E	Empirical constant (= 9.793)
U_p	Mean velocity of the fluid at the wall-adjacent cell centroid, p
k_p	Turbulence kinetic energy at the wall-adjacent cell centroid, p
y_p	Distance from the centroid of the wall-adjacent cell to the wall, p
μ	Dynamic viscosity of the fluid

It should be noted that ANSYS Fluent employs log-law when $y^* > 11.225$. Below that value, it applies the laminar stress-strain relationship which is

$$U^* = y^* \quad (2.2.4)$$

The boundary condition for k at the wall is as follows

$$\frac{\partial k}{\partial y} = 0 \quad (2.2.5)$$

in which y is the normal coordinate to the wall.

2.2.5 Matching the Wall-Function-Modified-for-Roughness and ABL Flow

The following so-called 7-step procedure to adjust boundary conditions for a log-law profile to ABL flow, which is suggested by Blocken is used in this study (Blocken, 2004). Log-law profile is as follows

$$U_{ABL}(y) = \frac{u_{ABL}^*}{\kappa} \ln\left(\frac{y + y_0}{y_0}\right) \quad (2.2.6)$$

Two requirements for compatibility are as follows

$$U_{p,LOW} = U_{p,ABL} \quad (2.2.7)$$

$$\tau_{w,p,LOW} = \tau_{w,p,ABL} \quad (2.2.8)$$

These two equations lead to

$$k = \frac{(u_{ABL}^*)^2}{\sqrt{C_\mu}} \left(\frac{y_p}{y_p + y_0}\right)^2 \quad (2.2.9)$$

$$\epsilon(y) = \frac{\left(u_{ABL}^* \cdot \frac{y_p}{y_p + y_0}\right)^3}{\kappa y} \quad (2.2.10)$$

and the roughness height is set to

$$K_s = y_0 \quad (2.2.11)$$

and roughness constant is calculated with the following equations, as for all the cases studied in this thesis, $K_s^+ > 90$

$$\Delta B = \frac{1}{\kappa} \ln(1 + C_{K_s} K_s^+) \quad (2.2.12)$$

in which ΔB is found by

$$A = \exp(\kappa \Delta B) \quad (2.2.13)$$

and

$$A = \frac{u_{ABL}^* E}{\nu} \cdot \frac{y_p^2}{y_p + y_0} \cdot \left(\frac{y_0}{y_p + y_0} \right)^{\frac{y_p + y_0}{y_p}} \quad (2.2.14)$$

For power-law profile, we have

$$U_{ABL}(y) = U_{ref} \left[\frac{y}{y_{ref}} \right]^{\alpha_p} \quad (2.2.15)$$

by applying the same compatibility requirements

$$k = \left(\frac{\alpha_p \kappa U_{ref}}{C_\mu^{\frac{1}{4}}} \left(\frac{y_p}{y_{ref}} \right)^{\alpha_p} \right)^2 \quad (2.2.16)$$

$$\epsilon(y) = \frac{\left(\alpha_p \kappa U_{ref} \left(\frac{y_p}{y_{ref}} \right)^{\alpha_p} \right)^3}{\kappa y} \quad (2.2.17)$$

For k- ω turbulence models, the use of Realizable k- ϵ model modifications and finding k- ω model parameters on that basis is suggested, using the following equation for ω calculation on the inlet boundary (Wilcox, 2006)

$$\omega = \frac{\epsilon}{C_\mu k} \quad (2.2.18)$$

Table 2.2.2 shows the modified inlet turbulence parameters for each velocity profile used in current study.

Table 2.2.2 - Modified inlet turbulence parameters for the velocity profiles used in this study

	Log-Law	Power-Law
Velocity Profile	$U_{ABL}(y) = \frac{u_{ABL}^*}{\kappa} \ln \left(\frac{y + y_0}{y_0} \right)$	$U_{ABL}(y) = U_{ref} \left[\frac{y}{y_{ref}} \right]^{\alpha_p}$
Turbulent Kinetic Energy	$k = \frac{(u_{ABL}^*)^2}{\sqrt{C_\mu}} \left(\frac{y_p}{y_p + y_0} \right)^2$	$k = \left(\frac{\alpha_p \kappa U_{ref}}{C_\mu^{\frac{1}{4}}} \left(\frac{y_p}{y_{ref}} \right)^{\alpha_p} \right)^2$
Turbulent kinetic energy dissipation	$\epsilon(y) = \frac{(u_{ABL}^* \frac{y_p}{y_p + y_0})^3}{\kappa y}$	$\epsilon(y) = \frac{(\alpha_p \kappa U_{ref} \left(\frac{y_p}{y_{ref}} \right)^{\alpha_p})^3}{\kappa y}$
Turbulent specific dissipation rate	$\omega = \frac{\epsilon(y)}{C_\mu k}$	$\omega = \frac{\epsilon(y)}{C_\mu k}$

2.3 Wind-Driven Rain

2.3.1 Numerical Solution to Wind and WDR

As previously mentioned, numerical solution comprises of the influence of turbulence models, inlet velocity profiles and boundary treatment. Accuracy of wind flow prediction by CFD needs to be investigated. In this section, the modeling results of wind flow around the building under study are compared to wind tunnel mean wind velocity measurements for validation. The modeling results of rain deposition on the east façade of the test building are compared to field measurements. Both the stand-alone building and surrounded building are studied.

On the procedure that led to this study, primarily, best meshing scheme was studied and found. This is done by investigating the proposed modifications on two-equation turbulence models and their effectiveness described in the section “Matching the Wall-Function-Modified-for-Roughness and ABL Flow” (Blocken, 2004). Consequently, wind solution is set up for different inlet velocity profiles and turbulence models of interest in (Blocken, 2004). Each case is validated and compared to wind tunnel data gathered at “Wind Tunnel Lab” at Concordia University (Chiu, 2016). The results of such validation on every case is presented in this chapter. Based upon that, various catch ratio cases are set up for each scheme of solution. The parameters are set based on field measurements done in Vancouver, British Columbia, on a six-story test building (Chiu, 2016). Each rain event chosen is a weighted average of multi-hour consecutive rain hours. Multiple chosen rain events for set building’s east façade in three configurations, without overhang and with 2’ and 4’ overhangs are solved. Such cases with and without an overhang are chosen to validate rain simulation with CFD and find the proper solution scheme to predict WDR more accurately with. The reason for such way of validation is to eliminate the effect of geometry on the validity of results. As the rain events chosen for averaging are transient rain and wind hours, and the direction is fluctuating, another study on the angle is performed to capture the effect of small change in angle of incidence of wind on the catch ratio. This study shows that $\pm 10^\circ$ range has a negligible effect on the final deposited rain on the façade, in such simulations. Furthermore, chosen CFD simulation scheme is developed to perform the simulations for various number of rain events, to be able to parametrically study WDR.

2.3.1.1 Building Geometry, Computational Domain, and Grid Study

Building under study is a six-story (mid-rise) rectangular residential building with a flat roof and a short parapet located in Vancouver, British Columbia, Figure 2.3.1. A mid-rise building is a building between 4 and 11 stories in height. As far as the terrain under study is concerned, the building sits atop an escarpment with the east façade facing the direction of the escarpment and is surrounded by 3-story residential buildings to its north and west and a highway to its east and south. The simulated building is 39.67 m long, 15.42 m wide, and 20.05 m high. A mechanical room measuring 6 m by 5.2 m and 2.4 m high is in the center of the main roof. The building façades face the cardinal directions with one of the long façade facing east, the prevailing wind direction. It is an open site within a suburban setting, which makes it an ideal site for WDR studies (Chiu, 2016).

Simulated building with its surroundings within 200-meter radius is depicted in Figure 2.3.2.

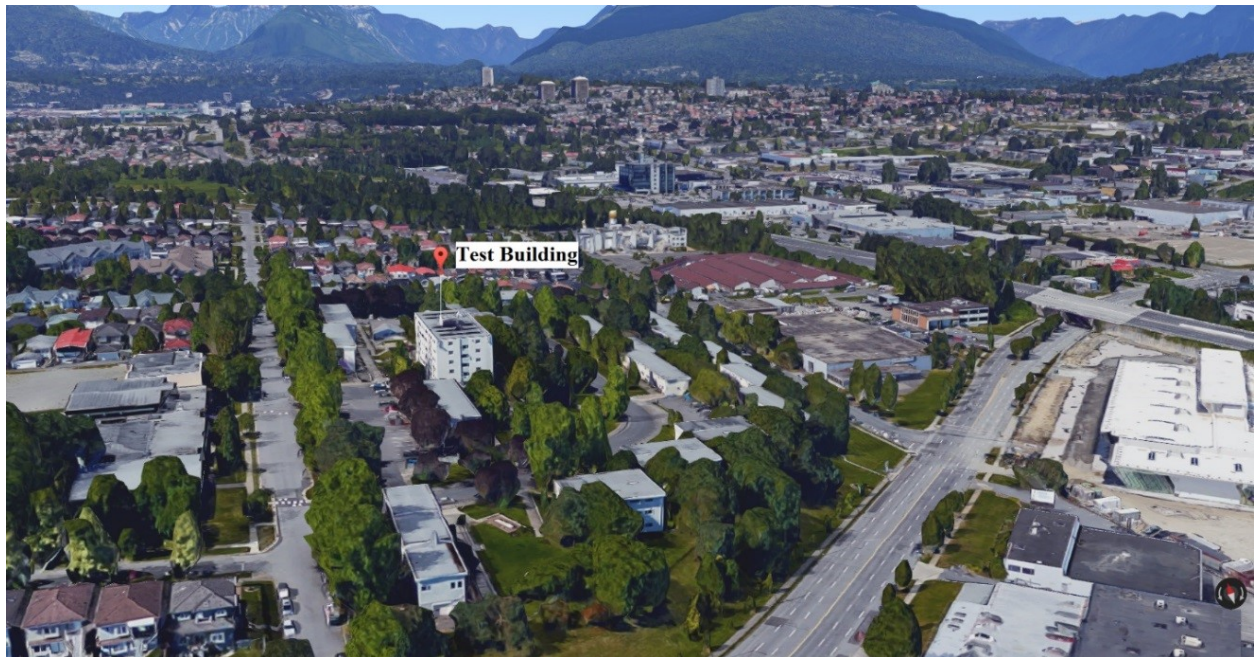


Figure 2.3.1 - Aerial view of the building site (Google Maps, 2017)

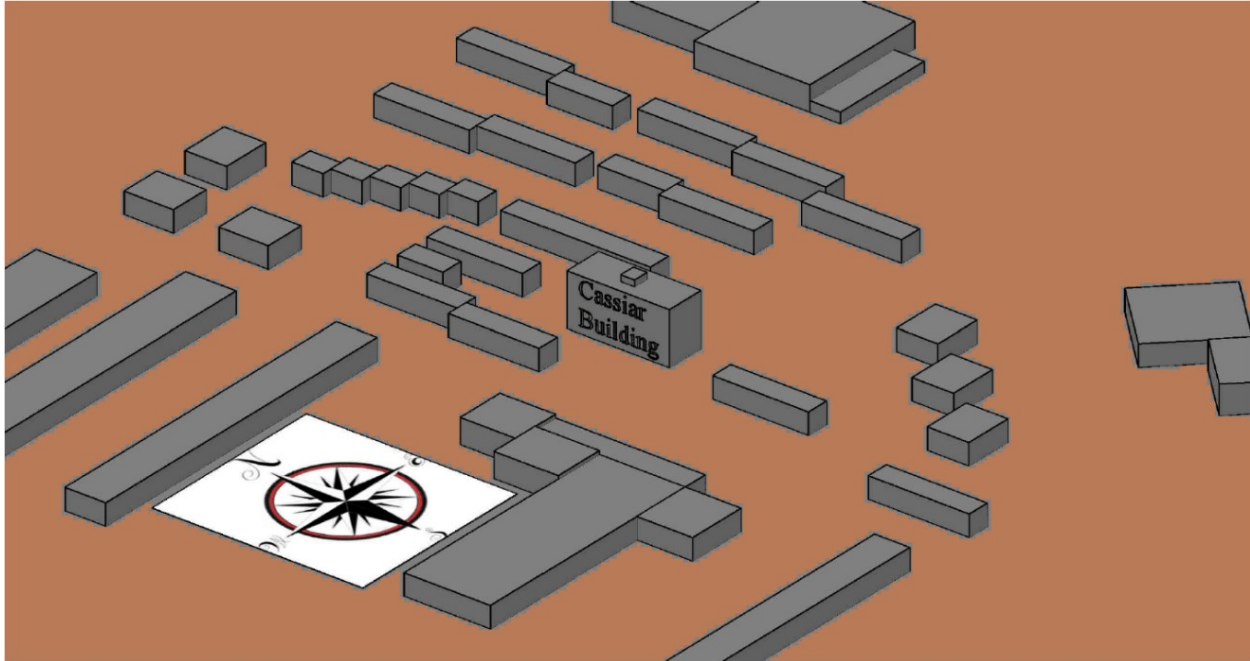


Figure 2.3.2 - Test building and its surrounding in the terrain

Table 2.3.1 - Computational domain size and discretization

Domain length (x)			650 m
Domain height (y)			100 m
Domain width (z)			190 m
Surface mesh	Size	Domain sides	0.5 m - ~3.99 m
		Building walls	0.5 m
Volume mesh	Type		Quadrangle
	Number of CV's		$\sim 1.56 \times 10^6$
	Type		Hexahedron

The computational domain chosen is shown in Figure 2.3.3. This domain with the setup shown in the figure is for the east façade being exposed to normal wind. The building is located at nearly the center of the domain on the bottom boundary, i.e. the ground. The information regarding the computational domain size and discretization is summarized in Table 2.3.1.

2.3.1.2 Blocking of the Mesh of the Domain

As shown in Figure 2.3.3, a unique blocking method is used in meshing the computational domain. This blocking is originated at the target building, with it being at the middle of the domain, on the ground, and scaled at 45° in each direction outward. This creates a cube in the

middle, comprising of 5 prisms, one scaling and sweeping the domain upward from the roof, and the rest in lateral directions.

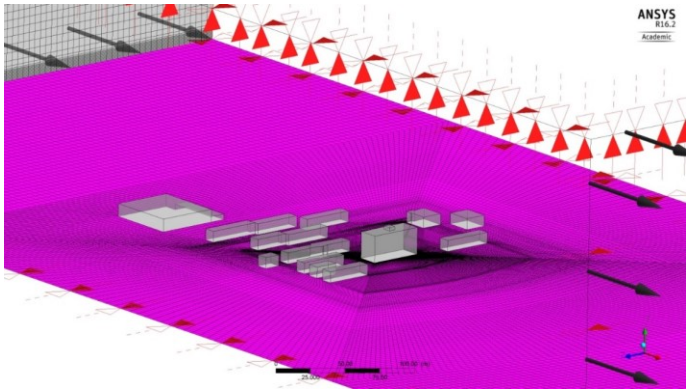
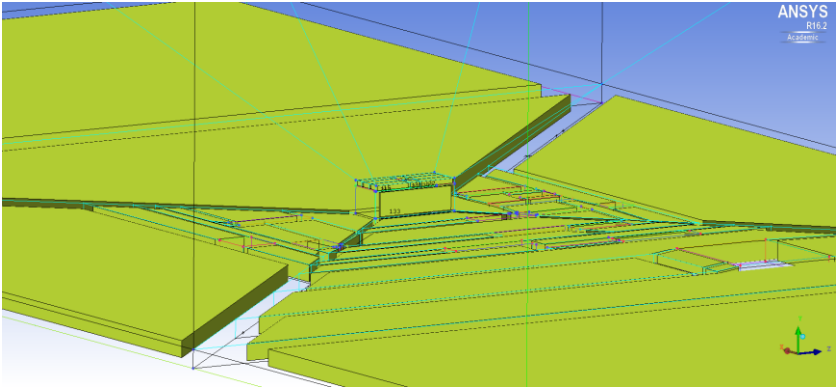
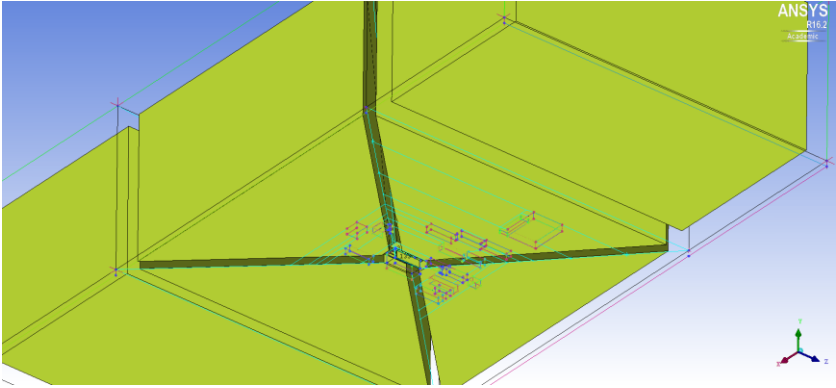


Figure 2.3.3 - Computational schematics with boundary conditions



- a - bottom blocks, the ones attached to the ground



- b - top blocks, ones attached the non-solid boundaries

Figure 2.3.4 - Blocking scheme of the computation domain

This method, which is shown for bottom blocks in Figure 2.3.4a, and top blocks in Figure 2.3.4b has advantages which are as follows:

- 1- This method allows great control on number of meshes on each side
- 2- Great deal of control on the computational expenses is achieved through the control on number of mesh nodes on each side
- 3- This method, unlike similar simulations of the literature results in a fully structured, hexahedral, mapped meshed domain
- 4- With the bottom blocks separated, one could control the y_p value for various terrains of interest, for the ground and solid boundaries of the test building modeled
- 5- Any change to the façade, including an addition of overhang, balconies, etc. is easily deployable
- 6- Mesh cell concentration is naturally high near the target building and low away from it
- 7- Low skewness factors generally throughout the meshed domain

There are disadvantages to this method as well, starting with high aspect ratio in certain cells. Especially, high aspect ratio away from the target building, near the ground far upstream and downstream. Another disadvantage is the meshing complexity and time spent for one geometry case. The latter is considerably less, when dealt with a stand-alone building modeling, and highly tangible for a surrounded one, due to the complexity of geometry and logistics of the surrounding buildings.

The placement of the model inside the domain must also be well-thought-out. Placing the building (with/out its surroundings) in the middle might not be a very reasonable strategy, even with abundant computational sources. Having said that, for all the cases solved in this thesis, including domain with or without the surrounding building, the test building is located at nearly the middle (5 m towards the inlet from the center of the domain), and that is due to the immense computational demand on the post-processing part of the study. To elaborate on that, on the building surrounded by its surrounding, as the leeward surrounding buildings are not counted in, the windward buildings' locations alongside the target building located the crowd in a proper position in the domain; that is leaning towards the inlet, and long enough leeward empty domain

till the outlet, for the downstream wind to develop before meeting the pressure outlet (Tominaga, et al., 2008). For post-processing simplification reasons, same location is chosen for the stand-alone building in this study. This arrangement meets the requirements suggested in (Tominaga, et al., 2008), at the expense of processing times.

2.3.1.3 Boundary Conditions

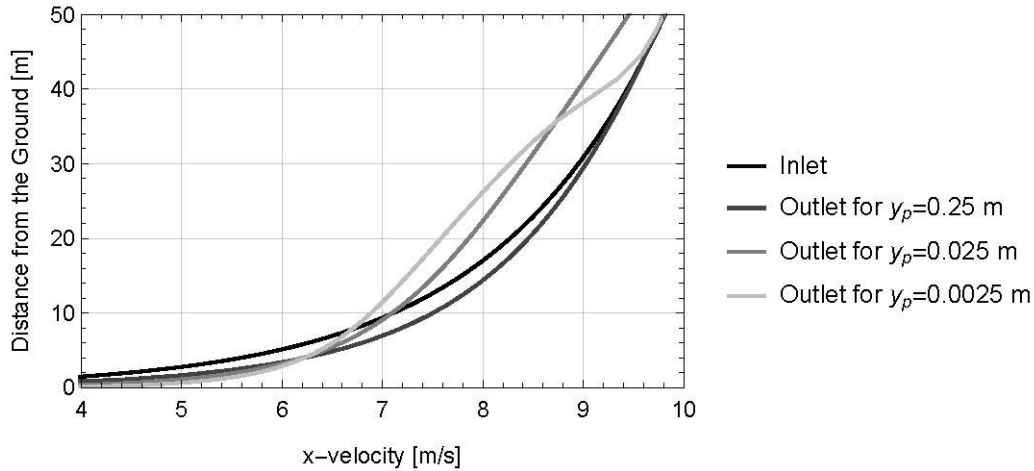
As discussed, a 7-step procedure proposed by Blocken to modify boundary conditions is followed for k- ϵ model (Blocken, 2004). For k- ω turbulence model, the author finds k- ω models' parameters following the k- ϵ model modification and by using Equation 2.3.1, for ω calculation on the inlet boundary (Wilcox, 2006). Standard wall functions for Realizable k- ϵ turbulence model in a dimensionless form is $U^* = \frac{1}{\kappa} \ln Ey^*$. von Karman constant, κ is fixed in the code to be 0.4187. $C_\mu = 0.09$ is a constant used in the modifications as well as a constant in Realizable k- ϵ (Wilcox, 2006). $y_p = 0.25$ is the distance from the center of the wall adjacent cell to the ground. The summary of boundary conditions is given in Table 2.3.2.

Table 2.3.2 - Summary of boundary conditions

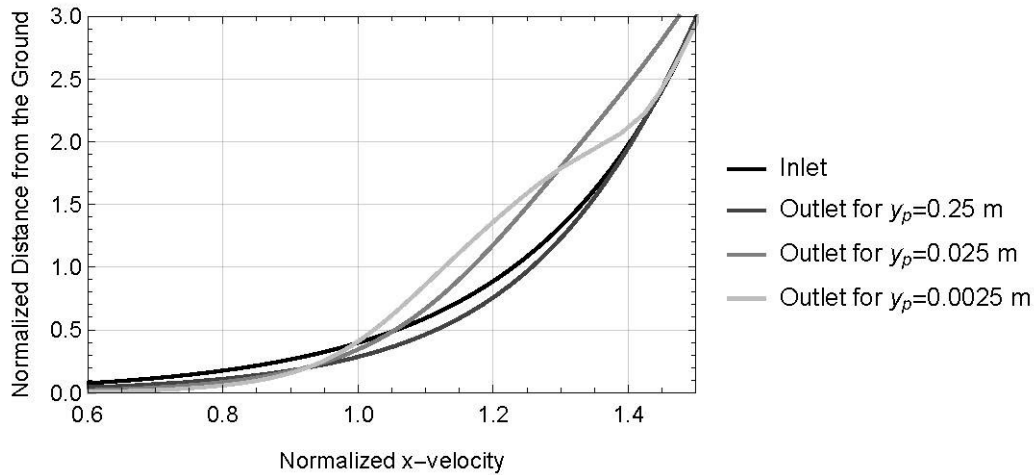
Boundary	Inlet	Sides/Top	Bottom	Outlet	Building	
Condition	Momentum	Table 2.2.2, Direction: Normal to boundary, $\alpha = 0.22$	Symmetry	No slip, impermeable	Backflow pressure ($\rho_0 = 0, gauge$)	No slip, impermeable
	Turbulence	Table 2.2.2	Symmetry	Roughness height ($K_s = y_0 = 0.152 m$)	$k_{backflow} = 1 m^2/s^2$, $\epsilon_{backflow} = 1 m^2/s^3$	Roughness height ($K_s = 0$), smooth wall
	DPM	-	-	Trap	-	Trap

2.3.1.4 Near-Wall-Cell Center-Point Distance to the Wall

The modifications mentioned in Table 2.2.2 for inlet boundary parameters are proposed to tackle the inhomogeneity imposed by adaption of ABL to wall functions. To study the effectiveness, three empty, two-dimensional $2000 m \times 500 m$ domains with y_p values of 0.0025, 0.025 and 0.25 m are solved with Realizable k- ϵ and standard wall functions.



- a - *x-velocity vs distance from the ground for different values of y_p at inlet and outlet of the empty domain*



- b - *Normalized x-velocity vs Normalized distance from the ground for at inlet and outlet of the empty domain*

Figure 2.3.5 - Inlet - Outlet comparison of velocity profiles, and turbulence parameters for different y_p values

Inlet and outlet horizontal velocity profile comparison is provided for each case, shown in Figure 2.3.5a, b. The residuals of continuity as the largest of all are let to be at a maximum of 10^{-12} . This justified the choice on the value of y_p . For that matter, y_p is chosen to be 0.25 m so that the homogeneity and the desired grid spacing on the building are met.

Figure 2.3.5a shows that due to the balance of viscous and kinetic forces, a solution to this problem with a two-equation turbulence model will show an acceleration near ground, no matter how the ground is treated. This acceleration alongside the satisfaction of continuity will result in deceleration just above the acceleration region attached to the ground. Above those regions, pretty much all the turbulence models, used in this study, predict the wind with precision, that is

under 5% margin of error. The trend of simulations varying the value of y_p , shows that as it increases, the inlet-outlet velocity profile mismatch reduces. This mismatch is a test for how the domain and turbulence model can simulate the ABL flow accurately, at least as far as the velocity field is concerned (Blocken, 2004).

As the value of y_0 is increased, turbulent dissipation rate, ϵ , as well as specific dissipation rate, ω , are both decreased, Figure 2.3.6.

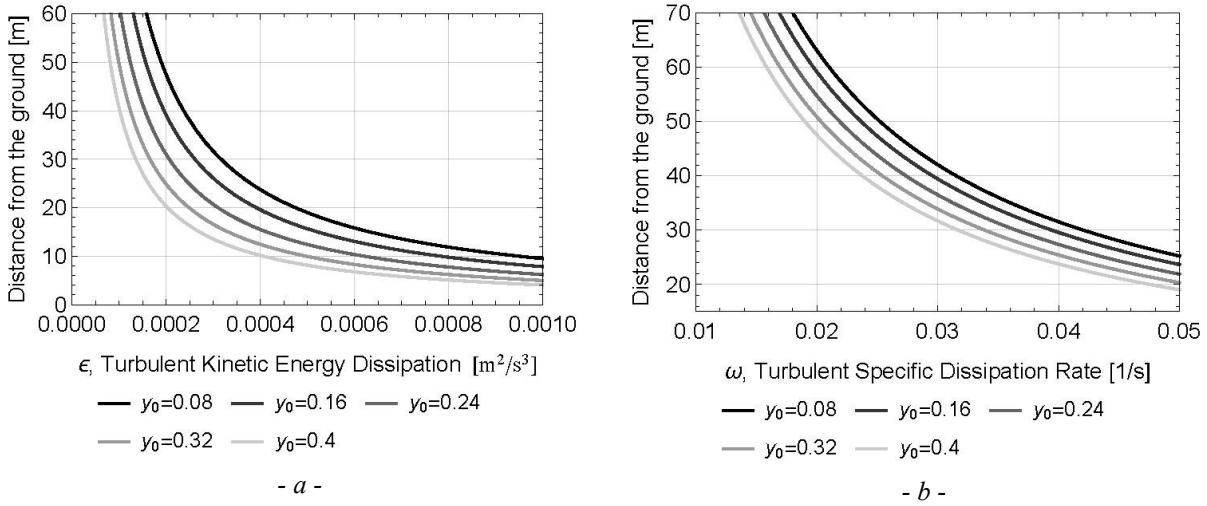


Figure 2.3.6 - (a) Turbulent dissipation rate (ϵ), and (b) specific dissipation rate (ω) versus vertical distance from the ground for different y_0 values, at the inlet

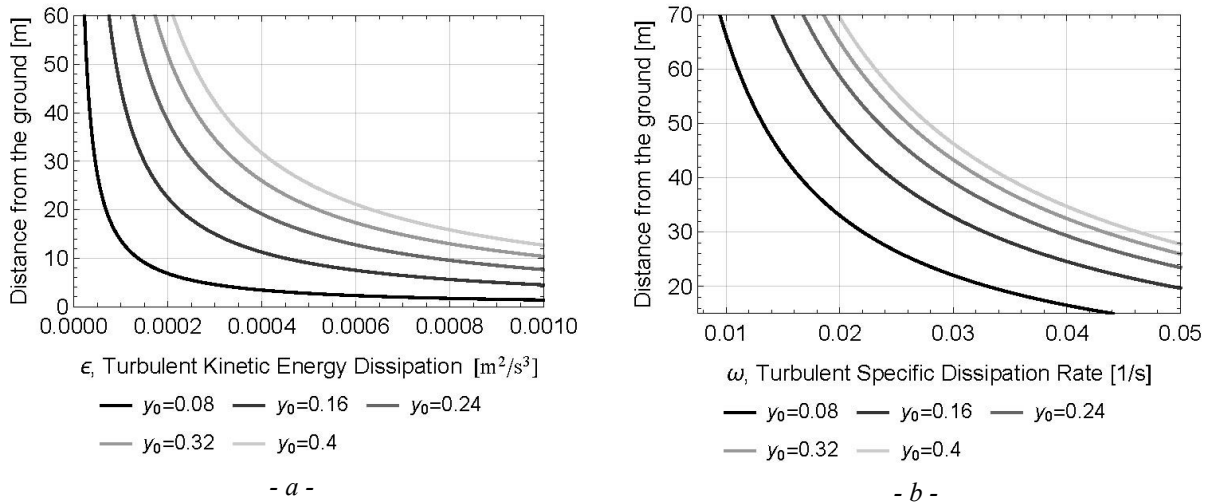


Figure 2.3.7 - (a) Turbulent dissipation rate (ϵ), and (b) specific dissipation rate (ω), versus vertical distance from the ground for different y_p values, at the inlet

Turbulent kinetic energy dissipation is preserved throughout the domain regardless of the value of y_p . Though as the value of y_p is increased, turbulent dissipation rate, ε , as well as specific dissipation rate, ω , are decreased. This could be mathematically proved using the governing equations¹. Though, the trend is shown in Figure 2.3.7.

Throughout the boundary though, for higher y_p , turbulent specific dissipation rate remains nearly unchanged. The reason for that is that k , turbulent kinetic energy and ε , turbulent dissipation rate, are both increased with the hike of y_p , at nearly the same rate. This could also be attributed to the fact that the wall treatment functions for both Standard $k-\omega$ and $k-\omega$ SST closure schemes are vanished and with them out of the picture, ABL with any inlet profile could fairly be observed throughout the domain.

Turbulent kinetic energy, k , increases throughout the domain with the reduction in y_p . The increase in turbulent kinetic energy is observed more accentuated as one departs from the ground. This results in more energetic turbulent eddies down through the domain. For the same value of y_p , $k-\omega$ SST has the least value of predicted k throughout the domain followed by Standard $k-\omega$ and finally Realizable $k-\varepsilon$. With the increase in y_p value, with Realizable $k-\varepsilon$ scheme, k is also increased.

One should notice that y_p and turbulence closure parameters are not the only variables that alter velocity near the ground as other parameters also play a role on its determination. In fact, study show that finer mesh does not necessarily result in a better determination of velocity in an external flow (Gousseau, et al., 2013).

The value of y^+ for the ground is shown in Figure 2.3.8 for Standard $k-\omega$, for surrounded and stand-alone building, and Realizable $k-\varepsilon$ only with surrounded building domains. The values are higher and beyond the suggested ranges in the literature. The recommended range is 25 to 35 for the upstream (Ariff, et al., 2009). The reason literature avoids reporting this turbulence parameter is that as the turbulence parameters of the inlet are manipulated, the reported y^+ values of the ground are not expected to remain within the anticipated region. The suggestion is that a value close to the lower bound ($y^+ \approx 30$) is most desirable (Fluent Inc., 1998).

¹ For the equations, refer to Section 2.2.5.

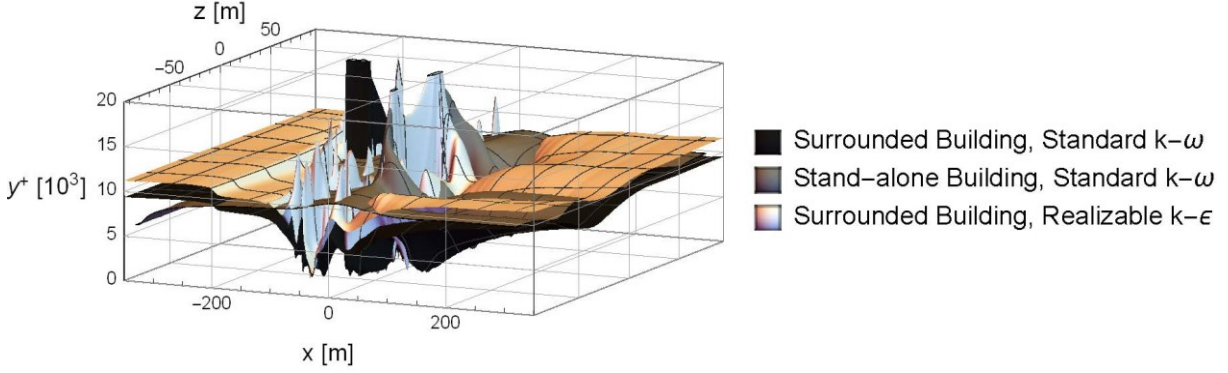


Figure 2.3.8 - y^+ value for ground boundary, with wind normal to the east façade, at $y_p = 0.25$ m

ANSYS is less strict (ANSYS®, 2015). For the $k-\omega$ models used, as they suggest, near-wall treatment formulation is robust as it is y^+ -insensitive. For when the wall functions are used, in this case for Realizable $k-\epsilon$, ANSYS recommends the use of $y^+ > 30$ in the entire domain. As one gets closer to the buildings in the middle of the domain, the value of y^+ increases significantly. This could be attributed to the values of the building wall roughness constants. As they are taken to be the default values, and this might be a proper treatment. Overall, the proposed ground boundary treatments are supposed to produce a proper value of y^+ . There is no guarantee on fitting y^+ in the proper range for Standard $k-\omega$. Having said that, even for Realizable $k-\epsilon$, near the buildings, y^+ is found to be considerably beyond aforementioned ranges.

2.3.1.5 Numerical Solution to Rain Phase

As the framework chosen is Lagrangian, the governing equation of motion of raindrops reduces to an ODE, based on the low concentration of rain phase as rain falls. The equation is:

$$\rho_w \frac{d^2 \vec{r}}{dt^2} = (\rho - \rho_w) \vec{g} + \vec{F}_D \quad (2.3.1)$$

ρ_w is density of water, \vec{r} is to be solved for, which is the position vector of the droplet, ρ is the density of air, \vec{g} is the gravitational acceleration and \vec{F}_D is the drag force, which is presented in the following equation:

$$\vec{F}_D = \left[C_D \left(\frac{\rho}{2} \left| \vec{u} - \frac{d\vec{r}}{dt} \right|^2 \right) A_{df} \right] \frac{\vec{u} - \frac{d\vec{r}}{dt}}{\left| \vec{u} - \frac{d\vec{r}}{dt} \right|} \quad (2.3.2)$$

Contribution of the $(\rho - \rho_w)\vec{g}$ term on the momentum equation governing the motion of droplet is attributed to the buoyancy on it in midair. A_{df} in Equation 2.3.2, is the frontal area of the droplet.

ANSYS Fluent is deployed for the solution to the wind for all the cases in this thesis. Pressure-based steady-state solver is chosen. As of the turbulence model, each scheme has its own viscous model. SIMPLE scheme is chosen for the pressure-velocity coupling. For the spatial discretization, standard pressure, second order upwind for momentum and turbulent kinetic energy and first order upwind for turbulent dissipation rate are chosen. At convergence, residuals of continuity as the largest residuals of all, reach a limit of 10^{-7} for Realizable k- ϵ and 10^{-11} for Standard k- ω and k- ω SST. Moreover, algebraic sum of pressure coefficient of all the building sides, which is the only wall boundary condition other than the ground, is monitored to perceive convergence.

Large enough number of particles are injected into the domain at empirically found locations, in form of a plane in mid-domain. Trial and error gives the best location of each plane so that the whole façade of interest is covered, conservatively, for every given raindrop diameter. Initial horizontal velocity is taken to be the x -velocity of inlet velocity profile at the distance of the injection plane from the ground. Terminal velocity (vertical velocity) is taken to be from the work of Gunn and Kinzer (Gunn & Kinzer, 1949). Discrete set of raindrop diameters is taken into consideration for the sake of numerical calculations.

Discrete Phase Model (DPM) module of ANSYS Fluent is used to find the trajectory of particles injected in the domain. A fourth-order Runge-Kutta integration scheme has been used to integrate Equation 2.3.1. The integration time-step is as follows:

$$\Delta t = \frac{\Delta t^*}{\lambda} \quad (2.3.3)$$

in which λ is the Step Length Factor and Δt^* is the estimated transit time. λ is inversely proportional to the integration time step and is coarsely identical to the number of time steps required to travel the current continuous phase control volume. Instead of specifying the length scale, “Step Length Factor”, λ is set to 5, with large enough value of Maximum Number of Steps, to make sure all the droplets are trapped at solid boundary. These values make a balance

between computational expense and accuracy needed, and are obtained by experiencing a small range of values.

A fourth-order curve is fit to the drag coefficients for falling raindrops measured (Gunn & Kinzer, 1949).

The curve is as follows

$$\log(C_D) = 0.0358 z^4 - 0.225 z^3 + 0.5731z^2 - 1.2462z + 1.4633 \quad (2.3.4)$$

with $z = \log(\text{Re}_d)$. A User-Defined Function is used to hook this to the solver.

A MATLAB code has been developed to calculate WDR catch ratio (Mohaddes Foroushani, et al., 2014). Catch ratio is the main parameter used to compare WDR simulation to field measurements. Specific catch ratio is defined as follows

$$\eta_d = \frac{R_{\text{wdr}}(d)}{R_h(d)} = \frac{A_h(d)}{A_f(d)} \quad (2.3.5)$$

where A_h is the area of a reference horizontal surface and A_f is the wetted area on the building façade, as seen in Figure 2.3.9 (Blocken, 2004). The equality above can be proved with assumption of no vaporization or condensation, using mass conservation which is as follows

$$R_h A_h = R_{\text{wdr}} A_f \quad (2.3.6)$$

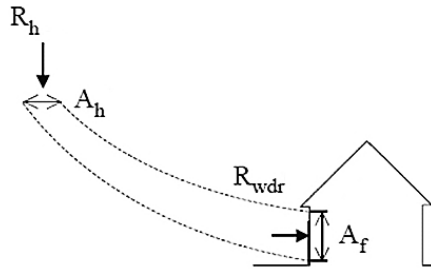


Figure 2.3.9 - Reference and vertical wetted areas that appear in the definition of catch ratio (Blocken, 2004)

Catch ratio is found by integration over the range of raindrop diameters. The raindrop size distribution by Best, as a weighting function, is used (Best, 1950).

$$\eta = \int \eta_d f(d) d d \quad (2.3.7)$$

The weighting function $f(d)$ is calculated based on the “flux-based” modification suggested by (Blocken, 2004) which is:

$$f_h(d) = \frac{f(d)V_t(d)}{\int_d f(d)V_t(d) dd} \quad (2.3.8)$$

Raindrops are injected into the domain in a specific area upstream of the building. The vertical velocity of injection is equal to the free falling terminal velocity (Gunn & Kinzer, 1949). The horizontal velocity of the raindrops is equal to that of the undisturbed wind at the same height above the ground as the injection plane. Trial and error settles the position of the injection planes, as long as the landing drops around the façade are conservatively low, and raindrops cover the façade entirely. No dissipation modeling is included in these simulations.

A trapezoid scheme is used to solve the integral in Equation 2.3.7, which is as follows

$$\eta = \sum_i f_h(d_i)\eta(d_i)\Delta d_i \quad (2.3.9)$$

to find the A_f in the cell, convex hull method is deployed and solved by gift wrapping method.¹

2.3.1.6 Rain Event Selection Procedure

A procedure is proposed by the author for choosing and creating appropriate rain events for the validation of rain simulation. The issue with hour-long data collected on the façade in the field is that unless there is high rainfall intensity, it is highly unreliable. That is the motivation to average the collected data so that it is a more reliable touchstone. The set procedure is as follows:

1. All the recorded hours are considered.
2. The hours that have rain are singled out.
3. Depending on the direction of wind on target façade, hours with directions within the range of set direction, with $\pm 10^\circ$ deviation are chosen (see Section 2.3.1.7).
4. Consecutive rain hours, including ones with only one dry hour gap, are chosen.
5. Weighted average of the wind speed of the selected hours with respect to horizontal rain fall intensity is calculated and taken for the made rain event:

¹ For details regarding the methods see (De Berg, et al., 2008).

$$U_{ave} = \frac{\sum_i U_i R_h^i}{\sum_i R_h^i} \quad (2.3.10)$$

in which U_i is the wind speed at i^{th} rain hour and R_h^i is the corresponding rainfall intensity.

6. Horizontal rain fall intensity is summed for the chosen rain hours:

$$R_{h-ave} = \frac{\sum_i R_h^i}{n} \quad (2.3.11)$$

in which n is the number of rain hours chosen for the selected rain event.

7. U_{10} is found based on U_{ave} using the following formula:

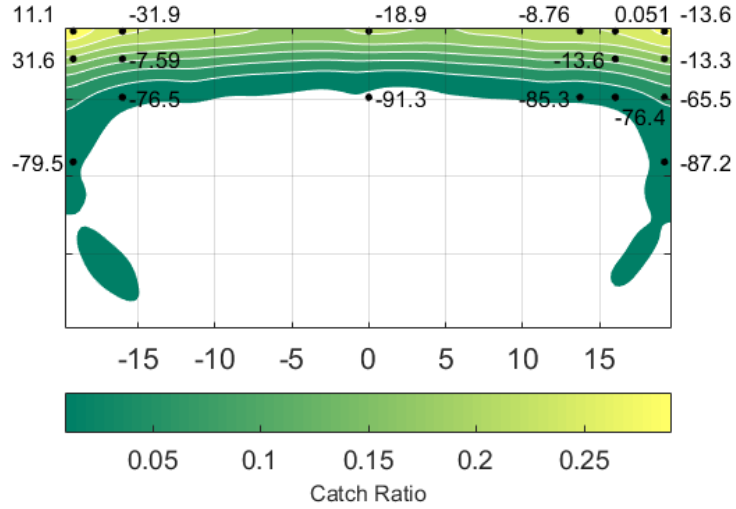
$$U_{10} = U_{ave} \cdot C \cdot \left(\frac{10}{h_{mech}} \right)^{\alpha_p} \quad (2.3.12)$$

in which the correction factor, C , is taken to be 0.88, which corresponds to the recommended 12% reduction from the wind tunnel measurements. The reason for this is the fact that the wind calculated at the level of the wind monitor is lower than wind speed at the same level in far upstream flow by that factor. h_{mech} is 26.82 m which is the altitude of the wind monitor installed on the building ($h_{mech} = 88'$). Lastly, α_p is taken to be 0.22, which is the exponent chosen to find the U_{10} , value of power-law velocity profile exponent.

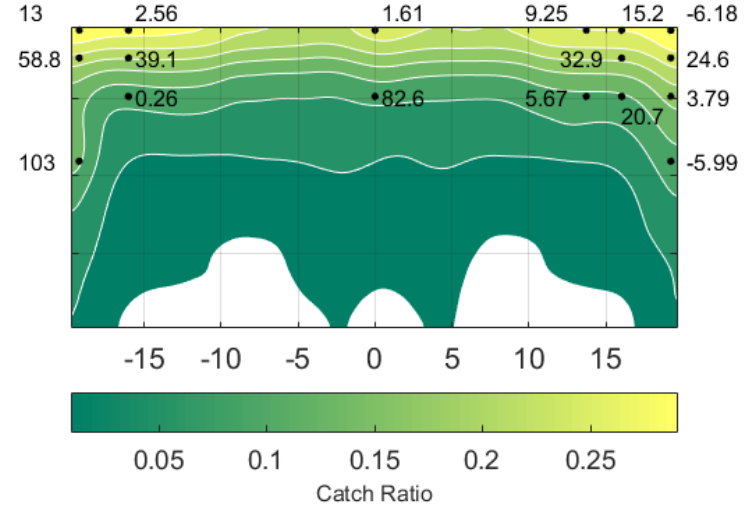
2.3.1.7 Effect of 10° Difference in Angle of Wind Blowing on the Façade on Catch Ratio Calculation

As discussed in Section 2.3.1.6, to create proper rain events for WDR validation, wind direction is chosen within a $\pm 10^\circ$ range. This section does a simple error analysis on how 5° and 10° change in wind direction would change the WDR prediction by the model used in this thesis.

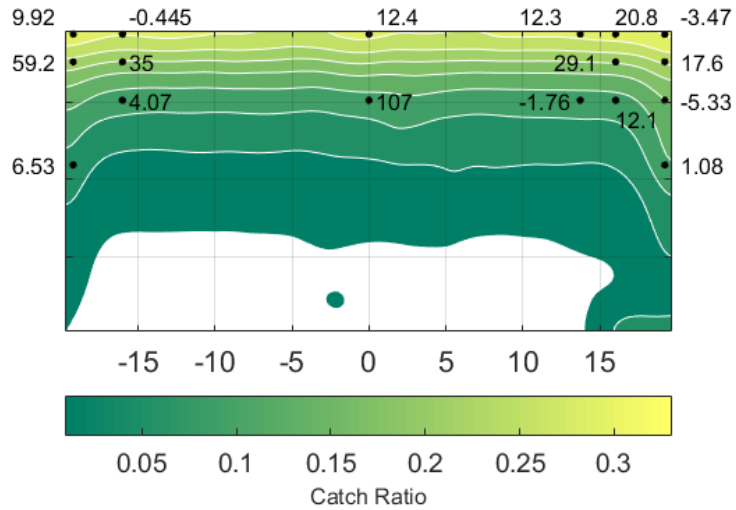
To achieve this goal, WDR catch ratio is found for normal wind on the east façade of the target building, alongside wind at 85° , and 80° onto the east façade, with the north façade being the second windward façade.



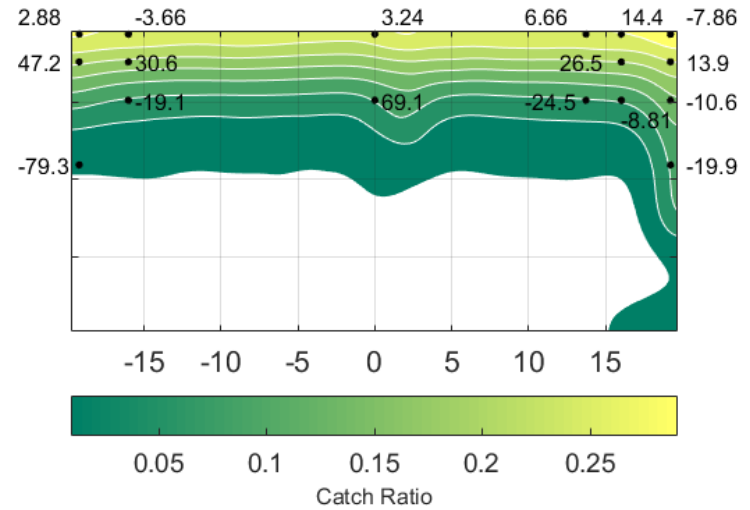
- a - Stand-alone building, normal wind



- b - Surrounded building, normal wind



- c - Surrounded building, oblique wind at 85°



- d - Surrounded building, oblique wind at 80°

Figure 2.3.10 - Catch ratio contours - error percentage on each measurement gauge, with wind on the east façade (and north in case of oblique wind), Standard $k-\omega$ with log-law inlet velocity profile. Black dots are error percentage compared to field measurement. Bottom white areas show zero catch ratio.

Table 2.3.3 - WDR event parameters used to study the effect small change in wind direction on catch ratio

Case	U_{10} [m/s]	R_h [mm/hr]	Angle of Incidence to East Façade (degrees)	Number of Particles Injected	Number of consecutive hours of measurement	Date	u_{ABL}^* [m/s]	y_0	α
1	2.415	3.16	90	250×400	15	Jan-2014	0.7	0.152	0.22

Catch ratio contours with error percentage of each gauge is presented in Figure 2.3.10 for normal, and oblique wind directions onto the east façade. The rain event parameters used in this study are presented in Table 2.3.3.

Error analysis shows that for top two rows of gauge points, alongside the top row, and side-edge gauge points maximum value of standard deviation for maximum and average error is 5.56%, which shows this small change in wind direction has negligible deviation from the mean, and consequently, the rain event procedure described in Section 2.3.1.6 as far as taking that $\pm 10^\circ$ range is concerned, is valid.

2.3.2 Experimental Solution to Wind and WDR

2.3.2.1 Wind Tunnel Measurements

Wind tunnel measurements have been conducted in Concordia’s ABL wind tunnel (Chiu, 2016). To model the field, a suburban exposure has been created using roughness elements and a scaled down test building with its surrounding buildings.

A 1:400 scale model of the test building and its surroundings within a 200-m radius have been fabricated and tested in the ABL wind tunnel. The 1:400 scale is selected based on the surroundings and successful simulations at this scale of the most important variables of the Atmospheric Boundary Layer under strong wind conditions carried out in this wind tunnel (Stathopoulos, 1984). The models are fabricated using extruded polystyrene foam insulation and glued to a particle board base. The test building in the field is located within a suburban environment, therefore, a similar exposure is simulated in the wind tunnel. To obtain a suburban wind profile, a mixture of roughness elements has been placed along the length of the test section of the tunnel. The roof of the wind tunnel was adjusted along the length of the test section to satisfy the condition of zero longitudinal pressure gradient for a suburban exposure. The test

building and its surroundings within a 200-m radius are shown in Figure 2.3.11. The test building model is 98 mm long, 38 mm wide, and 50 mm high. There is a mechanical room located on the center of the roof measuring 15 mm long, 13 mm wide, and 6 mm high.

A Series 100 Cobra probe was used to measure velocities in the wind tunnel. The Cobra Probe is a multi-hole pressure probe that provides dynamic, 3-component velocity and local static pressure measurements in real-time. The probe is capable of a linear frequency response from 0 Hz to more than 2 kHz and is available in various ranges for use between 2 m/s and 10 m/s (TurbulentFlow Instrumentation, 2011). Although the probe comes pre-configured, the accuracy was verified by comparing the mean values measured by the Cobra Probe with the measurements of a pitot static tube mounted at the same location.



Figure 2.3.11 - The test building and surrounding buildings within a 200-m radius placed in ABL wind tunnel (Chiu, 2016).

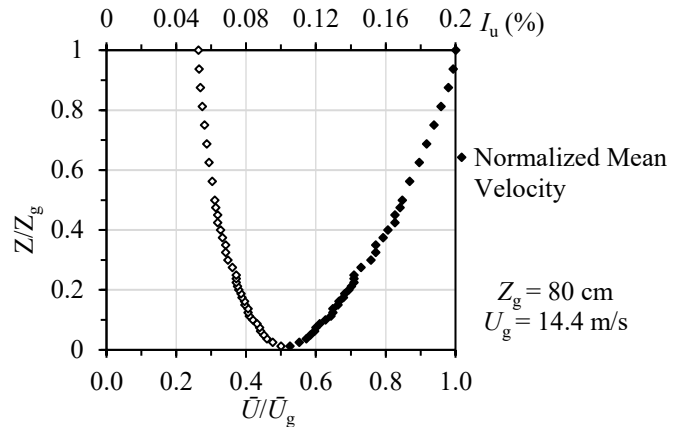
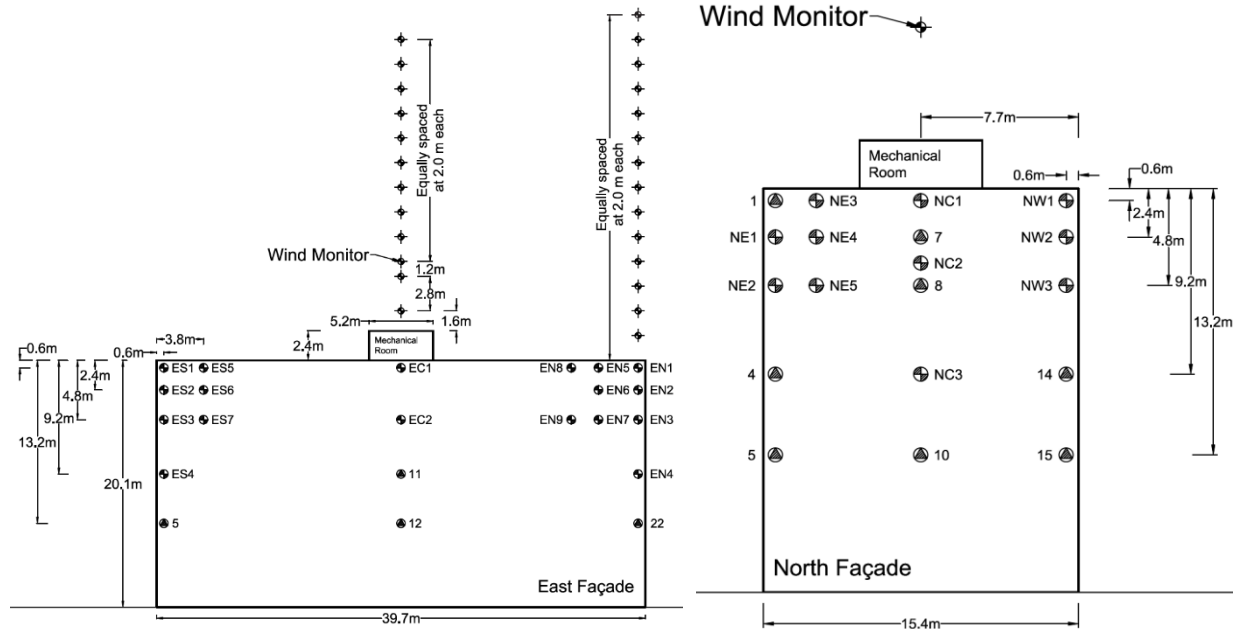


Figure 2.3.12 - Normalized mean velocity and turbulence intensity for a suburban exposure measured in the boundary layer wind tunnel (Chiu, 2016).

In addition, the measurements were checked for repeatability for the wind profile above the mechanical room roof and in front of the east façade. The average percentage difference between the two tests were 1% and 6% for the wind profile above the roof and the east façade, respectively.

The measurements were taken to establish

- 1- The suburban terrain with no model present;
- 2- Wind flow around the stand-alone test building, and



- b - Measurement locations in front of the east façade and above the mechanical room

- c - Measurement locations in front of north façade

Figure 2.3.13 - Location of wind velocity measurements around the test building, N, S, E, W stand for north, south, east, and west¹

2.3.2.2 Field Measurements

As discussed in Section 2.3.1.1, the test building is a six-story rectangular residential building with a flat roof and a short parapet located in Vancouver, British Columbia (see Figure 2.3.1). The parameters monitored include on-site weather conditions and WDR on façades. A weather station including a wind anemometer, a temperature, and relative humidity probe are mounted on top of a tripod cross-arm that is 4.6 m above the mechanical room located on top of the main roof of the test building, Figure 2.3.14.

The anemometer can measure wind speed with a range of 0–50 m/s with an accuracy of ± 0.2 m/s or 1% of reading. It can measure wind direction with a range of 0–360° with an accuracy of $\pm 0.3^\circ$. The horizontal rain gauge has a conical collection area (24.5 cm in diameter) constructed of gold anodized spun aluminum. The resolution of the tipping bucket is 0.1 mm/tip with an accuracy of 1% up to 50 mm/hr. The horizontal rain gauge is placed on the center of the main roof. Several customized WDR gauges are installed on building façades at strategically selected

¹ This figure is also presented in Appendix E - Catch Ratio Parametric Study and Section 4.3.

locations, Figure 2.3.13. These driving rain gauges are aluminum plate-type gauges consisting of a square collection area, 30.5 cm by 30.5 cm, for a total area of 930.3 cm². The rain gauge is designed with details to minimize measurement errors. The collector's rim height is kept at 25.4 mm, a low profile to minimize wind errors. The driving rain gauge has a dual tipping-bucket mechanism with a resolution of 0.06 mm/tip (Chiu, 2016).

Locations of WDR gauges on building façades are selected strategically based on the prevailing wind direction, building geometry and surroundings. These locations are shown in Figure 2.3.14.



Figure 2.3.14 - Schematics of the building and the mechanical room with the wind monitor mounted on top of it (Chiu, 2016)

2.3.3 Sources of Wind Simulation Error

A grid convergence study is carried out following the procedure suggested in (Mohaddes Foroushani, et al., 2014), using the Richardson extrapolation-based scheme proposed by Roy (Roy, 2004). Table 2.3.4 shows the results of the grid convergence study¹.

Wind flow grid convergence index is found to be 2.5% for the setup in this study. The area-weighted average pressure coefficient of the building has been used as the main field variable for calculating this index, alongside velocity.

There are multiple other sources of error. Notable one of them is the iterative convergence error which is associated with the iterative process of computational fluid dynamics, and residuals of every loop of executing numerically discretized PDE. Preferably, these residuals for all the

¹ For the formulation, refer to Appendix A - Discretization Error Formulation.

involved governing equations shall plummet to machine level of accuracy. The order of these values is presented for each simulation in the place of presentation of the simulation.

Table 2.3.4 - Calculations of discretization error

	ϕ = area-weighted average on pressure coefficient on surfaces: east, mechanical room, north, roof, south and west	ϕ = x-velocity on upstream 40 m vertical profile, 8 m above the ground	ϕ = x-velocity on upstream 160 m vertical profile, 10 m above the ground	ϕ = x-velocity on upstream 3.6 m vertical profile, 20 m above the ground, at S1 column	ϕ = x-velocity on top of the mechanical room, 27 m above the ground
N_1	7835555	7835555	7835555	7835555	7835555
N_2	3481796	3481796	3481796	3481796	3481796
N_3	1557386	1557386	1557386	1557386	1557386
r_{21}	1.31046	1.31046	1.31046	1.31046	1.31046
r_{32}	1.30758	1.30758	1.30758	1.30758	1.30758
ϕ_1	-12.6715	6.16619	7.15922	6.23977	8.99388
ϕ_2	-13.128	6.22095	7.17205	6.12159	8.92753
ϕ_3	-13.233	6.14218	7.14924	6.11752	9.05508
p	5.37571	1.35096	2.13878	12.3613	2.43024
ϕ_{ext}^{21}	-12.5323	6.04199	7.14283	6.2441	9.06529
e_a^{21}	3.60217%	0.888091%	0.179226%	1.89397%	0.737755%
e_{ext}^{21}	1.11115%	2.0557%	0.229435%	0.0693775%	0.787761%
GCI_{fine}^{21}	1.37367%	2.51786%	0.286137%	0.0867821%	0.992519%

Other sources of error are attributed to the models deployed in the simulations; to be specific, turbulence models and inlet velocity profile. Errors associated with turbulence models used are discussed in detail in the Wind Simulation section (Section 3.1), ensuing the presentation of results of validation and model comparisons. As far as the inlet velocity profile is concerned, a perfect undisturbed flow is taken as the approaching wind, which attributing to a real-life terrain is unequivocally imperfect. On top of all, wind is a transient phenomenon modeled in steady-state condition here, which poses issues with the nature of turbulence.

2.3.4 Sources of WDR Simulation Error

Main sources of error for this simulation (in no special order) are:

1. Inaccuracy of wind prediction near the façade, especially toward the middle of it

2. Lack of raindrop turbulence dispersion simulation in current study and *Streamtube* assumption¹
3. Errors attributed to drag modeling of the WDR
4. Rain event creation described in Section 2.3.1.6
5. Smoothing functions used to smoothen the final data obtained off WDR calculations
6. Discrete phase modeling of the rain, alongside the number of raindrops injected per raindrop diameter size
7. Intransient rain simulation

As far as the wind prediction is concerned (Section 2.3.3), as discussed, accuracy of rain simulation is predominantly dependent upon accurate wind prediction in this Lagrangian scheme of WDR simulations.

Raindrop turbulence dispersion and drag modeling of WDR are chosen to not be a part of this study intentionally, to reduce the complications of an already demanding theoretical and data gathering process of these simulations. As discussed in Literature Review section (Section 1.2.4), the errors attributed to these two factors are mostly reported negligible in the literature.

Mingling consecutive rain hours are, as described in Rain Event Selection Procedure section (Section 2.3.1.6), inevitable, due to predominantly low amount of rain collected on the test building. This, as the number of consecutive hours increase, is bolded. To make the raw data for catch ratio contour presentation, a smoothing function is used. This usage has its own level of error, which with higher order of smoothening, gets higher. Added to this is the fact that these rain hours are not entirely at 90° of angle onto the target façade, and there is error associated to this as well.

Choice of number of raindrop injected per raindrop diameter size chosen in this study is followed by recommendations made in (Mohaddes Froushani, 2013). Appendix B of that thesis describes

¹ Streamtube assumption refers to the fundamental assumption restricts the assumptions to the calculation of raindrops from closed streamtubes, which means the trajectories predicted are assumed to not intersect (Mohaddes Froushani, 2013).

that above a certain number of raindrops injected, sensitivity of catch ratio predicted to the number of raindrops injected becomes rather trivial.

And finally, intransient rain simulation is another source of error, as in real life, rain, much like wind is a transient occurrence.

2.3.5 Overhang Effectiveness

Section 1.3 presents some architectural apparatus to deviate the raindrop impingement. Overhang was introduced as the most effective means to protect a façade from WDR. Effectiveness index of an overhang is defined as follows (Foroushani Mohaddes, et al., 2014)

$$\delta_f = \left(\frac{\tilde{\eta} - \tilde{\eta}_{OH}}{\tilde{\eta}} \right) \times 100 \quad (2.3.13)$$

in which we have

$$\tilde{\eta} = \frac{1}{\sum_{i=1}^n A_i} \sum_{i=1}^n \tilde{\eta} A_i \quad (2.3.14)$$

Subscript OH stands for overhang, which differentiates measured catch ratio with the presence of an overhang as opposed to unprotected façade measured catch ratio denoted with no subscript. Calculating this effectiveness index over different portions on the façade, has an advantage of giving assessment means to figure out the effect of the overhang on the rain deposition at different areas. The portions studied are the following

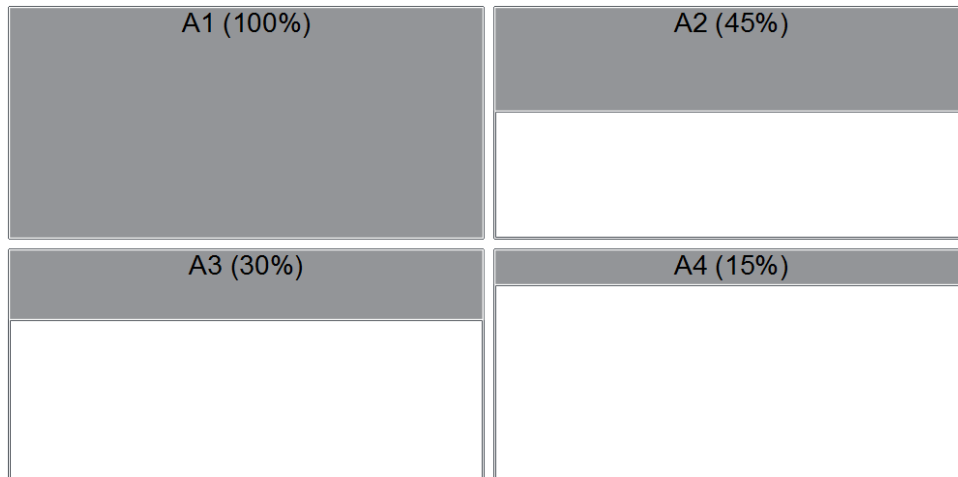


Figure 2.3.15 - Effectiveness index calculation portions on windward façade of the test building

Moreover, effectiveness could be defined for each point on the façade, as follows

$$\delta_p = \left(\frac{\eta - \eta_{OH}}{\eta} \right) \times 100 \quad (2.3.15)$$

η_{OH} is defined as the catch ratio at the same point, with the same wind and rain conditions, with the presence of an overhang protecting the façade of interest.

Chapter 3 VALIDATION, RESULTS, AND DISCUSSION

This section is dedicated to wind flow and WDR simulation validation, comparison amongst different turbulence models, presentation of various cases of wind flow solution, alongside multiple WDR event simulations and extensive parameter study on wind flow, WDR and overhang.

3.1 Wind Simulation

Multiple wind tunnel measurements have brought a thorough insight into how flow works around a stand-alone building and surrounded one. CFD solutions are validated, and consequently used in parameter study on wind flow around the test building. Later, the validated wind solution scheme is used to solve the rain impingement on the building's façade. This section deals with great number of aspects of wind simulation. Starting with validation, wind tunnel measurements are deployed to serve as touchstone for predicted data. That is done for Stand-alone and surrounded building schemes, for normal wind onto the east façade and wind coming at 45°, onto the east façade, in either north or south directions. Consequently, the validated data is used to do a brief comparison between multiple models used in this study, to compare the choice of models on turbulence related phenomena.

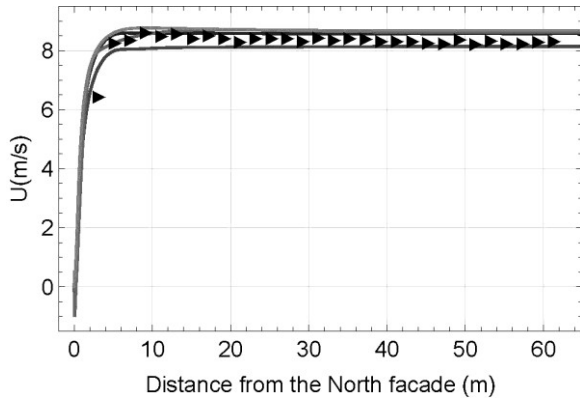
In the current study, first two models mentioned in Section 1.1, Power-law and Log-law are deployed and the results are compared to each other and wind tunnel measured data and the performance of each is studied.

3.1.1 Validation of Simulation on Stand-Alone Building

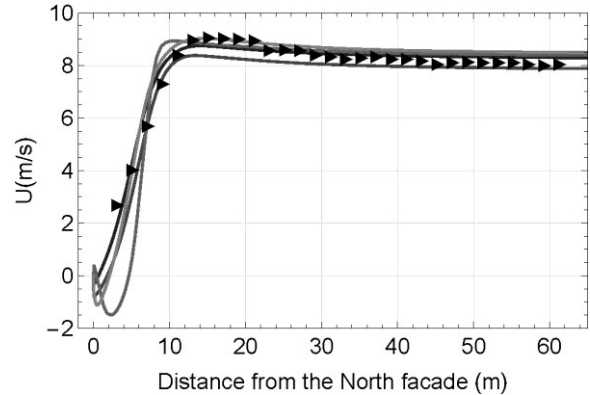
3.1.1.1 Normal Wind to the East Façade

Figure 3.1.1 shows several horizontal x -velocity value comparisons between measurement and simulated results. These include horizontal profile of location points normal to the north façade when the east façade is subjected to normal wind, and the landing base points of such points are depicted in Figure 2.3.13a and c, on the ground and north façade, respectively.

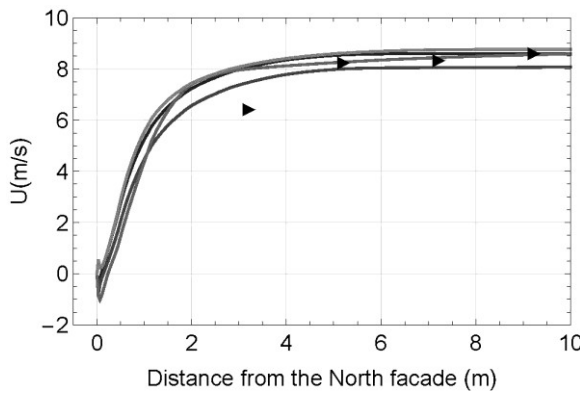
A general trend of agreement between measured and simulated data runs through graphs of Figure 3.1.1 which can also be inferred through noteworthy observations, that are the shape of the predicted profile and predictions near wall boundary, the north façade.



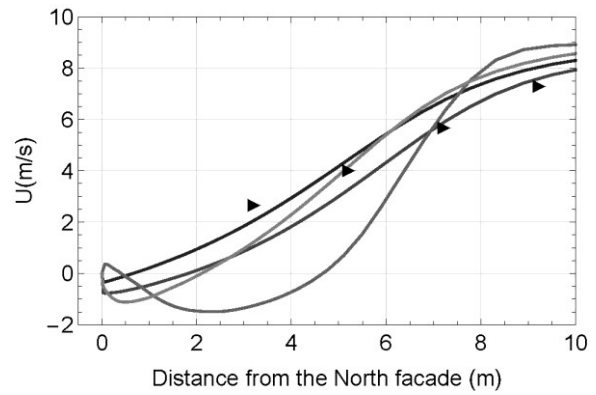
- a - Perpendicular profile to north façade at point 1, Figure 2.3.13c



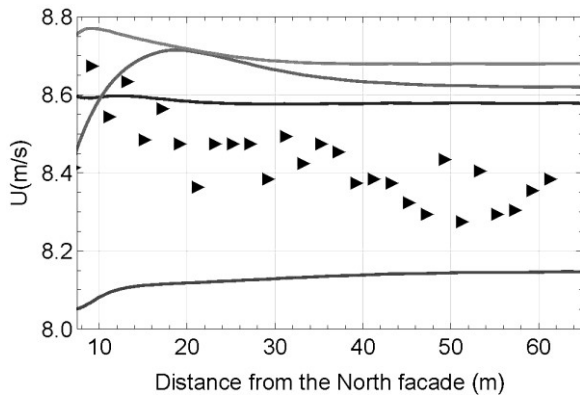
- b - Perpendicular profile to north façade at NW3, Figure 2.3.13c



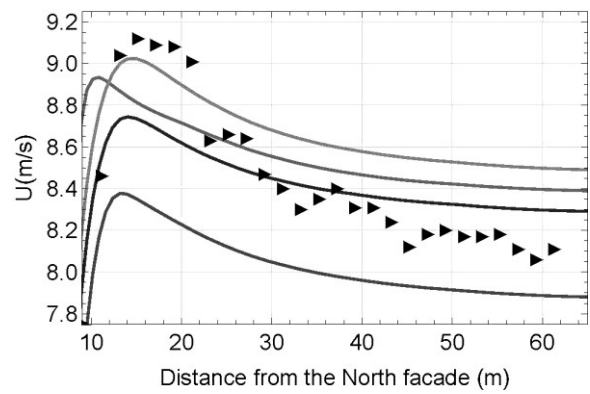
- c - Perpendicular profile to north façade at point 1, Figure 2.3.13c, magnified near the wall



- d - Perpendicular profile to north façade at NW3, magnified near the wall



- e - Perpendicular profile to north façade at point 1, Figure 2.3.13c, magnified away from the wall



- f - Perpendicular profile to north façade at NW3, magnified away from the wall

- ▶ Measurement
- k- ϵ Realizable, log-law
- k- ϵ Realizable, power-law
- k- ω SST, log-law
- Standard k- ω , log-law

Figure 3.1.1 - x-velocity on a horizontal profile, alongside value comparison, on stand-alone building exposed at normal wind on the east façade

As far as the shape is concerned, Standard $k-\omega$, follows measurement data points more precisely. That does not mean that the overall standard deviation of the simulated data is less than the other three schemes of simulation.

In fact, in those terms $k-\varepsilon$ Realizable with log-law velocity profile performs the best amongst them all. This can be attributed to the fact that away from the boundary, relatively, $k-\varepsilon$ Realizable is a better fit to simulate adiabatic boundary layer flow with.

Near boundary simulation is rather different. As the profiles are set at different locations across the north façade which is 15.42 m wide and 20.06 m high, every profile base point on the façade undergoes a different flow across the domain, due to the setting of the building and the wind direction. For instance, point 1 is towards the windward façade, and NW3 on the same figure rather shows a downstream region of the façade basepoint. This certainly goes through the eddy on the lateral side of the building, as shown later in Figure 3.1.11 and Figure 3.1.12. NW3 on Figure 3.1.1b is downstream, in the middle of the lateral eddy formed due to the presence of the boundary in front of the wind. Streamlines of the lower level measurement points are depicted in Figure 3.1.12.

Due to all that came, the nature of simulation of wind in such region, near-wall-boundary will dramatically be influenced by the turbulence model chosen. The size and distance of the center of the lateral eddy is also contributing to this difference in simulation under different regimes.

On a different note, as one gets towards the roof from the ground, the eddy gets smaller as the x -velocity is increased. Reynolds number is increased which means the momentum forces are dominant over viscous forces; which results in a less influence of boundary on the flow, and consequently straight and undisturbed flow around the building. $k-\omega$ SST still predicts a backflow which is an indication of an alleviated recirculation. The other two turbulence models rather do not find an eddy in that region, towards the middle and the downstream of the façade (no negative x -velocity). On near wall simulation, $k-\omega$ SST behaves significantly different than the rest.

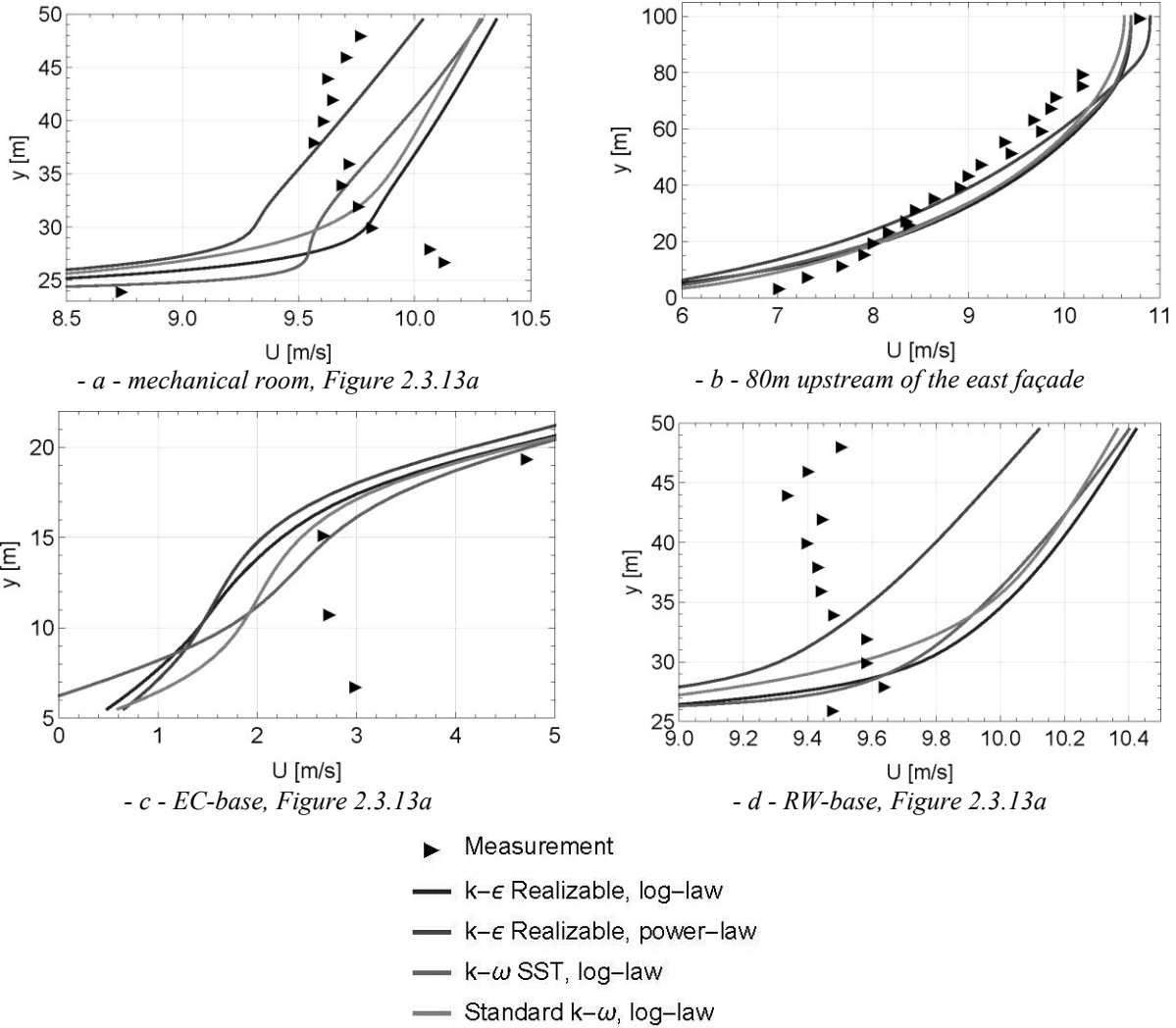


Figure 3.1.2 - *x-velocity on vertical profile, with value comparison to wind tunnel measurement, on stand-alone building exposed to normal wind on the east façade¹*

Figure 3.1.2a shows a comparison between measured x -velocity and simulated, using CFD over on top of the mechanical building, on a vertical profile, on a stand-alone building. This comparison shows that $k-\omega$ SST finds the trend of the measured data in the boundary layer region, near the wall, better than the rest of the models. As one departs from the vicinity of the wall, $k-\epsilon$ Realizable with power-law inlet velocity profile performs better than the rest of the models on the profile. With proper distance from the boundary, approximately 15 m, $k-\epsilon$ Realizable outperforms the rest of the models. This pattern is observed on all the upstream vertical profiles for x -velocity. Figure 3.1.2b shows 80 m vertical profiles from the east façade,

¹ To find the error percentage values, go to Appendix B - Error Percentage Plots

upstream of stand-alone buildings, respectively. On average, Standard $k-\omega$ shows a better agreement than the rest of the models below the midrise building height, 20 m. Above that, $k-\varepsilon$ Realizable outperforms the rest of the models, by a good margin, Figure 3.1.2a, b.

On the side-edge gauge points, that is the gauges on the north and south edges of the east façade, one can suspect that $k-\omega$ SST overall performs better than other models. As one gets closer to the middle of the façade and far from the side edges, the order changes as the performance of Standard $k-\omega$ and $k-\varepsilon$ Realizable on a log-law inlet velocity profile are on par with each other and better than $k-\omega$ SST. $k-\omega$ SST tends to overpredict and $k-\varepsilon$ Realizable with a power-law velocity inlet profile rather underpredicts the velocity in that region, compared to wind tunnel data. Marching more towards the center of the façade, comes the EN3-base column on the east façade, this pattern is repeated as $k-\omega$ SST overpredicts and $k-\varepsilon$ Realizable with a power-law velocity inlet profile underpredicts the measured data. Overall, Standard $k-\omega$ and $k-\varepsilon$ Realizable on a log-law inlet velocity profile show a good agreement with wind tunnel, which is less than 10% difference.

As far as the center of the façade is concerned, there is more to be discussed. As the building is not surrounded and the wind is perpendicular, the domain and the solution should be symmetrical. This never happens in practice, neither in wind tunnel nor in even a fully symmetrical domain. Though the domain and meshing strategy used in this study is rather not symmetrical to higher decimal places. This is simply due to the division of domain width by the number of mesh cells in the same direction, and the fact that that the value of dimensions could not be divisible by the number of mesh cells in that direction. The trailing decimal digits of the domain dimensions and meshing and initial values do not match on symmetrical sides of the domain and the solver is set on double precision. All that results in asymmetry in solution.

Having said that, the center line, is theoretically on the symmetry plane of the domain. Which means that is approximately where the stagnation point is located.

Around that region, especially towards the ground, down below of the façade, the wind significantly slows down which results in the highest order of errors found in the simulation. This is because two-equation turbulence models rather fail to simulate proper eddy recirculation and consequently velocity field in low speed regions of the field, (see Figure 3.1.2c).

Measurement in the wind tunnel finds the velocity to be less than 3 m/s and the closest this scheme of solution finds the velocity to that number is under Standard $k-\omega$ at nearly 1 m/s. Above that height, on an average basis, Standard $k-\omega$ and $k-\omega$ SST rather perform on the same level with least amount of error followed by $k-\varepsilon$ Realizable with log-law inlet velocity profile and $k-\varepsilon$ Realizable with power-law inlet velocity profile.

It is noteworthy that the effect of continuity is also clearly observed. Under such geometry, the centerline of the east façade goes under the circulation of the upstream eddy. That eddy works as a semi-closed system rather than a penetrable control volume. The fact that the size and distance of those eddies to the adjacent wall boundary are comparable in all the four models studied, an overprediction near the roof results in an underprediction near the ground. This effect is observed throughout the domain, on any vertical profile.

On the building's roof, there is three more vertical profiles studied. The bases of these profiles are depicted in Figure 2.3.13a. On the corner profile towards the north and east façade one could observe that Standard $k-\omega$ performs better than the bunch on the near wall – boundary layer region – simulation. Far from the roof on the same vertical profiles, $k-\varepsilon$ Realizable with power-law inlet velocity profile is the best fit, same as its performance on mechanical room or any vertical profile away from the boundary, in almost every case. Overall, the choice in that region much like the profile above the mechanical room should be $k-\omega$ SST, as it features a median of both $k-\varepsilon$ Realizable away from the boundary and Standard $k-\omega$ near the boundary.

Figure B.1 shows the error percentage of the comparison of set values. These graphs rather show the size of the domain is also set appropriately in lateral direction as the error percentage of simulated results compared to measurement on either side of the domain, is less than 5% under any modeling regime.

3.1.1.2 Oblique Wind on the East and South Façades

For a stand-alone building exposed at 45° on the east and south façades, overall, all the four models find the profile of the x -velocity over the mechanical room on par with each other and within a proper margin of error, 5%, as shown in Figure 3.1.3a. Though it is notable that as for the previous cases, $k-\varepsilon$ Realizable with power-law velocity inlet will predict the results slightly better than the rest of the crowd, 3% on average, see Figure 3.1.3a.

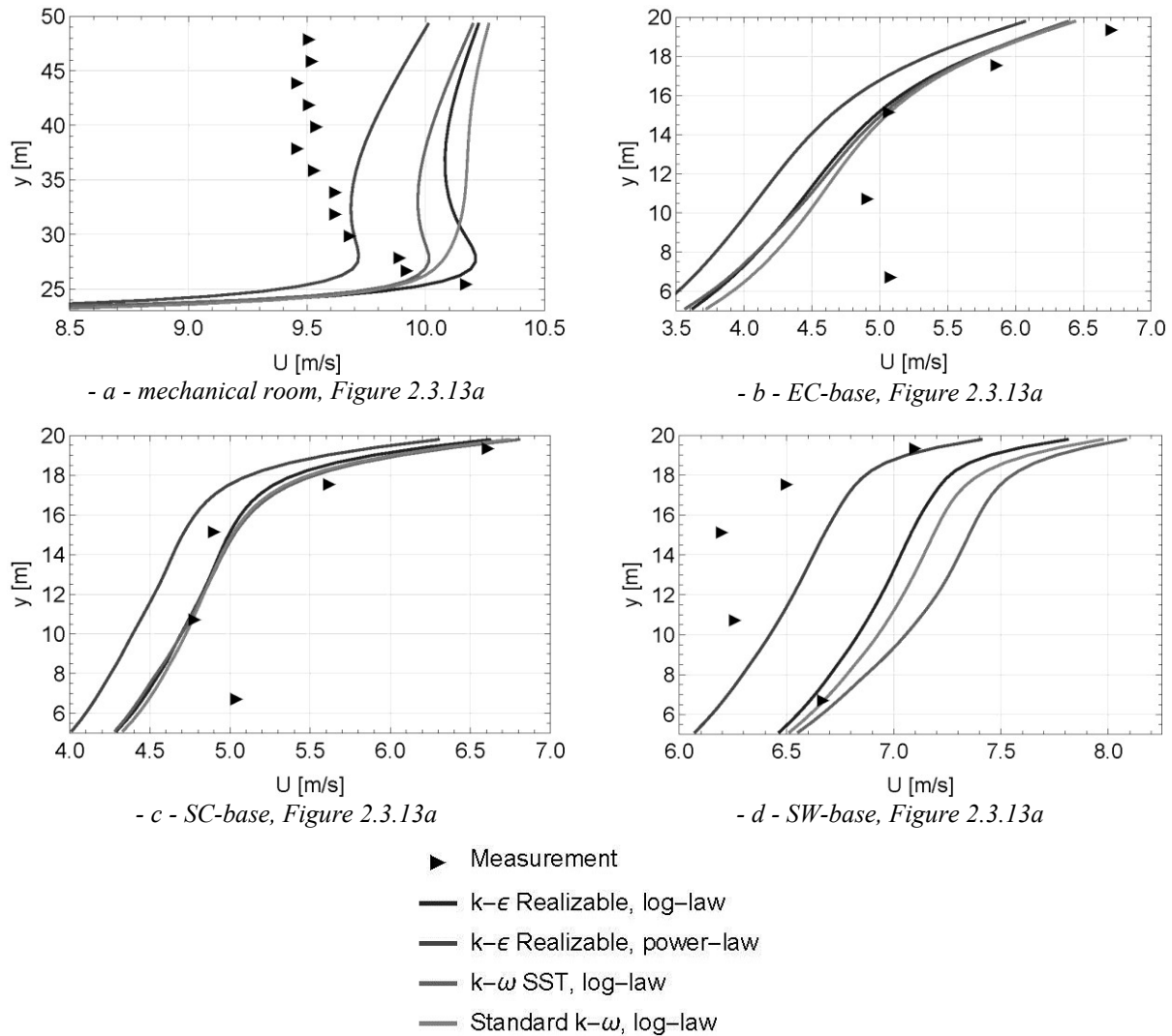


Figure 3.1.3 - x-velocity value comparison on a vertical profile, with stand-alone building exposed at 45° wind on the east and south façades¹

On the note of façade measurement points, the turbulence models under log-law velocity inlet find the wind tunnel measurements rather precisely, that is less than 8% of error margin. $k-\epsilon$ Realizable on a power-law velocity inlet underpredicts the measurements on the east façade almost everywhere. On the downstream measurement over vertical profile of the east façade. Overprediction of two-equation turbulence models in that region results in a better performance of $k-\epsilon$ Realizable on a power-law velocity inlet for the top half of the east façade in that region and overprediction of other models based on log-law velocity inlet profile.

¹ To find the error percentage values, go to Appendix B - Error Percentage Plots

As far as the South façade is concerned, Figure 3.1.3c and d, which happen to be the upstream side of the façade when the building is exposed to wind at that angle, there is underprediction by all the models everywhere on that vertical profile. Though k- ϵ Realizable with power-law inlet velocity find the velocity to be less than other models.

Overall, the error margin in that region is between -5% at near the roof to -30% near the ground, bearing in mind that k- ϵ Realizable with power-law inlet velocity nearly 5% off on every measurement point than the other three, Figure 3.1.3. At the middle of the south façade, Figure 3.1.3c, k- ϵ Realizable with power-law inlet velocity profile again finds lower values for the velocity than other models. The results find the measurement at a much lower margin of error, between +4% to -12%, excluding k- ϵ Realizable with power-law inlet velocity profile, Figure 3.1.3c.

Marching towards downstream of the façade, the underprediction fades away and turns into more precise and consequently overprediction of CFD at the west edge of the south façade, Figure 3.1.3d. So much so that singularity of k- ϵ Realizable with power-law inlet velocity in finding the results to be lower than the rest of the models makes it a better fit as this model shows a better agreement with wind tunnel measurements. It is noteworthy to state that at this region of domain, studied models fail to properly fit the shape of the wind tunnel measurements, Figure 3.1.3d.

Regardless, Figure 3.1.3d shows a $\pm 7\%$ margin of error for k- ϵ Realizable with power-law inlet which happens to be feature as the best model in this region and -7% to 20% margin of error.

Overall, for the stand-alone building under oblique wind load, inlet velocity profile is rather more important than the choice between turbulence models under study in this thesis. Power-law scheme predicts the velocity to be less than the equivalent low-law inlet velocity profile.

3.1.2 Validation of Simulations on Surrounded Building

3.1.2.1 Normal Wind to the East Façade

A fact about the graphs of CFD comparison to wind tunnel measurement on a surrounded building is that on the side that the concentration of surrounding buildings upstream is lower,

south side of the east façade, Figure 2.3.2, the error percentage of the comparison on the east façade simulation points is lower by a margin of nearly 10%, Figure B.4b and e,¹.

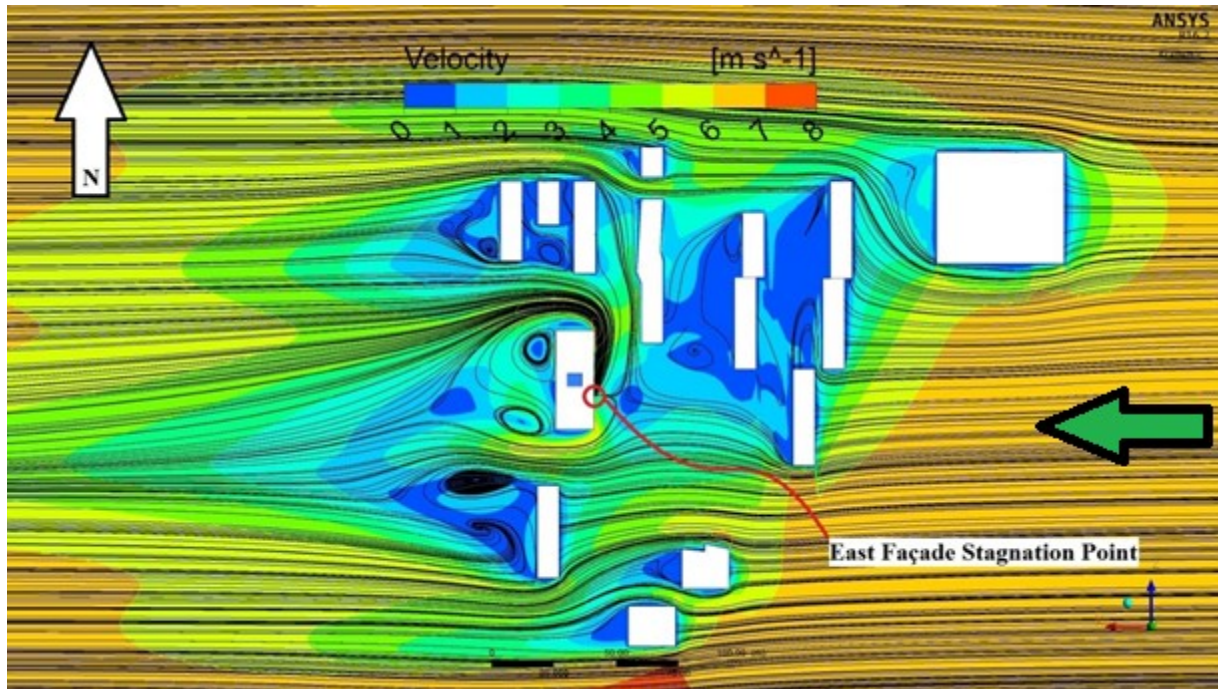


Figure 3.1.4 - Velocity contour (plan view) and streamlines at 5 m above the ground, alongside the location of stagnation point, around surrounded test building, exposed to normal wind on the east façade, Standard $k-\omega$ with $U_{10} = 6.7$ m/s, left pointing arrow shows inlet wind direction²

Moreover, the stagnation point is now shifted toward the south edge of the east façade, Figure 3.1.4, versus a symmetrical stand-alone building where the stagnation point is theoretically in the middle. The concentration of the upstream surrounding buildings also physically describes this phenomenon. On the south edge, the east façade sees a less dense upstream building concentration which allows the flow to gain momentum in that region and consequently, as the velocity there is higher than the upstream region of the north edge side, the stagnation point clearly shifts towards the south edge, see Figure 3.1.4.

For a surrounded building, under normal wind on the east façade, the shape of the profile 3 m above the mechanical room is closely followed by all four models, Figure 3.1.5a. Though $k-\epsilon$ Realizable with power-law inlet velocity tends to overpredict the wind tunnel measurements,

¹ See Appendix B - Error Percentage Plots

² Inlet wind directions in figures in this thesis are all from left to right, except for the ones that indicate north direction

more than other models. As far as the façade measurements are concerned, because of the surrounding upstream buildings, the results of the simulations are slightly altered by the turbulence model used (Figure 3.1.5b to d).

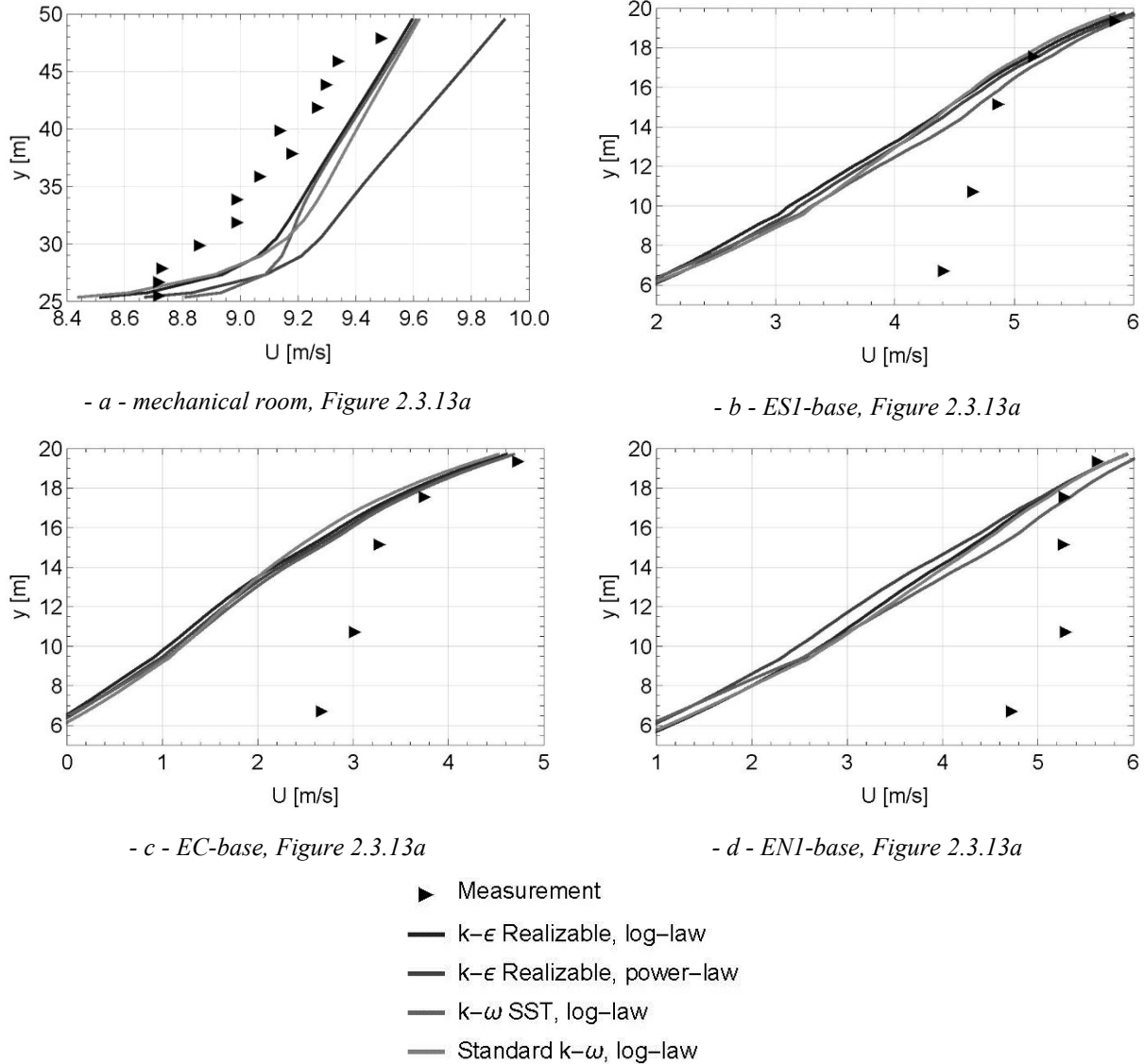


Figure 3.1.5 - x-velocity value comparison on vertical profile, with the surrounded building exposed to normal wind on the east façade¹

As far as the measurement points on the lower three-quarters of the façade are concerned, CFD almost all the time underpredicts the wind tunnel measurement. It is also important to notice that

¹ To find the error percentage values, go to Appendix B - Error Percentage Plots

EC-base (Figure 2.3.13a and Figure 3.1.4) is still the closest to the stagnation point and rather far from the edges which results in it seeing the lowest values for the velocity upstream, less than 3 m/s, Figure 3.1.5d.

On the simulations above the mechanical room, Figure 3.1.5a, all four models find these measurements within an error percentage margin of 5%. For the top three measurement points, which are on top quarter portion of the façade, all four models find the measurement with small margin of error, less than 20%, Figure 3.1.5b to d. This error margin for the edge measurement points goes down to 10%, Figure 3.1.5b to d.

Overall, one can observe that the choice of two-equation turbulence models, or inlet velocity profile, for the surrounded building simulations, is a lot less important than the same problem, in simulating stand-alone building. It is noteworthy to mention that $k-\omega$ SST tends to overpredict x -velocity near the façade that other three turbulence models used.

3.1.2.2 Oblique Wind on the East and South Façades

For a surrounded building exposed to 45° wind onto the east and south façades of the building, over the mechanical room above the roof, on a vertical profile, Figure 3.1.6a, the highest error margins are attributed to Standard $k-\omega$ and the best fit is $k-\varepsilon$ Realizable with power-law velocity profile. What is noteworthy to discuss is that amongst all four models studied, $k-\omega$ SST rather finds a lower velocity near the mechanical room (wall boundary) compared to the rest and the rate of change of x -velocity to the distance from the ground is higher than the rest of the models. Predictions by $k-\omega$ SST above the mechanical room shows that the first calculation node except for the non-slip wall boundary gives a value for x -velocity to be less than 2 m/s, Figure 3.1.6a. This is compared to more than 6.5 m/s value of the same node predicted by the other three models. Though, all four models assume comparable values as one departs nearly 2 m from the wall boundary on that profile. The simulation results in that region are in the range of -4% to 8%.

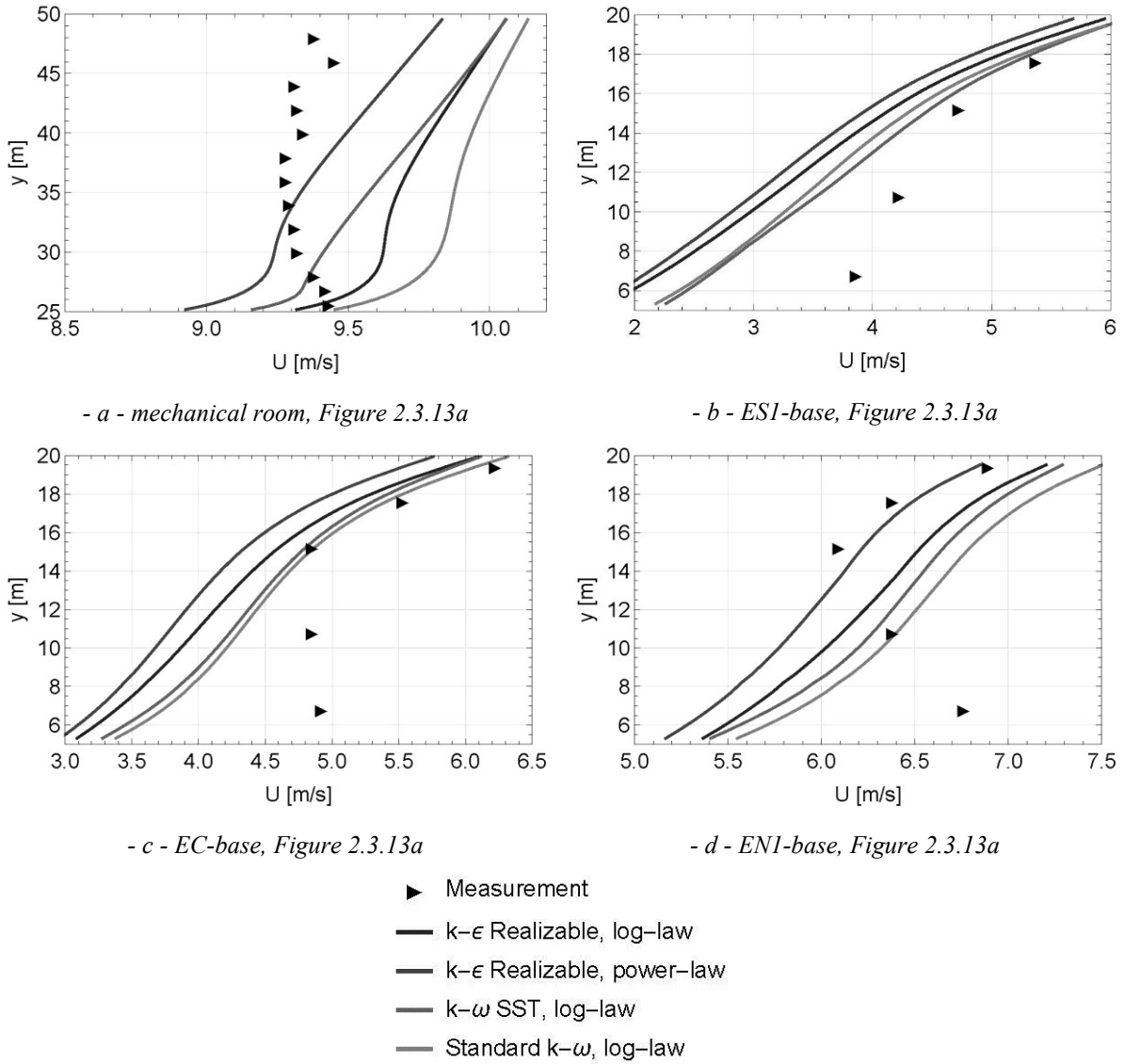


Figure 3.1.6 - x -velocity value comparison on vertical profile, with surrounded building exposed to 45° wind on the east and south façades¹

On the east façade measurements when exposed to oblique wind, unlike the case with normal wind on the east façade, the surrounded building simulations are rather responsive to the turbulence model used. This sensitivity is accentuated as one marches onto the north façade measurement comparisons. $k-\epsilon$ Realizable with power-law inlet velocity profile finds the lowest x -velocity values, then comes $k-\epsilon$ Realizable with log-law inlet velocity profile and then it is between Standard $k-\omega$ and $k-\omega$ SST. On the south side, which is the front edge of the building

¹ To find the error percentage values, go to Appendix B - Error Percentage Plots

when it is facing the wind at 45° on the east and south façades, Standard $k-\omega$ finds x -velocity to be lower than what $k-\omega$ SST predicts it. Though on the center and the north edge, that order is reversed, Figure 3.1.6b to d. Notable thing is that the highest difference between the prediction of all the models is 1 m/s which occurs at the top half of the façade. On the downstream side of the east façade, which is the north edge, the simulation fails to find the shape of the measurement as the flow tends to accelerate near the ground and two-equation models used in this study fail to imitate that pattern in those regions, Figure 3.1.6d.

On the north façade measurements under slanted wind on the east and south façades at 45° , one should note that the north façade is on the leeward of the building. Simulation of such eddies - bearing in mind that the physical value of velocity is considerably low in that region, is beyond the strength of two-equation turbulence models. Second reason that error percentage in that region reaches those high values is that the surrounding buildings in the leeward area of the test building under any wind direction are not simulated in the current study for simplification purposes. That contributes to the unrealistic results. Though a couple of things are noticeable. Firstly, Standard $k-\omega$ imitates the shape in that region better than the rest of the models. Secondly, it also features the least amount of errors amongst all.

3.1.2.3 Oblique Wind on the East and North Façades

As far as the east façade measurement points are concerned, starting with the south edge of the east façade, Figure 3.1.7b, much like downstream of 45° wind on the east and south façades, there is an acceleration on the bottom two points which our two-equation turbulence models fail to predict. Though much like 45° wind on the east and south façades, here on wind on the east and north façades, $k-\varepsilon$ Realizable with power-law inlet velocity profile rather finds the x -velocity to be lower than the other models, on façade measurement points. This difference is less than 0.5 m/s at maximum. For these points across the east façade, the error percentage is less than 10% for $k-\varepsilon$ Realizable with power-law inlet velocity profile for all the points on the top half of the façade, Figure 3.1.7b to d.

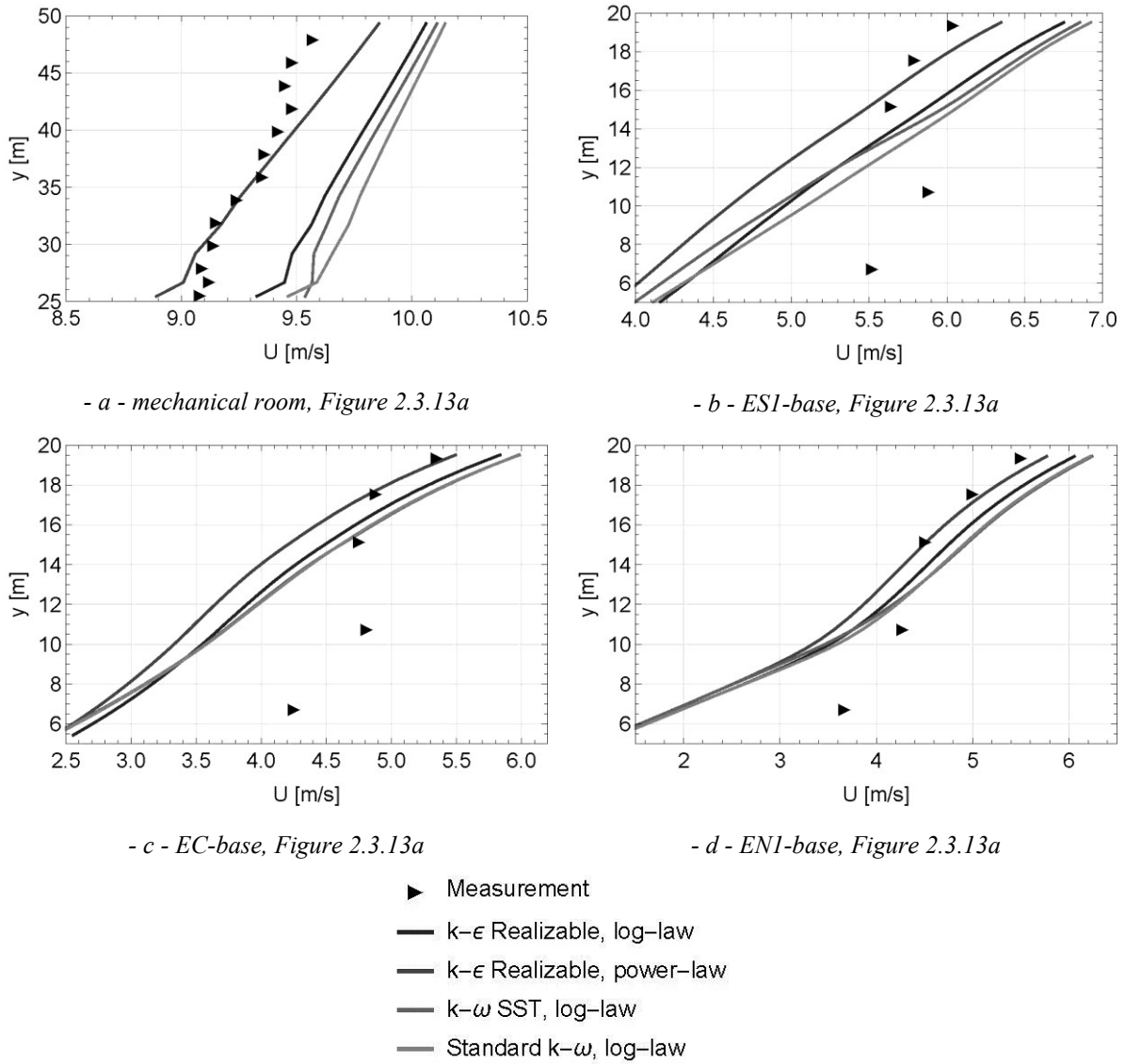


Figure 3.1.7 - x-velocity value comparison on vertical profile, with surrounded building exposed to 45° wind on the east and north façades¹

In the same manner, as when the wind blows on the east and south façades, on the upstream points on the top half, ES1-base and ES2-base (Figure 2.3.13), $k-\omega$ SST finds the velocity to be higher than Standard $k-\omega$ by a small margin, here with wind blowing on the east and north, on EN1-base and EN2-base (Figure 2.3.13), $k-\omega$ SST predicts the velocity a bit higher than Standard $k-\omega$. As one marches towards the center and downstream, which here are the south

¹ To find the error percentage values, go to Appendix B - Error Percentage Plots

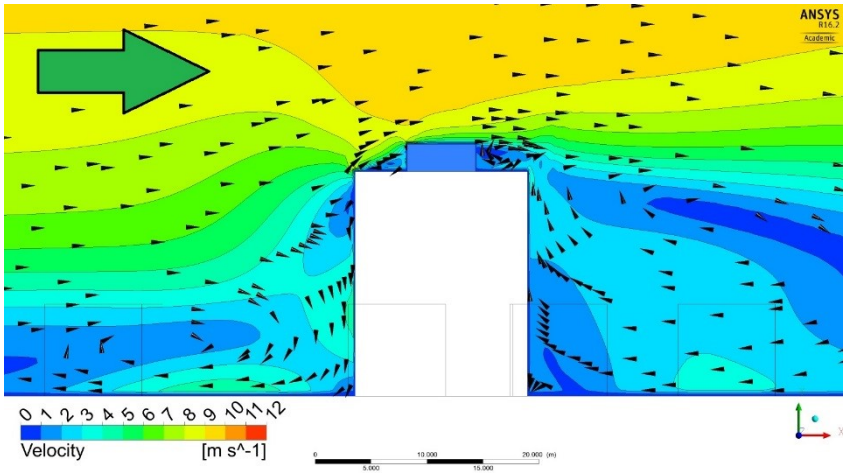
edge (ES1-base and ES2-base) of the east façade, Standard $k-\omega$ finds a higher velocity than $k-\omega$ SST, again, by a very small margin.

Studying the results on the north façade, much like the stand-alone building exposed to 45° wind onto the east and south façades (Section 3.1.1.2), Figure 3.1.3, for which the east edge of the south façade was the upstream side, NE-base (Figure 2.3.13), CFD simulations underpredict x -velocity. As one marches towards downstream, which is the west edge, the underprediction fades away and replaces with overprediction. As one moves towards the west edge of the north façade, NC-base (Figure 2.3.13), at the center of the façade, the results are more accurate. Towards the west edge, there is an overprediction which makes $k-\varepsilon$ Realizable with power-law inlet velocity profile a better fit, much like the stand-alone building simulations exposed to 45° wind onto the south and east façades (Section 3.1.1.2). The overall error percentage margin on this side of the building is less than 30% on the top half points and much higher on the bottom half, due to failure of two-equation turbulence models to find the pattern of x -velocity in that region. On the center and downstream region of the façade, the overall margin of error in simulation is less than 30% and less than 15% respectively, because of what already discussed.

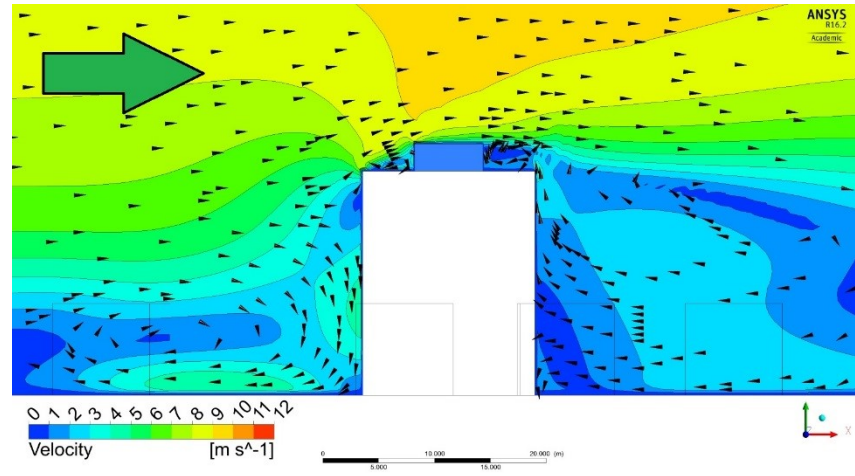
With wind blowing onto the east and north façades at 45° , $k-\varepsilon$ Realizable with power-law velocity inlet profile finds the x -velocity with the lowest margin of error, $\pm 2\%$ above the mechanical room, Figure 3.1.7a. Coming after in prediction precision are all the other models under log-law velocity inlet profile with an error margin of 3% to 7%.

3.1.3 Comparison amongst Turbulence Models

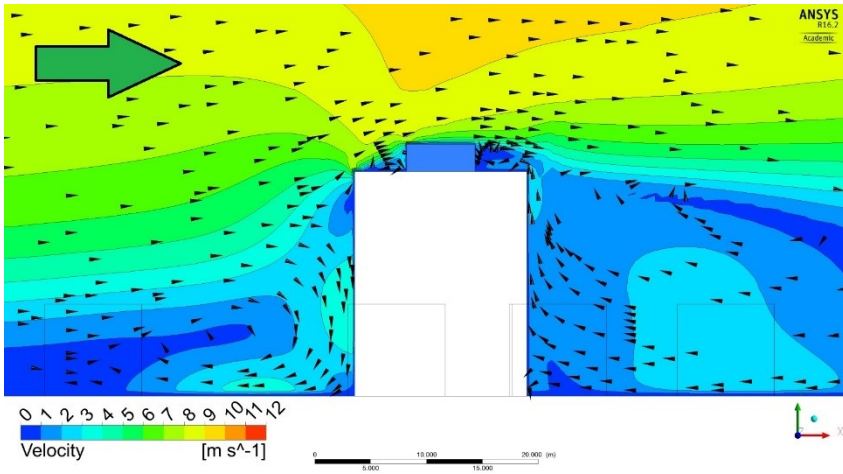
Comparing contours of velocity and field of velocity vector on a mid-plane that cuts the east and west façades in half, Figure 3.1.8, one can notice the difference between the size of eddies predicted up and downstream of the building near the corresponding façades. The center of the major eddy predicted upstream of the building, near the east façade is farthest from the building in $k-\omega$ SST, Figure 3.1.8f and b, then comes Standard $k-\omega$, Figure 3.1.8a and e, and then $k-\varepsilon$ Realizable, Figure 3.1.8c and g. This observation is rather different for a stand-alone building, Figure 3.1.8e, f, g and h, as the distance of the center of set upstream eddy is considerably predicted to be closer to both the adjacent wall boundaries, the ground, and the east façade, than for surrounded building.



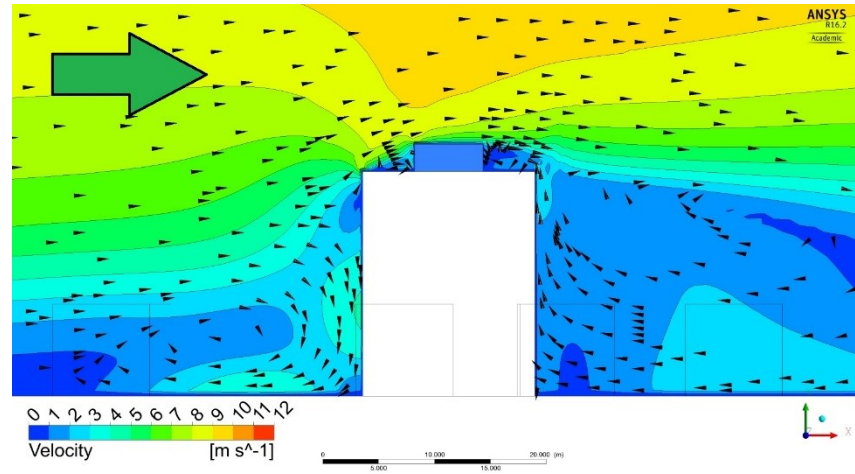
- a - Standard $k-\omega$, log-law velocity profile, surrounded building



- b - $k-\omega$ SST, log-law velocity profile, surrounded building

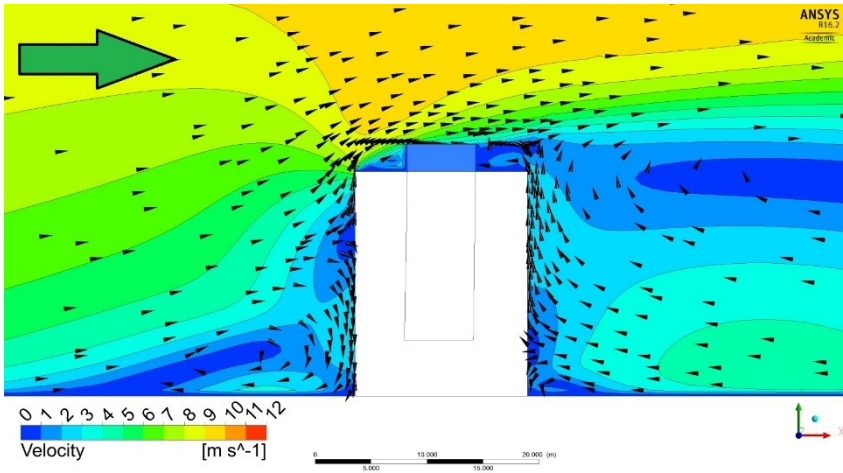


- c - $k-\epsilon$ Realizable, log-law velocity profile, surrounded building

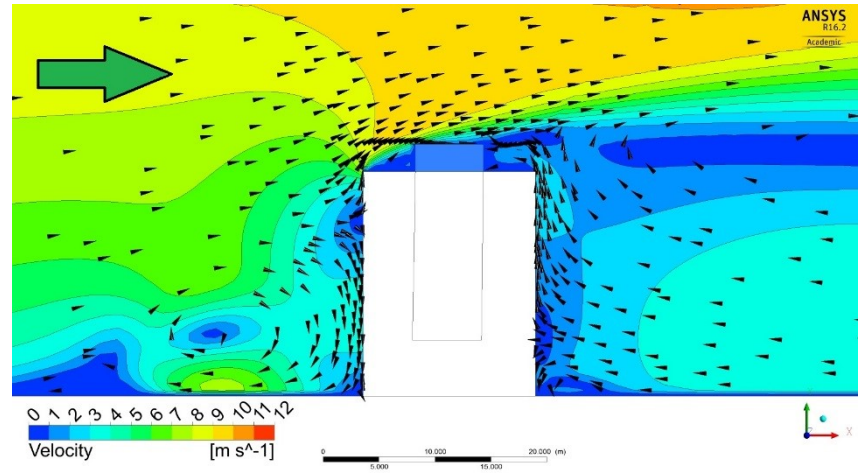


- d - $k-\epsilon$ Realizable, power-law velocity profile, surrounded building

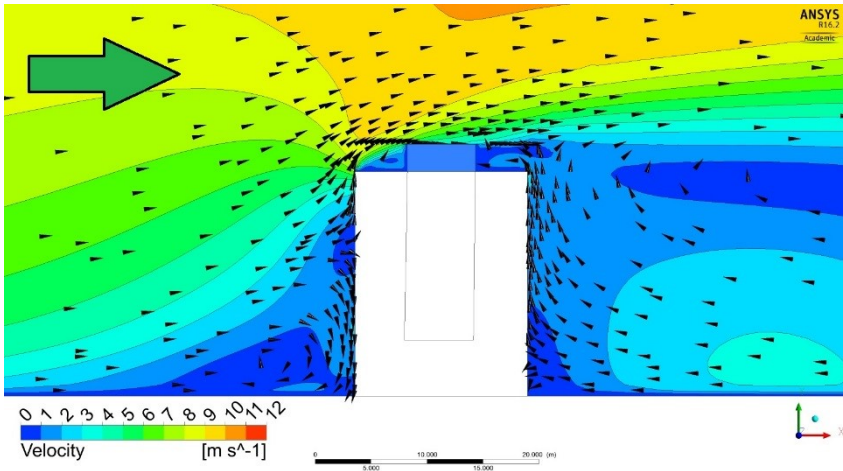
Figure 3.1.8 (Continued)



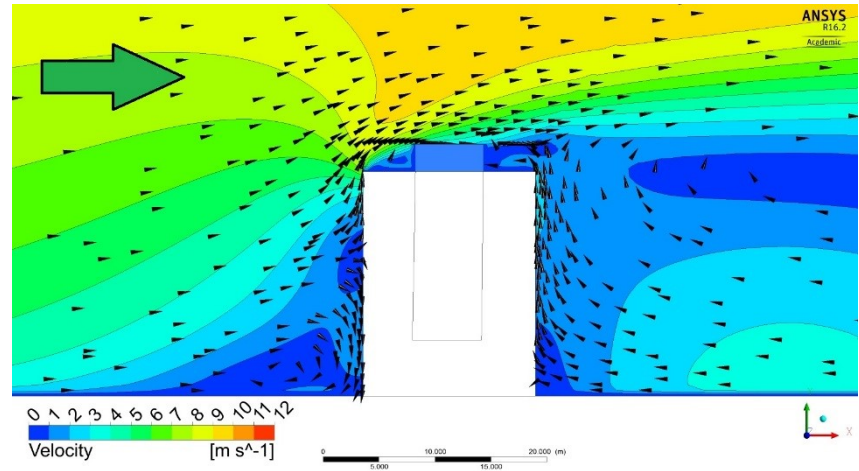
- e - Standard $k-\omega$, log-law velocity profile, stand-alone building



- f - $k-\omega$ SST, log-law velocity profile, stand-alone building



- g - $k-\epsilon$ Realizable, log-law velocity profile, stand-alone building



- h - $k-\epsilon$ Realizable, power-law velocity profile, stand-alone building

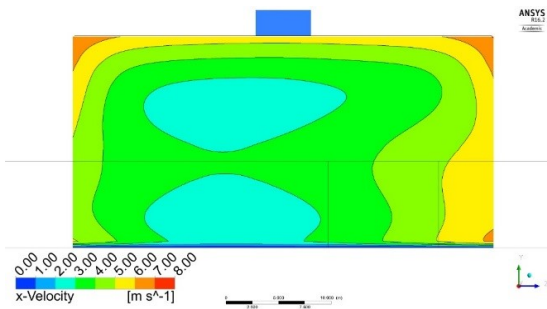
Figure 3.1.8 - Contours of velocity and field of velocity at $z = 0$ plane, around surrounded test building exposed to normal wind to the east façade, for $U_{10} = 6.7$ m/s, arrow shows inlet wind direction

Stagnation point of the east façade (façade that faces upstream-ward wind) is predicted at nearly the same location for all the models for a surrounded building. In contrast, stand-alone building finds the stagnation point rather more towards the ground than the surrounded building domain, Figure 3.1.8d and h.

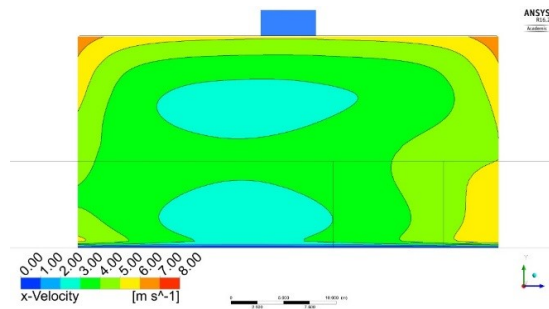
As far as the trailing eddy is concerned, stand-alone building solution finds a much larger one in comparison to a surrounded building solution. As far as the proximity of the center of the eddy is concerned, this time, the center of the eddy in Standard $k-\omega$ is closer to the leeward, west façade. This can be explained using continuity equation and the fact that the major upstream eddy is found to be farther from the east façade in this model compared to the rest. There is also one more noteworthy observation to be made and that is the size of the minor eddy down near the ground, adjacent to the west façade, leeward façade. This is found to be less accentuated in terms of size and proximity to the adjacent wall boundaries in both $k-\varepsilon$ Realizable under log or power-law inlet velocity profiles, whilst there is negligible difference between log and power-law solutions to the domain in those terms. $k-\omega$ SST predicts completely different contours and shape of wind velocity field for a stand-alone building compared to other turbulence models. This is in terms of size of upstream major eddy, velocity magnitude and location of stagnation point on the east façade, Figure 3.1.8f.

Standard $k-\omega$ predicts the velocity near the east façade, on a surrounded building, higher than other models, towards the edges, Figure 3.1.9. As one hovers off the edges, towards the center of the façade, this trend is less observed in the center, Standard $k-\omega$ and $k-\omega$ SST predict higher speed at that region than $k-\varepsilon$ Realizable.

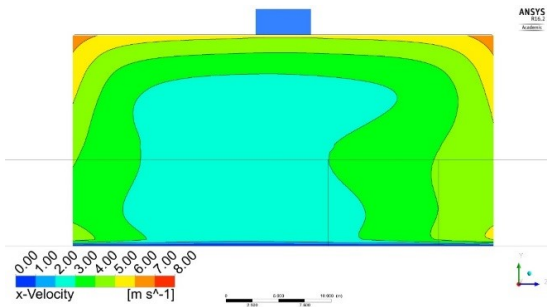
A stand-alone building in the domain will be predicted a by symmetrical contour near the façade. Top corner edges also are predicted rather with a higher x -velocity in a stand-alone building domain than the surrounded one. Comparison amongst Figure 3.1.9e, f, g and h shows that unlike the surrounded building in this case, the choice of turbulence model alters predicted wind around the stand-alone building considerably. $k-\omega$ SST the highest magnitudes of normal velocity are predicted by in the middle of the façade, Figure 3.1.9f. Though as one compares that to a surrounded building, the center parts of it rather act differently as they are under predicted.



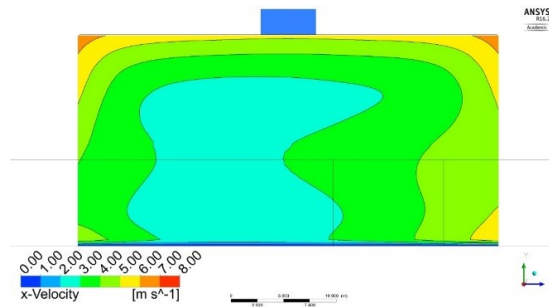
- a - Standard $k-\omega$ with log-law velocity profile, surrounded building



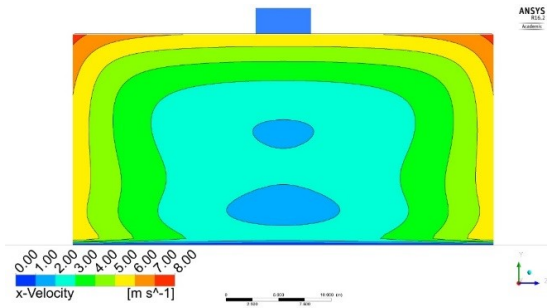
- b - $k-\omega$ SST with log-law velocity profile, surrounded building



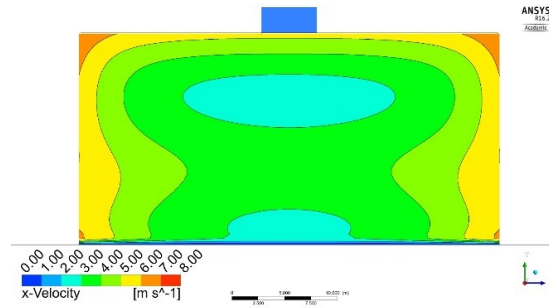
- c - $k-\epsilon$ Realizable with log-law velocity profile, surrounded building



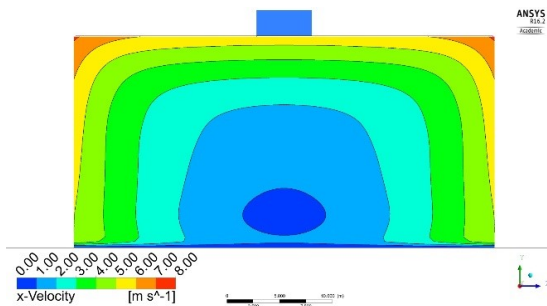
- d - $k-\epsilon$ Realizable with power-law velocity profile, surrounded building



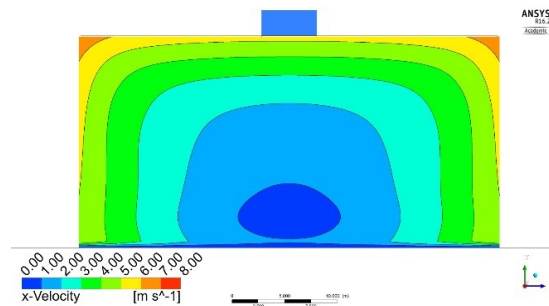
- e - Standard $k-\omega$ with log-law velocity profile, stand-alone building



- f - $k-\omega$ SST with log-law velocity profile, stand-alone building



- g - $k-\epsilon$ Realizable with log-law velocity profile, stand-alone building



- h - $k-\epsilon$ Realizable with power-law velocity profile, stand-alone building

Figure 3.1.9 - Contour of velocity magnitude at 3.6 m upstream of the east façade, around surrounded test building exposed to normal wind on the east façade at $U_{10} = 6.7$ m/s

Figure 3.1.10 demonstrates a clearer and more comprehensive image of the upstream and trailing major and minor eddies for four cases under study. This clearly shows a bigger size of upstream eddy predicted by $k-\omega$ SST and a rather extended one windward. One can observe how each model finds turbulent kinetic energy on the z -bisector plane in Figure 3.1.10. It is rather obvious that Standard $k-\omega$ predicts a higher kinetic energy upstream near the east façade's top edge. More so on the region above the mechanical room and in the downstream trailing eddy region. This is less accentuated in $k-\omega$ SST, which predicts the lowest turbulent kinetic energy almost everywhere on that plane. It is noteworthy to mention that lower amount of turbulent kinetic energy is essentially lower amount of kinetic energy extracted from the mean flow.

Figure 3.1.11 shows streamlines and velocity contour of the wind field at 19.45 m above the ground; solved for surrounded test building, at $U_{10} = 6.7$ m/s using four modeling schemes studied.

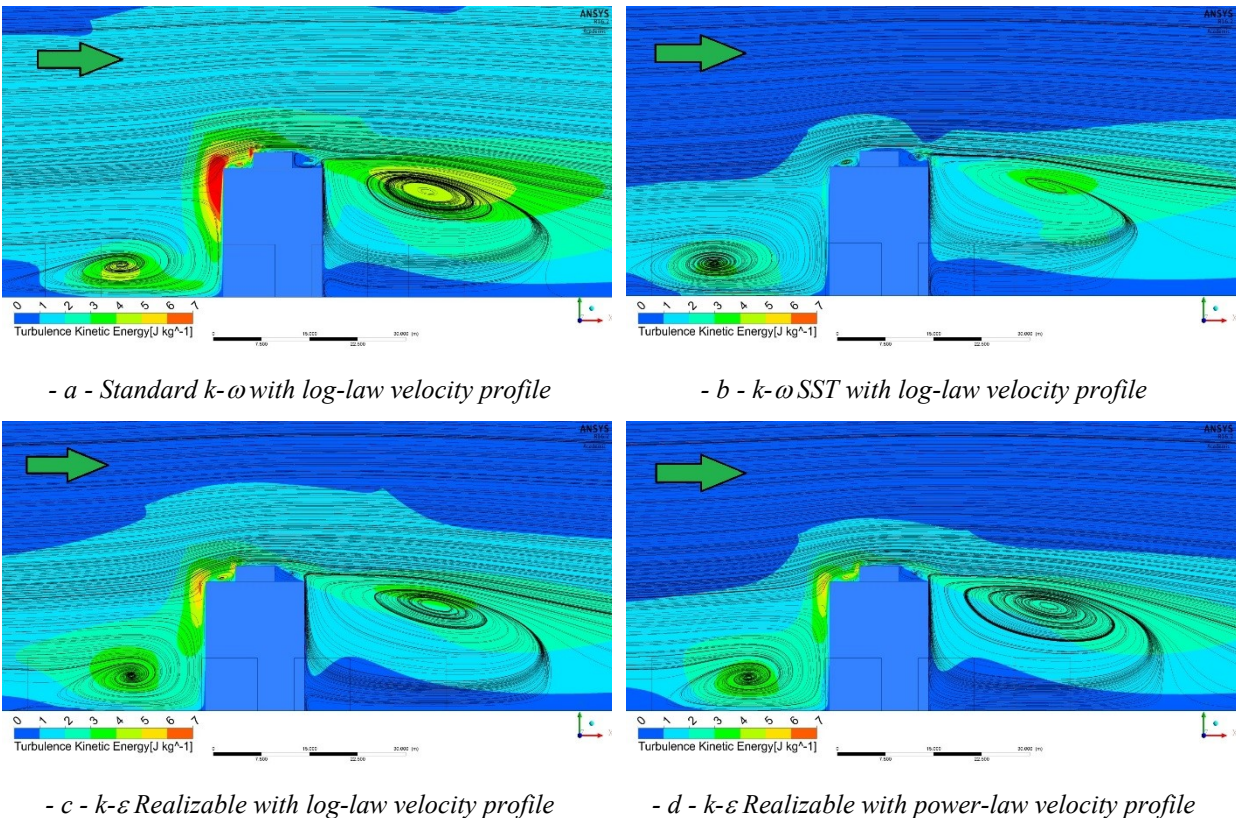
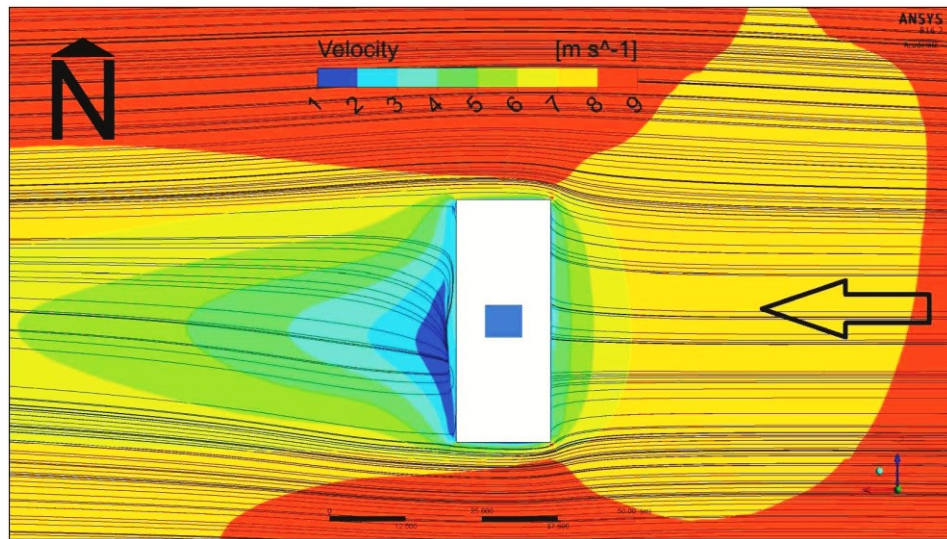


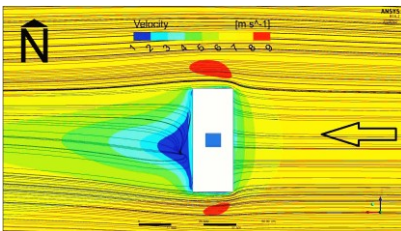
Figure 3.1.10 - Streamlines of the wind velocity with turbulent kinetic energy at mid z -plane, around surrounded test building exposed to normal wind to the east façade at $U_{10} = 6.7$ m/s, arrow shows inlet wind direction

Comparing Figure 3.1.11a to the graphs of $k-\omega$ SST and $k-\varepsilon$ Realizable (Figure 3.1.11b and Figure 3.1.11c respectively), reveals that in general, Standard $k-\omega$ predicts a higher velocity in the upstream (red regions), and both sides of the building. Though the order of velocity predicted near the building and downstream, as well as the size of velocity contours in those regions are comparable.

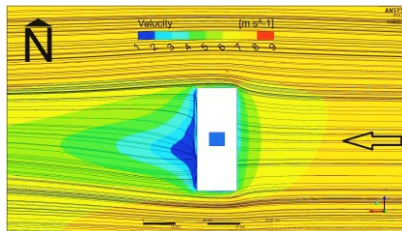
Same observation could be made on the contours and streamlines of velocity at a height of 15.23 m above ground, which happens to be the measurement level of ES3 and EN3, Figure 3.1.12. Another considerable difference between the predictions is the leeward wind in the immediate vicinity of the building. In that region, Standard $k-\omega$ and $k-\omega$ SST both rather find the wind higher than $k-\varepsilon$ Realizable. Figure 3.1.12 shows that the size of the horizontal leeward eddy predicted by $k-\varepsilon$ Realizable is considerably larger than that of Standard $k-\omega$ and $k-\omega$ SST. Same is observed for the vertical leeward eddy, depicted in Figure 3.1.10.



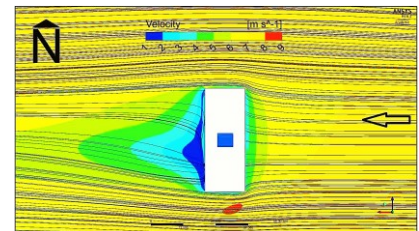
- a - Standard $k-\omega$ with log-law velocity profile



- b - $k-\omega$ SST with log-law velocity profile

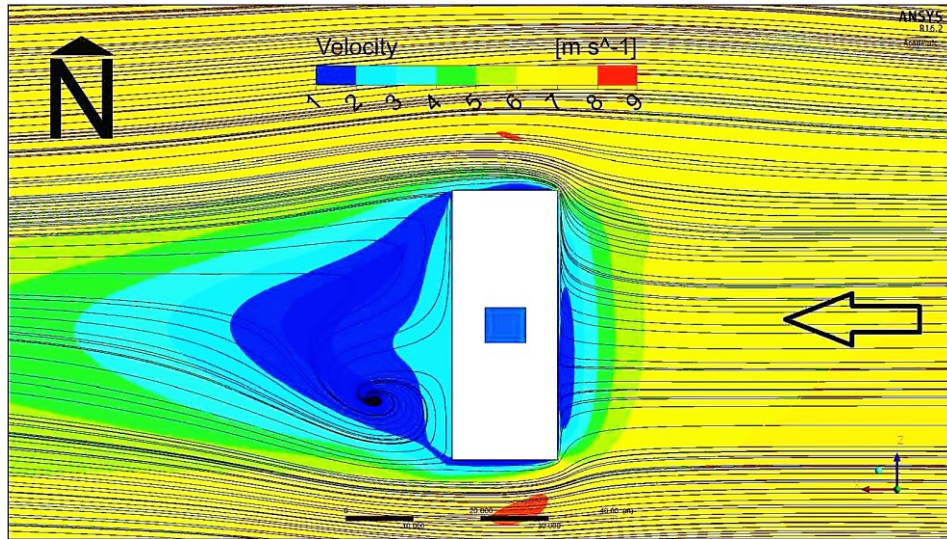


- c - $k-\varepsilon$ Realizable with log-law velocity profile

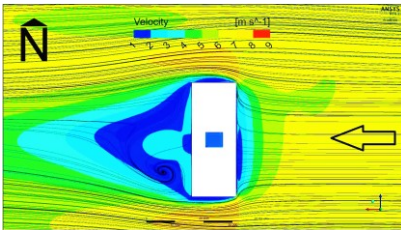


- d - $k-\varepsilon$ Realizable with power-law velocity profile

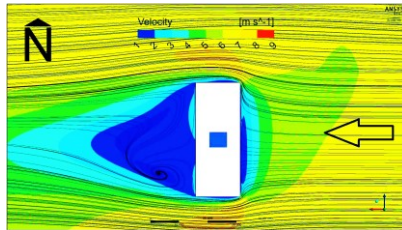
Figure 3.1.11 - Velocity contour (top view) and streamlines at 19.45 m above the ground (at the level of ES1 and EN1 gauges, Figure 2.3.13b), around surrounded test building exposed to normal wind to the east façade, at $U_{10} = 6.7$ m/s, arrow shows inlet wind direction



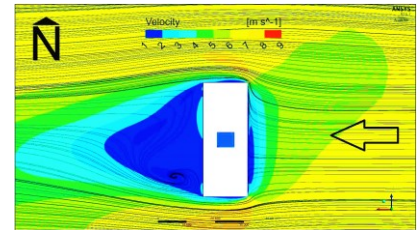
- a - Standard $k-\omega$ with log-law velocity profile



- b - $k-\omega$ SST with log-law velocity profile



- c - $k-\epsilon$ Realizable with log-law velocity profile



- d - $k-\epsilon$ Realizable with power-law velocity profile

Figure 3.1.12 - Velocity contour (top view) and streamlines at 15.23 m above the ground (at the level of ES3 and EN3 gauges, Figure 2.3.13b), around surrounded test building exposed to normal wind to the east façade, at $U_{10} = 6.7$ m/s, arrow shows inlet wind direction

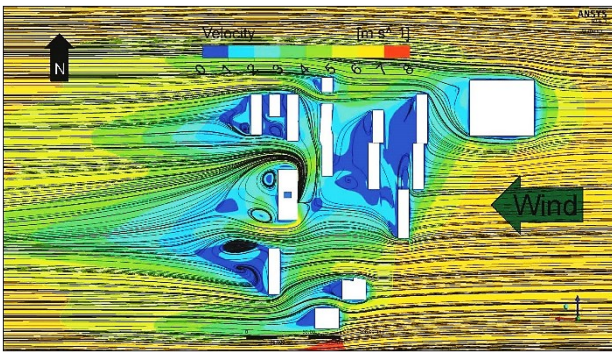
Comparison between Figure 3.1.11 and Figure 3.1.12 shows that as one gets closer to the ground, the size of the leeward and windward eddies, as well as the recirculation regions on the north and south sides of the façade increase. Same marching results in a reduction in velocity almost everywhere in the domain.

Comparison between Figure 3.1.12a, b, c and d shows that the side and the center distance of the lateral eddy is found to be the highest under $k-\omega$ SST amongst all. Then comes Standard $k-\omega$ and the least is $k-\epsilon$ Realizable.

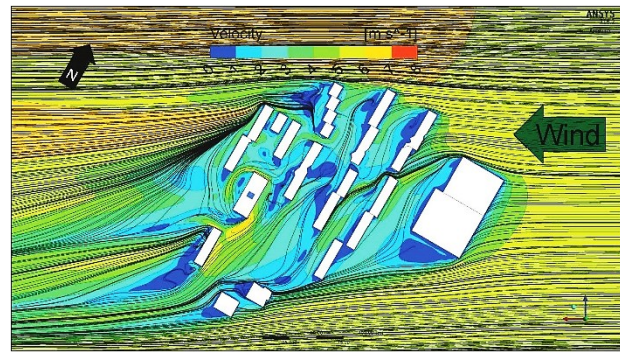
3.1.4 Oblique Wind Parametric Study

As there will be a study on effect of wind direction on catch ratio, as well as on effectiveness of the overhang (see Wind Direction Effect on Overhang Effectiveness section), it is noteworthy to

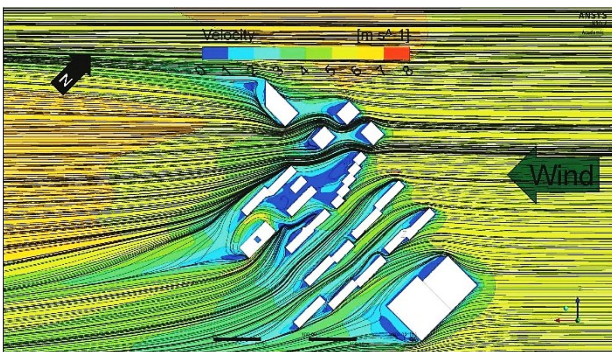
study the contour of velocity magnitude and horizontal streamlines of the velocity on a plane parallel to the ground, 5 m off it. One thing to notice is that off the surrounding buildings taken into consideration for wind-tunnel measurements, shown in Figure 2.3.2 and Figure 2.3.11, with the wind rotating off the normal to the east façade position, upstream and downstream building's positions change. That and due to what went down in surrounding buildings simulations, led to the elimination and addition of some of the buildings as the wind changes angles. As the wind onto the east façade changes angle from normal to it towards normal to the north façade, and since the building arrays are extended in perpendicular direction to wind coming at normal direction onto the east façade, the high pressure leeward blue colored regions behind the buildings become smaller as the shape of the buildings for those wind directions is more aerodynamic, shown in Figure 3.1.13.



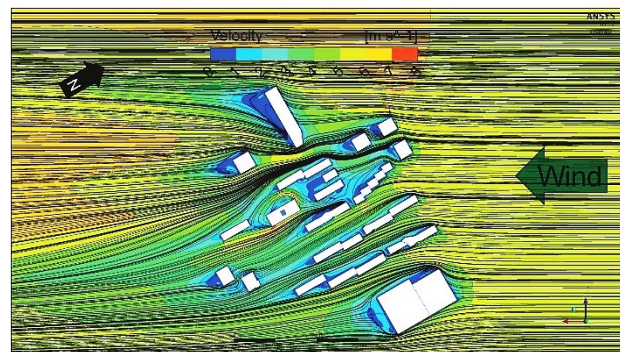
- a - Wind normal onto the east façade



- b - Wind at 30° onto the east and north façades



- c - Wind at 45° onto the east and north façades



- d - Wind at 60° onto the east and north façades

Figure 3.1.13 - Velocity magnitude contour (plan view) and streamlines at 5 m above the ground, around surrounded test building, exposed to normal wind on the east façade, Standard $k-\omega$ with $U_{10} = 6.7$ m/s

3.1.5 Wind Simulation Summary

On top of the building, the most accurate model is k- ϵ Realizable wind power-law inlet velocity profile. On the windward façade, near the roof, Standard k- ω performs the best amongst all the models. This is mostly due to the observations made in Section 3.1.1.1 (specifically Figure 3.1.2) on the stand-alone building. Surrounded building simulations show a small amount of change in the results in that region. As discussed in multiple sections of wind validation, simulations on the lower quarter of the building observe high margins of error as two-equation turbulence models used in current study fail to find flow accurately in those regions. This is not an issue for this thesis' scope which is WDR simulation on a mid-rise building as the catch ratio is predominantly zero for lower parts of the façade in a 1-4 m/s U_{10} range of wind; which is the typical wind speed in the region of the building under study. Leeward side of the building also is inaccurately simulated; though amongst the models used, Standard k- ω features the lowest error percentages. For all that came, Standard k- ω with log-law inlet velocity profile is recommended as a global best fit.

3.2 Rain Simulation

This section deals with rain simulation validation with on-site field measurements. From stand-alone to surrounded building, under four models studied in this thesis, multiple created rain events (see Section 2.3.1.6) are deployed to find the best possible fit among the four for rain simulation, in various regions of the medium-rise test building, under normal wind onto its east façade. Figure 3.2.1 shows an insight to what come in this section, raindrop trajectory prediction.

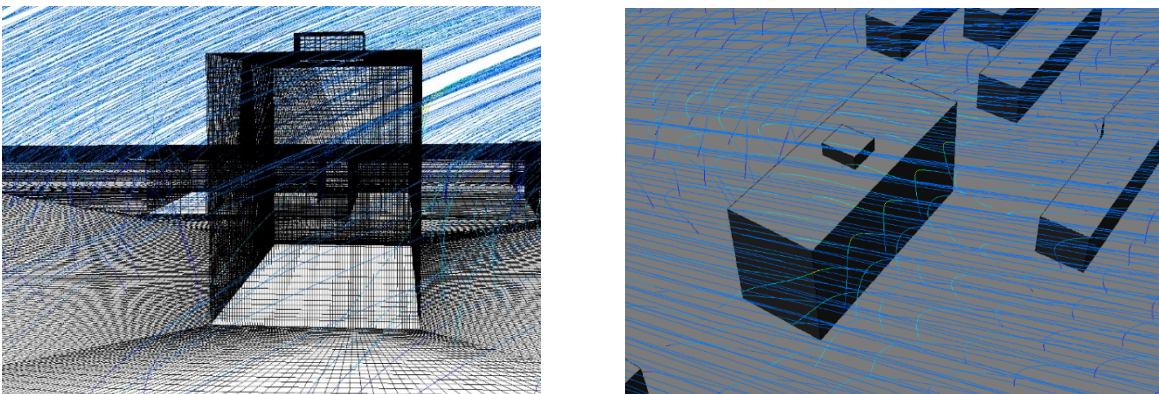


Figure 3.2.1 - $U_{10} = 6.7$ m/s raindrop trajectories for $d = 0.6$ mm, around surrounded test building exposed to normal wind on the east façade

Much like the Wind Simulation section (Section 3.1), followed by validation, here comes depiction of rain impingement onto the façade for multiple raindrop diameters, and contours of catch ratio for various cases. Contours of near-façade x -velocity is used to describe the rainfall impingement for different raindrop diameters and catch ratio contours on the façade overall.

Addressing the main goal of this study, which is effect of façade overhang on protecting the façade from rain, simulations of on-site overhangs in two sizes are validated with various rain events. Consequently, effectiveness of these overhangs is parametrically studied, over rainfall intensity, overhang width, multiple portions of the façade and wind speed.

3.2.1 Validation and Model Comparison of Simulation on Stand-Alone Building

Notable fact about validating rain simulations is due to prominent wind direction being onto the east façade of the test building in the terrain of location, proper data for oblique WDR is scarce. Consequently, WDR validation in this thesis, unlike wind, is validated using only normal wind on the east façade.

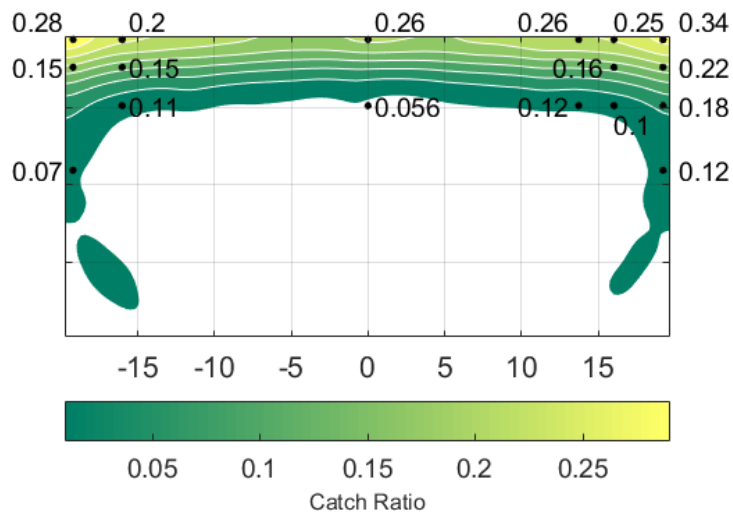
Another mentionable point about the validations is that unlike parameter study that high wind speeds are used, on-site disposable WDR events are rather at low wind speed range (between U_{10} of 0.5 m/s to 3 m/s) which makes the validation of the phenomenon at higher range (above 6 m/s) rather undecided, and dependable upon the lower range.

For the simple geometry of stand-alone building domain, two WDR events are created, and numerically solved for four models used in this study and the simulations are validated using only these two. The rain events used in this section are presented in Table 3.2.1.

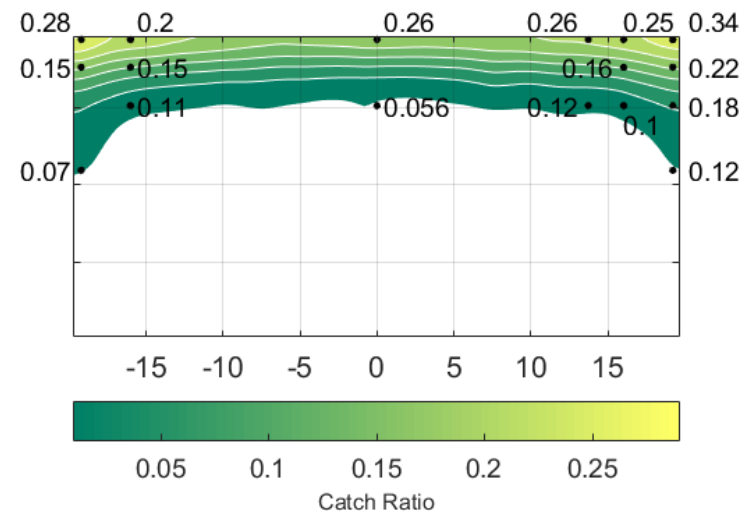
Figure 3.2.2 shows the validation of WDR simulation using stand-alone building domain, based on Event 1 in Table 3.2.1.

Table 3.2.1 - WDR event parameters for stand-alone building validation

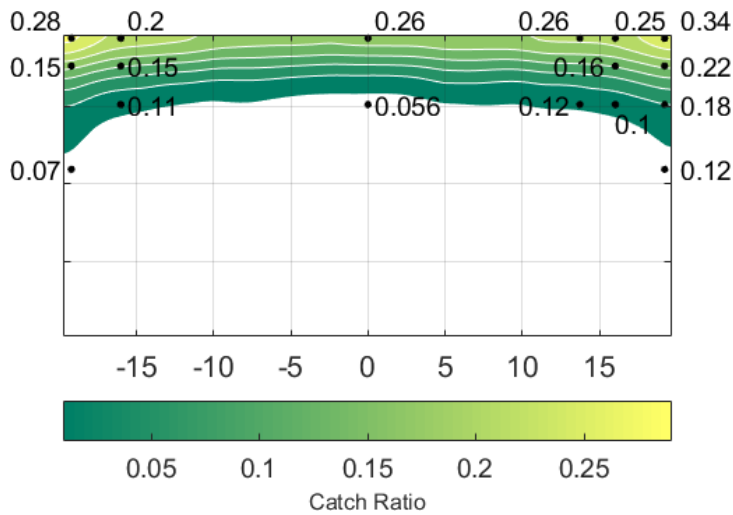
Event	U_{10} [m/s]	R_h [mm/hr]	Number of particles injected per raindrop diameter size	Number of consecutive hours of measurement	Date
1	2.41	3.16	250×400	15	Jan-2014
2	2.67	0.82	250×400	12	Oct-2014



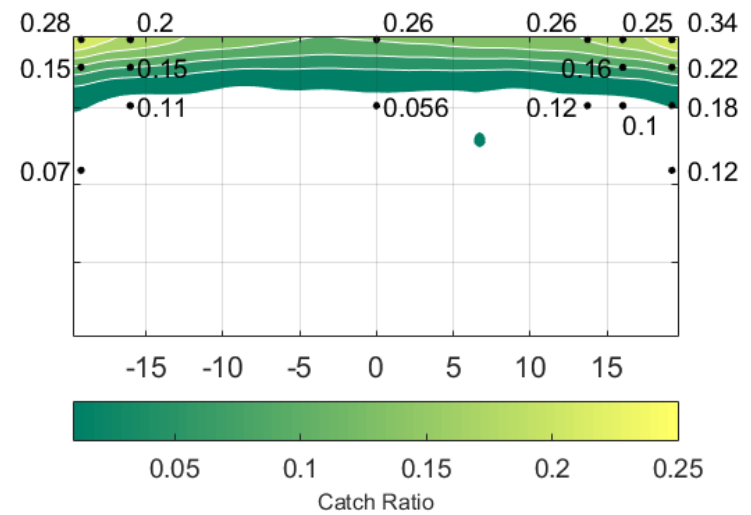
- a - Standard $k-\omega$, log-law velocity profile



- b - $k-\omega$ SST, log-law velocity profile



- c - $k-\epsilon$ Realizable, log-law velocity profile



- d - $k-\epsilon$ Realizable, power-law velocity profile

Figure 3.2.2 - Catch ratio CFD prediction comparison to field measurements, for Event 1 (Table 3.2.1) simulation of WDR, stand-alone building exposed to normal wind on the east façade. Black dots are field measurement catch ratio values. Bottom white areas show zero catch ratio.

All four models are used to predict the catch ratio and the results are presented in the figure. Quantitative error analysis shows that Standard $k-\omega$ model has the lowest maximum error and least mean value of errors for both top-edge gauge points and top two rows (ES1, ES5, EC1, EN8, EN5, EN1, ES2, ES6, EN6 and EN2 in Figure 2.3.13b).

Amongst points ES1, ES2, EN1 and EN2 (Figure 2.3.13b), for the top two points on either side edges, i.e. ES1, ES2 and EN1, EN2, the Standard $k-\omega$ has the lowest maximum error and lowest absolute deviation from the mean. $k-\omega$ SST method has the least mean value of errors, although the difference between $k-\omega$ SST and Standard $k-\omega$ is negligible (less than 2%).

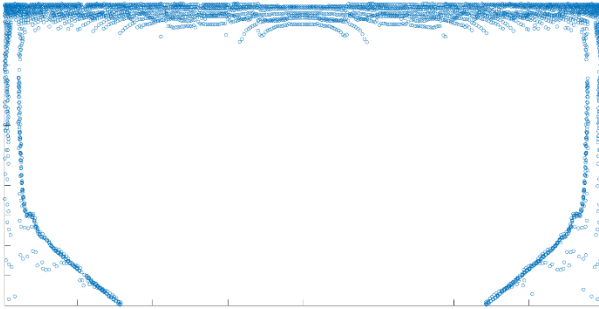
For points on the center column (EC1, EC2, 11 and 12 in Figure 2.3.13b), $k-\omega$ SST has the lowest maximum error and the least absolute deviation from the mean Standard $k-\omega$ has the least mean value of errors.

For points on the edge of north corner, i.e. EN1, EN2, EN3 and EN4 (Figure 2.3.13b), the Standard $k-\omega$ has the lowest maximum error and the least mean value of errors. The $k-\omega$ SST has the least absolute deviation from the mean although the difference between $k-\omega$ SST and Standard $k-\omega$ is negligible (less than 1%).

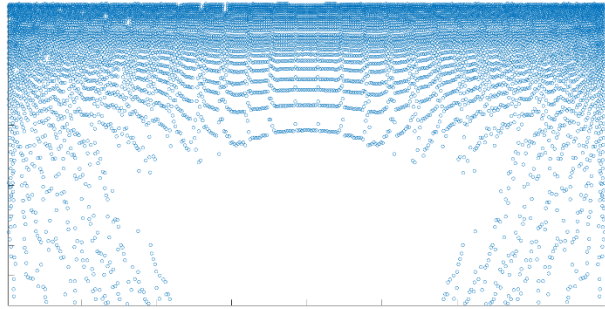
For the second column points on the north corner of the east façade, i.e. EN5, EN6 and EN7 (Figure 2.3.13b), the Realizable $k-\epsilon$ with log-law inlet velocity profile has the lowest maximum error, although the difference between $k-\omega$ SST and Standard $k-\omega$ and Realizable $k-\epsilon$ with log-law inlet velocity profile is negligible (less than 3%). Standard $k-\omega$ method has the least mean value of errors. Similar observations are made on the south side of the façade.

Figure 3.2.3 shows the raindrop impingement for 0.6 mm and 1.2 mm raindrop sizes predicted by all the four models used in this study, for Event 2 on Table 3.2.1. Different patterns show how the contour of predicted wind near the façade is indeed important on WDR prediction for a stand-alone simulation scheme.

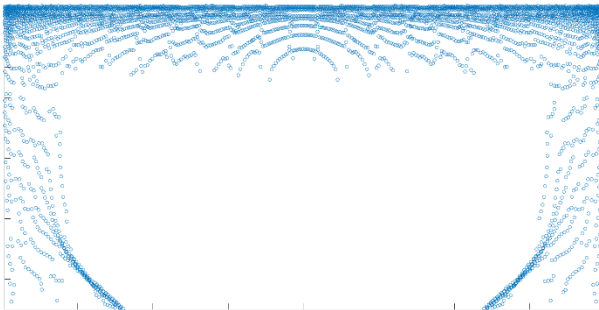
Overall, this study shows that the best choice amongst the four models is rather a Standard $k-\omega$ method with log-law inlet velocity profile, for a medium-rise building in a suburban terrain, modeled stand-alone.



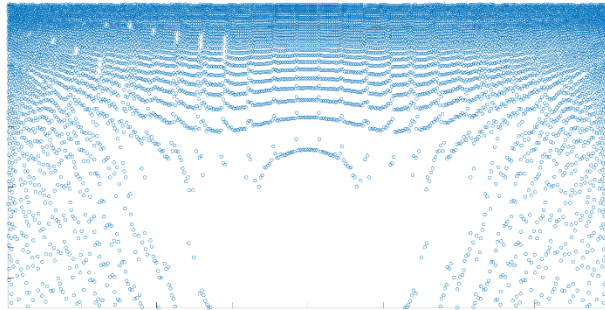
- a - Standard $k-\omega$, log-law velocity profile, $d = 0.6$ mm



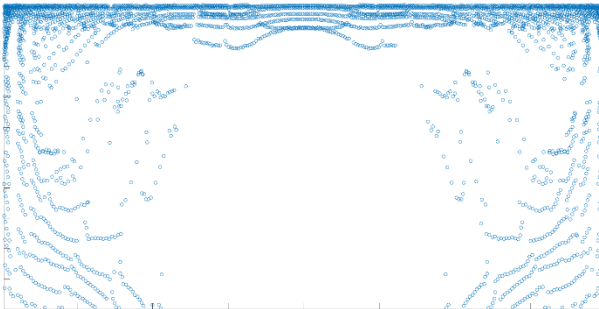
- b - Standard $k-\omega$, log-law velocity profile, $d = 1.2$ mm



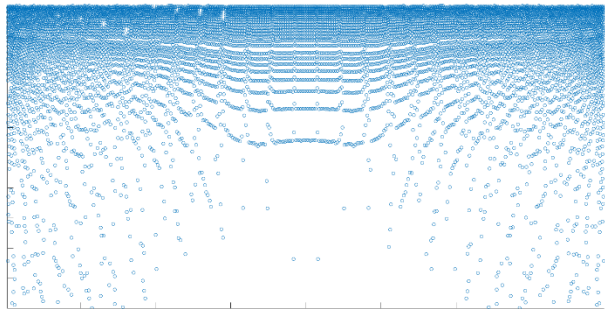
- c - $k-\omega$ SST, log-law velocity profile, $d = 0.6$ mm



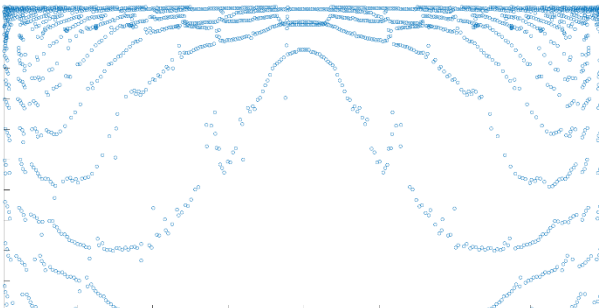
- d - $k-\omega$ SST, log-law velocity profile, $d = 1.2$ mm



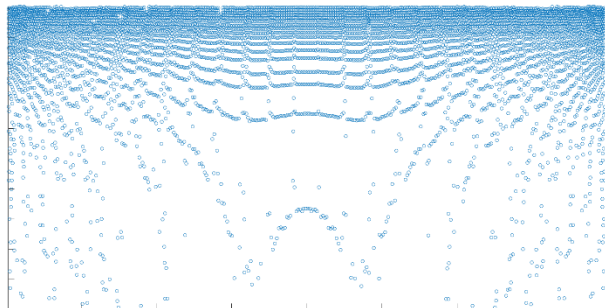
- e - $k-\epsilon$ Realizable, log-law velocity profile,
 $d = 0.6$ mm



- f - $k-\epsilon$ Realizable, log-law velocity profile,
 $d = 1.2$ mm



- g - $k-\epsilon$ Realizable, power-law velocity profile,
 $d = 0.6$ mm



- h - $k-\epsilon$ Realizable, power-law velocity profile,
 $d = 1.2$ mm

Figure 3.2.3 - Raindrop impingement for 0.6 mm and 1.2 mm raindrop sizes, with wind normal to the east façade, Event 2 on Table 3.2.1

3.2.2 Validation and Model Comparison of Simulation on Surrounded Building with Unprotected Façade

Surrounded test building, unlike the stand-alone one is never exposed at symmetrical wind in the case studied in this thesis. That results in an unbalanced contour of concentration, which is essentially unsymmetrical raindrop impingement contour on the east façade (see Figure 3.2.5). As discussed in Normal Wind to the East Façade section (Section 3.1.2.1), wind on the side that sees less buildings, on the upstream, is rather brisker, in velocity component perpendicular to the façade. For smaller raindrops, the larger that component, the more concentrated the raindrop impingement on the façade.

Rain events studied in this section for validation of the WDR simulation, are presented in Table 3.2.2. Noticeable data about Table 3.2.2 is that data is directly collected from Event 3 and Event 5, without operations recommended in Rain Event Selection Procedure section (Section 2.3.1.6). That is only an hour of data collection, raw data from the measurement gauges are taken to be reference point for validation. The reason for that is either high value of rainfall intensity, R_h , or high wind speed, essentially high U_{10} .

Simulation domain parameters are taken to be the same for all those events, and are presented in Table 3.2.3.

As far as validations are concerned, for top two rows of gauges on the façade, Figure 3.2.4a, which are located on the east façade, near the roof, there is predominantly a 20% margin of error of CFD simulations to field measurements. This can be attributed to two major reasons, which are related to the wind prediction in this case, as the turbulence dispersion for the rain phase is not solved.

Though for these measuring points, gauges on either side edges of the east façade, the error percentage is predominantly within a 10% margin of error. The reason that these points are predicted by CFD better than the top two row points, is the distance from the stagnant region in the middle of the façade

Accuracy of prediction of catch ratio of the top corner edge points, EN1 for instance, delivers both arguments home. 5% margin of error of catch ratio is less than the accuracy of measurement tools on the field.

Table 3.2.2 - Wind and WDR parameters of the rain events created to validate simulations on surrounded unprotected building, exposed to normal wind on the east façade

	U_{10} [m/s]	u^*_{ABL} [m/s]	y_0 [m]	y_p [m]	Roughness Constant	R_h [mm/hr]	Number of consecutive hours	Date
Event 1	1.86	0.18	0.152	0.25	3.37217	1.8	2	Sep, Oct 2013
Event 2	2.37	0.24	0.152	0.25	3.37235	6.35	2	Sep, Oct 2013
Event 3	1.54	0.15	0.152	0.25	3.372	4.4	1	Sep, Oct 2013
Event 4	2.69	0.27	0.152	0.25	3.37243	1.45	2	Sep, Oct 2013
Event 5	4.60	0.46	0.152	0.25	3.37267	1.8	1	Sep, Oct 2013
Event 6	2.80	0.28	0.152	0.25	3.37245	1.85	2	Sep, Oct 2013

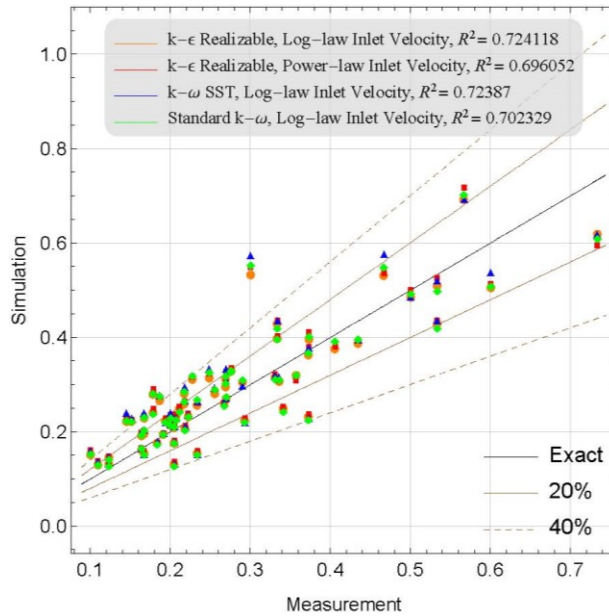
Table 3.2.3 - Computational domain size and discretization for surrounded building, exposed to normal wind on the east façade

Domain length (x)							1041.69 m
Domain height (y)							247.113 m
Domain width (z)							511.2224 m
Surface mesh	Size	Domain sides				~0.44 m - ~7m	
		Building walls				~0.12 m - ~0.48 m	
Volume mesh	Type					Quadrangle	
	Number of CV's					4891431	
	Type					Hexahedron	
	Min Cell Volume					2.79E-03 m ³	
						Max Cell Volume 2.28E+02 m ³	

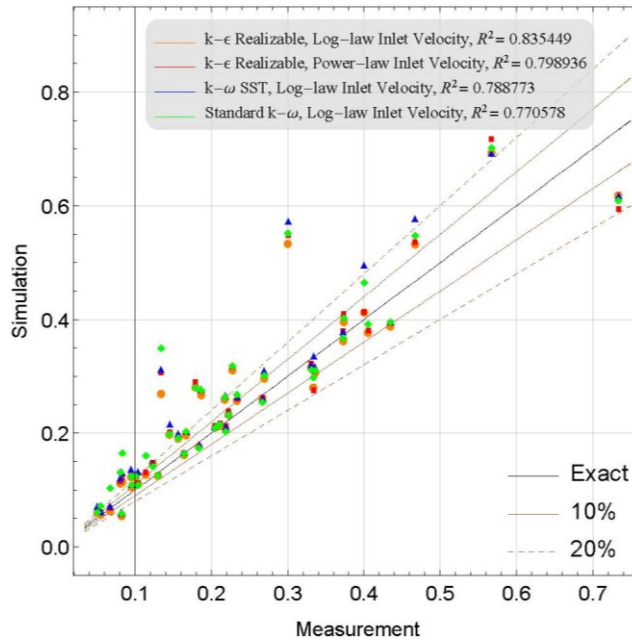
As discussed, towards the middle of the façade, and lower regions, the wind prediction is less accurate and for the fact that the air is stagnant, the catch ratio prediction is not accurate. EC2 is the closest gauge point to the center of the façade, and sees the highest error percentage, because of what was described already.

Another important reading off Figure 3.2.4 is the predominant trend of low difference in prediction, by model change. This validation shows that the choice of two-equation turbulence models used in this thesis and velocity inlet profile on the catch ratio prediction for the surrounded building located in a suburban terrain, exposed to normal wind on the target façade, is rather trivial. There are two major reasons for what discussed on the results. As discussed in Wind Simulation section (Section 3.1), in comparison to stand-alone simulations, the near façade wind prediction is less sensitive to the choice amongst turbulence models. Second reason is attributed to what discussed in Section 2.3.3. Errors associated with this simulation on WDR, including lack of rain phase turbulence dispersion and drag modeling, are also partially responsible for insensitivity of the results to turbulence and inlet velocity profile for such modeling scheme. The low difference in results of the models used are also shown in Figure 3.2.6, which shows contours of catch ratio and error percentage on each gauge location.

Figure 3.2.5 shows the raindrop impingement for 0.5 mm and 1.0 mm raindrop sizes predicted by all the four models used in this study, for Event 2 on Table 3.2.2. More similarity is found between the models' prediction in this case, compared to stand-alone simulations. That results in closer specific catch ratio (Equation 2.3.5) prediction between the models and consequently closer catch ratio values across the façade, Figure 3.2.2.

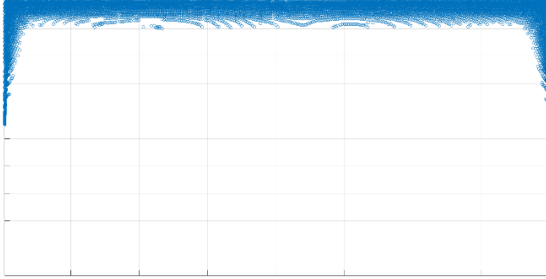


- a - Top two rows of gauges - adjacent to the roof

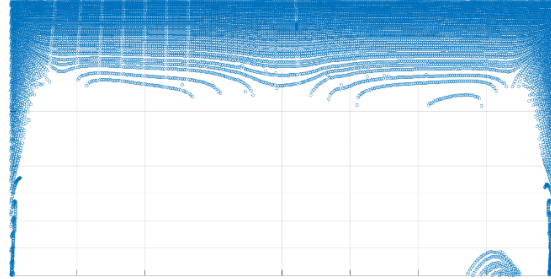


- b - Side-edge gauges - adjacent to the north and south façades

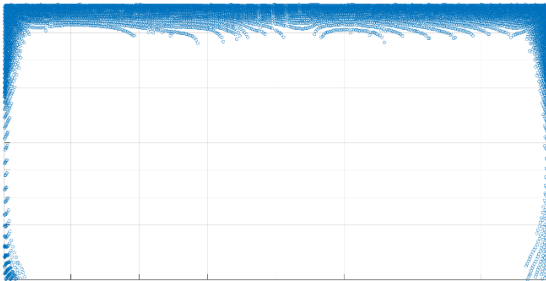
Figure 3.2.4 - WDR simulation validation of surrounded unprotected building domain, at various locations, with east façade exposed at normal wind onto the east façade, multiple rain events



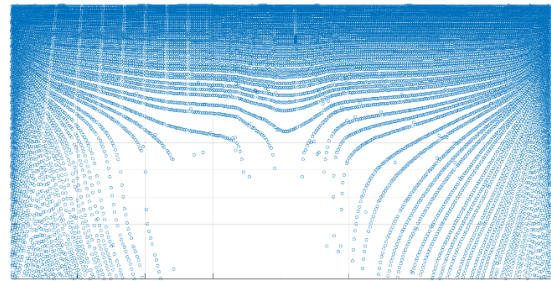
- a - Standard $k-\omega$, log-law velocity profile, $d = 0.5$ mm



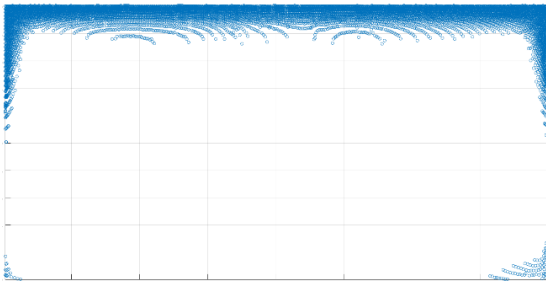
- b - Standard $k-\omega$, log-law velocity profile, $d = 1.0$ mm



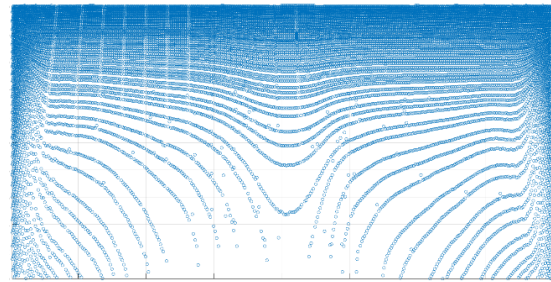
- c - $k-\omega$ SST, log-law velocity profile, $d = 0.5$ mm



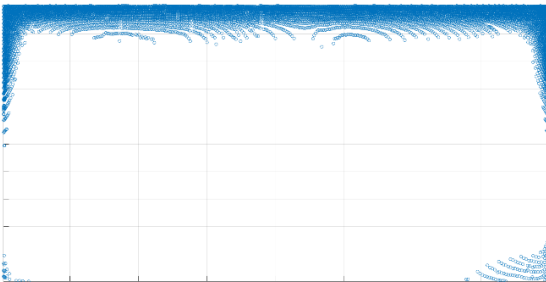
- d - $k-\omega$ SST, log-law velocity profile, $d = 1.0$ mm



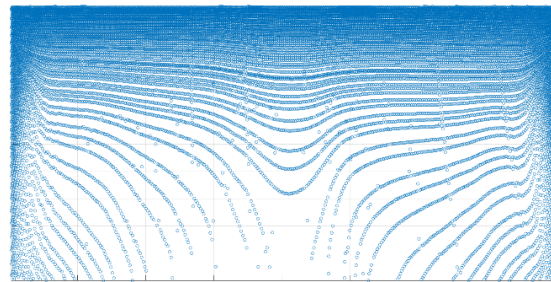
- e - $k-\epsilon$ Realizable, log-law velocity profile,
 $d = 0.5$ mm



- f - $k-\epsilon$ Realizable, log-law velocity profile,
 $d = 1.0$ mm

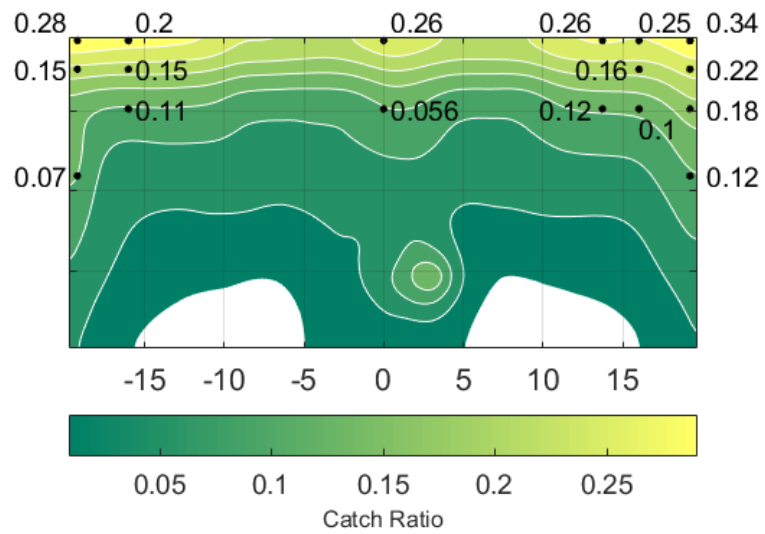


- g - $k-\epsilon$ Realizable, power-law velocity profile,
 $d = 0.5$ mm

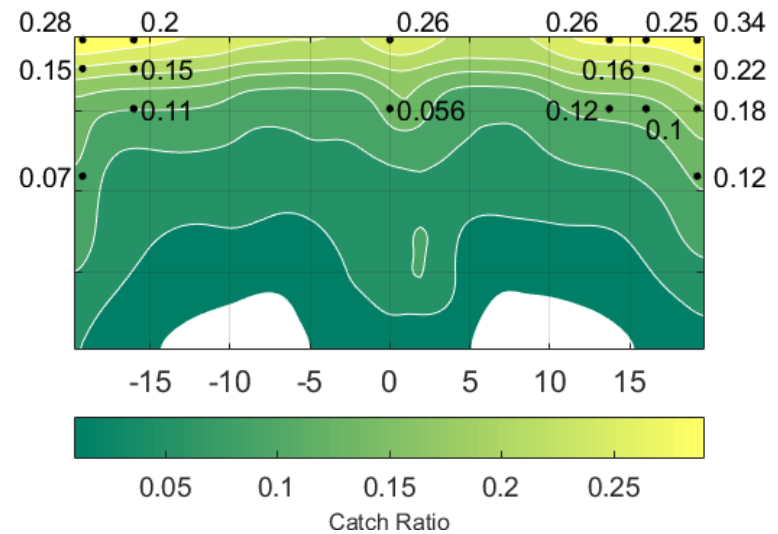


- h - $k-\epsilon$ Realizable, power-law velocity profile,
 $d = 1.0$ mm

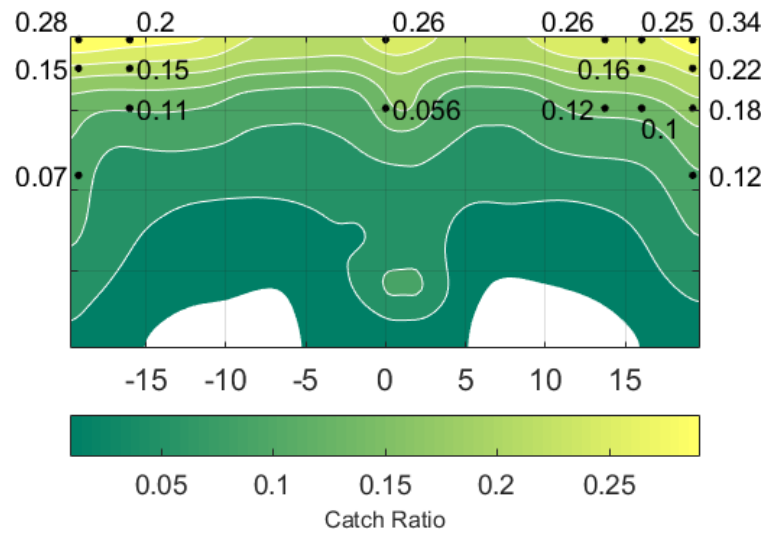
Figure 3.2.5 - Raindrop impingement for 0.5 mm and 1.0 mm raindrop sizes, with wind normal to the east façade, Event 2 on Table 3.2.2



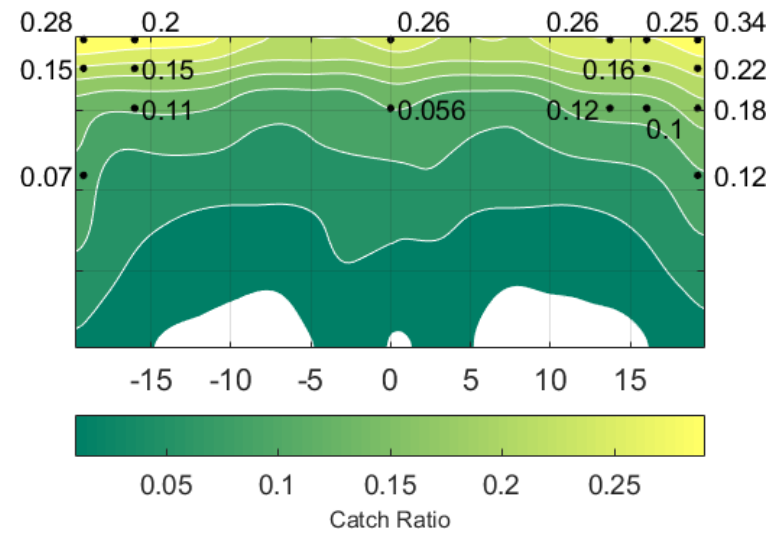
- a - Standard $k-\omega$, log-law velocity profile



- b - $k-\omega$ SST, log-law velocity profile



- c - $k-\epsilon$ Realizable, log-law velocity profile



- d - $k-\epsilon$ Realizable, power-law velocity profile

Figure 3.2.6 - Catch ratio CFD prediction error percentage, for Event 1 (Table 3.2.1). Black dots are field measurement catch ratio. Bottom white areas show zero catch ratio.

3.2.3 Validation and Model Comparison of Simulation on Surrounded Building with Protected Façade

As the main objective of this work is to assess and quantify the performance of an overhang, two sizes of overhang are deployed onto the test building's east façade and multiple rain events are created to validate the CFD predictions. As already discussed in Section 3.2.1, due to small variation of results between multiple models, validation of CFD prediction is limited to one model for simulations with building equipped with an overhang. This model is taken to be Standard k- ω , with log-law inlet velocity profile, recommended model for stand-alone building simulations.

3.2.3.1 2' On-Site Overhang

Rain events used for validation of simulations of CFD with 2' on-site overhang, are presented in Table 3.2.4, with computational domain size and discretization details in Table 3.2.5.

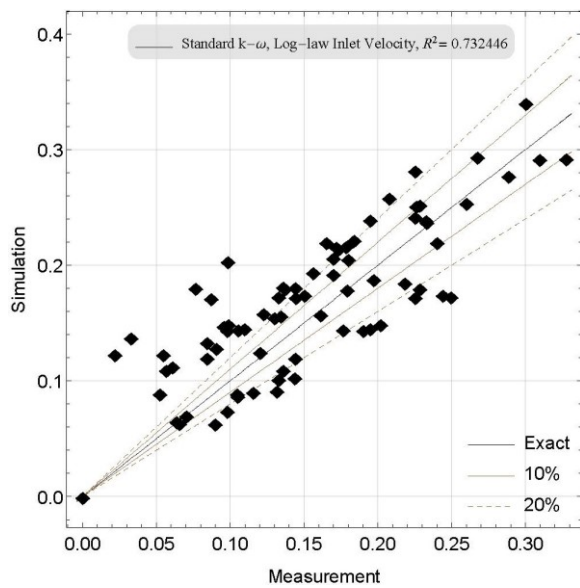
Figure 3.2.7 shows model validation for surrounded building protected with 2' on-site overhang.

Table 3.2.4 - Wind and WDR parameters of the rain events created to validate simulations on surrounded protected building, exposed to normal wind on the east façade

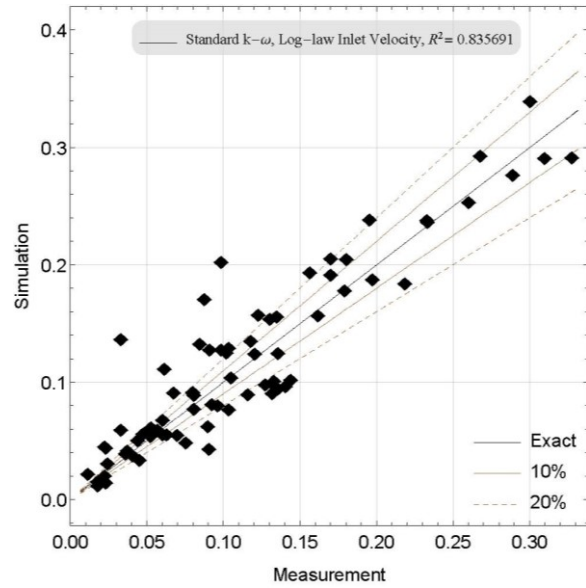
	U_{10} [m/s]	u^*_{ABL} [m/s]	Y_0 [m]	Y_p [m]	Roughness Constant	R_h [mm/hr]	Number of consecutive hours	Date
Event 1	1.58	0.16	0.152	0.25	3.37203	0.53	10	Mar 2015
Event 2	2.24	0.22	0.152	0.25	3.37232	1.1	7	Mar 2015
Event 3	1.97	0.19	0.152	0.25	3.37222	0.70	19	Mar 2015
Event 4	1.82	0.18	0.152	0.25	3.37215	1.4	7	Mar 2015
Event 5	2.16	0.21	0.152	0.25	3.37229	1.6	4	Mar 2015
Event 6	1.50	0.15	0.152	0.25	3.37197	1.67	3	Mar 2015
Event 7	1.82	0.18	0.152	0.25	3.37215	1.37	16	Mar 2015
Event 8	2.25	0.22	0.152	0.25	3.37232	1.53	6	Mar 2015
Event 9	1.28	0.13	0.152	0.25	3.37179	0.86	8	Mar 2015
Event 10	1.83	0.18	0.152	0.25	3.37216	1.21	16	Mar 2015
Event 11	2.16	0.21	0.152	0.25	3.37229	1.48	7	Apr 2017
Event 12	1.51	0.15	0.152	0.25	3.37198	0.92	6	Apr 2017
Event 13	2.44	0.24	0.152	0.25	3.37237	0.67	6	May 2017

Table 3.2.5 - Computational domain size and discretization for surrounded building, exposed to normal wind on the east façade

Domain length (x)							1041.69 m
Domain height (y)							247.113 m
Domain width (z)							511.2224 m
Surface mesh							
		Size			Domain sides		~0.44 m - ~7m
					Building walls		~0.12 m - ~0.48 m
		Type					Quadrangle
		Number of CV's					3350190
Volume mesh		Type					Hexahedron
		Min Cell Volume					4.27E-04 m ³
		Max Cell Volume					3.65E+02 m ³

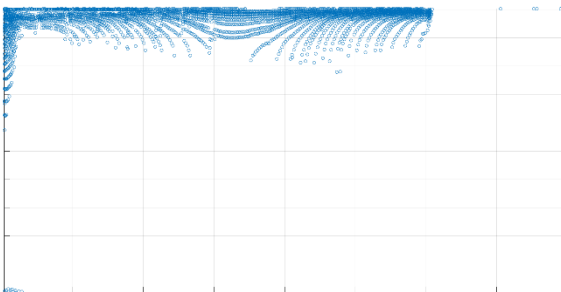


- j - Top two rows of gauges - adjacent to the roof

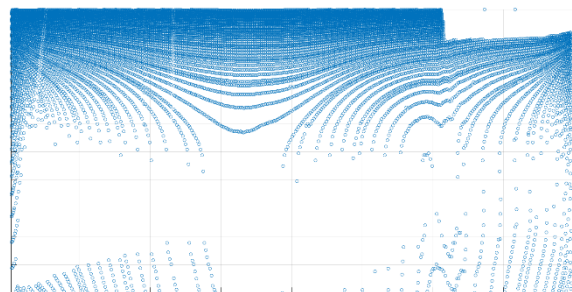


- k - Side-edge gauges - adjacent to the north and south façades

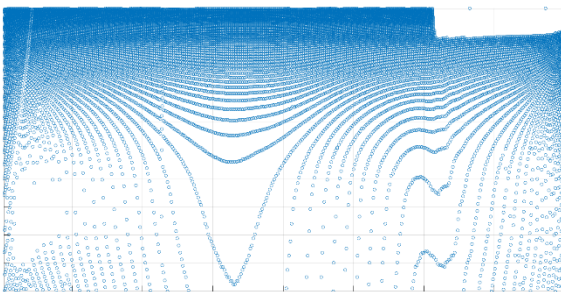
Figure 3.2.7 - WDR simulation validation of surrounded protected building with 2' overhang, at various locations, with the east façade exposed at normal wind onto the east façade, multiple rain events



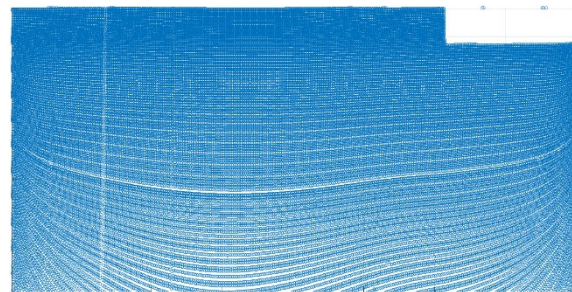
- a - $d = 0.3 \text{ mm}$



- b - $d = 0.8 \text{ mm}$



- c - $d = 0.9 \text{ mm}$



- d - $d = 3 \text{ mm}$

Figure 3.2.8 - Raindrop impingement on the east façade of the test building, equipped with 2' overhang, for different raindrop diameters, around surrounded building exposed to normal wind on the east façade, Event 2 in Table 3.2.4, with Standard $k-\omega$ and log-law inlet velocity profile

10% to ~20% error margin for top two rows of gauges (Figure 3.2.7a) alongside side-edge gauges (Figure 3.2.7b) are observed for such scheme of simulation, for the geometry involved.

Raindrop impingement on the east façade protected by 2' on-site overhang for different raindrop diameters, for Event 2 in Table 3.2.4, is depicted in Figure 3.2.8. Noticeable observation about the graphs is the fact that the façade with the presence of a partially covering overhang divides into two sections, protected and unprotected regions, shown in Figure 3.2.9. The unprotected region, designated by 1, has a line of symmetry, and the protected region is as if it is augmented to region 1. That line of symmetry, one way or another, is present on the façade, regardless of the size of the overhang.

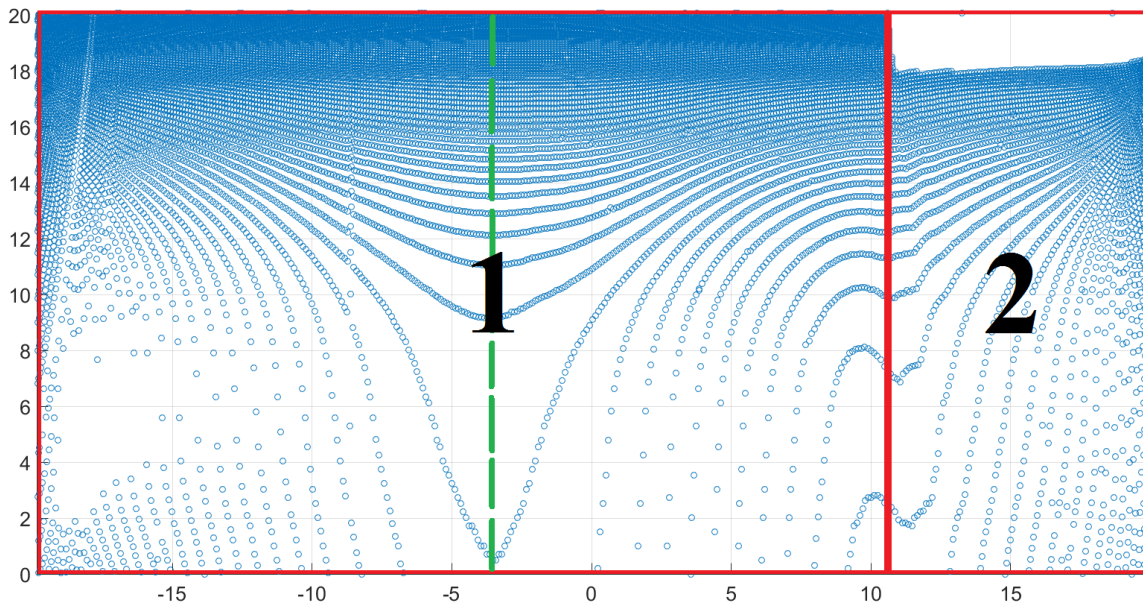


Figure 3.2.9 - Regions of protected façade with non-covering overhang, Figure 3.2.8c, region 2 is protected, 1 is unprotected

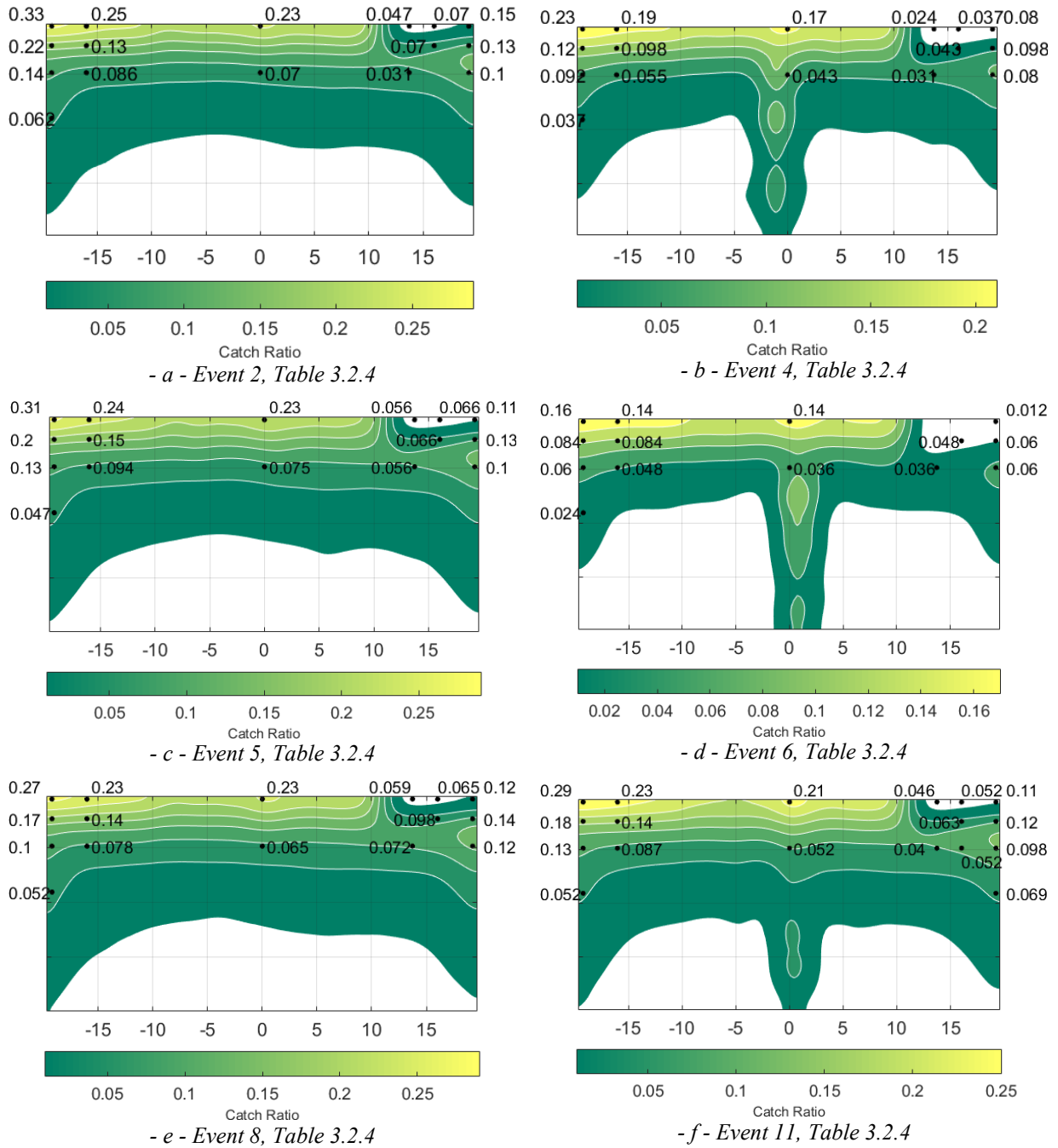


Figure 3.2.10 - Catch ratio comparison of CFD with field measurements for the east façade of the surrounded test building equipped with 2' overhang, exposed to normal wind, with Standard $k-\omega$ on log-law inlet velocity. Black dots are field measurement catch ratio. Bottom white areas show zero catch ratio.

Figure 3.2.10 shows contour of catch ratio as well as comparison between CFD results and field measurements at gauge points for six of the events in Table 3.2.4, solved with Standard $k-\omega$.

3.2.3.2 4' On-Site Overhang

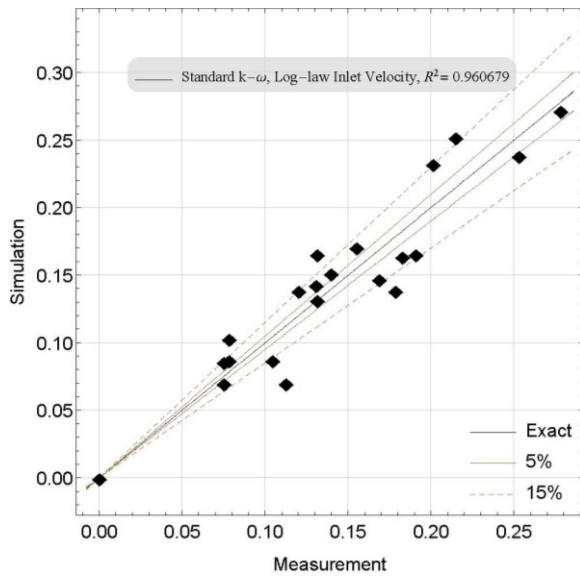
Much like 2' on-site overhang, rain events used for validation of simulations of CFD with 4' on-site overhang, are studied and presented, in Table 3.2.6, with computational domain size and discretization details in Table 3.2.7.

Table 3.2.6 - Wind and WDR parameters of the rain events created to validate simulations on surrounded protected building, exposed to normal wind on the east façade

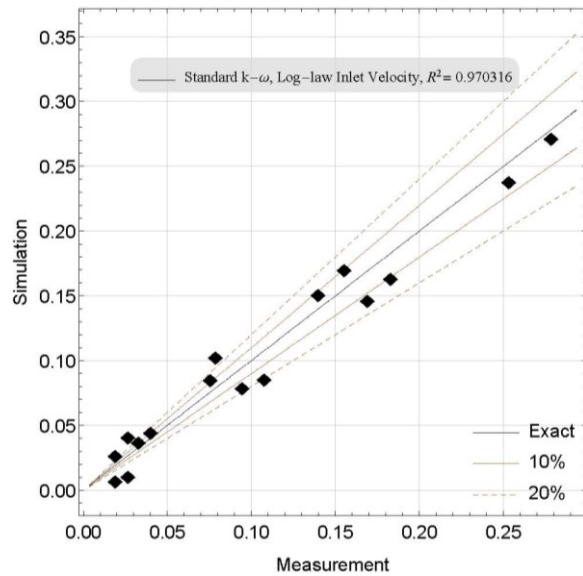
	U_{10} [m/s]	u_{ABL}^* [m/s]	y_0 [m]	y_p [m]	Roughness Constant	R_n [mm/hr]	Number of consecutive hours	Date
Event 1	2.12	0.21	0.152	0.25	3.37228	1.26	12	December 2014
Event 2	2.03	0.20	0.152	0.25	3.37224	0.84	22	December 2014
Event 3	1.14	0.11	0.152	0.25	3.37165	0.8	4	December 2014
Event 4	1.28	0.13	0.152	0.25	3.3718	0.76	6	December 2014

Table 3.2.7 - Computational domain size and discretization for surrounded building, exposed to normal wind on the east façade

Domain length (x)		1041.69 m
Domain height (y)		247.113 m
Domain width (z)		511.2224 m
Surface mesh	Size	Domain sides ~0.44 m - ~7m
		Building walls ~0.12 m - ~0.48 m
Volume mesh	Type	Quadrangle
	Number of CV's	3421960
	Type	Hexahedron
	Min Cell Volume	1.86E-03 m ³
	Max Cell Volume	3.55E+02 m ³



- i - Top two rows of gauges - adjacent to the roof



- j - Side-edge gauges - adjacent to the north and south façades

Figure 3.2.11 - WDR simulation validation of surrounded protected building with 4' overhang, at various locations, with the east façade exposed at normal wind onto the east façade, multiple rain events

Figure 3.2.11 in previous page shows model validation for surrounded building protected with 2' on-site overhang.

5% to ~15% error for top two rows of gauges (Figure 3.2.11a) alongside side-edge gauges (Figure 3.2.7a) are observed for such scheme of simulation, for the geometry involved.

Raindrop impingement on the east façade protected by 4' on-site overhang for different raindrop diameters, for Event 2 in Table 3.2.4, is depicted in Figure 3.2.12.

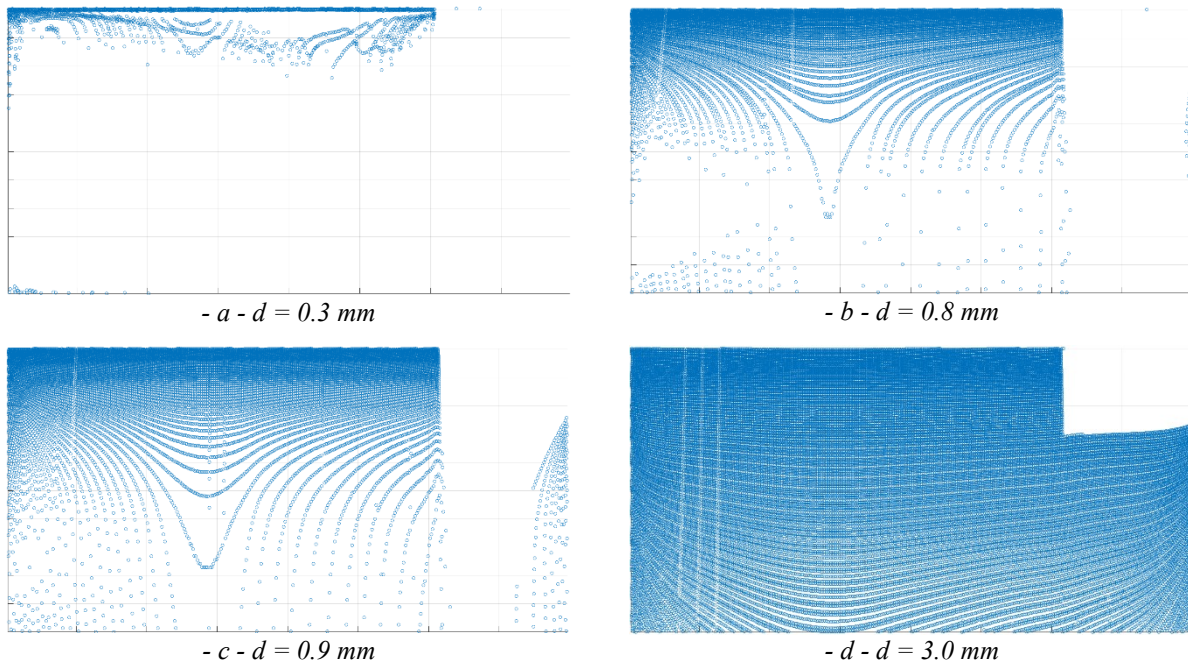


Figure 3.2.12 - Raindrop impingement on the east façade of the test building, equipped with 4' overhang, for different raindrop diameters, around surrounded building exposed to normal wind on the east façade, Event 1 in Table 3.2.6, with Standard $k-\omega$ and log-law inlet velocity profile

Figure 3.2.13 shows contour of catch ratio as well as comparison between CFD results and field measurements at gauge points for six of the events in Table 3.2.6, solved with Standard $k-\omega$ and log-law inlet velocity profile.

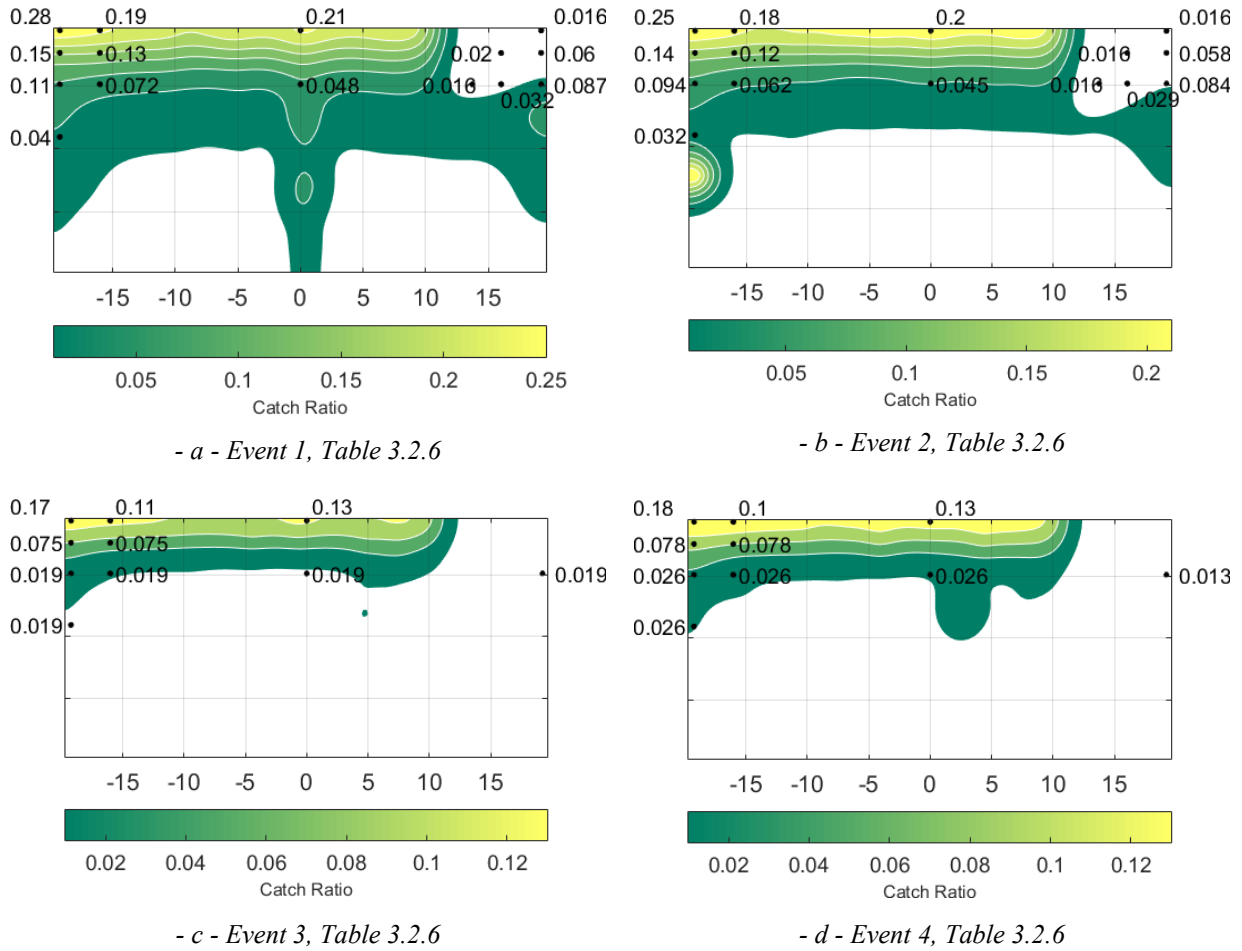


Figure 3.2.13 - Catch ratio comparison of CFD with field measurements for the east façade of the surrounded test building equipped with 4' overhang, exposed to normal wind, with Standard $k-\omega$ and log-law inlet velocity profile. Black dots are field measurement catch ratio. Bottom white areas show zero catch ratio.

3.2.4 Rain Parametric Study with Oblique Wind Direction on Unprotected Façade

The set of oblique wind directions studied is depicted in Figure 3.2.14.

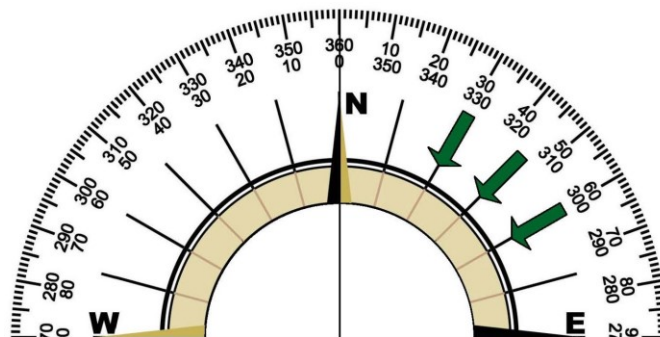


Figure 3.2.14 - Set of oblique wind directions studied

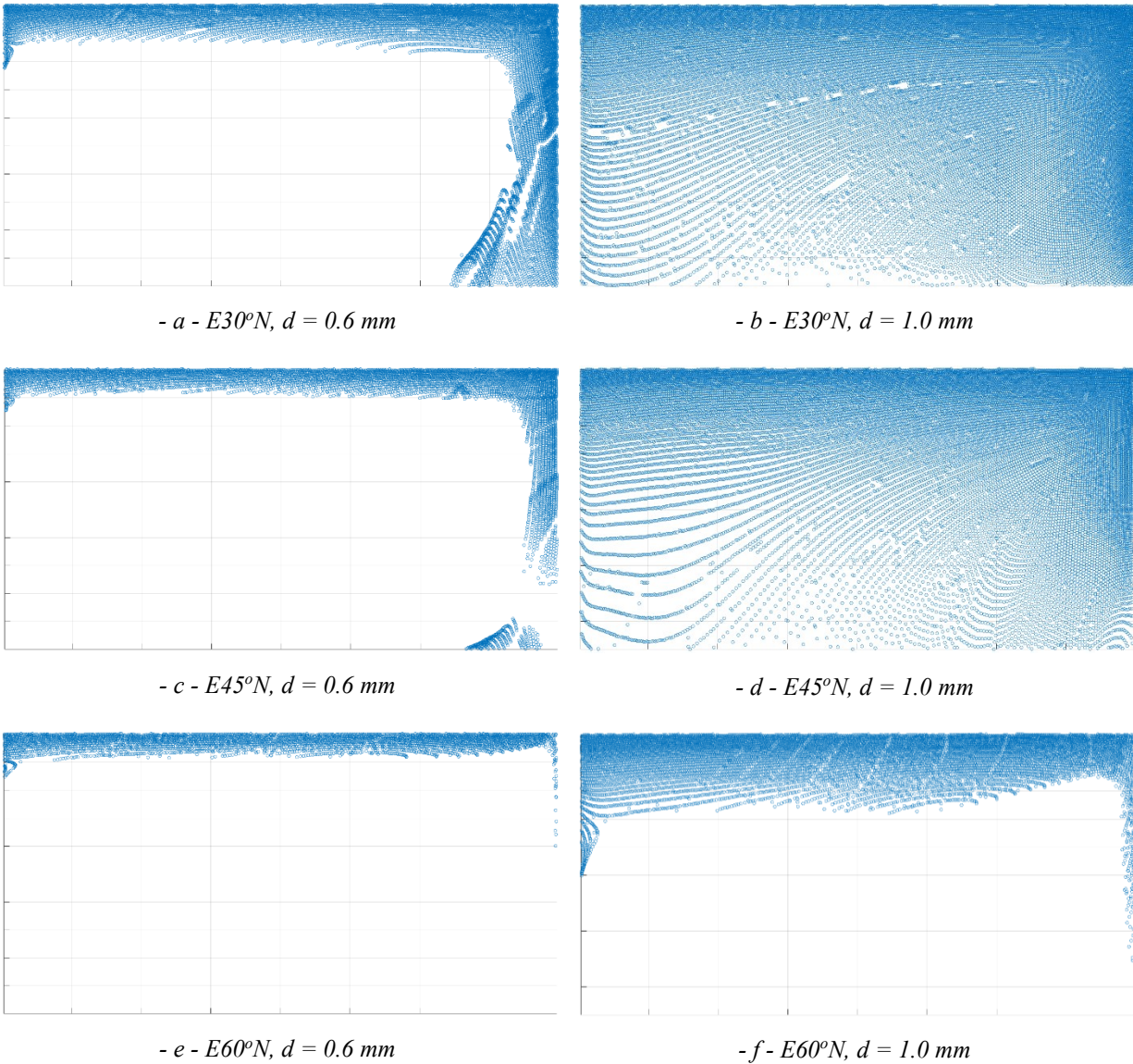


Figure 3.2.15 - Raindrop impingement for 0.6 mm and 1.0 mm raindrop sizes, Standard $k-\omega$, log-law velocity profile, $U_{10} = 6.7 \text{ m/s}$, and $R_h = 4 \text{ mm/hr}$, oblique wind direction, unprotected façade

Raindrop impingement contours for comparison between oblique wind directions for unprotected façade are presented in Figure 3.2.15.

As the wind direction turns more towards the north façade, rain impingement on the east façade obviously reduces. This is reflected on the catch ratio contour of the east façade as well, depicted in Figure 3.2.16. Downstream portion of the façade, alongside the general value of catch ratio on the façade reduce with an increase in East-North wind angle. This is to the extent that the bottom

half of the downstream side of the façade exposed to oblique wind remains dry, according to the predictions.

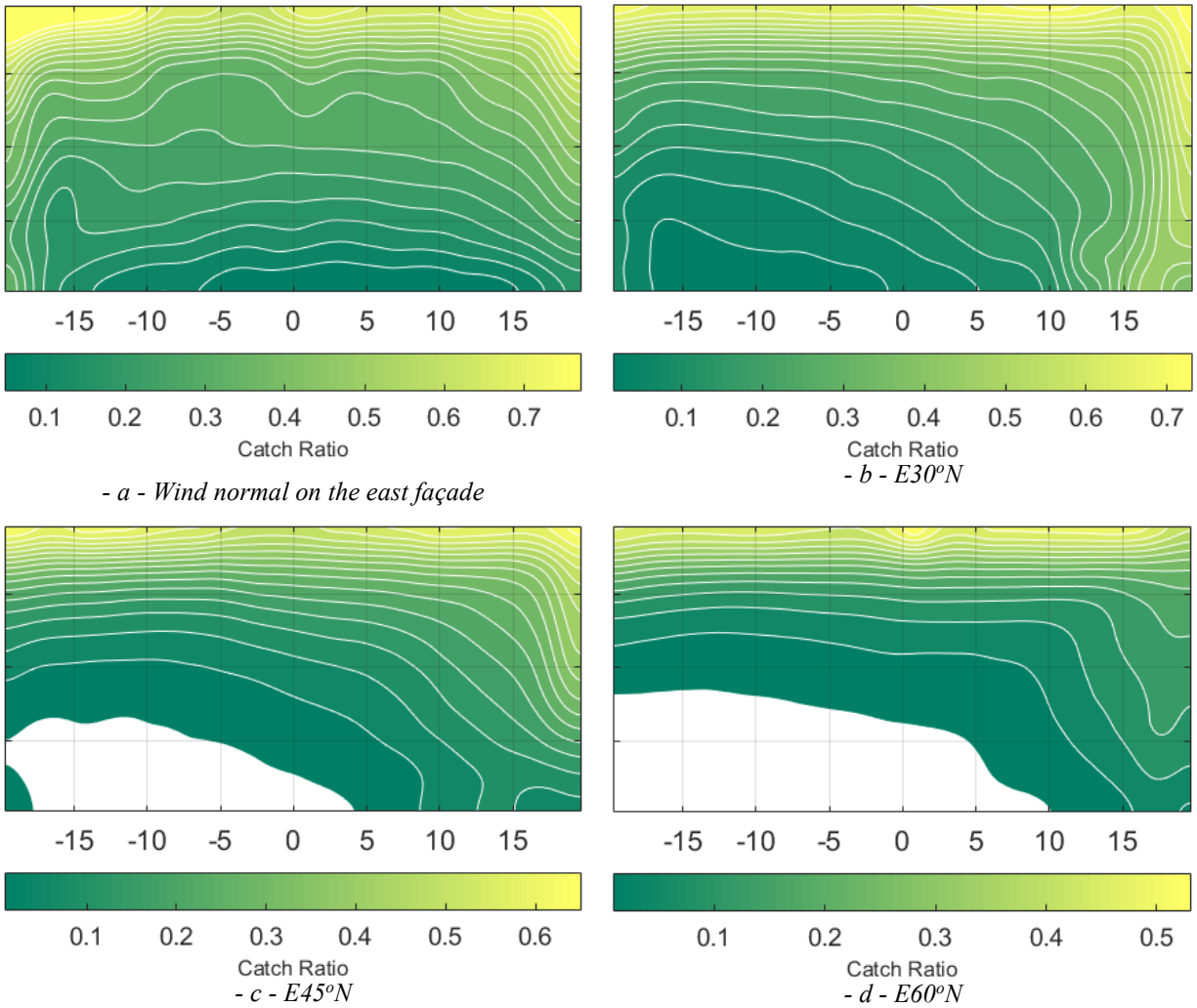


Figure 3.2.16 - Catch ratio comparison of normal and oblique wind on the unprotected east façade of the surrounded test building, with Standard $k-\omega$ on log-law inlet velocity, $U_{10} = 6.7$ m/s and $R_h = 4$ mm/hr. White areas show zero catch ratio.

3.2.5 Rain Parametric Study with Oblique Wind Direction on Protected Façade

For the same wind direction set presented in Figure 3.2.14, raindrop impingement contours for comparison between oblique wind directions for protected façade with façade-covering 3' overhang, for raindrop diameters of 1.0 and 0.6 mm, are presented in Figure 3.2.17.

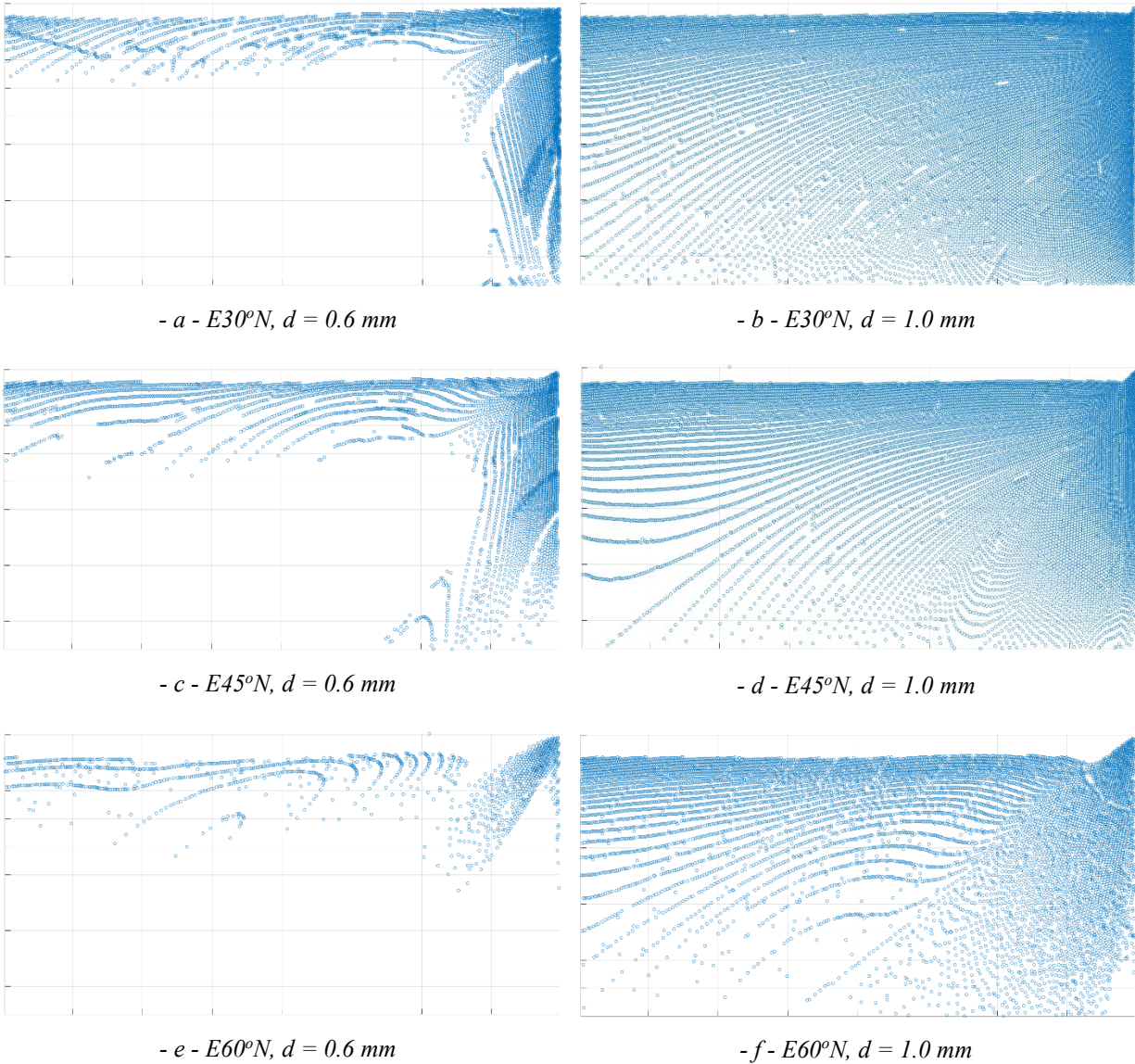


Figure 3.2.17 - Raindrop impingement for 0.6 mm and 1.0 mm raindrop sizes, Standard $k-\omega$, log-law velocity profile, $U_{10} = 6.7 \text{ m/s}$ and $R_h = 4 \text{ mm/hr}$, oblique wind direction, protected façade

First thing to notice is that the dry strip on the top region of the façade which is due to direct presence of the overhang. Much like unprotected façade, as the angle of the wind increases towards the north direction, general rain impingement reduces and, the presence of the façade results in the growth of the dry strip on the top region of the façade. This directly impacts the catch ratio, depicted in Figure 3.2.18.

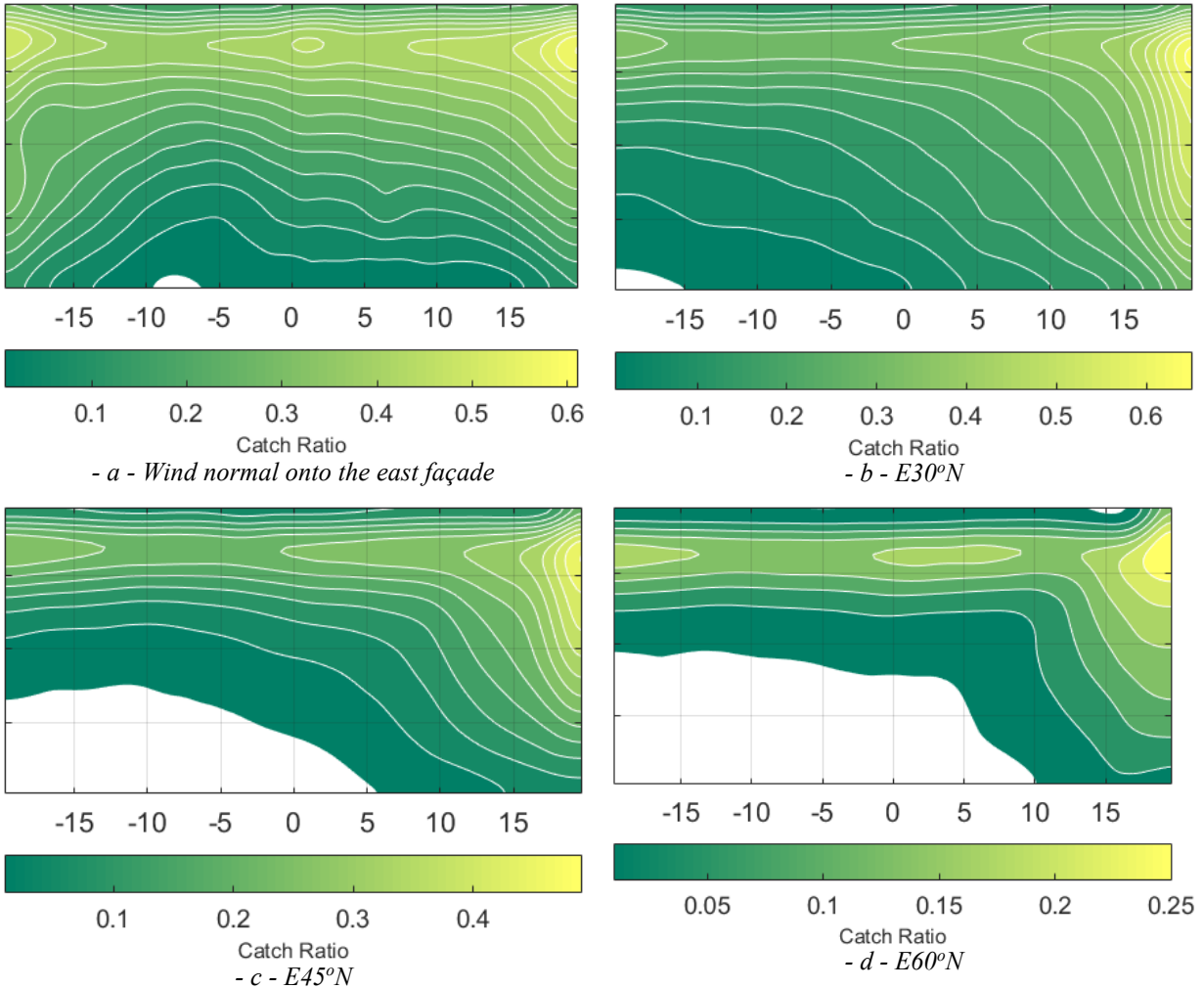


Figure 3.2.18 - Catch ratio comparison of normal and oblique wind on the protected east façade with 3' overhang, of the surrounded test building, with Standard $k-\omega$ on log-law inlet velocity, $U_{10} = 6.7 \text{ m/s}$ and $R_h = 4 \text{ mm/hr}$. White areas show zero catch ratio.

3.2.6 Rain Simulation Summary

As discussed in Section 3.1.5, Standard $k-\omega$ is introduced as the best fit for this study amongst the models used. For stand-alone building WDR simulations, Figure 3.2.2 shows that Standard $k-\omega$ features the lowest deviation from the field measurement. Although the change from model to model on the WDR simulation results for the surrounded building is negligible, again, as a global measure, we take Standard $k-\omega$ as the best fit for such simulations.

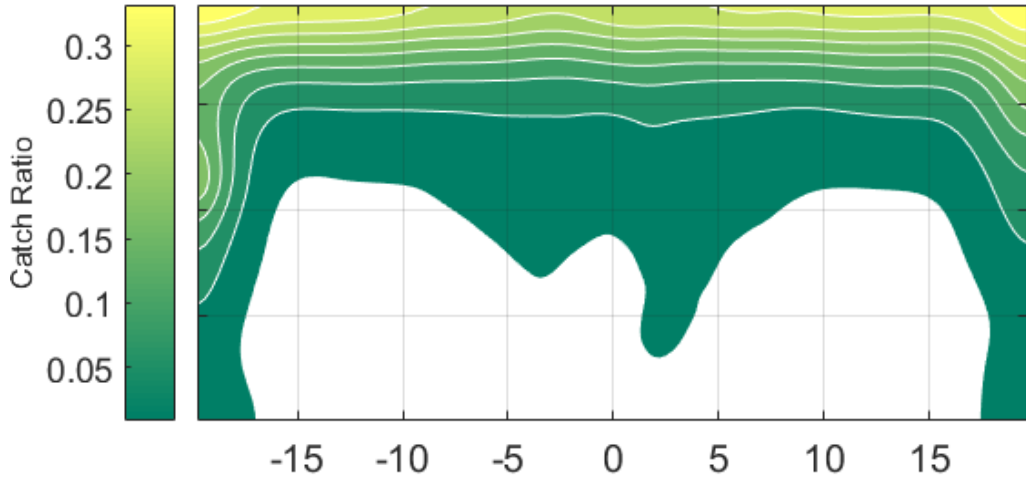
Chapter 4 OVERHANG EFFECTIVENESS PARAMETRIC STUDY

This chapter deals with studying the overhang effectiveness for various overhang shapes and sizes, under different rain and wind conditions, for different portions of the façade or various measurement tools installed on the façade, alongside multiple wind directions.

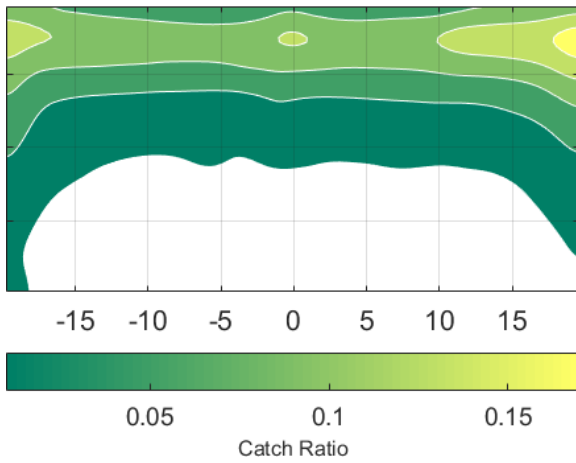
For these simulations, the test building, protected with 1', 2', 3' and 4' with its surroundings is exposed to normal wind onto the east façade. Multiple rain and wind conditions are also taken into consideration to study the effectiveness in 4 different regions of the façade, alongside on each catch ratio measurement gauge location.

4.1 Façade Covering Overhang

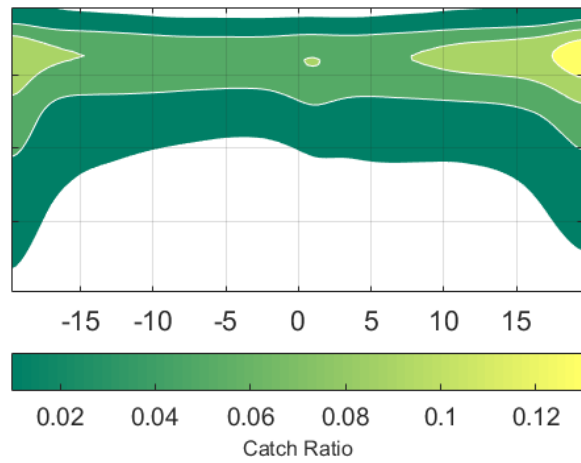
Figure 4.1.1 shows the smoothed data with gauge catch ratio values for unprotected façade, on all graphs, for the sake of comparison, for a single rain event. Not only is there a zero-deposition area at the top of the façade, which is directly due to the protection of the overhang, but the presence of it significantly affects the contour of the catch ratio across the façade, by changing the velocity near that region. This is also depicted in the contour of x -velocity near the façade, which is given in Figure 4.1.2. Not only the top strip of the façade that is directly protected by the overhang, depending on the size of it, but the presence of it considerably changes the contour of x -velocity near the façade.



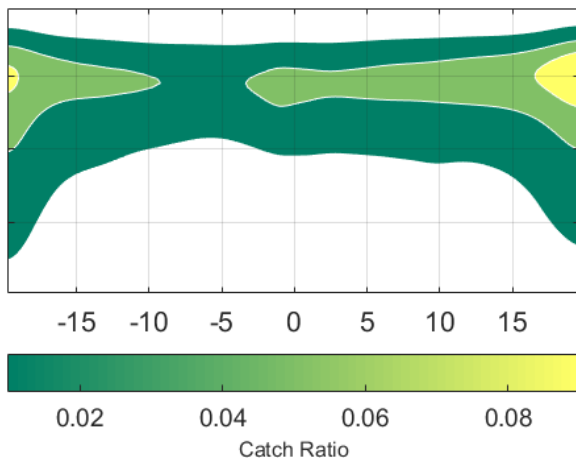
- a - No overhang



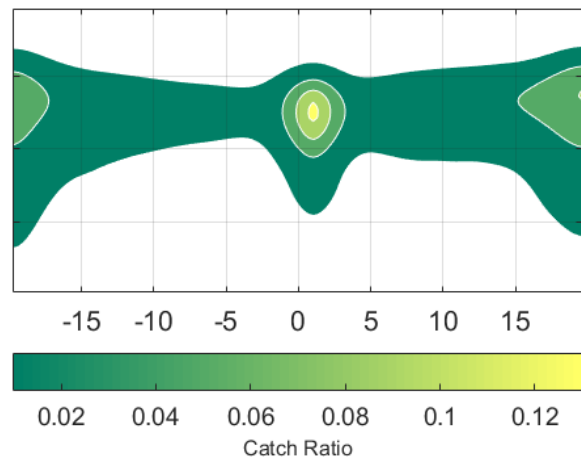
- b - Protected with 1' overhang



- c - Protected with 2' overhang

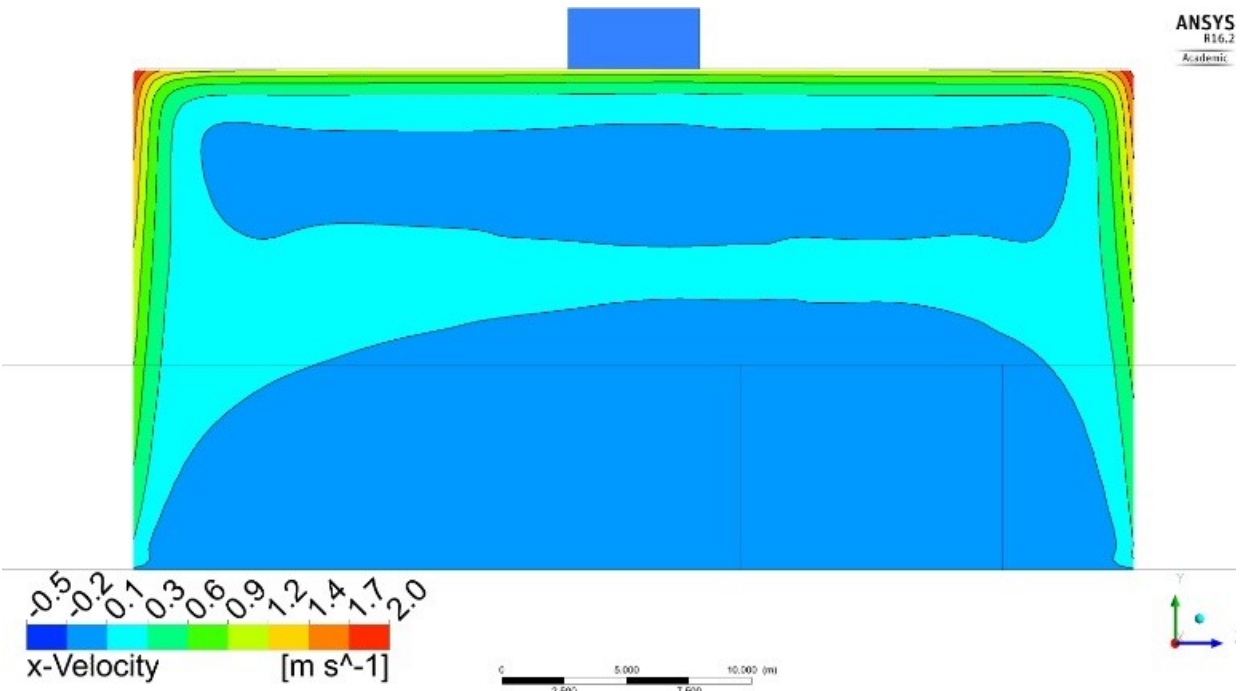


- d - Protected with 3' overhang

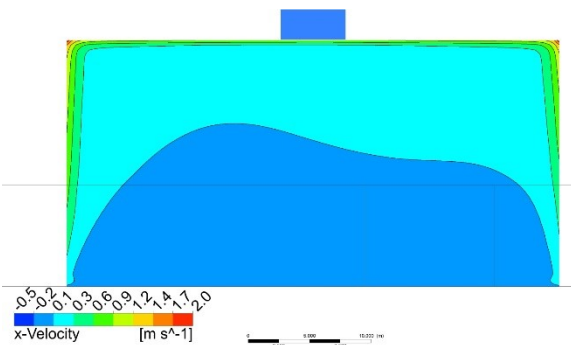


- e - Protected with 4' overhang

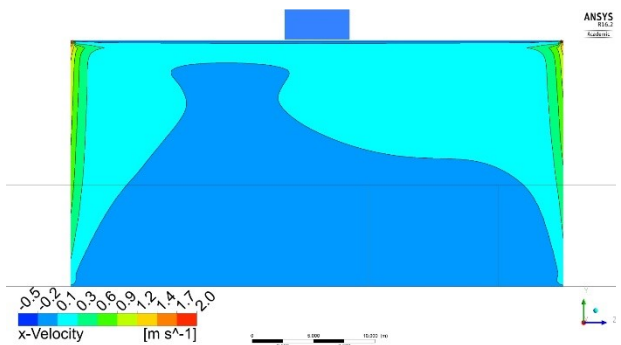
Figure 4.1.1 - Catch ratio contour of smoothed data on the east façade with surrounded building unprotected and protected with façade covering overhang, $U_{10} = 3.0$ m/s, $R_h = 4.16$ mm/hr. White areas show zero catch ratio.



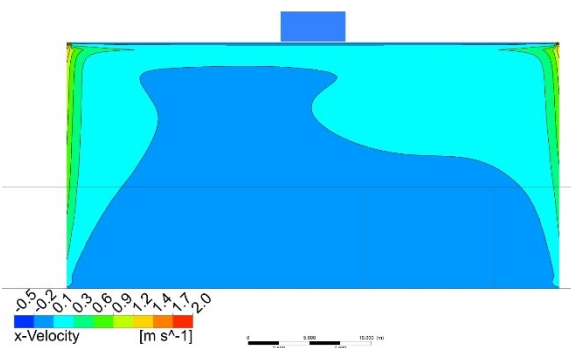
- a - No overhang



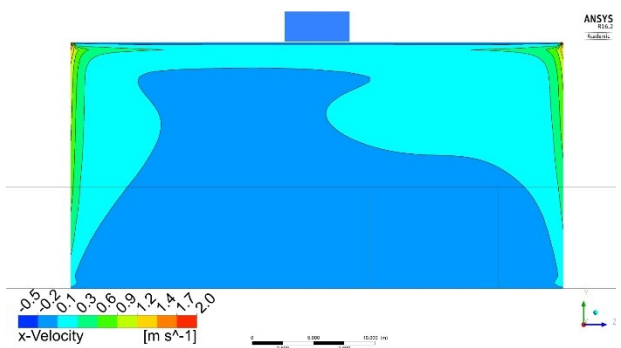
- b - with 1' overhang



- c - with 2' overhang



- d - with 3' overhang



- e - with 4' overhang

Figure 4.1.2 - Contour of x-velocity on a plane 0.5 m upstream of the east façade, with surrounded building unprotected and protected with façade covering overhang, $U_{10} = 6.7$ m/s, $R_h = 4.0$ mm/hr

This is in a fashion that as the size increases, the x -velocity value at the middle of the façade decreases (shown in Figure 4.1.2 by noticing the fact that the darkest blue region grows more into the façade as the overhang size increases). The asymmetry observed on contours on Figure 4.1.2 is attributed to the effect of the surrounding buildings on the predicted wind around the test building.¹

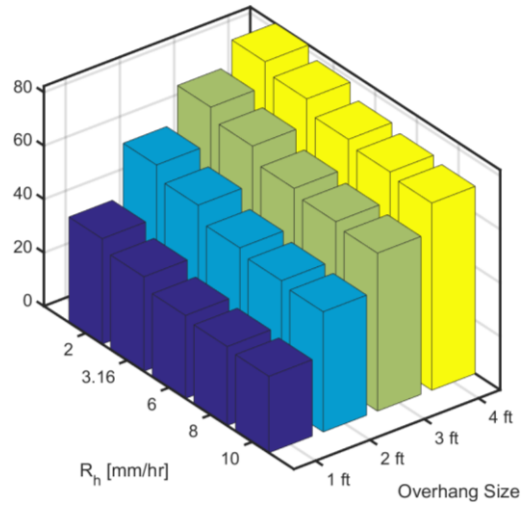
4.1.1 Effectiveness Index

The effectiveness of the façade covering overhang is studied in extent. Figure 4.1.3 is the study of the effectiveness over rainfall intensity and overhang size. For any portion of the façade, as the size of the overhang increases, the effectiveness increases. With a hike in rainfall intensity, the overhang effectiveness decreases. Though the effect of rainfall intensity on the effectiveness of the overhang is less than the effect of size of the overhang. Moreover, Figure 4.1.3d shows that the effect of rainfall intensity on the top 15% portion of the façade, A4 (Figure 2.3.15), is less tangible, although it follows the same pattern.

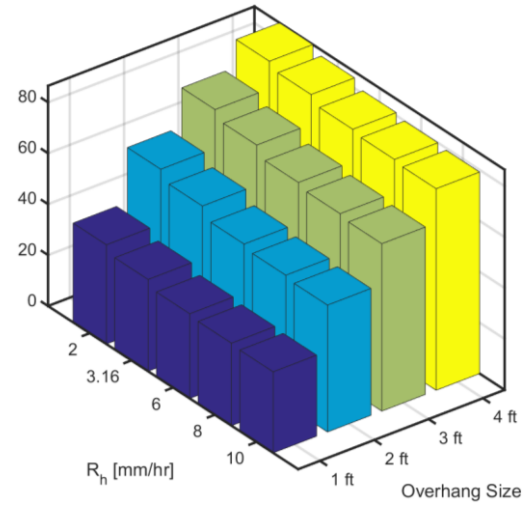
Figure 4.1.4 shows the sensitivity of effectiveness index to rainfall intensity more clearly.

Moreover, this figure shows how considering less portion of the façade will result in a less effectiveness of the overhang. As one marches from A1 to A4, the effectiveness increases. This pattern is ubiquitous regardless of rainfall intensity and size of overhang.

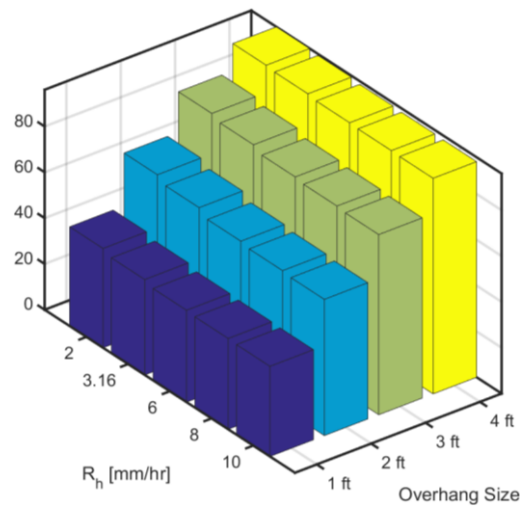
¹ Find the contour of velocity magnitude in Appendix D - Velocity Contours



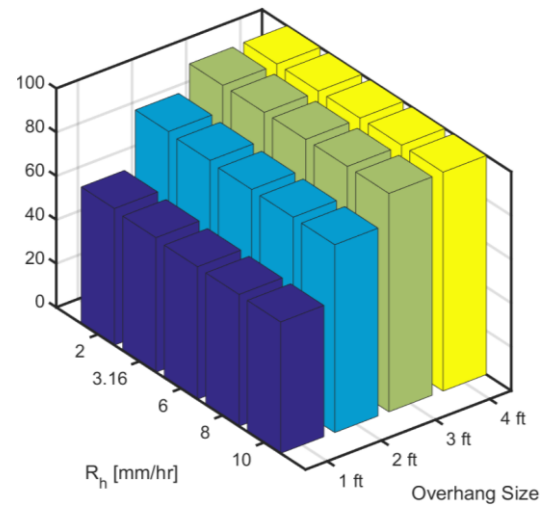
- a - A1 (100%)



- b - A2 (top 45%)

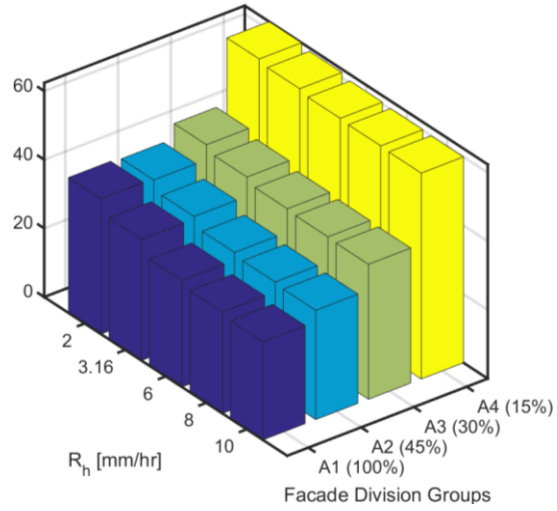


- c - A3 (top 30%)

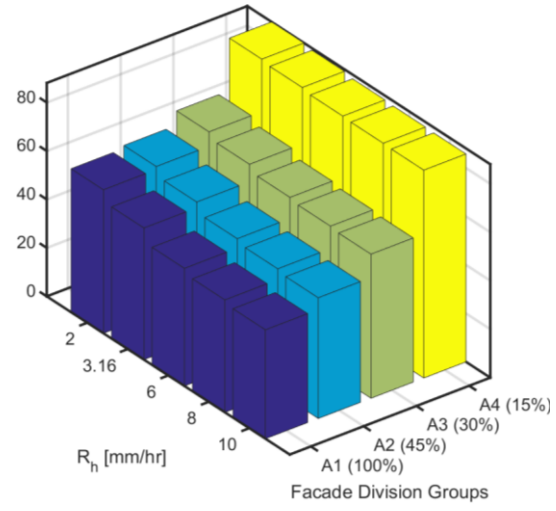


- d - A4 (top 15%)

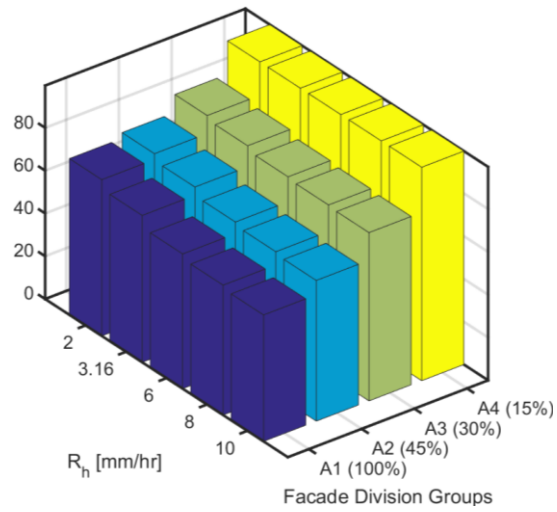
Figure 4.1.3 - Effectiveness index of the overhang over different overhang sizes under different rainfall intensities



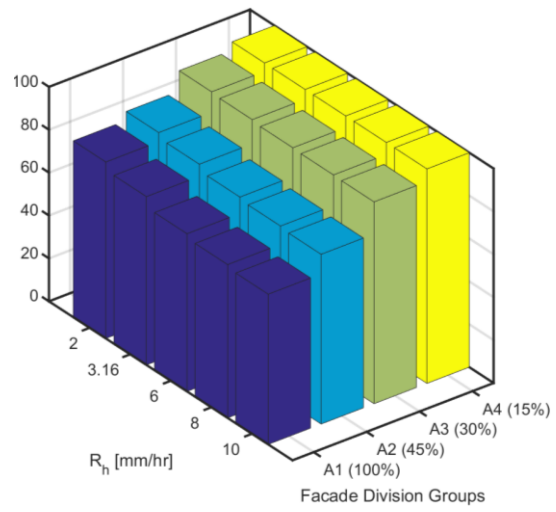
- a - 1' overhang



- b - 2' overhang



- c - 3' overhang



- d - 4' overhang

Figure 4.1.4 - Effectiveness index of the overhang over different rainfall intensities under different façade division groups

4.2 On-Site Overhang

For this simulation, the test building is taken with its upstream surrounding buildings, and wind is taken to be approaching at normal angle onto the east façade, Figure 4.2.1. Four overhang sizes are used 2' and 4'. Also, another parameter that have been a source of change is taken to be rainfall intensity. R_h is taken to be 2, 3.16, 6, 8 and 10 mm/hr. The overhang is taken to be across its length, at uniform size.

The catch ratio contours of the east façade exposed to normal wind are presented here. The raw data followed by the smoothed contours, Figure 4.2.2.

Same observations for the protected portion of the façade are to be made on Figure 4.2.2. Not only is there a protected strip on the top portion of the façade, but the entire façade topped by the on-site overhang is affected. Catch ratio measurements shown are the field measurements for the uncovered façade. This comparison shows that the overhang presence is considerably effective even for the middle portion of the façade.

Figure 4.2.3 shows that the unprotected portion of the façade is barely affected by the installed 20-ft-long overhang. More on that, the protected side is changed, drastically by both 2' and 4' overhangs. This effect though is less accentuated towards the bottom half of the façade.



Figure 4.2.1 - The east façade at normal wind, surrounded by upwind buildings equipped with 4' on-site overhang

Effectiveness index variations can be studied for two different sides of the façade as the overhang does not cover it entirely. Effectiveness index study of partial overhang on the whole façade is presented in Figure 4.2.4. Indices increase as the overhang size increases and decrease as the rainfall intensity increases. This suggests that longer overhang is indeed effective in protecting the façade for any portion of it. Moreover, as the rain gets more intense, overhang of any size becomes less effective in protecting the façade. Effectiveness index for the protected portion only is depicted in Figure 4.2.5 and Figure 4.2.6. These figures also attest the observations made for façade-covering overhang. With an increase in the size of the overhang, the effectiveness of it increases. Higher rainfall intensity interprets in less value of effectiveness of overhang of any size. As the upper portions of the façade are concerned, going from A1 to A4, the effectiveness of the overhang increases, meaning, the upper parts of the façade are protected more effectively.

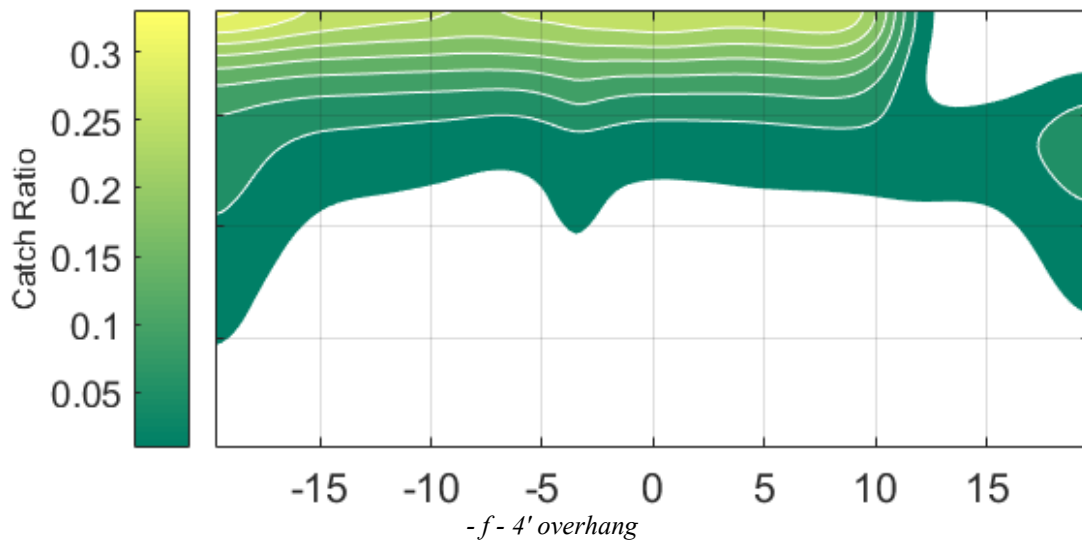
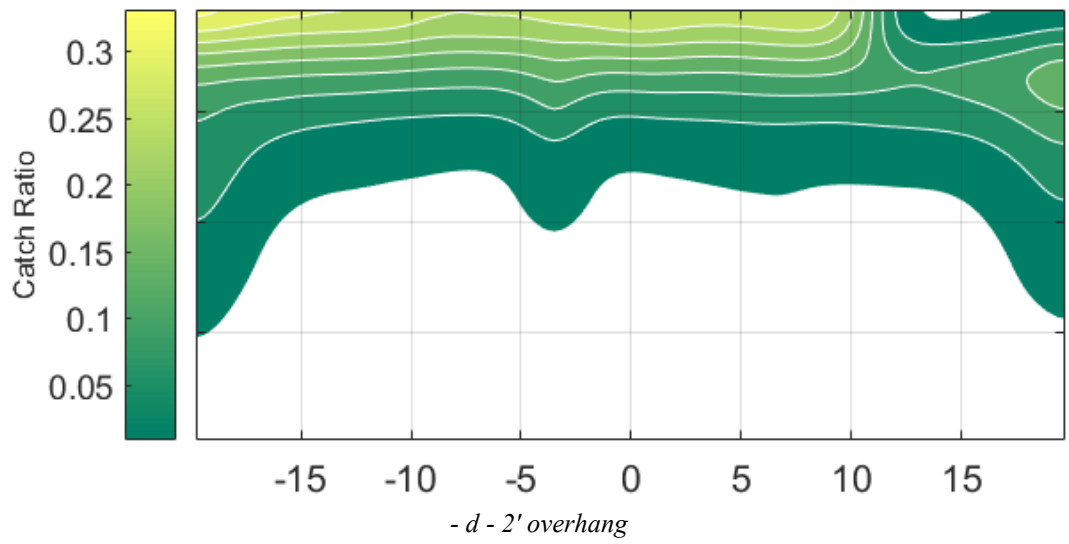
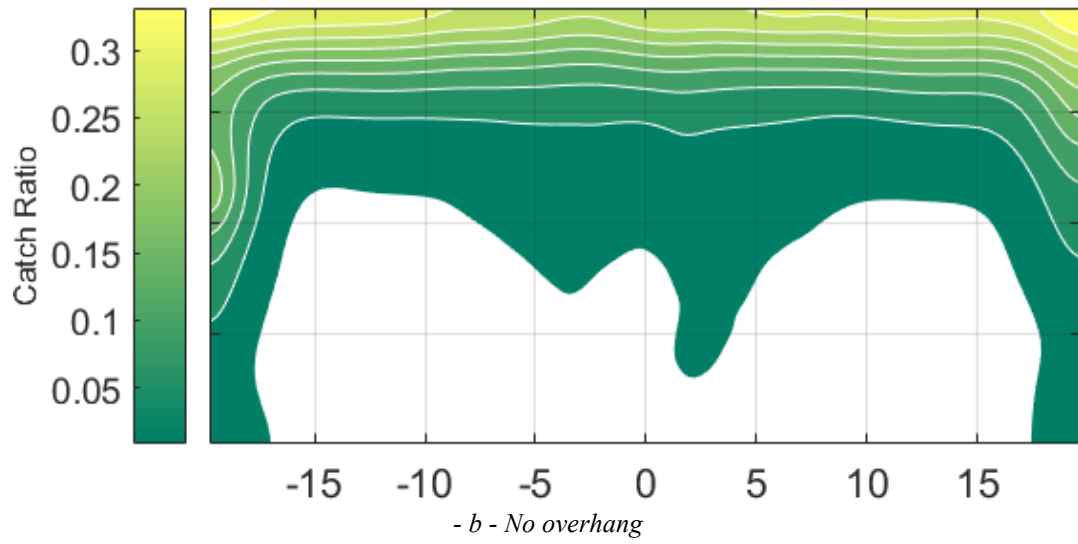
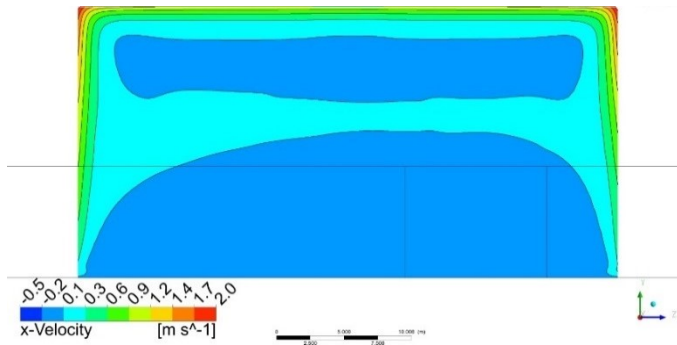
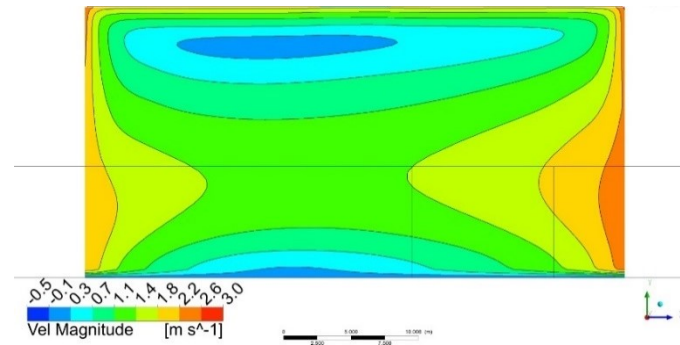


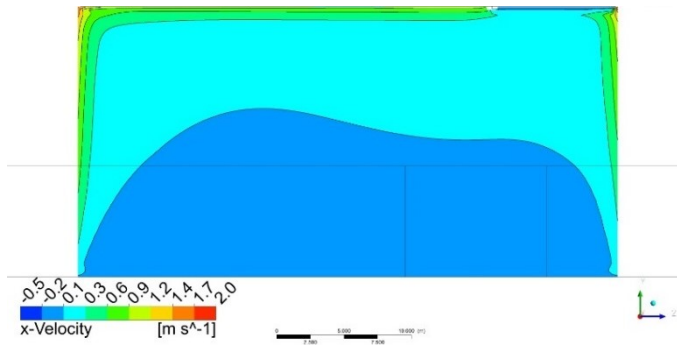
Figure 4.2.2 - Catch ratio contour of raw data on the east façade, with surrounding buildings, on-site overhang. White areas show zero catch ratio.



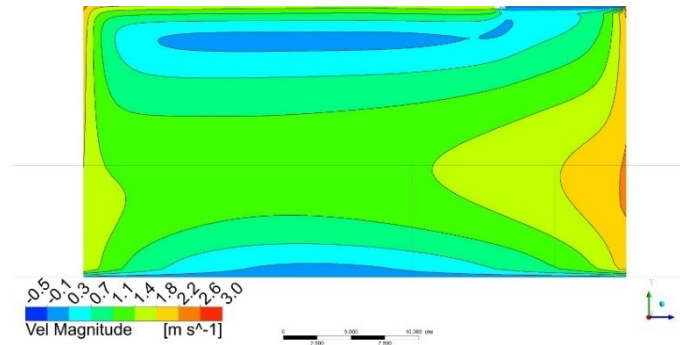
- a - No overhang, x-velocity



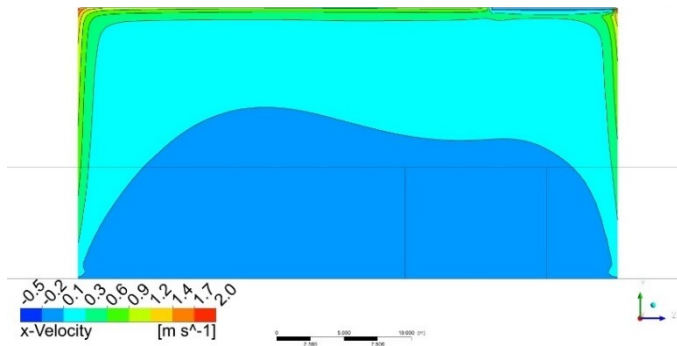
- b - No overhang, velocity magnitude



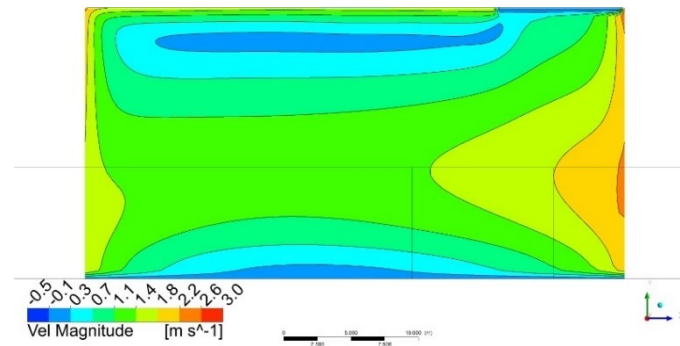
- c - 2' overhang, x-velocity



- d - 2' overhang, velocity magnitude

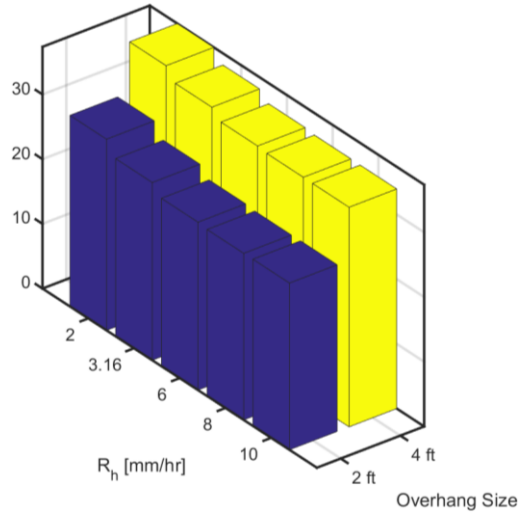


- e - 4' overhang, x-velocity

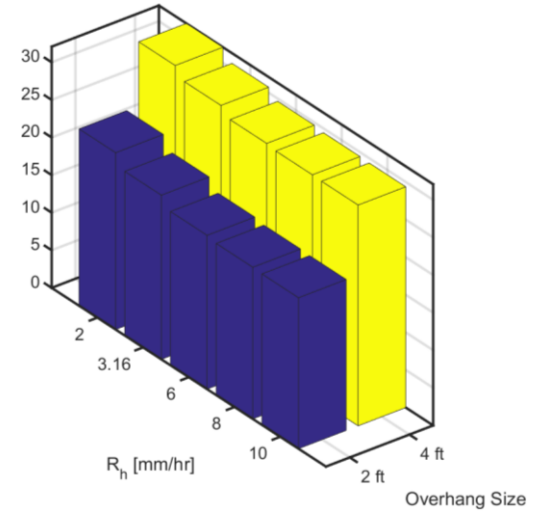


- f - 4' overhang, velocity magnitude

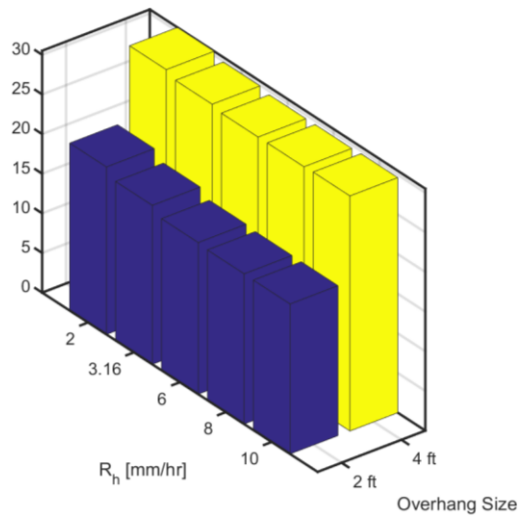
Figure 4.2.3 - Contour comparison 0.5 m upstream of the east façade, with surrounding buildings, on-site overhang



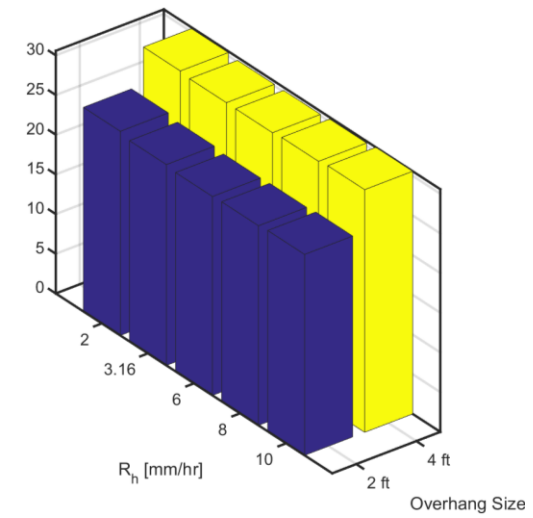
- a - A1 (100%)



- b - A2 (top 45%)

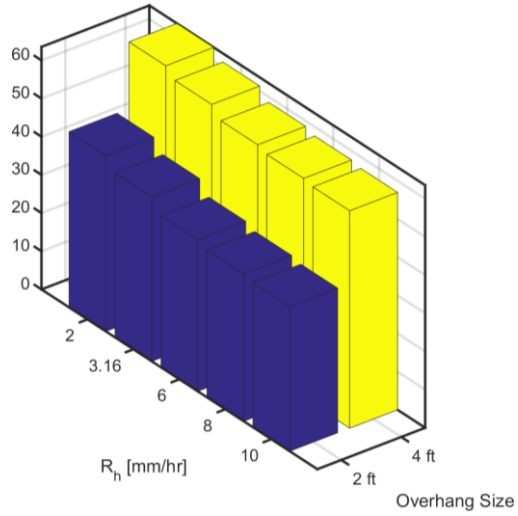


- c - A3 (top 30%)

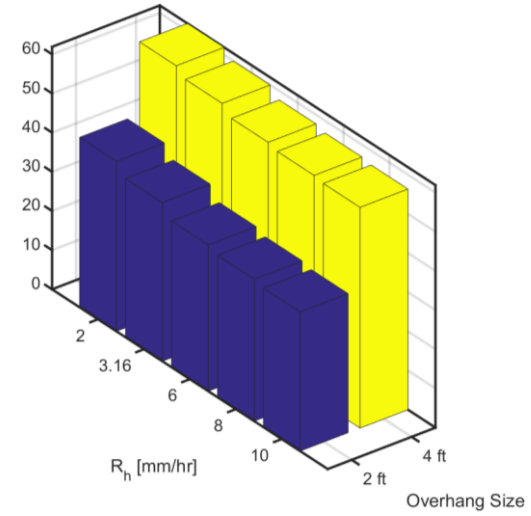


- d - A4 (top 15%)

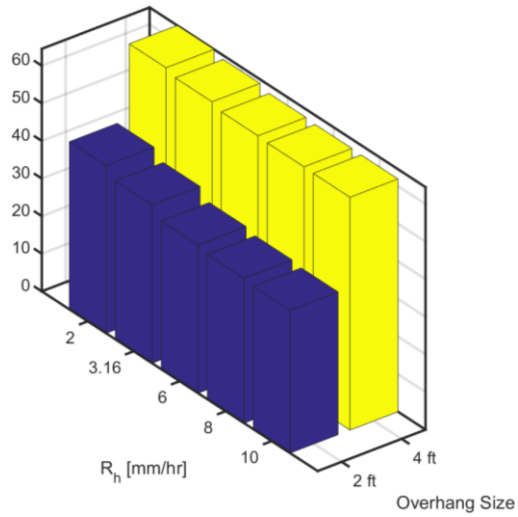
Figure 4.2.4 - Effectiveness index of the overhang over different overhang sizes under different rainfall intensities, full façade calculation



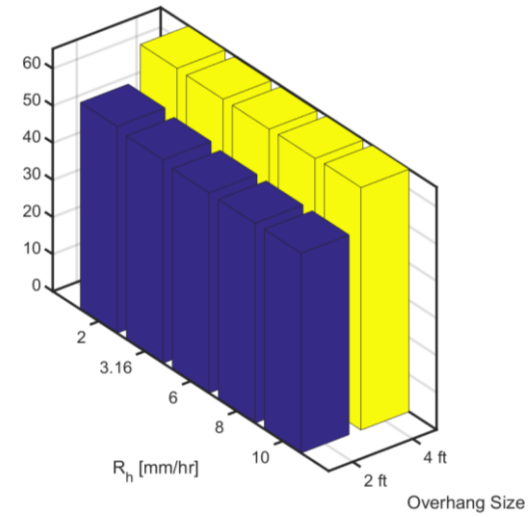
- a - A1 (100%)



- b - A2 (top 45%)



- c - A3 (top 30%)



- d - A4 (top 15%)

Figure 4.2.5 - Effectiveness of the overhang over different overhang sizes under different rainfall intensities, protected portion calculation

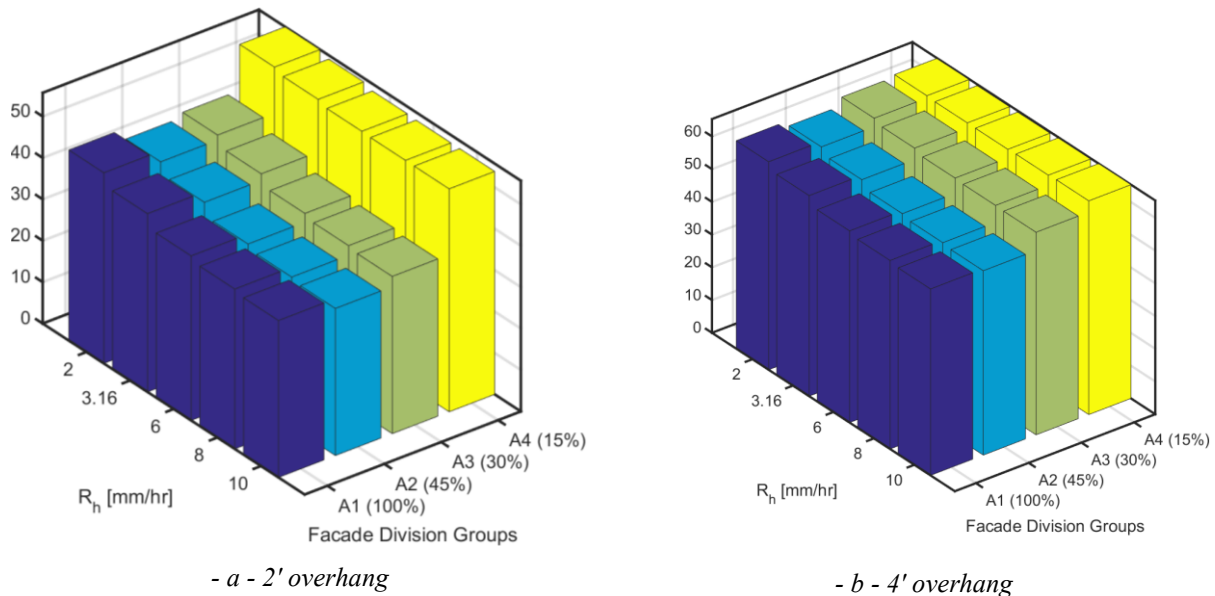


Figure 4.2.6 - Effectiveness of the overhang over different rainfall intensities under different façade division groups, protected portion calculation

4.3 Wind Speed Effect on Overhang Effectiveness

To study the wind speed effect on the effectiveness of an overhang, façade covering overhang with a width of 3' is chosen and simulated. The set of U_{10} values is chosen to be

$$\{1, 2, 3, 4, 5, 6, 6.7, 7, 8, 9, 10\} \text{ m/s}$$

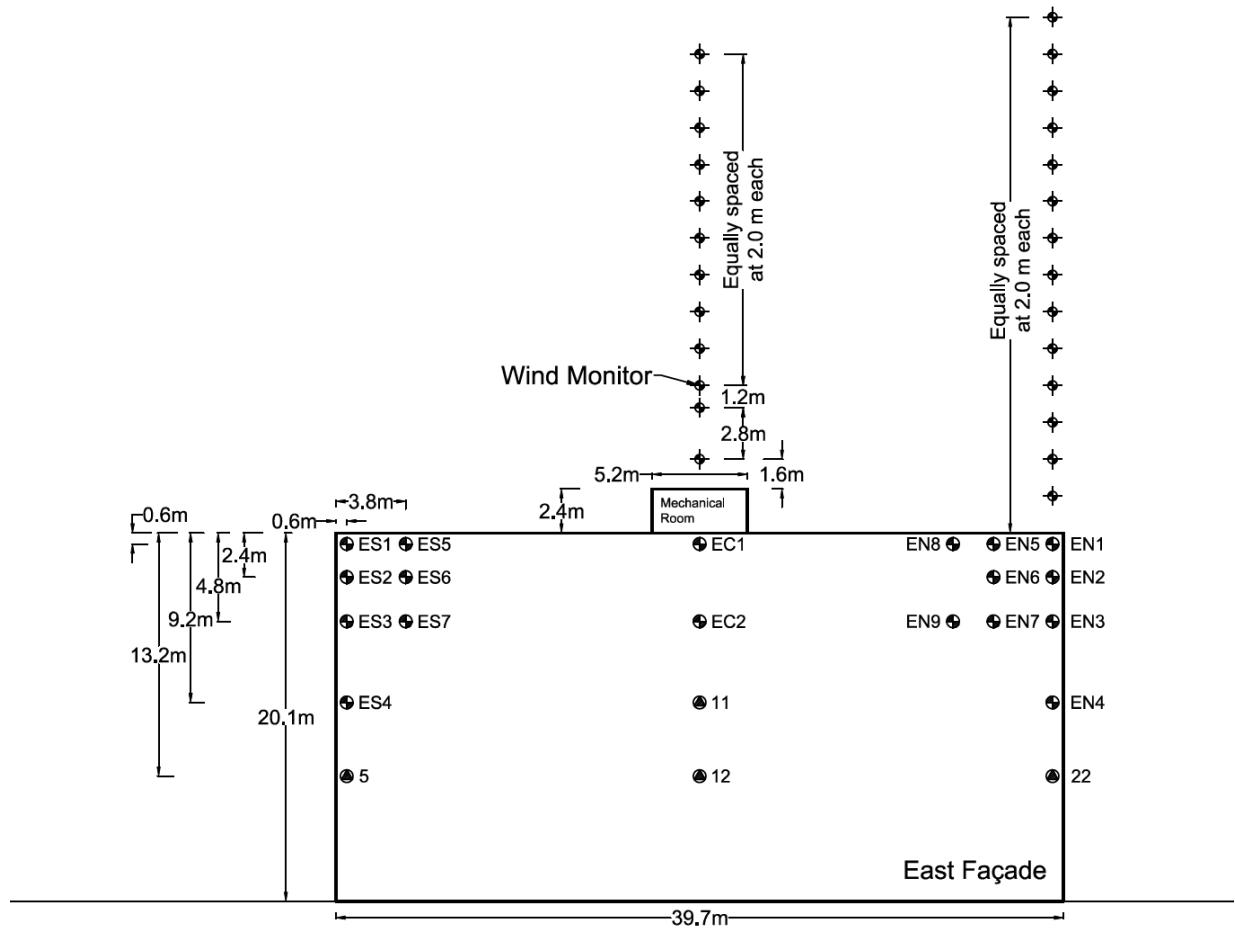
and rainfall intensity, R_h , range of values is chosen to be

$$\{0, 1, 2, 3, 4, 5, 6, 8, 10, 12, 15, 20, 25, 30, 35, 40, 50\} \text{ mm/hr}$$

Prior to presenting the graphs of effectiveness parameter study in this section, simple wind velocity trend investigation is done to measure the linearity of x -velocity at various points near the windward façade, the east façade, versus the change in U_{10} value. The results are presented in Figure 4.3.1. Since the east façade measurement points are named quite a bit of times in this section, Figure 2.3.13b from Section 2.3.2.1 is presented here again.

Although Point 12 on Figure 2.3.13b is in the middle of the façade, R-squared value for the x -velocity values at EC-base distance from the façade, shows a linear prediction versus U_{10} value,

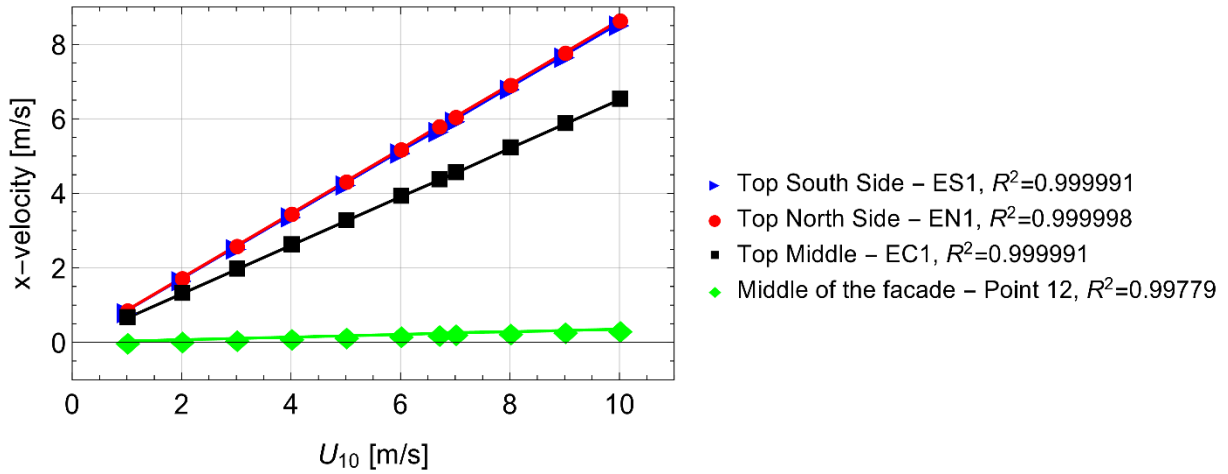
Figure 4.3.1. In other cases, R-squared value is found to be within 10^{-6} order of difference from unity, which is perfect linearity.



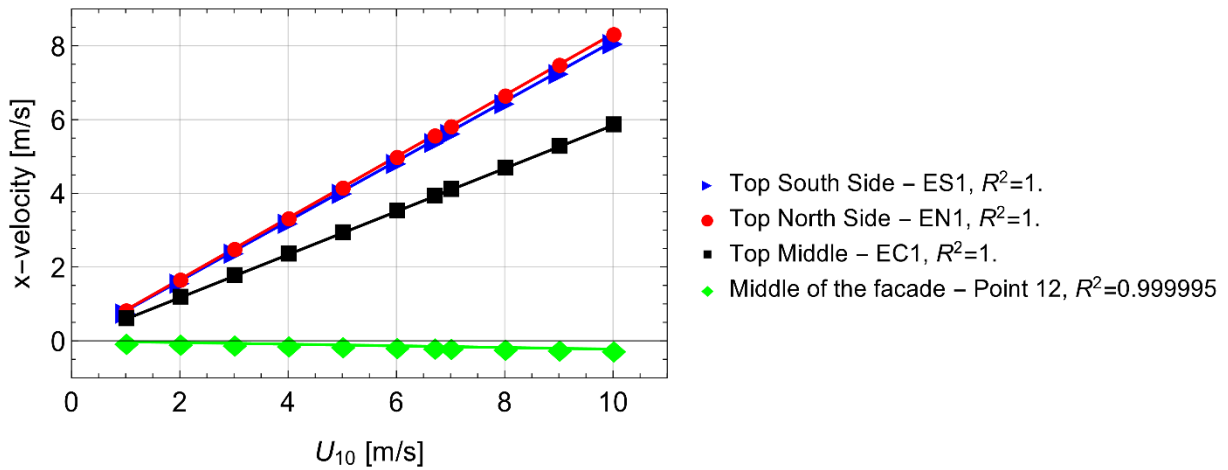
- b - Measurement locations in front of the east façade and above the mechanical room

Figure 2.3.13 - Location of wind velocity measurements around the test building

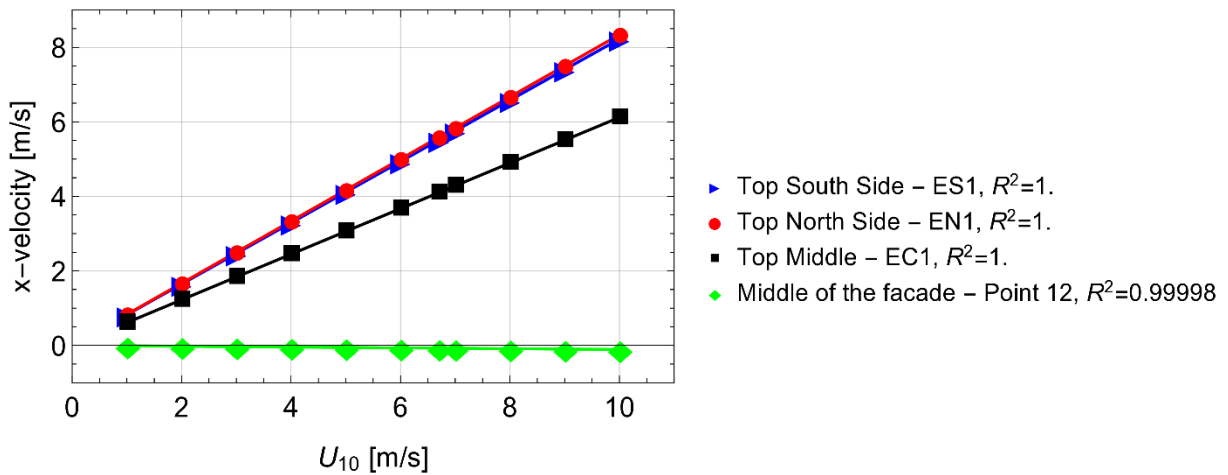
Parametric study of catch ratio variation in Figure 4.3.2 shows that no matter where on the façade, or what the wind speed or rainfall intensity, catch ratio increases with an increase in wind speed, also increases with an increase in rainfall intensity. Noticeable fact about 3' façade-covering overhang on the test building is that it is capable of keeping the top strip of the façade dry up to U_{10} value of 4 m/s. Same observation is made for on-site overhang, which is deployed on the north side of the east façade, at a 20' length. For that case, shown in Figure 4.3.2f, the overhang is capable of keeping the top strip of the façade dry, under the protected region, region 2 of Figure 3.2.9; while the top strip of the unprotected region is rather wet at any condition, Figure 4.3.2e.



- a - Unprotected façade

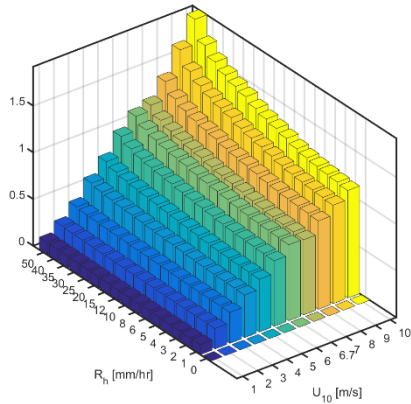


- b - Protected façade with 3' façade-covering overhang

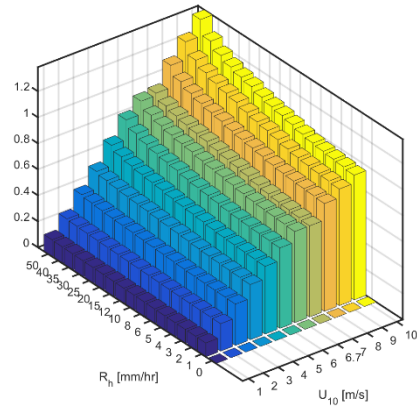


- c - Protected façade with 3' on-site overhang

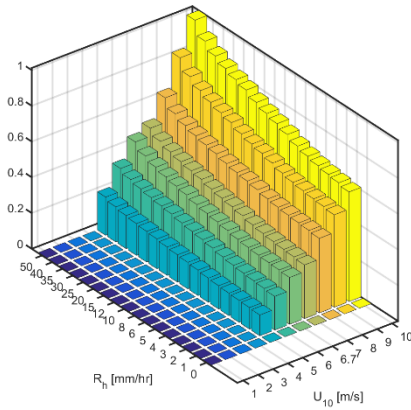
Figure 4.3.1 - x-velocity at various points on the east façade, on corresponding vertical base, Figure 2.3.13b, versus U_{10} value



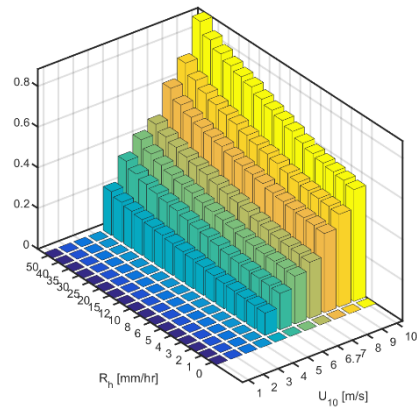
- a - ESI, unprotected *façade*



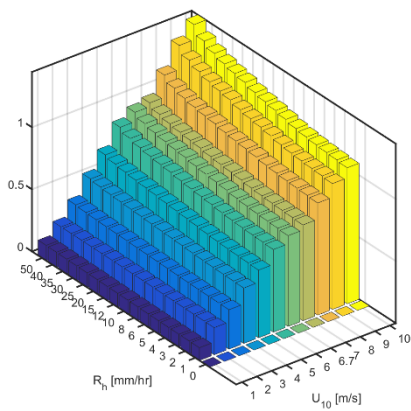
- b - ENI, unprotected *façade*



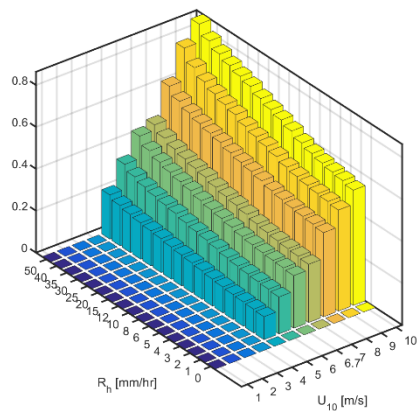
- c - ESI, protected *façade* with 3' *façade*-covering overhang



- d - ENI, protected *façade* with 3' *façade*-covering overhang



- e - ESI, protected *façade* with 3' on-site overhang

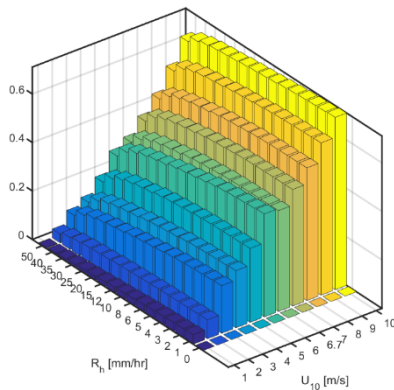


- f - ENI, protected *façade* with on-site overhang

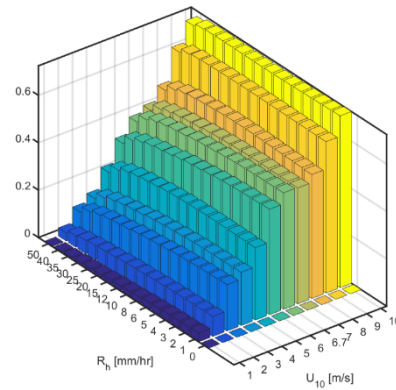
Figure 4.3.2 - Catch ratio parametric study for protected and unprotected windward *façade*, the east *façade*, exposed to normal wind at different rates, at ESI and ENI

Another observation made is by comparing Figure 4.3.2e to Figure 4.3.2a. One could observe that even with a 30' long overhang, installed on the north side of the east façade, the unprotected south side takes less WDR amounts. This shows that no matter how much of the façade is directly covered by an overhang – due to change in the entire dynamic of the rain in the vicinity of the target façade – rain deposition, and consequently effectiveness of the overhang calculated on the entire façade is going to be influenced.

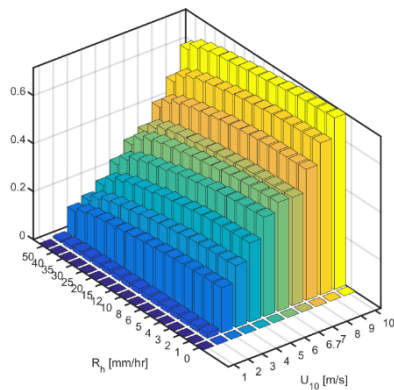
One should notice that the trend described is not applicable to the entire façade. As it turns out, catch ratio increases as wind speed increases, no matter where one is on the façade. Though, that is not the case for the rainfall intensity. Rainfall intensity of the gauges located on the edges of the façade follow the trend described; that is the more intense the rain, the more the catch ratio. Though as one hovers around on the inner sides of the façade, closer to the center, they find that with an increase in rainfall intensity, catch ratio decreases. This is shown for two inner catch ratio measurement locations on the façade, which are EC2 and EN9, Figure 4.3.3.



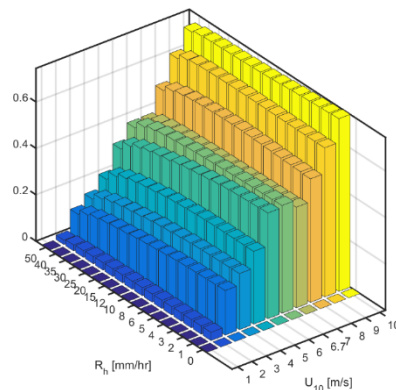
- a - EC2, unprotected façade



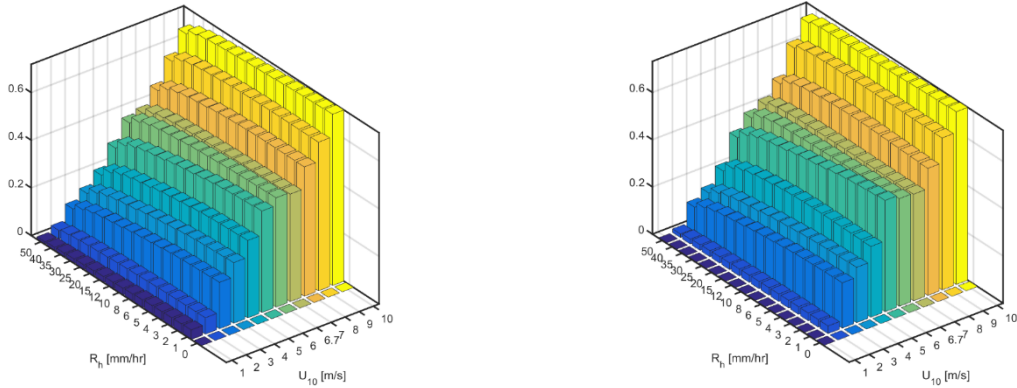
- b - EN9, unprotected façade



- c - EC2, protected façade with 3' façade-covering overhang



- d - EN9, protected façade with 3' façade-covering overhang



- e - EC2, protected façade with 3' on-site overhang - f - EN9, protected façade with on-site overhang

Figure 4.3.3 - Catch ratio parametric study for protected and unprotected windward façade, the east façade, exposed to normal wind at different rates, at EC2 and EN9¹

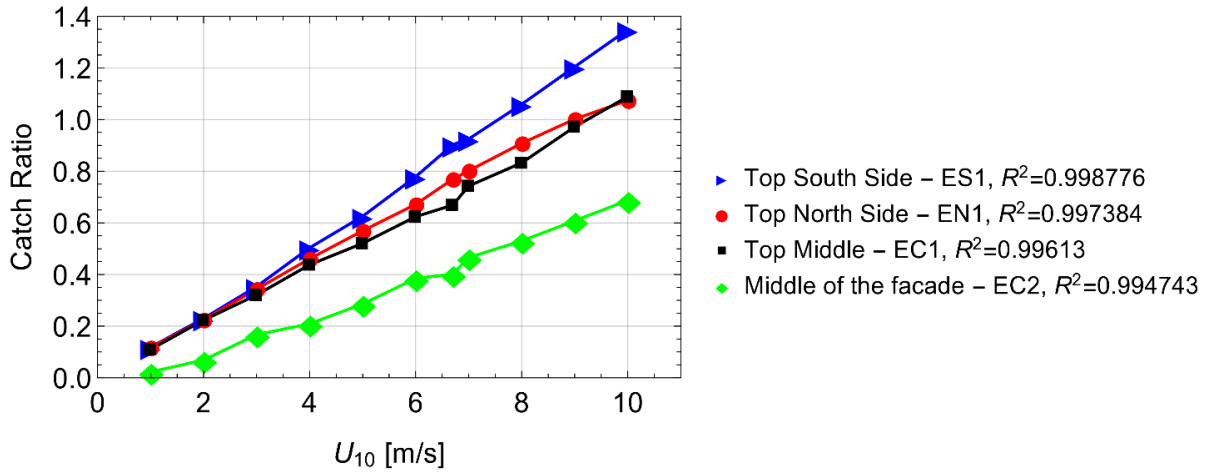
The study of linearity of catch ratio with respect to undisturbed far upstream wind speed (or U_{10}) is also worth mentioning before the effectiveness is being presented.

Figure 4.3.4 shows what Figure 4.3.1 would present for x -velocity near the façade, but this time for catch ratio at ES1, EN1, EC1 and EC2 gauge points on the east façade, Figure 2.3.13b. This figure shows that even catch ratio predicted is rather linearly dependent upon U_{10} , speed of the undisturbed wind far upstream at 10 m above the ground, with regression R-squared values close to 1.

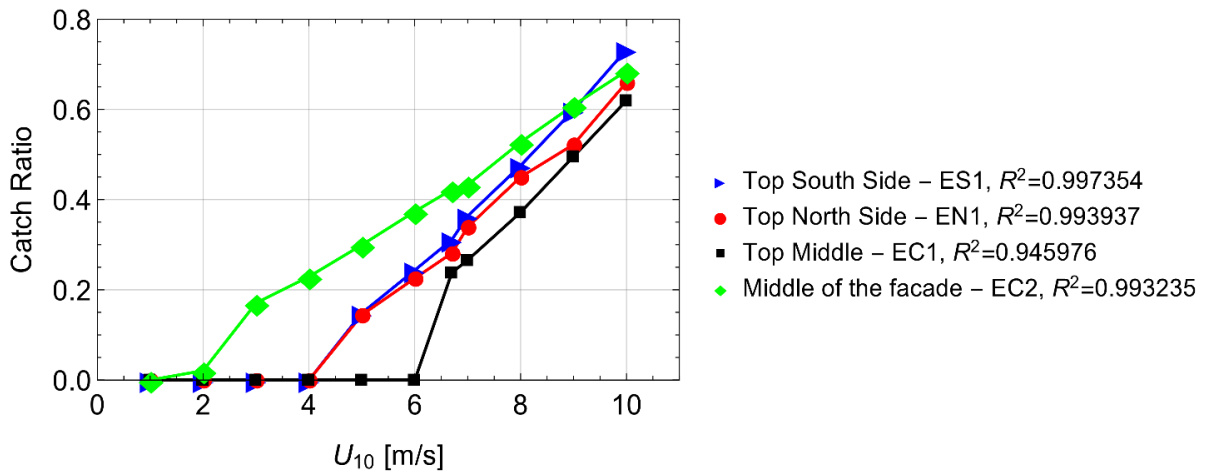
For the calculation of R-squared values shown in Figure 4.3.4, non-zero catch ratio values and the first zero at highest value of U_{10} existent, are counted in. As shown, the results are staggering. Almost all the cases, protected or unprotected, at any location on the façade show a linear relationship between catch ratio predicted and the wind speed at undisturbed far upstream. Except for EC1 on a protected façade with façade-covering overhang, which shows a R-squared value of approximately 0.946, the rest of the calculations show a distance margin to unity within the order of 10^{-3} .

Overall, this data shows that with proper simulations, a handbook style database for the catch ratio might be achievable.

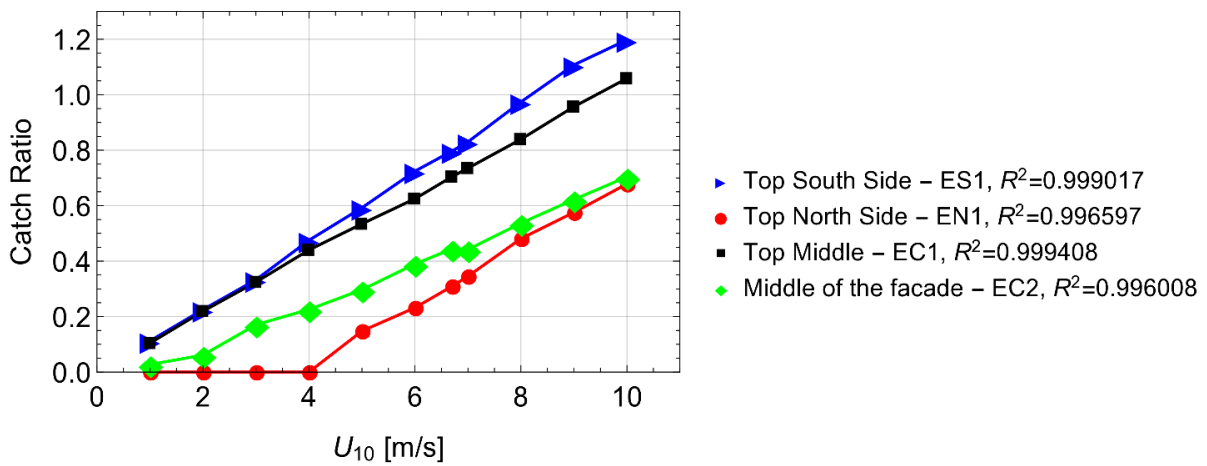
¹ Catch ratio parametric study is presented for other gauges on the east façade in Appendix E - Catch Ratio Parametric Study



- a - Unprotected façade

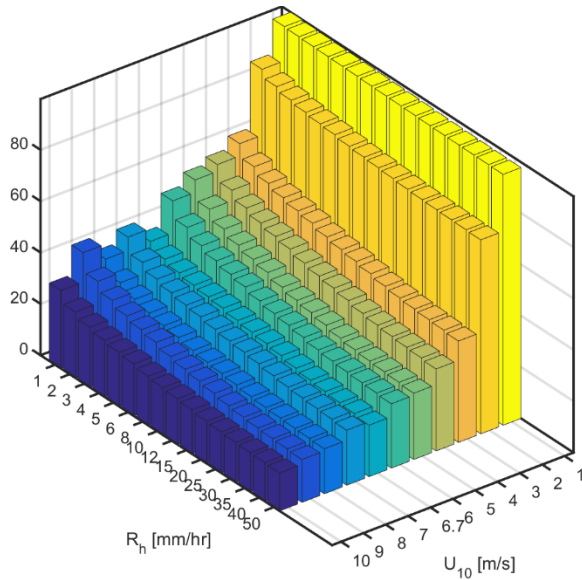


- b - Protected façade with 3' façade-covering overhang

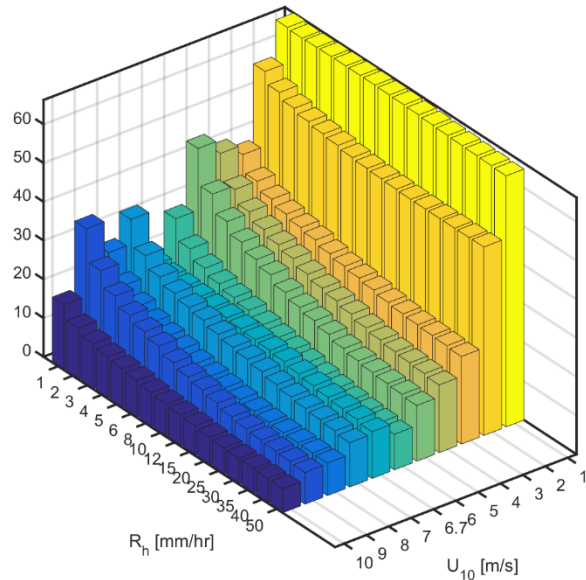


- c - Protected façade with 3' on-site overhang

Figure 4.3.4 - Catch ratio at various measurement gauges on the east façade, Figure 2.3.13b, versus U_{10} value



- a - 3' façade-covering overhang



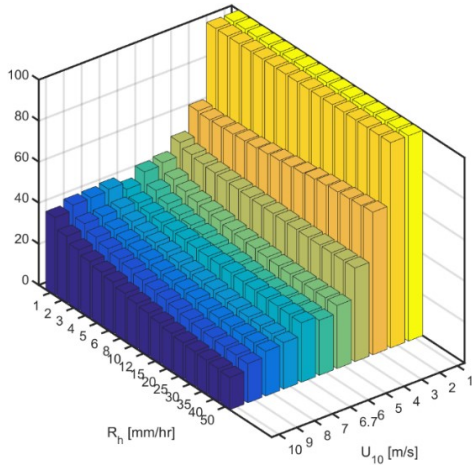
- b - 3' on-site overhang, calculated for region 2 only,
Figure 3.2.9

Figure 4.3.5 - Effectiveness of overhang (in percent) on windward façade, exposed to normal wind at different rates, and rain in different intensities, at A1 (100% of the façade)¹

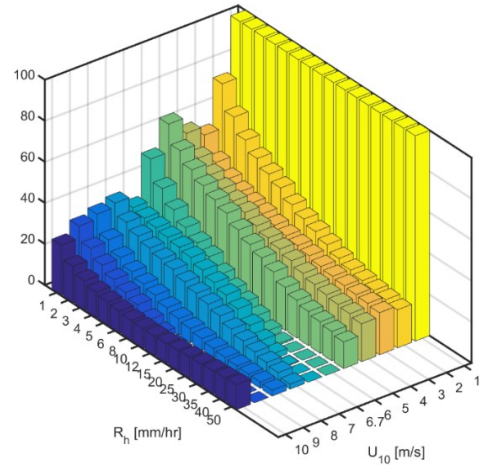
The effectiveness of the overhang, for protected portions of the façade are presented in Figure 4.3.5.

General observation made is as rainfall intensity increases, overhang effectiveness, no matter what the width, decreases. With an increase in wind speed, the effectiveness decreases as well. Minor out of points on the graphs that do not follow the trend are due to smoothing of the raw data. Catch ratio for unprotected and protected façade are both smoothed and effectiveness is calculated on the smoothed data. Effectiveness of a few measurement points on the façade are also presented in Figure 4.3.6. On these graphs, also one can predominantly observe the same trend followed, which is with an increase in rainfall intensity and wind speed, point effectiveness decreases. More on that, point effectiveness contours are presented for a few cases of rainfall and wind speed in Figure 4.3.6.

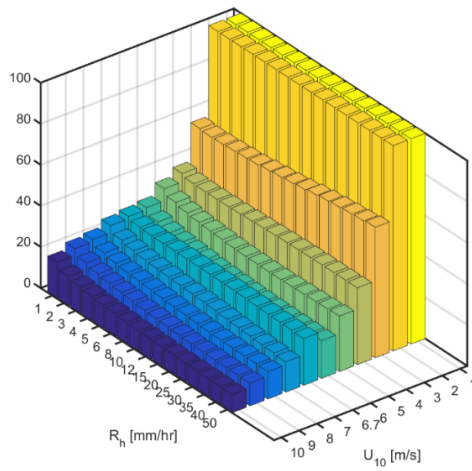
¹ Find the effectiveness for other portions of the façade in Appendix F - Effectiveness Charts



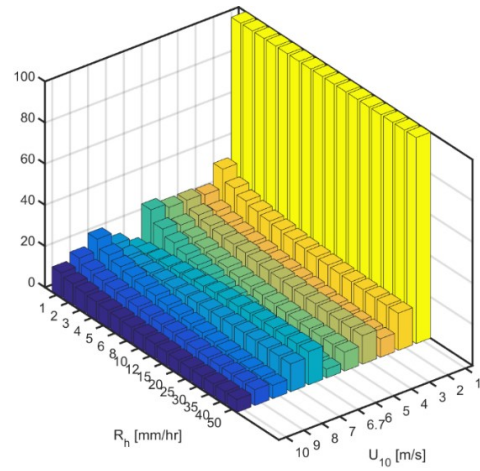
- a - ES2, protected façade with 3' façade-covering overhang



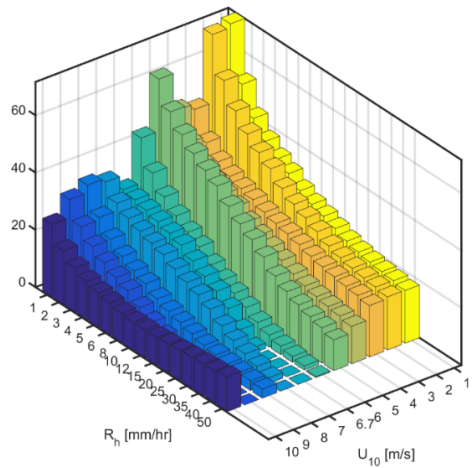
- b - EN4, protected façade with 3' façade-covering overhang



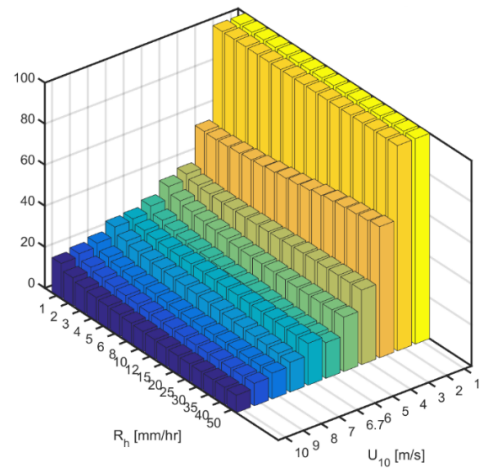
- c - EN2, protected façade with 3' façade-covering overhang



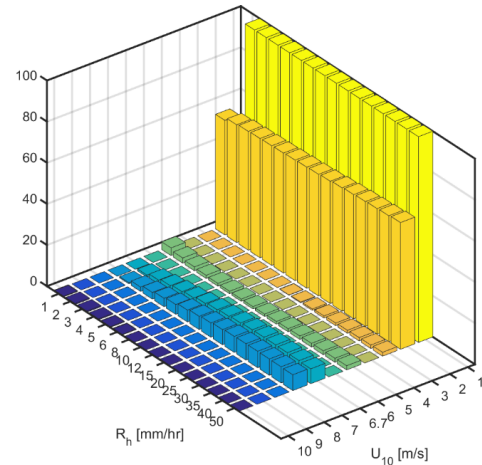
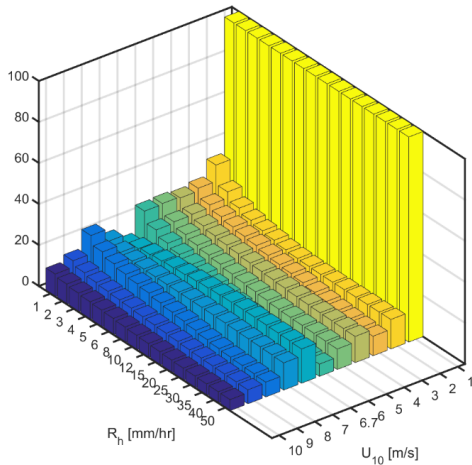
- d - EN4, protected façade with 3' façade-covering overhang



- e - ES4, protected façade with 3' on-site overhang



- f - EN2, protected façade with on-site overhang

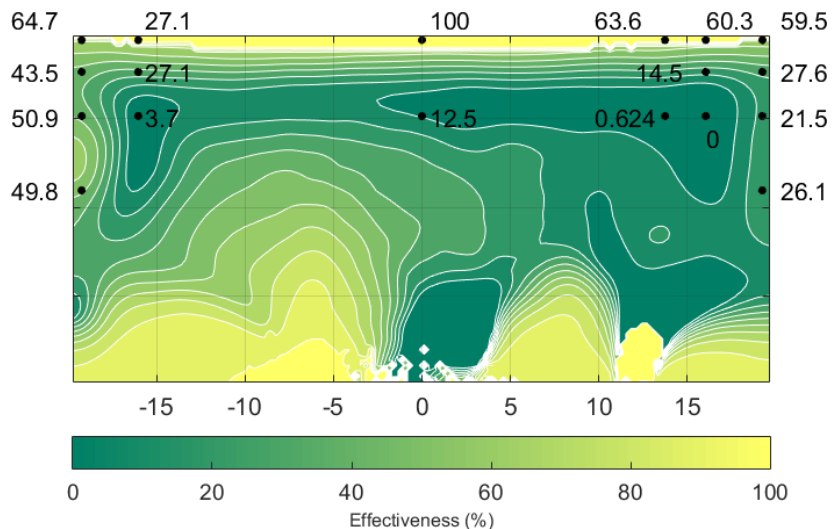


- g - EN4, protected façade with on-site overhang

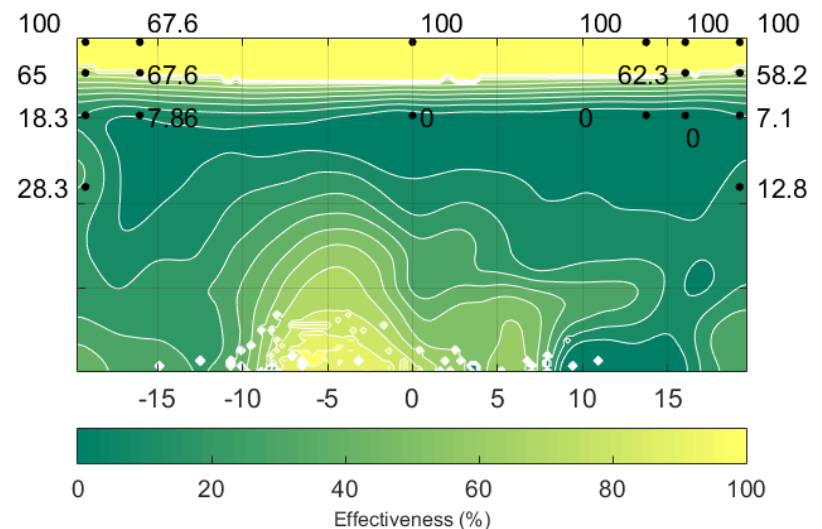
- h - EN9, protected façade with on-site overhang

Figure 4.3.6 - Point effectiveness (in percent) parametric study for protected windward façade, the east façade, exposed to normal wind at different rates

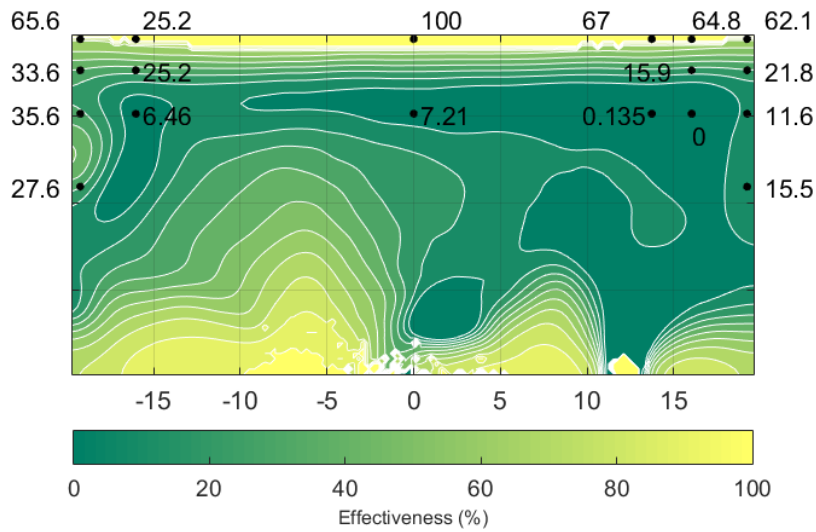
For the same reason discussed for out of order points on catch ratio parametric study, smoothing the catch ratio data results in a rather haphazard contour of effectiveness across the façade for any case presented. Though, with exception, the presence of overhang of any size is clearly depicted on any of the façade contours presented in Figure 4.3.7 for façade-covering 3' overhang, and Figure 4.3.8 for on-site 3' overhang.



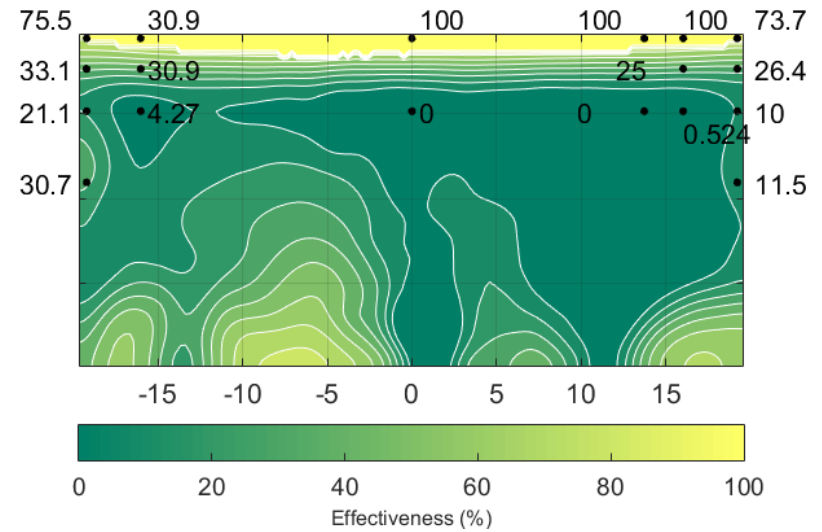
- a - $R_h = 1 \text{ mm/hr}$ and $U_{10} = 6 \text{ m/s}$



- b - $R_h = 10 \text{ mm/hr}$ and $U_{10} = 3 \text{ m/s}$



- c - $R_h = 4 \text{ mm/hr}$ and $U_{10} = 6 \text{ m/s}$



- d - $R_h = 10 \text{ mm/hr}$ and $U_{10} = 5 \text{ m/s}$

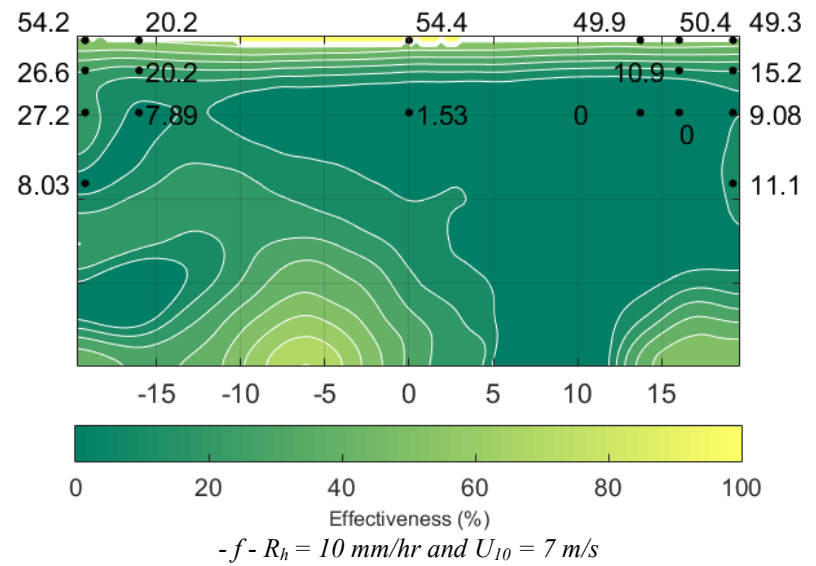
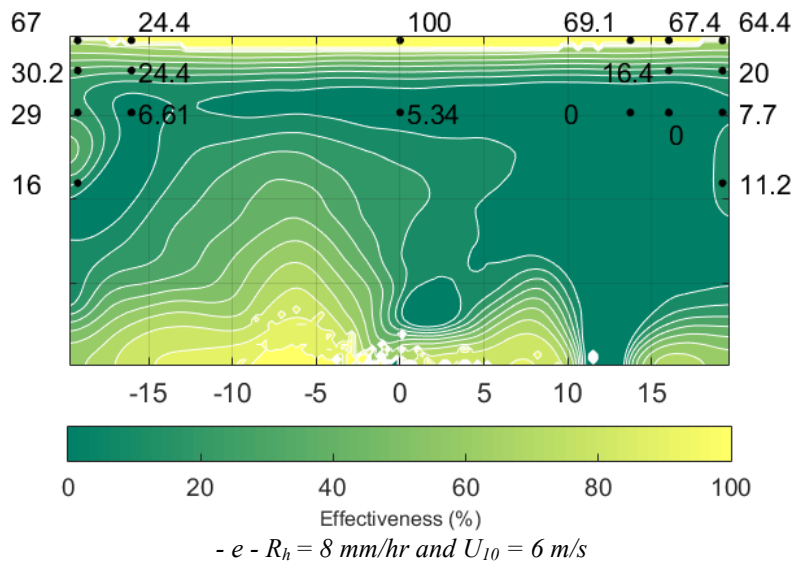
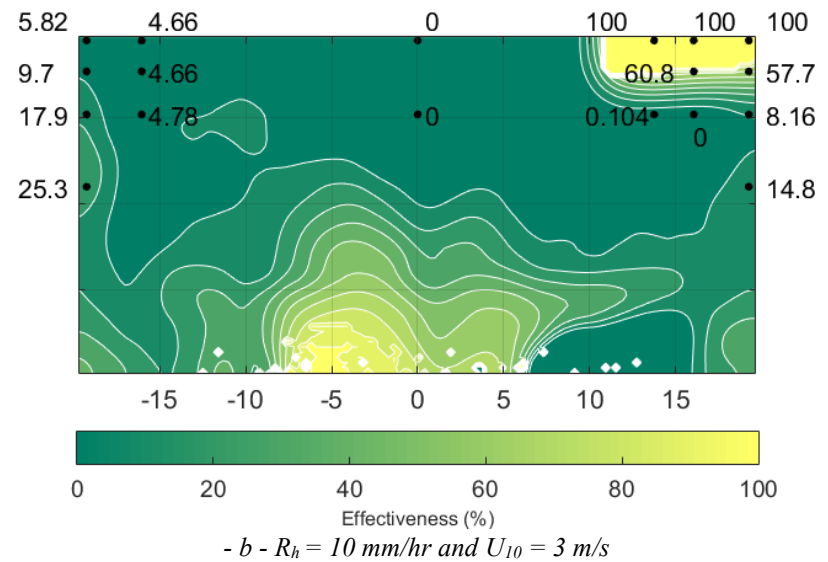
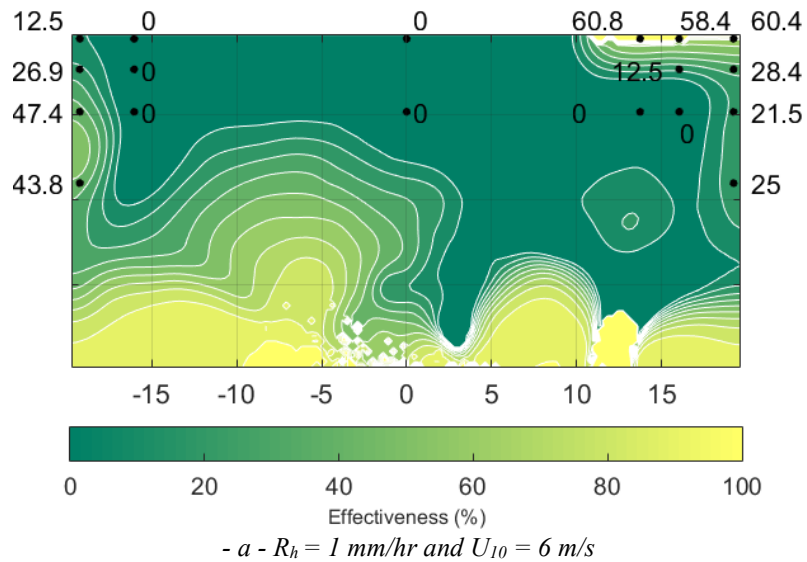
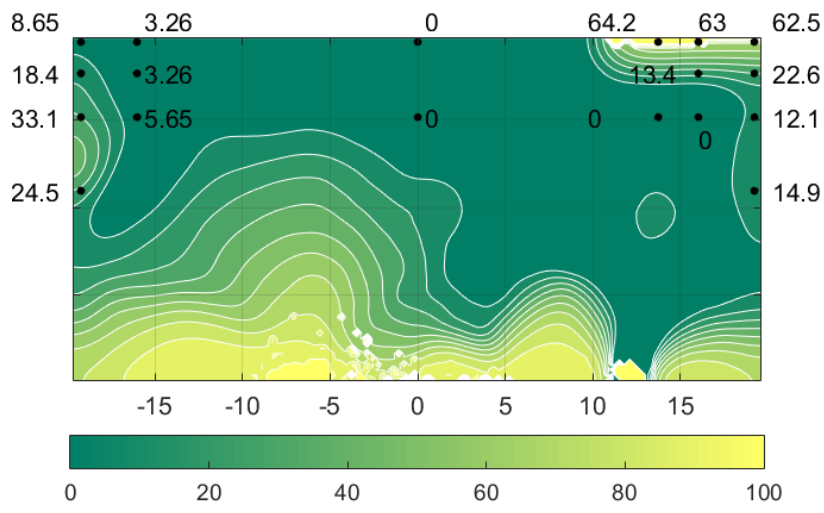
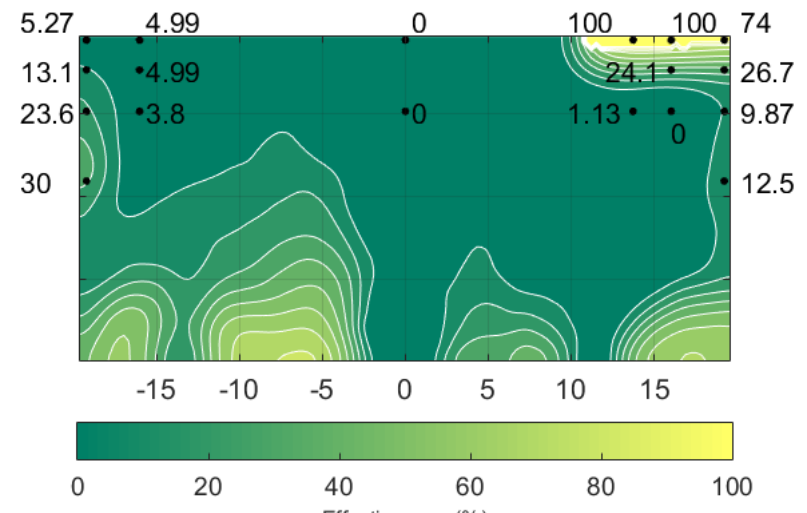


Figure 4.3.7 - Effectiveness contour on the east façade, with surrounding buildings, façade-covering overhang

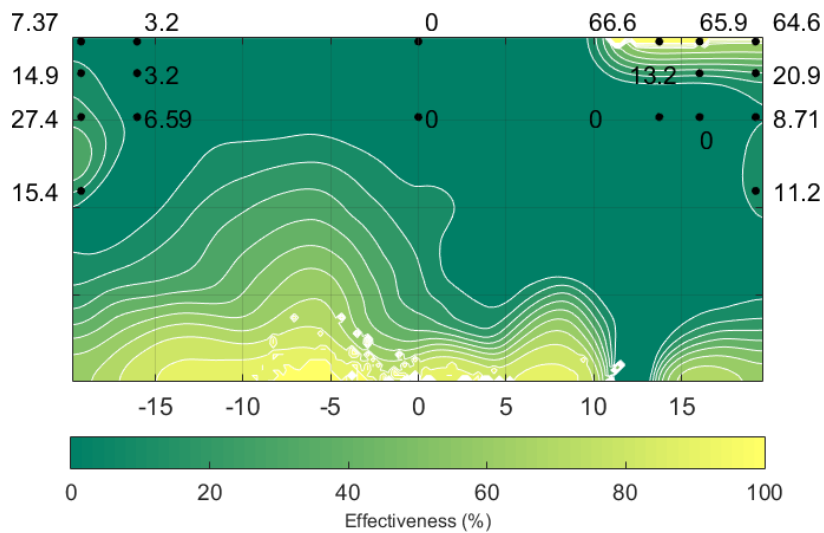




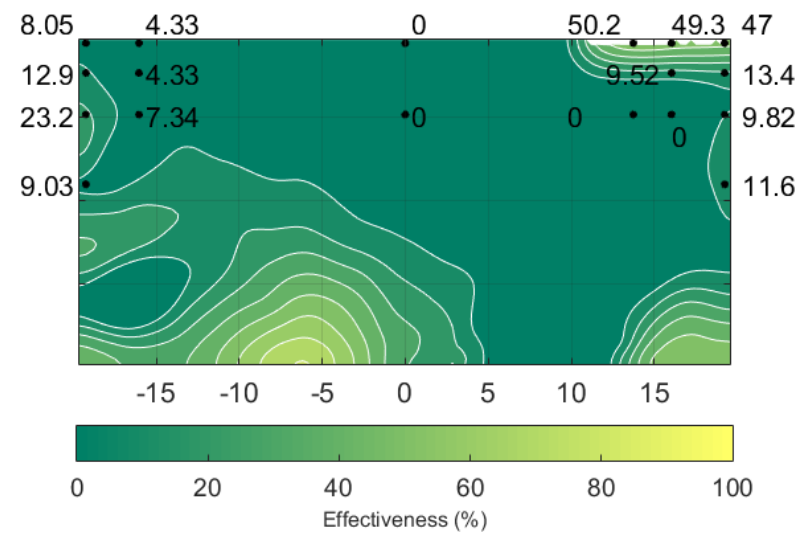
- c - $R_h = 4 \text{ mm/hr}$ and $U_{10} = 6 \text{ m/s}$



- d - $R_h = 10 \text{ mm/hr}$ and $U_{10} = 5 \text{ m/s}$



- e - $R_h = 8 \text{ mm/hr}$ and $U_{10} = 6 \text{ m/s}$



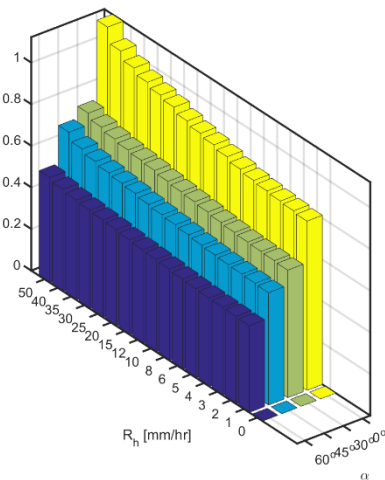
- f - $R_h = 10 \text{ mm/hr}$ and $U_{10} = 7 \text{ m/s}$

Figure 4.3.8 - Effectiveness contour on the east façade, with surrounding buildings, on-site overhang. White spots show zero effectiveness.

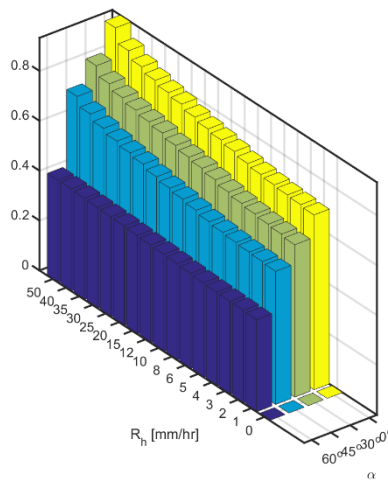
4.4 Wind Direction Effect on Overhang Effectiveness

To study the wind direction effect on the effectiveness of an overhang, façade covering overhang with a width of 3' is chosen and simulated. The set of wind directions used is presented in Figure 3.2.14, and rainfall intensity range of values is chosen to be

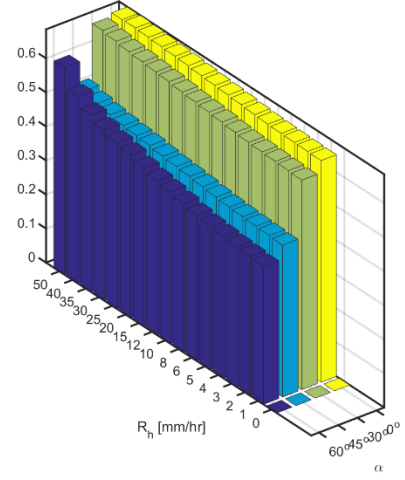
$$\{0, 1, 2, 3, 4, 5, 6, 8, 10, 12, 15, 20, 25, 30, 35, 40, 50\} \text{ mm/hr}$$



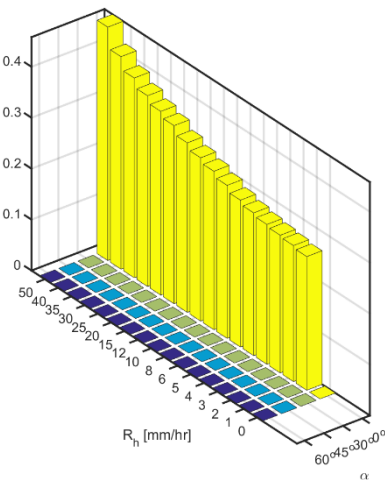
- a - ESI, unprotected façade



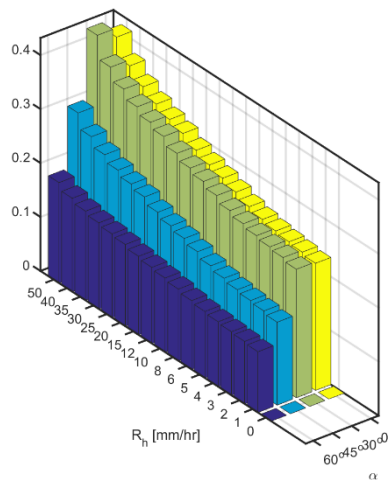
- b - ENI, unprotected façade



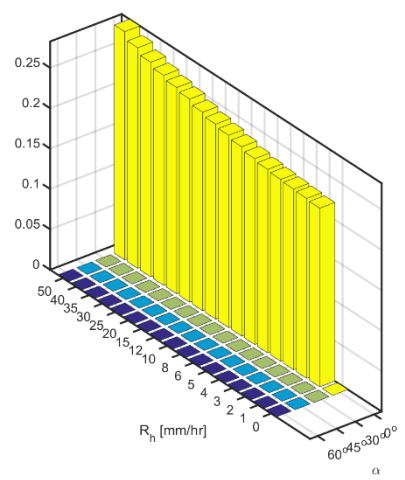
- c - ECI, unprotected façade



- d - ESI, protected façade with 3' façade-covering overhang



- e - ENI, protected façade with 3' façade-covering overhang



- f - ECI, protected façade with 3' façade-covering overhang

Figure 4.4.1 - Catch ratio parametric study for protected and unprotected windward façade, oblique wind on the east and north façades, at ESI, ECI, and ENI, Figure 2.3.13b, Standard $k\text{-}\omega$ with log-law inlet velocity profile, $U_{10} = 6.7 \text{ m/s}$ and $R_h = 4 \text{ mm/hr}$

Figure 4.4.1 shows parametric study for gauge catch ratio on ES1, EN1 and EC1, top row gauges, Figure 2.3.13b. with an increase in rainfall intensity, catch ratio for these gauges increase, at any wind direction. With an increase in wind angle towards the north, catch ratio on the façade decreases. Though, surprisingly, the top strip of the façade at leeward side (south side of the east façade) might get more rain than the windward side in some cases. Due to proximity of EN1 to the side edge, it gets rain on protected façade at any angle studied under any rainfall intensity. Another reason is that EN1, as opposed to ES1, is on the windward side (the north side of the east façade, see Figure 4.4.1e and d).

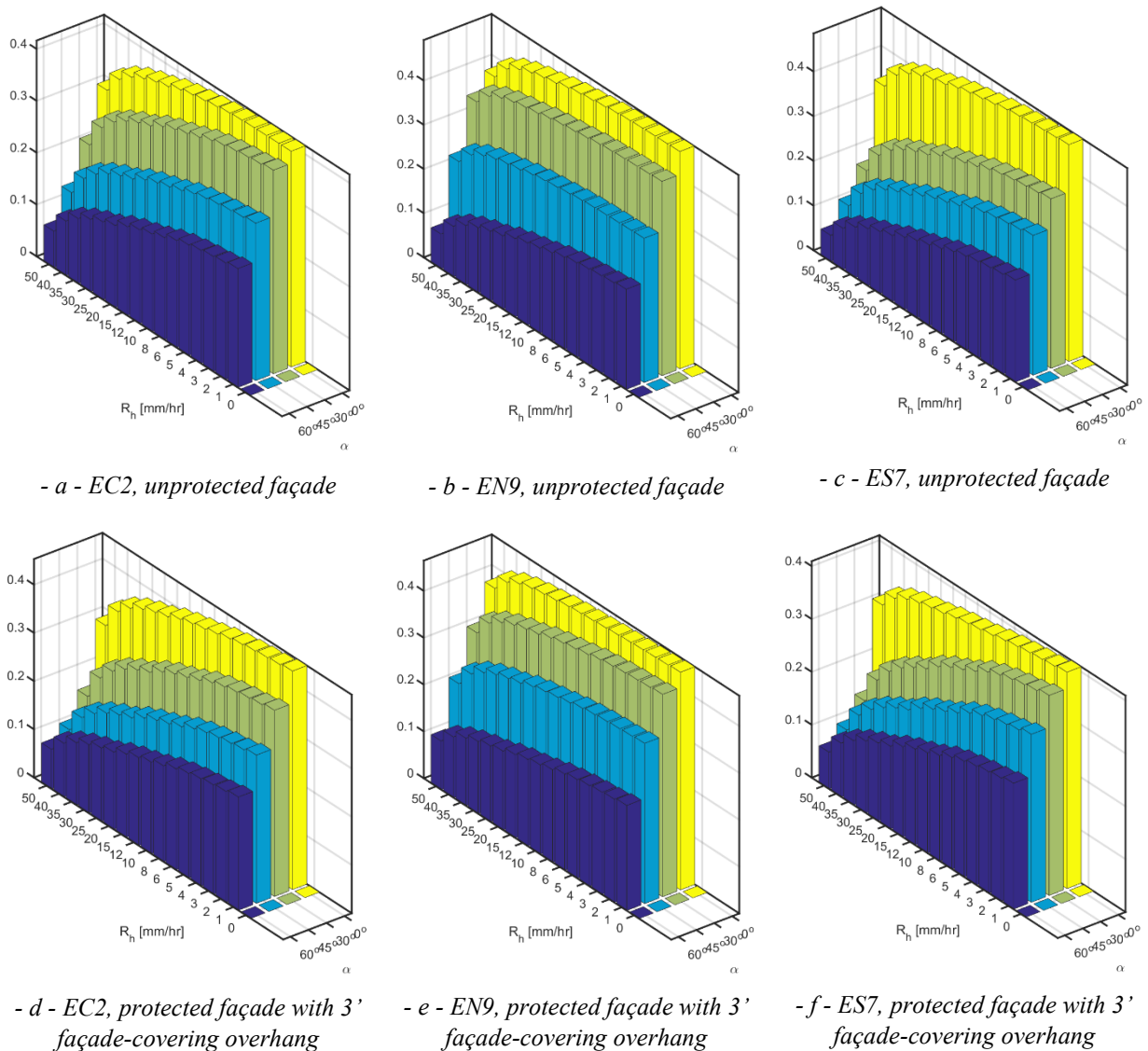
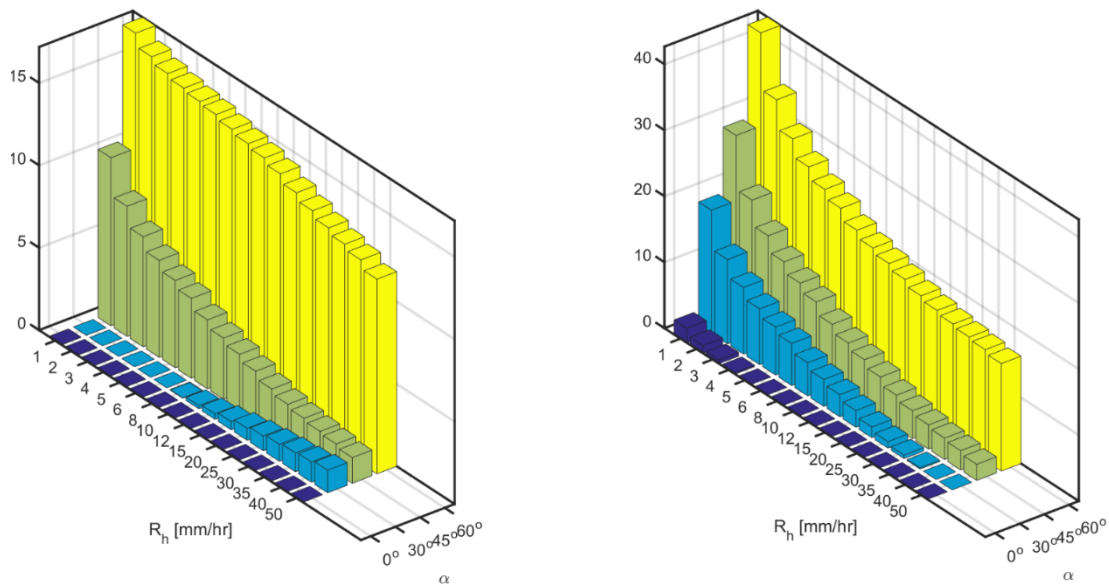


Figure 4.4.2 - Catch ratio parametric study for protected and unprotected windward façade, oblique wind on the east and north façades, at EC2, EN9, and ES7, Figure 2.3.13b, Standard $k-\omega$ with log-law inlet velocity profile, $U_{10} = 6.7$ m/s and $R_h = 4$ mm/hr

For the inner gauges, that is gauges more towards the center of the façade, the same order for wind direction holds; which is with the wind rotating towards the north façade from the east, catch ratio decreases. Though, with an increase in rainfall intensity, catch ratio decreases, Figure 4.4.2.

Following equations in Section 2.3.5, one can find the point effectiveness on EN3 and ES3 gauges on either side of the east façade, presented in Figure 4.4.3.



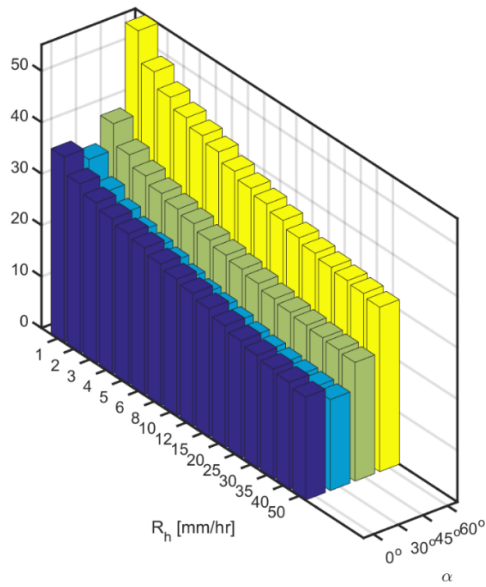
- a - EN3, protected façade with 3' façade-covering overhang

- b - ES3, protected façade with 3' façade-covering overhang

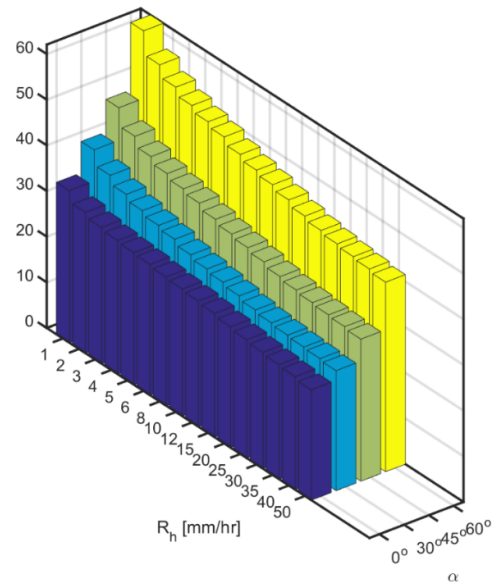
Figure 4.4.3 - Point effectiveness (in percent) parametric study for protected windward façade, the east façade, exposed to oblique wind on the east and north façades, Standard $k-\omega$ with log-law inlet velocity profile, $U_{10} = 6.7$ m/s and $R_h = 4$ mm/hr

The trend shows that with an increase in wind angle towards the north, overhang effectiveness increases. This is because physically the presence of the overhang is more dominant over the east façade as the wind rotates towards the north façade; to the point that when wind is normal at the north façade, the east façade is almost dry. Small amount of WDR on the east façade in this condition is due to leeward turbulence driving smaller raindrops onto the façade, which in practice is negligible in catch ratio calculation. Alongside that, much like any other case, with an increase in rainfall intensity, point effectiveness reduces.

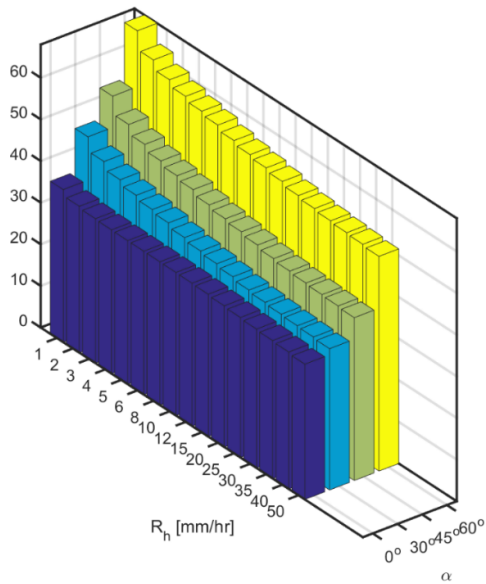
Same manner is followed with façade effectiveness. With an increase in wind angle towards the north façade, effectiveness of the façade-covering overhang increases. Also, more rainfall intensity, results in a reduction in effectiveness, for any portion of the façade, shown in Figure 4.4.4. The contour of point effectiveness of the overhang on the east façade is presented in Figure 4.4.5.



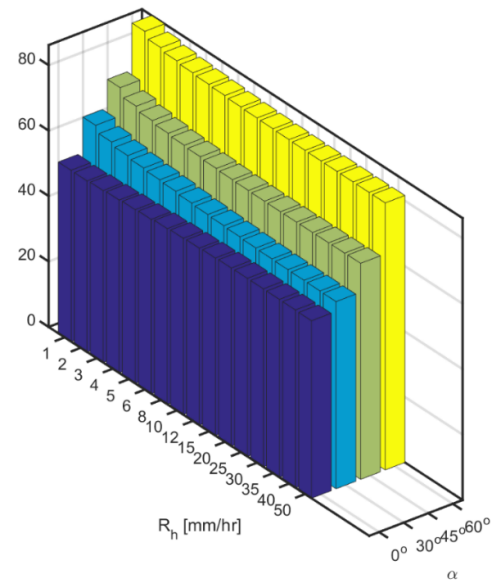
- a - A1 (100% of the façade)



- b - A2 (45% of the façade)



- c - A3 (30% of the façade)



- d - A4 (15% of the façade)

Figure 4.4.4 - Effectiveness of overhang (in percent) on the east façade, exposed to oblique wind at angles on the east and north façades, and rain in different intensities, Standard $k-\omega$ with log-law inlet velocity profile, $U_{10} = 6.7 \text{ m/s}$ and $R_h = 4 \text{ mm/hr}$

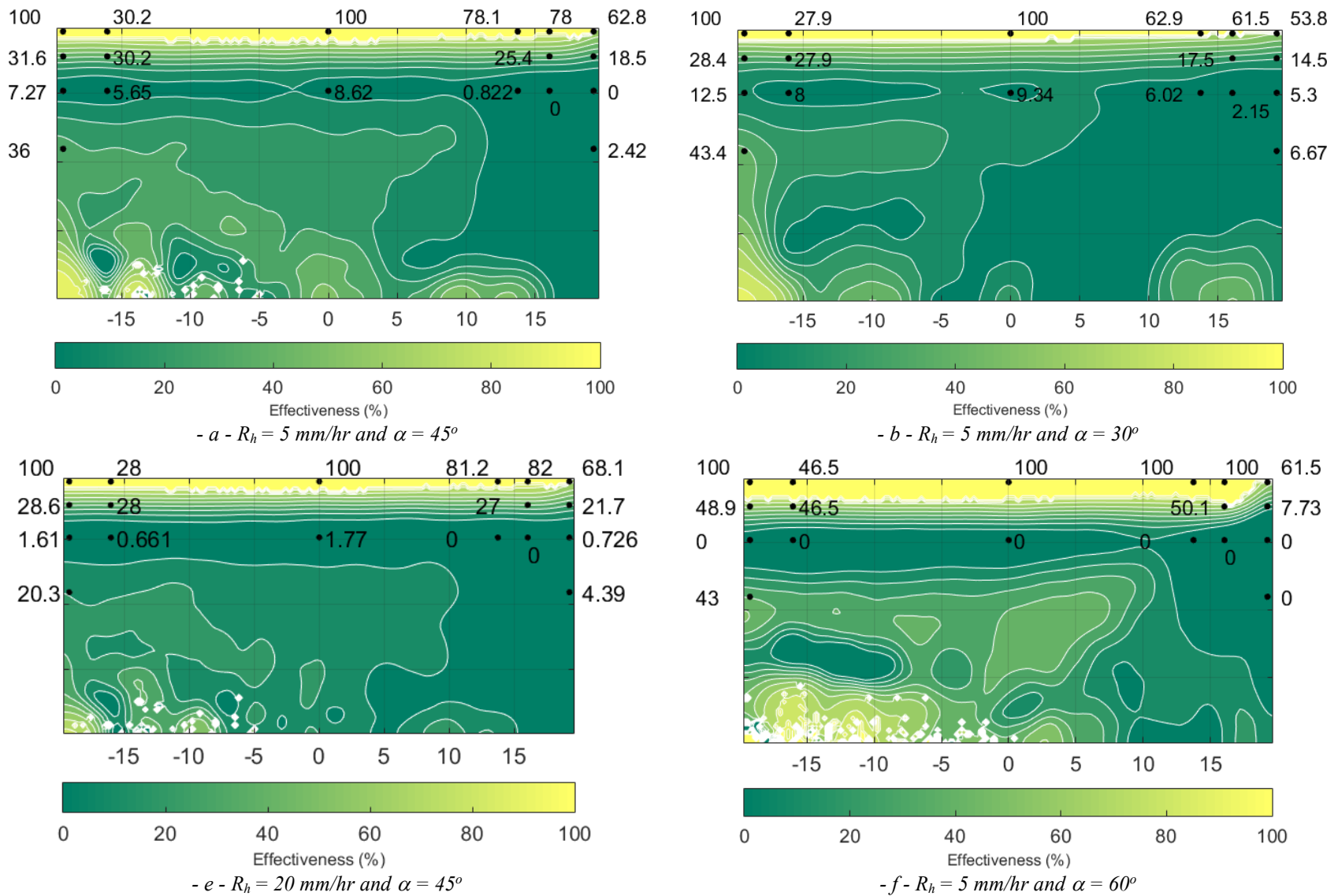


Figure 4.4.5 - Effectiveness contour on the east façade, with surrounding buildings, 3' façade-covering overhang, oblique wind. White spots show zero effectiveness.

Chapter 5 CONCLUSIONS AND RECOMMENDATIONS

Numerical simulations, and validation of them with indoor and outdoor measurements are the essence of this study. Inclusive literature review, given in Chapter 1, followed by the discussion of methodology and verification of the models used in this work, Chapter 2, followed by validations and result presentation brought in Chapter 3 are tent poles of the work. Detailed study of overhang effectiveness parametric study, catch ratio parametric study and turbulence model validation and recommendations, for various regions of the test building windward façade simulation, for various rain and wind conditions are highlights of current thesis.

Present chapter delves into conclusive remarks made across the aforementioned chapters. The body of the thesis is shaped and the idea of it is presented more organized, in a nut shell. Added to that is the second part of the current chapter which gives guidelines and recommendations to the future studies of the same kind.

5.1 Conclusions

Reasons for the necessity of the study were brought and bolded which is the moisture penetration causing the windward façade of any building exposed to fail. Two major goals followed in the thesis are addressed thoroughly. The secondary goal was validation and recommendations made on the choice between the turbulence modeling techniques proposed as the solution to the multiphase flow dealt with in wind and WDR simulation. Major and primary goal of the study is parametric study of the overhang, primarily the effectiveness relationship with multiple factors influencing it. This script fully studies all those factors and makes recommendations.

Considering the long history of study on wind and WDR, to the knowledge of the author, the factors and their influence on wind prediction, catch ratio, and consequently effectiveness of overhang delved into in current thesis, are not considered all in one study nor in detail. Major questions, unanswered in preceding theses and papers are answered.

Medium-rise building studied in this work is located in a suburban terrain and was exposed to various wind and rain cases which were simulated numerically using a coupled MATLAB code and ANSYS Fluent scheme. MATLAB code handles the post-processing catch ratio computations of the results obtained from injection of raindrops in various sizes into the pre-solved steady-state wind around the target building, using ANSYS Fluent. Extensive cases are

prepared for validation of the multiple turbulence models used to find the proper fit for proper geometry, protected or unprotected, surrounded, or stand-alone building, at any region on the windward façade.

5.1.1 Modeling and Validation

Following the patterns captured on the preservation of velocity profile throughout the empty domain, having a y_p value closer to the value of K_s , the roughness height, as much as possible is suggested. Though, there are drawbacks. Of such, the fact that precision is required on the simulation of low-rise buildings should be mentioned. On a sub-urban terrain, this issue is rather accentuated having the building and its surrounding to be shorter than 4 stories (low-rise building). For mid-rise and high-rise buildings, due to the fact that rain is mainly deposited over near the top of the façade, precision, at the bottom, near the ground sounds rather obsolete. Therefore, using a two-equation turbulence model on such scale, it is recommended that the y_p value is taken to be as high as possible, which is in the order of roughness height, K_s .

It is possible and might be recommended to solve a domain with stand-alone building. This is rather when one is interested in the top gauges of a mid-rise building in a sub-urban terrain. The simplicity of meshing such domain and low computation and temporal costs, alongside the low error margin difference compared to surrounded domain makes the stand-alone building zone rather appealing. The difference between the modeling techniques, turbulence and inlet velocity profiles are rather considerable in a stand-alone building domain. The recommendation for the mid-rise building on a sub-urban terrain, as far as both wind on the upstream façade and catch ratio comparison to measurements in the wind tunnel and on the field, are concerned, is Standard $k-\omega$, on the log-law inlet velocity profile. Anywhere else, that is away from the wall boundary (a rooftop-high distance), that is on either vertical or horizontal profiles, $k-\varepsilon$ Realizable with log-law inlet velocity profile matches the measurements better than the rest of the modeling techniques.

Wind around the surrounded building on the other hand is rather less influenced by the turbulence model, or by the inlet velocity profile for that matter. The difference between velocities in all the models are less than 5% and consequently the catch ratio value difference is negligible. This could be attributed to two major reasons. Concentration of surrounding buildings results in a considerable reduction in velocity down below near the ground around the building.

In cases, this reduction is as high as 50%. This considerable reduction is followed by a reduction in accuracy of prediction in the two-equation turbulence models used in this study, and consequently small difference between the set schemes. This is strictly relevant to wind solution. Second major reason would more effectively influence the raindrop tracking. Due to the lack of turbulence dispersion in modeling in the current study, the smaller, less dense raindrops are more likely to be prone to inaccuracy in modeling using such scheme. Although the contribution of very small raindrop impingement to the overall catch ratio value on the bottom half of the exposed façade is extremely low, in higher wind loads, and for the majority of raindrop sizes, turbulence dispersion is a factor that is being entirely neglected here.

Overall, this study shows that simulating a stand-alone building has its benefits and could be accurate enough. For a mid-rise building under normal wind conditions, using a Standard $k-\omega$ turbulence model under log-law inlet velocity profile is recommended. If more accuracy is required towards the lower parts of the façade, at the expense of complexity of meshing and computing time and resources, surrounded building should be modeled. In that case, the factor of turbulence model on the catch ratio predicted is negligible.

CFD model is proved reliable when compared to field WDR measurements for top strip, and side edges of windward façade, and higher variation/error at the center and lower part is due to the choice of y_p , nature of two-equation turbulence models in that region and not using turbulent dispersion on the rain phase.

To summarize, for the top strip of the windward façade, the east façade, the best fit to simulate the stand-alone building is Standard $k-\omega$ with log-law inlet velocity profile. Standard $k-\omega$ is also the best fit to simulate WDR for the regions on the sides edges. Overall, considering the middle of the façade as well, the best fit to simulate WDR on a stand-alone medium-rise building located in a sub-urban terrain is Standard $k-\omega$ with log-law inlet velocity profile. When it comes to WDR simulation on a surrounded medium-rise building in a sub-urban terrain, the model choice is less influential to the final prediction of the WDR on the windward façade.

Either way, two-equation turbulence models alongside the inlet velocity profiles used in the thesis are a proper fit for the WDR and wind simulation, for the upper portion of the six-story building located in a suburban terrain; top half of the windward façade that is. All the simulation,

for wind or WDR, for the protected or unprotected façade, regardless of parameters of the events, for side and top edges, are validated and reported within proper margins of error.

x -velocity near the façade is found to have a perfect linear relationship with wind speed at undisturbed far upstream.

5.1.2 Parametric Study

Catch ratio increases with an increase in wind speed, no matter what the rest of the parameters are with rain or geometry. Though, same rule does not apply to rainfall intensity. More intense rain results in higher catch ratio for the catch ratio measurement location of gauges located at the top and side edges. Though, for the middle of the façade, with an increase in the rainfall intensity, study show that the catch ratio decreases. Those predictions are also influenced by the surrounding building's locales, terrain logistics, as well.

Parametric study on overhangs shows that with an increase in the width of the overhang, regardless of the wind and rain conditions, overhang effectiveness on the façade increases. With the overhang width increase, x -velocity in the vicinity of the façade decrease, which results in decrease in WDR and consequently higher effectiveness, for any portion of the façade. Same observation is made for the partially protected façade, that is with an increase in overhang width, effectiveness of the protected portion of the façade increases.

Any overhang shape or size will protect the higher portions of the façade better than the façade taken into consideration in a larger portion taken from the top. Regardless of any parameter involved, the higher the windspeed, the less effective the façade is in protecting the façade.

Rainfall intensity works in an inverse fashion with effectiveness. Meaning, for fully or partially protected façade, overhang of any size is less effective in protecting the façade from rain deposition with more intense rain. As far as the point effectiveness is concerned, for the side and top edges of the windward façade, same relationship between effectiveness and rainfall intensity rules.

Final remarks will be on the effect of wind angle. The more oblique the wind, the less the catch ratio captured on the façade, and the more the effectiveness of the overhang, on any portion of the façade.

5.1.3 Summary

To summarize the conclusive remarks, current study shows that:

- Standard $k-\omega$ with log-law inlet velocity profile performs better universally in wind and WDR prediction near the windward façade. Although, $k-\varepsilon$ Realizable with power-law inlet velocity profile shows lower errors away from the ground for wind simulation.
- Stand-alone building simulation is usable in cases which only the top portions of the mid-rise building façade are considered, away from the ground.
- Catch ratio increases as
 - wind speed increases,
 - rainfall intensity,
 - increases – for side edges,
 - decreases – for inner parts of the façade,
 - wind is more perpendicular to the façade,
 - overhang size decreases.
- Overhang effectiveness increases
 - as higher portions of the façade are considered,
 - overhang size increases,
 - rainfall intensity decreases,
 - wind speed decreases,
 - wind is more oblique on the façade.

5.2 Recommendations

Although the current study hits a broad range of problems faced in the WDR simulation field extensively, there are angles missed that are to be dealt with in future works.

Building geometry is one of those angles missed entirely in this work. Although multiple overhang shapes and sizes are simulated and studied, for stand-alone and surrounded building, the dimensions of the building itself is overlooked. Different heights of buildings, including the study of a high-rise and sky-scraper alongside other dimension ratios, between height, width and length are to be studied to see the conclusions made for a mid-rise building are held or rejected. Moreover, different terrain roughness heights are to be considered, most importantly a building in urban terrain.

Transient wind and rain are aspects overlooked in this study as well. Nature of wind and rain, and in general turbulent flow like WDR, is transient. Transient solution to such problem is an aspect to be considered, to confirm the conclusions and recommendations made in this study. Multiple other modeling schemes including DNS and LES can contribute to the validation of the recommendations and conclusions. Added to that is the use of an Eulerian coordinate system simulation that eases up the tedious task of a transient approach to the multiphase WDR simulation.

Finally, to give a robust handbook-themed WDR and overhang database, although this work is detailed in the parametric study, there is a whole lot more of work to be done. Currently, the code and cases setup in this study have a high efficiency in wind solution and WDR calculations, that resulted in this range of simulations. Though, to prepare a database for WDR, a higher computational capacity and efficiency is needed.

REFERENCES

- Abadie, M. O. & Mendes, N., 2008. Numerical assessment of turbulence effect on the evaluation of wind-driven rain specific catch ratio. *International Communications in Heat and Mass Transfer*, December, 35(10), pp. 1253-1261.
- Abuku, M. y otros, 2009. On the validity of numerical wind-driven rain simulation on a rectangular low-rise building under various oblique winds. *Building and Environment*, March, 44(3), pp. 621-632.
- An, K., Fung, J. & Yim, S., 2013. Sensitivity of inflow boundary conditions on downstream wind and turbulence profiles through building obstacles using a CFD approach. *Journal of Wind Engineering and Industrial Aerodynamics*, Volumen 115, pp. 137-149.
- ANSYS®, 2015. *Release 16.2, Help System, Fluent Theory Guide*, ANSYS, Inc., s.l.: ANSYS Inc..
- Ariff, M., Salim, S. M. & Cheah, S. C., 2009. *Wall y^+ Approach for Dealing with Turbulent Flow over a Surface Mounted Cube: Part 1 - Low Reynolds Number*. Melbourne, CSIRO.
- Aynsley, R. M., Melbourne, W. H. & Vickery, B. J., 1977. *Architectural Aerodynamics*. London: Applied Science Publishers.
- Baheru, T., Chowdhury, A. G., Pinelli, J.-P. & Bitsuamlak, G., 2014. Distribution of wind-driven rain deposition on low-rise buildings: Direct impinging raindrops versus surface runoff. *Journal of Wind Engineering and Industrial Aerodynamics*, October, Volumen 133, pp. 27-38.
- Bell, W. E., 2001. *Stones*. s.l.:Seal Books.
- Best, A. C., 1950. The size distribution of raindrops. *Q.J.R. Meteorol. Soc.*, January, 76(327), pp. 16-36.
- Blocken, B., 2004. *"Wind-driven rain on Buildings"*, Ph.D. Thesis. Lueven: Katholieke Universiteit Leuven.
- Blocken, B. y otros, 2011. Intercomparison of wind-driven rain deposition models based on two case studies with full-scale measurements. *Journal of Wind Engineering and Industrial Aerodynamics*, April, 99(4), pp. 448-459.
- Blocken, B. & Carmeliet, J., 2002. Spatial and temporal distribution of driving rain on a low-rise building. *Wind and Structures*, 5(5), pp. 441-462.
- Blocken, B. & Carmeliet, J., 2004. A review of wind-driven rain research in building science. *Wind Engineering and Industrial Aerodynamics*, November, 92(13), pp. 1079-1130.
- Blocken, B. & Carmeliet, J., 2005. *Computational Fluid Dynamics simulations of wind-driven rain on a low-rise building: new validation efforts*. s.l., s.n., pp. 428-435.

- Blocken, B. & Carmeliet, J., 2006. The influence of the wind-blocking effect by a building on its wind-driven rain exposure. *Journal of Wind Engineering and Industrial Aerodynamics*, February, 94(2), pp. 101-127.
- Blocken, B. & Carmeliet, J., 2007. Validation of CFD simulations of wind-driven rain on a low-rise building facade. *Building and Environment*, July, 42(7), pp. 2530-2548.
- Blocken, B. & Carmeliet, J., 2010. Overview of three state-of-the-art wind-driven rain assessment models and comparison based on model theory. *Building and Environment*, March, 45(3), pp. 691-703.
- Blocken, B. & Carmeliet, J., 2010. Overview of three state-of-the-art wind-driven rain assessment models and comparison based on model theory. *Building and Environment*, March, 45(3), pp. 691-703.
- Blocken, B., Carmeliet, J. & Stathopoulos, T., 2007. CFD evaluation of wind speed conditions in passages between parallel buildings-effect of wall- function roughness modifications for the atmospheric boundary layer flow. *Journal of Wind Engineering and Industrial Aerodynamics*, October, 95(9-11), pp. 941-962.
- Blocken, B., Derome, D. & Carmeliet, J., 2013. Rainwater runoff from building facades: A review. *Building and Environment*, February, Volumen 30, pp. 339-361.
- Blocken, B., Dezsö, G., van Beeck, J. & J., C., 2010. Comparison of calculation models for wind-driven rain deposition on building facades. *Atmospheric Environment*, May, 44(14), pp. 1714-1725.
- Blocken, B., Roels, S. & Carmeliet, J., 2004. Modification of pedestrian wind comfort in the Silvertop Tower passages by an automatic control system. *Journal of Wind Engineering and Industrial Aerodynamics*, August, 92(10), pp. 849-873.
- Blocken, B., Stathopoulos, T. & Beeck, J. v., 2016. Pedestrian-level wind conditions around buildings: Review of wind-tunnel and CFD techniques and their accuracy for wind comfort assessment. *Building and Environment*, Volumen 100, pp. 50-81.
- Blocken, B., Stathopoulos, T. & Carmeliet, J., 2007. CFD simulation of the atmospheric boundary layer: wall function problems. *Atmospheric Environment*, January, 41(2), pp. 238-252.
- Blocken, B., Stathopoulos, T., Carmeliet, J. & Hensen, J. L., 2011. Application of CFD in building performance simulation for the outdoor environment: an overview. *Journal of Building Performance Simulation*, 4(2), pp. 157-184.
- Briggen, P., Blocken, B. & Schellen, H., 2009. Wind-driven rain on the facade of a monumental tower: Numerical simulation, full-scale validation and sensitivity analysis. *Building and Environment*, 44(8), pp. 1675-1690.
- Catalano, P. & Amato, M., 2003. An evaluation of RANS turbulence modelling for aerodynamic applications. *Aerospace Science and Technology*, October, 7(7), pp. 493-509.

Chang, T.-J. & Wu, Y.-T., 2003. Wind-driven rain distributions around street canopies. *JAWRA Journal of the American Water Resources Association*, June, 39(3), p. 545–562.

Chiu, V., 2016. *The Effect of Overhang on Wind-Driven Rain Wetting for a Mid-Rise Building*. Montreal: Concordia University.

Choi, E. C. C. & CSIRO. Division of Building, Construction and Eng., 1991. Numerical simulation of wind-driven rain falling onto a 2-D building. In: *Proceedings of the Asian Pacific Conference on Computational Mechanics*, 11-13 December. pp. 1721-1728.

Coccal, O. y otros, 2014. Flow structure and near-field dispersion in arrays of building-like obstacles. *Journal of Wind Engineering and Industrial Aerodynamics*, February, Volumen 125, pp. 52-68.

Cochran, L. & Derickson, R., 2011. A physical modeler's view of Computational Wind Engineering. *Journal of Wind Engineering and Industrial Aerodynamics*, April, 99(4), pp. 139-153.

Cook, N. J., 1997. The Deaves and Harris ABL model applied to heterogeneous terrain. *Journal of Wind Engineering and Industrial Aerodynamics*, 66(3), pp. 197-214.

Csanady, G. T., 1963. Turbulent Diffusion of Heavy Particles in the Atmosphere. *Journal of the Atmospheric Sciences*, 1 May, 20(3), pp. 201-208.

Cui, D., Mak, C., Kwok, K. & Ai, Z., 2016. CFD simulation of the effect of an upstream building on the inter-unit dispersion in a multi-story building in two wind directions. *Journal of Wind Engineering and Industrial Aerodynamics*, Volumen 150, pp. 31 - 41.

Cutler, J. C. & Morris, C., 2014. *Dictionary of Energy*. Second ed. Amsterdam: Elsevier.

Davenport, A. G., 1960. Rationale for determining design wind velocities. *ASCE Journal of the Structural Division*, 1 October, 86(5), p. 39–68.

Davenport, A. G., 1960. Rationale for determining design wind velocities. *ASCE Journal of the Structural Division, Proceedings American Society Civil Engineers*, 01 5, Volumen 86, pp. 39-68.

Davenport, A. G., 1961. The application of statistical concepts to the wind loading of structures. *Proceedings of the Institution of Civil Engineers*, August, 19(4), pp. 449-472.

De Berg, M., Cheong, O., van Kreveld, M. & Overmars, M., 2008. *Computational Geometry; Algorithms and Applications*. s.l.:Springer-Verlag Berlin Heidelberg.

Delaunay, D., Lakehal, D. & Pierrat, D., 1995. Numerical approach for wind loads prediction on buildings and structures. *Journal of Wind Engineering and Industrial Aerodynamics*, July, 57(2-3), pp. 307-321.

Durbin, P., 1996. On the k- ϵ stagnation point anomaly. *International Journal of Heat and Fluid Flow*, February, 17(1), pp. 89-90.

- Ehrhard, J. & Moussiopoulos, N., 2000. On a new nonlinear turbulence model for simulating flows around building-shaped structures. *Journal of Wind Engineering and Industrial Aerodynamics*, 88(1), pp. 91-99.
- Elghobashi, S., 1994. On predicting particle-laden turbulent flows. *Applied Scientific Research*, 52(4), pp. 309-329.
- Elsharawy, M., Stathopoulos, T. & Galal, K., 2012. Wind-induced torsional loads on low buildings. *Journal of Wind Engineering and Industrial Aerodynamics*, Volumen 104-106, pp. 40-48.
- Flower, J. W. & Lawson, T. V., 1972. On the laboratory representation of rain impingement on buildings. *Atmospheric Environment (1967)*, January, 6(1), pp. 55-60.
- Fluent Inc., 1998. *Fluent 5 User's Guide*, s.l.: s.n.
- Foroushani Mohaddes, S. S., Ge, H. & Naylor, D., 2014. Effects of roof overhangs on wind-driven rain wetting of a low-rise cubic building: A numerical study. *Journal of Wind Engineering and Industrial Aerodynamics*, February, Volumen 125, p. 38–51.
- Franke, J., Hellsten, A., Schlunzeh, H. & Carissimo, B., 2010. *The Best Practise Guideline for the CFD simulation of flows in the urban environment: an outcome of COST 732*. Chapel Hill, North Carolina, USA, s.n., p. 8.
- Gaetani, I., 2013. *Energy saving potential of night natural ventilation in the urban environment: the effect of wind shielding and solar shading*. Milan(Lombardy): Politecnico di Milano.
- Ge, H., Chiu, V. & Stathopoulos, T., 2017. Effect of overhang on wind-driven rain wetting of facades on a mid-rise building: Field measurements. *Building and Environment*, June, Volumen 118, pp. 234-250.
- Ge, H. & Krpan, R., 2009. *Wind-Driven Rain Study in the Coastal Climate of British Columbia*, s.l.: Technical Report Submitted to Canada Mortgage and Housing Corporation.
- Google Maps, 2017. *Cassiar Street, Vancouver, BC*, s.l.: s.n.
- Gousseau, P., Blocken, B. & van Heijst, G., 2013. Quality assessment of Large-Eddy Simulation of wind flow around a high-rise building: Validation and solution verification. *Computers & Fluids*, 25 June, Volumen 79, pp. 120-133.
- Gunn, R. & Kinzer, G. D., 1949. The Terminal Velocity of Fall for Water Droplets in Stagnant Air. *American Meteorological Society*, August, 6(4), pp. 243-248.
- Hall, R. C., 1997. *Evaluation of Modelling Uncertainty: CFD Modelling of Near-field Atmospheric Dispersion*, Surrey: WS Atkins Consultants Ltd..
- Hangan, H., 1999. Wind-driven rain studies. A C-FD-E approach. *Journal of Wind Engineering and Industrial Aerodynamics*, 81(1-3), p. 323–331.

- Hang, J., Luo, Z., Sandberg, M. & Gong, J., 2013. Natural ventilation assessment in typical open and semi-open urban environments under various wind directions. *Building and Environment*, December, Volumen 70, pp. 318-333.
- Hanna, S. y otros, 2002. Comparisons of model simulations with observations of mean flow and turbulence within simple obstacle arrays. *Atmospheric Environment*, 36(32), pp. 5067-5079.
- Hargreaves, D. & Wright, N., 2007. On the use of the k- ϵ model in commercial CFD software to model the neutral atmospheric boundary layer. *Journal of Wind Engineering and Industrial Aerodynamics*, May, 98(5), pp. 355-369.
- Hazleden, D. G. & Morris, P. I., 1999. *Designing for durable wood construction: The 4 DS*. Vancouver, BC, Canada, Fraunhofer IRB.
- Hershfield, M., 1996. *Survey of building envelope failures in the coastal climate of British Columbia*. [En línea]
Available at: <http://publications.gc.ca/collections/Collection/NH18-22-98-102E.pdf>
- Huang, S. & Li, Q., 2010. Numerical simulations of wind-driven rain on building envelopes based on Eulerian multiphase model. *Journal of Wind Engineering and Industrial Aerodynamics*, December, 98(12), pp. 843-857.
- Huang, S., Li, Q. & Xu, S., 2007. Numerical evaluation of wind effects on a tall steel building by CFD. *Journal of Constructional Steel Research*, 63(5), pp. 612-627.
- Joubert, E., Harms, T. & Venter, G., 2015. Computational simulation of the turbulent flow around a surface mounted rectangular prism. *Journal of Wind Engineering and Industrial Aerodynamics*, July, Volumen 142, pp. 173-187.
- Kim, H.-S., Lee, S. & Choi, G., 2009. *Numerical Simulation of Wind Around Building Complex*. Taipei, Taiwan, International Association for Wind Engineering, pp. 1-7.
- Kim, S.-E. & Boysan, F., 1999. Application of CFD to environmental flows. *Journal of Wind Engineering and Industrial Aerodynamics*, May, 81(1-3), pp. 145-158.
- Kim, W., Tamura, Y. & Yoshida, A., 2015. Interference effects on aerodynamic wind forces between two buildings. *Journal of Wind Engineering and Industrial Aerodynamics*, Volumen 147, pp. 186-201.
- Kolmogorov, A. N., 1942. "Equations of Turbulent Motion of an Incompressible Fluid". *Izvestia Academy of Sciences, USSR; Physics*, Volumen 6, pp. 56-58.
- Kubilay, A., Derome, D., Blocken, B. & Carmeliet, J., 2013. CFD simulation and validation of wind-driven rain on a building facade with an Eulerian multiphase model. *Building and Environment*, March, Volumen 61, pp. 69-81.
- Kubilay, A., Derome, D., Blocken, B. & Carmeliet, J., 2014. Numerical simulations of wind-driven rain on an array of low-rise cubic buildings and validation by field measurements. *Building and Environment*, November, Volumen 81, pp. 283-295.

- Kubilay, A., Derome, D., Blocken, B. & Carmeliet, J., 2015. Numerical modeling of turbulent dispersion for wind-driven rain on building facades. *Environmental Fluid Mechanics*, February, 15(1), pp. 109-133.
- Kubliay, A., Derome, D., Blocken, B. & Carmeliet, J., 2014. Numerical simulations of wind-driven rain on an array of low-rise cubic buildings and validation by field measurements. *Building and Environment*, pp. 283-295.
- Lakehal, D. y otros, 1995. Euler-Lagrangian simulation of raindrop trajectories and impacts within the urban canopy. *Atmospheric Environment*, pp. 3501-3517.
- Lauder, B. & Spalding, D., 1974. The numerical computation of turbulent flows. *Computer Methods in Applied Mechanics and Engineering*, 3(2), pp. 269-289.
- Lourenço, P. B., Luso, E. & Almeida, M. G., 2006. Defects and moisture problems in buildings from historical city centres: a case study in Portugal. *Building and Environment*, February, 41(2), pp. 223-234.
- Melaragno, M. G., 1992. *Wind in Architectural and Environmental Design*. 1st ed. New York: Van Nostrand Reinhold Company.
- Menter, F. R., 1993. *Zonal Two Equation $k-\omega$ Turbulence Models for Aerodynamic Flows*. Orlando, FL; United States, NASA, p. 22p.
- Mirzaei, P. A. & Carmeliet, J., 2013. Dynamical computational fluid dynamics modeling of the stochastic wind for application of urban studies. *Building and Environment*, December, Volumen 70, pp. 161-170.
- Mohaddes Foroushani, S. S., 2013. *A numerical study of the effects of overhangs on the wind-driven rain wetting of building facades*. Toronto(Ontario): Ryerson University.
- Mohaddes Foroushani, S. S., Ge, H. & Naylor, D., 2014. Effects of roof overhangs on wind-driven rain wetting of a low-rise cubic building: A numerical study. *Journal of Wind Engineering and Industrial Aerodynamics*, February, Volumen 125, p. 38–51.
- Montazeri, H. & Blocken, B., 2013. CFD simulation of wind-induced pressure coefficients on buildings with and without balconies: Validation and sensitivity analysis. *Building and Environment*, Volumen 60, pp. 137-149.
- Moneghi, M. A. & Kargarmoakhar, R., 2016. Aerodynamic Mitigation and Shape Optimization of Buildings: Review. *Journal of Building Engineering*, Volumen 6, pp. 225-235.
- Murakami, S., 1998. Overview of turbulence models applied in CWE-1997. *Journal of Wind Engineering and Industrial Aerodynamics*, Volumen 74-76, pp. 1-24.
- Nore, K. y otros, 2007. A dataset of wind-driven rain measurements on a low-rise test building in Norway. *Building and Environment*, May, 42(5), pp. 2150-2165.
- Oke, T. R., 1987. *"Boundary layer climates"*. 2nd ed. Methuen(Massachusetts): Methuen.

- Ozmen, Y., Baydar, E. & Beeck, J. v., 2016. Wind flow over the low-rise building models with gabled roofs having different pitch angles. *Building and Environment*, Volumen 95, pp. 63-74.
- Pérez-Bella, J. M. y otros, 2013. Combined use of wind-driven rain and wind pressure to define water penetration risk into building façades: The Spanish case. *Building and Environment*, June, Volumen 64, pp. 46-56.
- Pettersson, K., Krajnovi, S., Kalagasidis, A. & Johansson, P., 2016. Simulating wind-driven rain on building facades using Eulerian multiphase with rain phase turbulence model. *Building and Environment*, Volumen 106, pp. 1-9.
- Poe, E. A., 1843. *The Black Cat*. s.l.:United States Saturday Post.
- Reiter, S., 2008. *Validation Process for CFD Simulations of Wind Around Buildings*. Londres, s.n., p. 18.
- Reynolds, O., 1895. "On the Dynamical Theory of Incompressible Viscous FLuids and the Determination of the Criterion". *Philosophical Transactions of the Royal Society of London*, 186(Series A), p. 123.
- Richards, P., Hoxey, R. & L.J., S., 2001. Wind pressures on a 6 m cube. *Journal of Wind Engineering and Industrial Aerodynamics*, December, 89(14-15), pp. 1553-1564.
- Roy, C. J., 2004. *Verification of Codes and Solutions in Computational Simulation*. Norway, s.n.
- Shih, T. H. y otros, 1995. A new $k-\epsilon$ eddy viscosity model for high reynolds number turbulent flows. *Computers and Fluids*, 24(3), pp. 227-238.
- Shih, T.-H., Zhu, J. & Lumley, J. L., 1993. *A Realizable Reynolds Stress Algebraic Equation Model*. Cleveland(Ohio): NASA Technical Memorandum 105993.
- Stathopoulos, T., 1984. Adverse Wind Loads on Low Buildings Due to Buffeting. *Journal of Structural Engineering*, October, 110(10), pp. 2374-2392.
- Stathopoulos, T., 1984. Design and fabrication of a wind tunnel for building aerodynamics. *Journal of Wind Engineering and Industrial Aerodynamics*, 16(2), pp. 361-376.
- Surry, D. & Incelet, D., 1995. *Simulation of wind-driven rain and wetting patterns on buildings*, Ottawa: s.n.
- Tang, W. & Davidson, C. I., 2004. Erosion of limestone building surfaces caused by wind-driven rain: 2. Numerical modeling. *Atmospheric Environment*, October, 38(33), pp. 5601-5609.
- Toja-Silva, F. y otros, 2015. Roof region dependent wind potential assessment with different RANS turbulence models. *Journal of Wind Engineering and Industrial Aerodynamics*, July, Volumen 142, pp. 258-271.
- Tominaga, Y., 2015. Flow around a high-rise building using steady and unsteady RANS CFD: Effect of large-scale fluctuations on the velocity statistics. *Journal of Wind Engineering and Industrial Aerodynamics*, July, Volumen 142, pp. 93-103.

Tominaga, Y., Mochida, A., Murakami, S. & Sawaki, S., 2008. Comparison of various revised $k-\epsilon$ models and LES applied to flow around a high-rise building model with 1:1:2 shape placed within the surface boundary layer. *Journal of Wind Engineering and Industrial Aerodynamics*, April, 96(4), pp. 389-411.

Tominaga, Y. et al., 2008. AIJ guidelines for practical applications of CFD to pedestrian wind environment around buildings. *Journal of Wind Engineering and Industrial Aerodynamics*, October-November 2008, 96(10-11), pp. 1749-1761.

Tsuchiya, M. y otros, 1997. Development of a new $k-\epsilon$ model for flow and pressure fields around bluff body. *Journal of Wind Engineering and Industrial Aerodynamics*, April-June, Volumen 67-68, pp. 169-182.

TurbulentFlow Instrumentation, 2011. *Getting Started - Series 100 Cobra Probe*. Victoria: TurbulentFlow.

van Mook, F., 2002. *Driving rain on building envelopes.*, Eindhoven, The Netherlands: Eindhoven University Press.

von Hooff, T., Blocken, B. & van Harten, M., 2011. 3D CFD simulations of wind flow and wind-driven rain shelter in sports stadia: Influence of stadium geometry. *Building and Environment*, January, 46(1), pp. 22-37.

Wang, H., Hou, X. & Deng, Y., 2015. Numerical simulations of wind-driven rain on building facades under various oblique winds based on Eulerian multiphase model. *Journal of Wind Engineering and Industrial Aerodynamics*, July, Volumen 142, pp. 82-92.

Wang, K., 2005. *Modeling terrain effects and application to the wind loading of low buildings*. Montreal(Quebec): Concordia University.

Wilcox, D. C., 2006. *"Turbulence Modeling for CFD"*. Third ed. California: DCW Industries.

Wright, N. & Easom, G., 2003. Non-linear $k-\epsilon$ turbulence model results for flow over a building at full-scale. *Applied Mathematical Modelling*, 27(12), pp. 1013-1033.

Yakhot, V. & Smith, L. M., 1992. The renormalization group, the ϵ -expansion and derivation of turbulence models. *Journal of Scientific Computing*, March, 7(1), pp. 35-61.

Yap, C., 1987. *Turbulent Heat and Momentum Transfer in Recirculating and Impinging Flows (Ph.D. thesis)*. Manchester: Faculty of Technology, University of Manchester.

Yoshie, R. y otros, 2007. Cooperative project for CFD prediction of pedestrian wind environment in the Architectural Institute of Japan. *Journal of Wind Engineering and Industrial Aerodynamics*, October, 95(9-11), pp. 1551-1578.

Zhang, A., Gao, C. & Zhang, L., 2005. Numerical simulation of the wind field around different building arrangements. *Journal of Wind Engineering and Industrial Aerodynamics*, 93(12), pp. 891-904.

Zhang, A. & Gu, M., 2008. Wind tunnel tests and numerical simulations of wind pressures on buildings in staggered arrangement. *Journal of Wind Engineering and Industrial Aerodynamics*, 96(10-11), pp. 2067-2079.

APPENDICES

Appendix A - Discretization Error Formulation¹

Since cell sizes are different, a representative grid size h is found using the following formula

$$h = \left[\frac{1}{N} \sum_{i=1}^N (\Delta V_i) \right]^{\frac{1}{3}} \quad (\text{A.1})$$

in which N is the total number of cells used for the computations. Grid refinement factors are defined as follows, $h_1 < h_2 < h_3$

$$r_{21} = \frac{h_2}{h_1} \quad (\text{A.2})$$

$$r_{32} = \frac{h_3}{h_2} \quad (\text{A.3})$$

To calculate the apparent order p of the method, the following expression is used

$$p = \frac{1}{\ln r_{21}} |\ln |\epsilon_{32}/\epsilon_{21}| + q(p)| \quad (\text{A.4})$$

in which

$$q(p) = \ln \left(\frac{r_{21}^p - s}{r_{32}^p - s} \right) \quad (\text{A.5})$$

$$s = \text{sgn} \left(\frac{\epsilon_{32}}{\epsilon_{21}} \right) \quad (\text{A.6})$$

and

$$\epsilon_{21} = \phi_2 - \phi_1 \quad (\text{A.7})$$

$$\epsilon_{32} = \phi_3 - \phi_2 \quad (\text{A.8})$$

$$\phi_{\text{ext}}^{21} = (r_{21}^p \phi_1 - \phi_2) / (r_{21}^p - 1) \quad (\text{A.9})$$

$$\phi_{\text{ext}}^{32} = (r_{32}^p \phi_1 - \phi_2) / (r_{32}^p - 1) \quad (\text{A.10})$$

¹ (Roy, 2004)

$$e_a^{21} = \left| \frac{\phi_1 - \phi_2}{\phi_1} \right| \quad (\text{A.11})$$

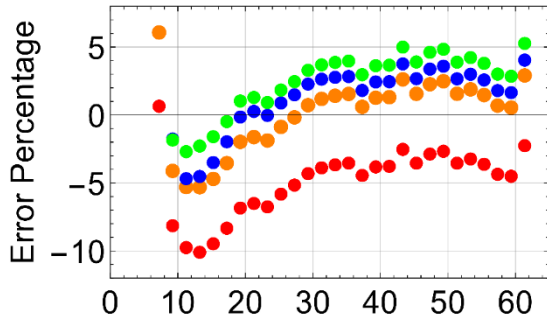
$$e_{\text{ext}}^{21} = \left| \frac{\phi_{\text{ext}}^{21} - \phi_1}{\phi_{\text{ext}}^{21}} \right| \quad (\text{A.12})$$

$$e_{\text{ext}}^{21} = \left| \frac{\phi_{\text{ext}}^{21} - \phi_1}{\phi_{\text{ext}}^{21}} \right| \quad (\text{A.13})$$

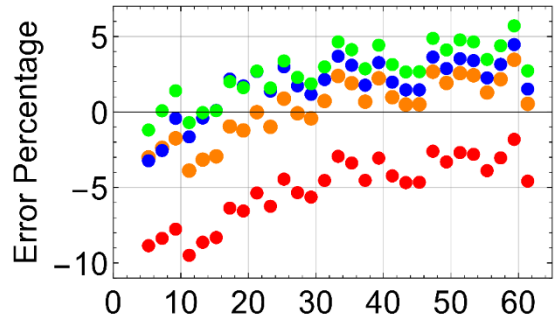
In the fine-grid convergence index,

$$GCI_{\text{fine}}^{21} = \frac{1.25e_a^{21}}{r_{21}^p - 1} \quad (\text{A.14})$$

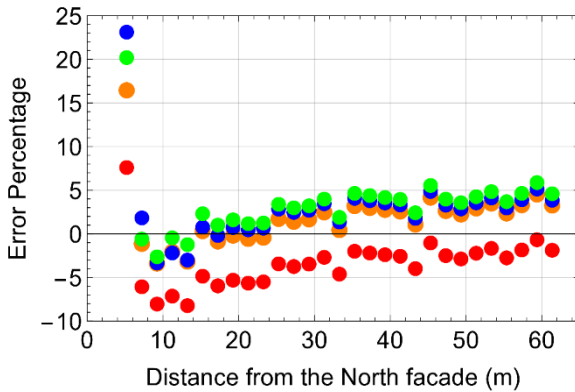
Appendix B - Error Percentage Plots



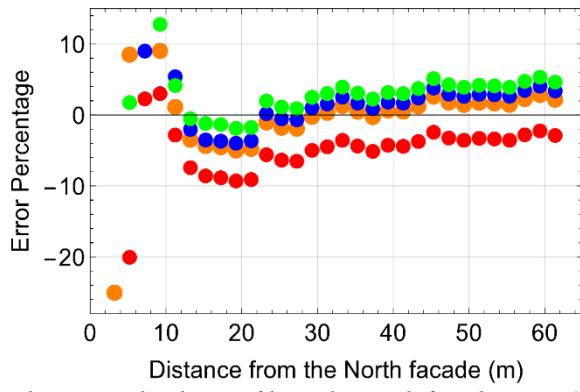
- a - Perpendicular profile to the north façade at point 8, Figure 2.3.13c



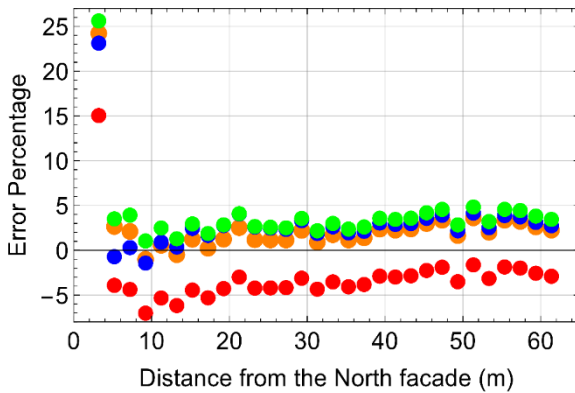
- b - Perpendicular profile to the north façade at NE2, Figure 2.3.13c



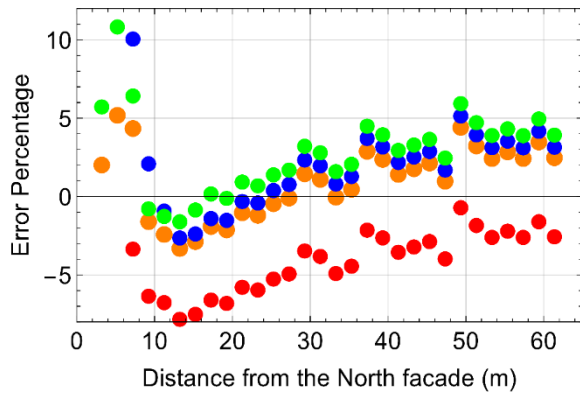
- c - Perpendicular profile to the north façade at NCI, Figure 2.3.13c



- d - Perpendicular profile to the north façade at NW3, Figure 2.3.13c



- e - Perpendicular profile to the north façade at point 1, Figure 2.3.13c



- f - Perpendicular profile to the north façade at NW1, Figure 2.3.13c

- k- ϵ Realizable, Log-law Inlet Velocity
- k- ϵ Realizable, Power-law Inlet Velocity
- k- ω SST, Log-law Inlet Velocity
- Standard k- ω , Log-law Inlet Velocity

Figure B.1 - x -velocity error percentage on a horizontal profile, normal to the north façade at different locations, with the stand-alone building exposed to normal wind on the east façade

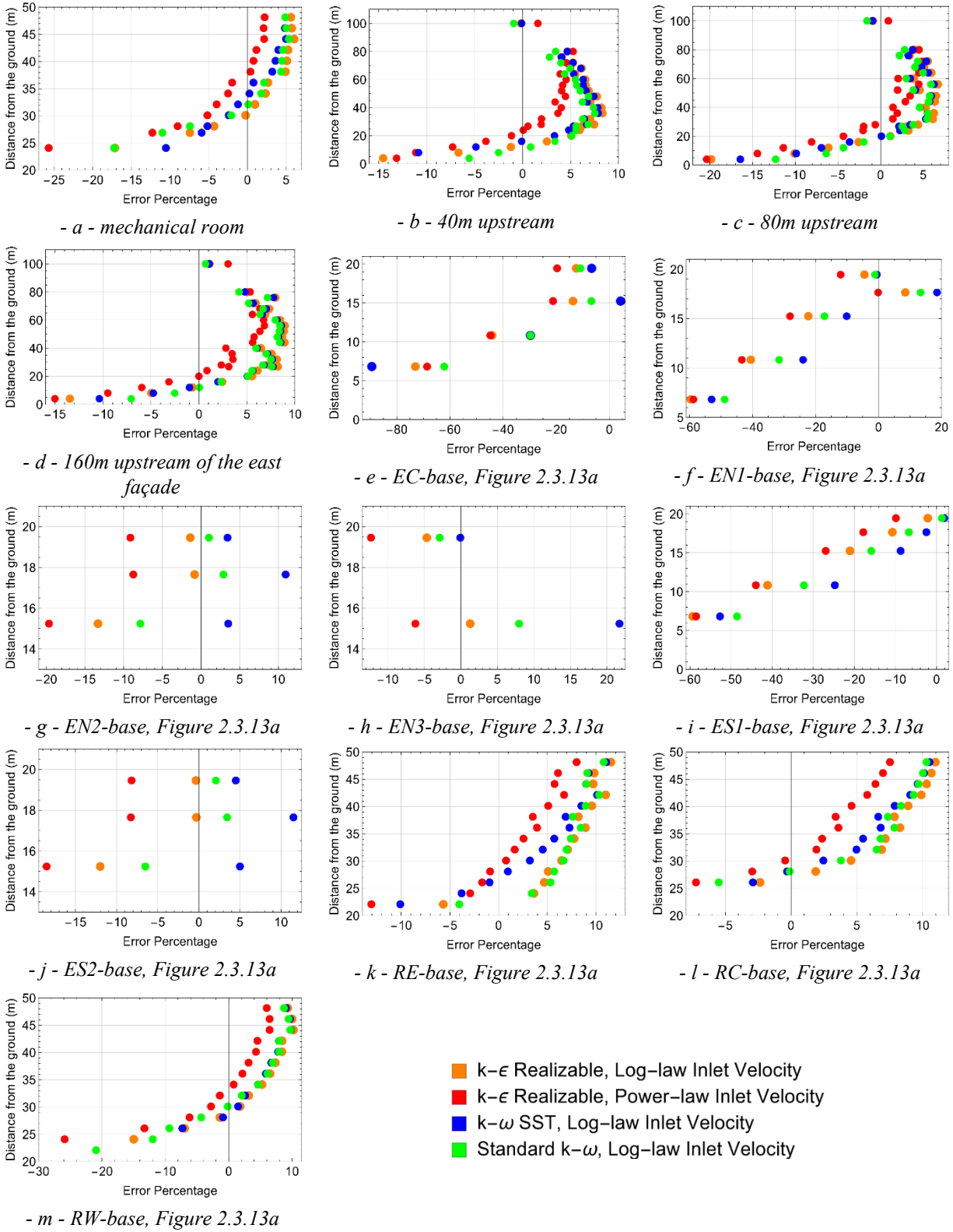
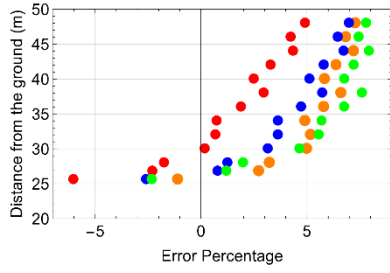
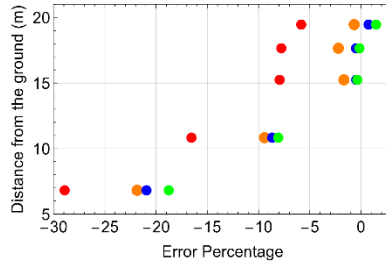


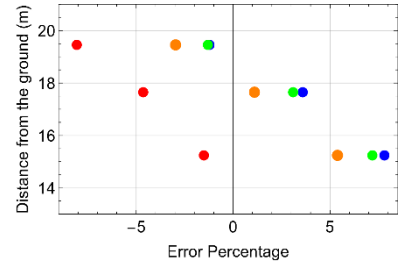
Figure B.2 - x -velocity error percentage on vertical profile, with value comparison to wind tunnel measurement, on stand-alone building exposed to normal wind on the east façade



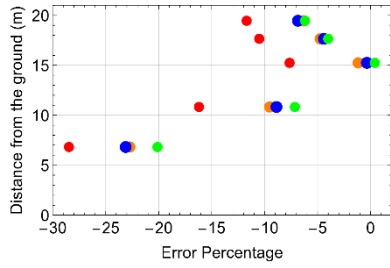
- a - mechanical room



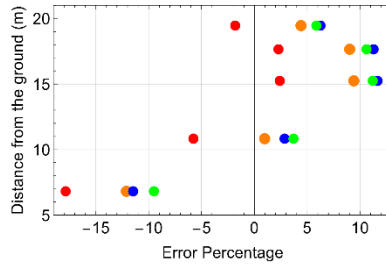
- b - ESI-base, Figure 2.3.13a



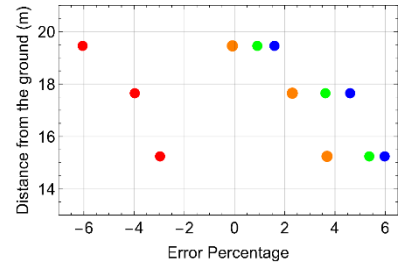
- c - ES2-base, Figure 2.3.13a



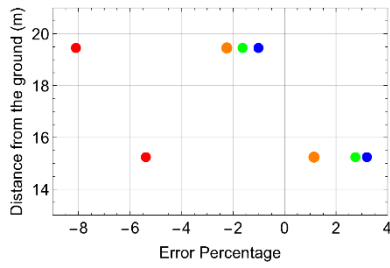
- d - EC-base, Figure 2.3.13a



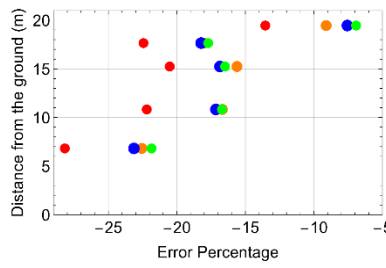
- e - EN1-base, Figure 2.3.13a



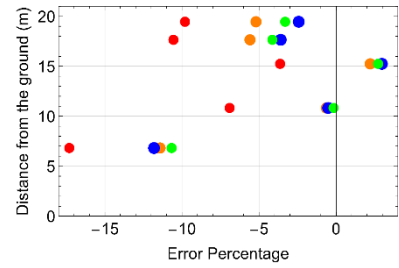
- f - EN2-base, Figure 2.3.13a



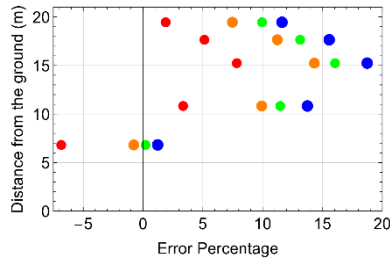
- g - EN3-base, Figure 2.3.13a



- h - SE-base, Figure 2.3.13a



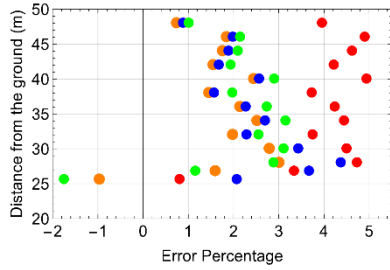
- i - SC-base, Figure 2.3.13a



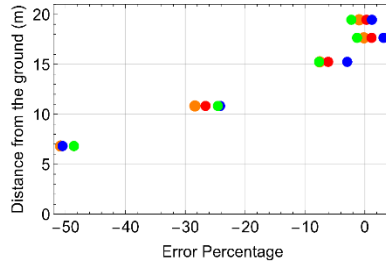
- j - SW-base, Figure 2.3.13a

- $k-\epsilon$ Realizable, Log-law Inlet Velocity
- $k-\epsilon$ Realizable, Power-law Inlet Velocity
- $k-\omega$ SST, Log-law Inlet Velocity
- Standard $k-\omega$, Log-law Inlet Velocity

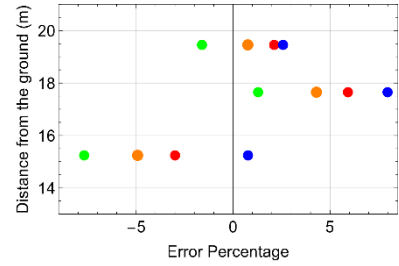
Figure B.3 - x -velocity error percentage on vertical profile, with stand-alone building exposed at 45° wind on the east and south façades



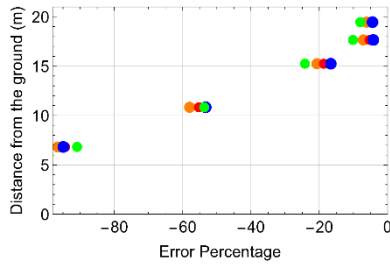
- a - mechanical room



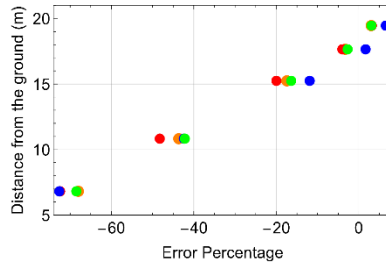
- b - ESI-base, Figure 2.3.13a



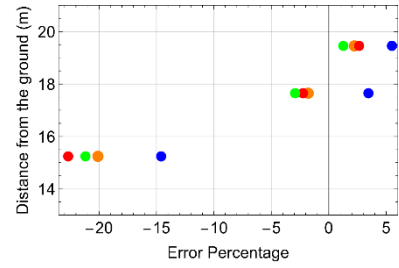
- c - ES2-base, Figure 2.3.13a



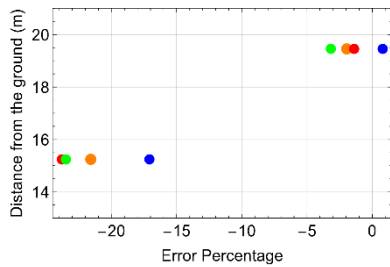
- d - EC-base, Figure 2.3.13a



- e - EN1-base, Figure 2.3.13a



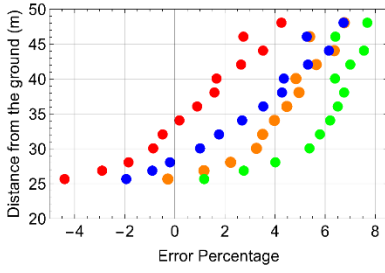
- f - EN2-base, Figure 2.3.13a



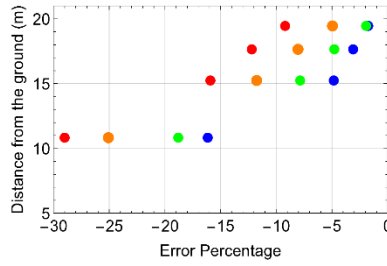
- g - EN3-base, Figure 2.3.13a

- $k-\epsilon$ Realizable, Log-law Inlet Velocity
- $k-\epsilon$ Realizable, Power-law Inlet Velocity
- $k-\omega$ SST, Log-law Inlet Velocity
- Standard $k-\omega$, Log-law Inlet Velocity

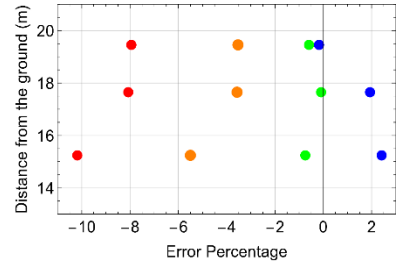
Figure B.4 - x-velocity error percentage on vertical profile, with surrounded building exposed to normal wind on the east façade



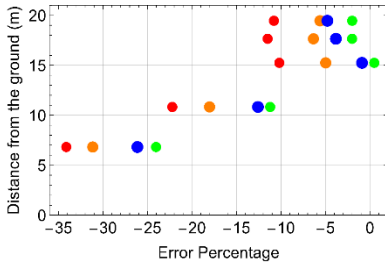
- a - mechanical room



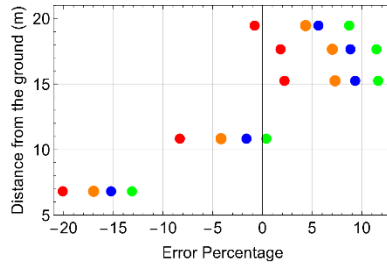
- b - ES1-base, Figure 2.3.13a



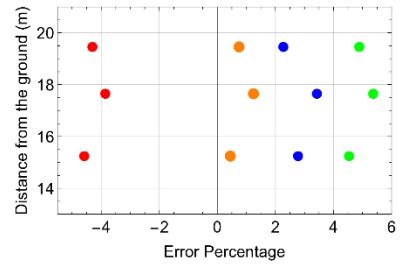
- c - ES2-base, Figure 2.3.13a



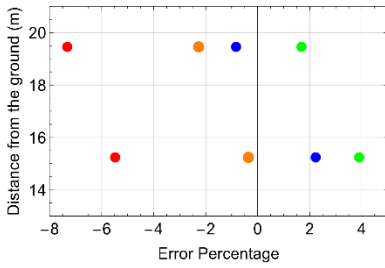
- d - EC-base, Figure 2.3.13a



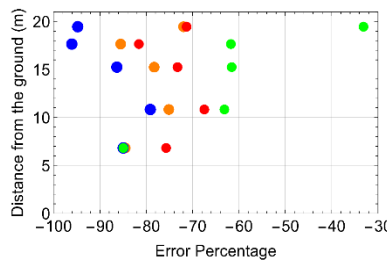
- e - EN1-base, Figure 2.3.13a



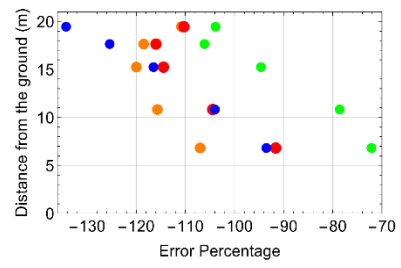
- f - EN2-base, Figure 2.3.13a



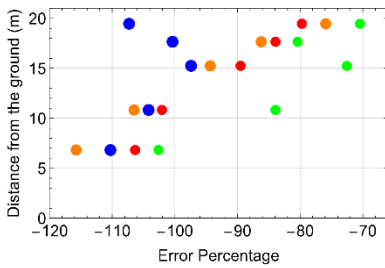
- g - EN3-base, Figure 2.3.13a



- h - NE-base, Figure 2.3.13a



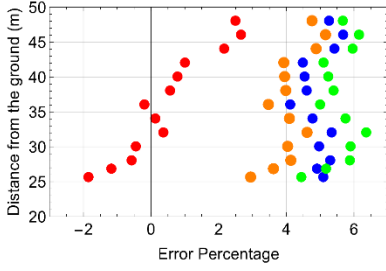
- i - NC-base, Figure 2.3.13a



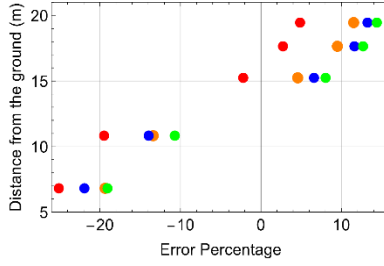
- j - NW-base, Figure 2.3.13a

- $k-\epsilon$ Realizable, Log-law Inlet Velocity
- $k-\epsilon$ Realizable, Power-law Inlet Velocity
- $k-\omega$ SST, Log-law Inlet Velocity
- Standard $k-\omega$, Log-law Inlet Velocity

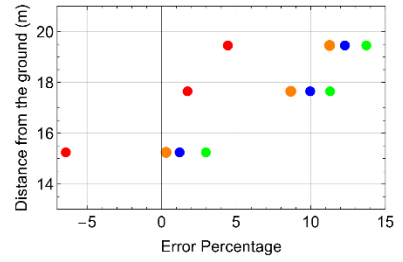
Figure B.5 - x -velocity error percentage on vertical profile, with surrounded building exposed to 45° wind on the east and south façades



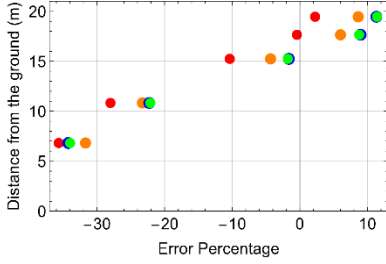
- a - mechanical room



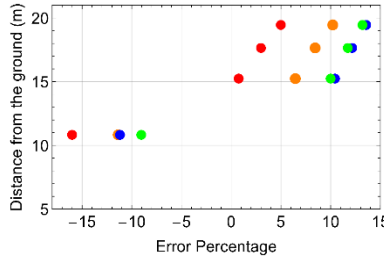
- b - ES1-base, Figure 2.3.13a



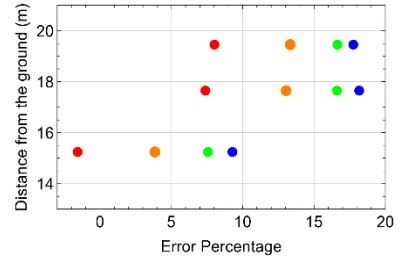
- c - ES2-base, Figure 2.3.13a



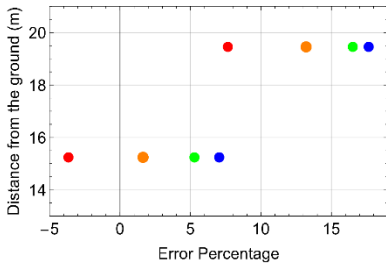
- d - EC-base, Figure 2.3.13a



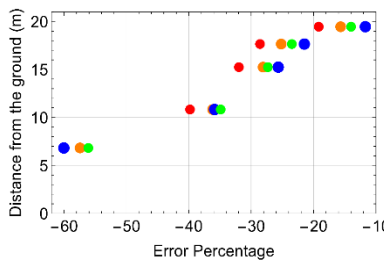
- e - EN1-base, Figure 2.3.13a



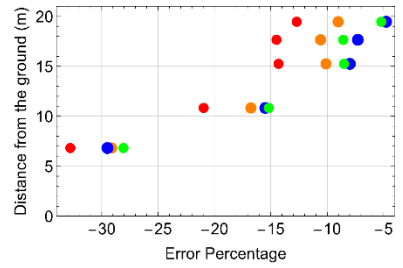
- f - EN2-base, Figure 2.3.13a



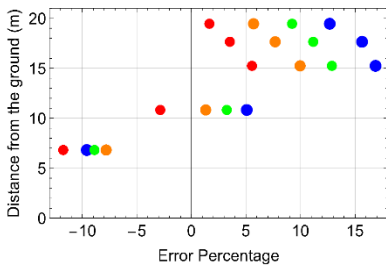
- g - EN3-base, Figure 2.3.13a



- h - NE-base, Figure 2.3.13a



- i - NC-base, Figure 2.3.13a



- j - NW-base, Figure 2.3.13a

- $k-\epsilon$ Realizable, Log-law Inlet Velocity
- $k-\epsilon$ Realizable, Power-law Inlet Velocity
- $k-\omega$ SST, Log-law Inlet Velocity
- Standard $k-\omega$, Log-law Inlet Velocity

Figure B.6 - x -velocity error percentage on vertical profile, with surrounded building exposed to 45° wind on the east and north façades

Appendix D - Velocity Contours

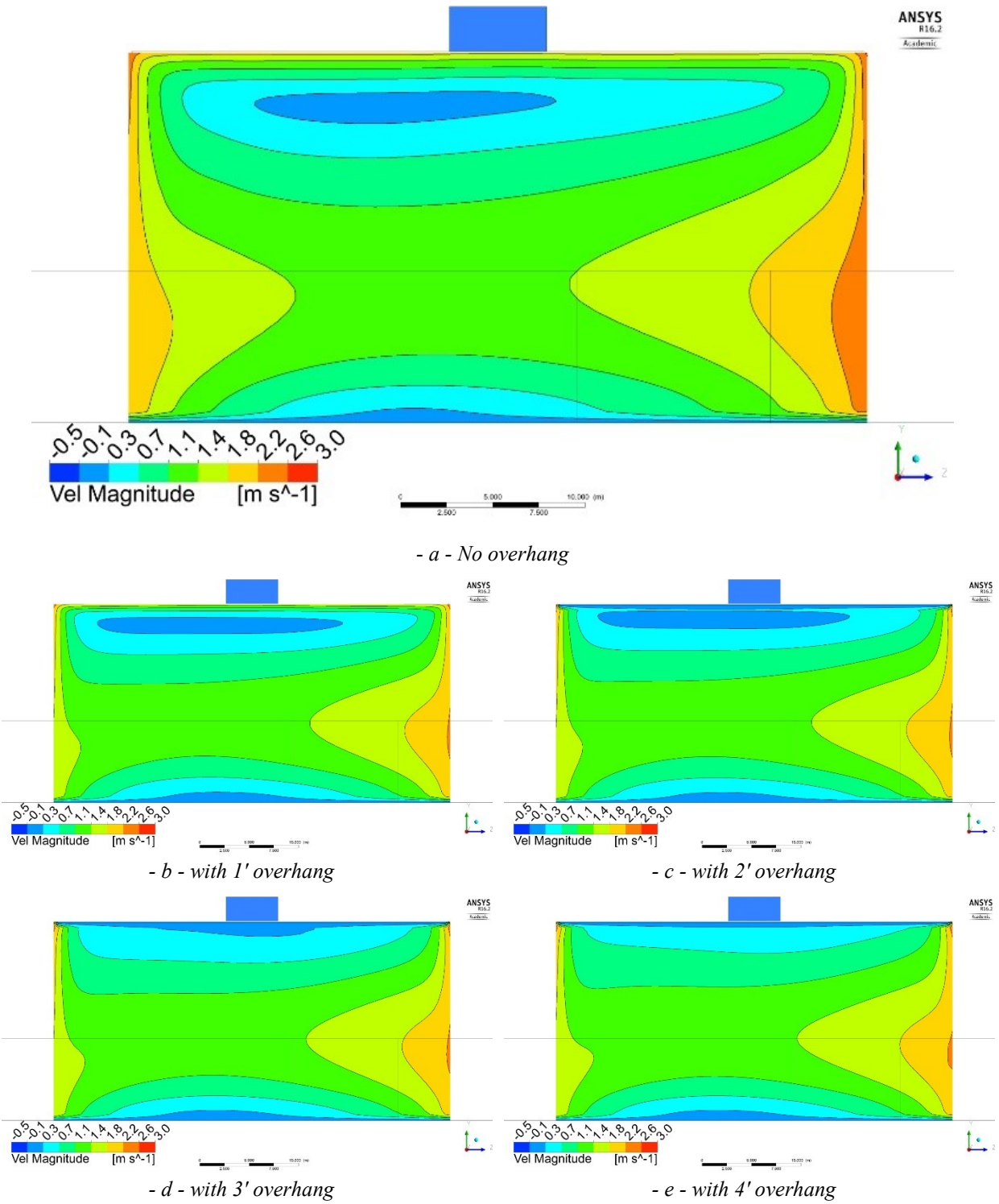
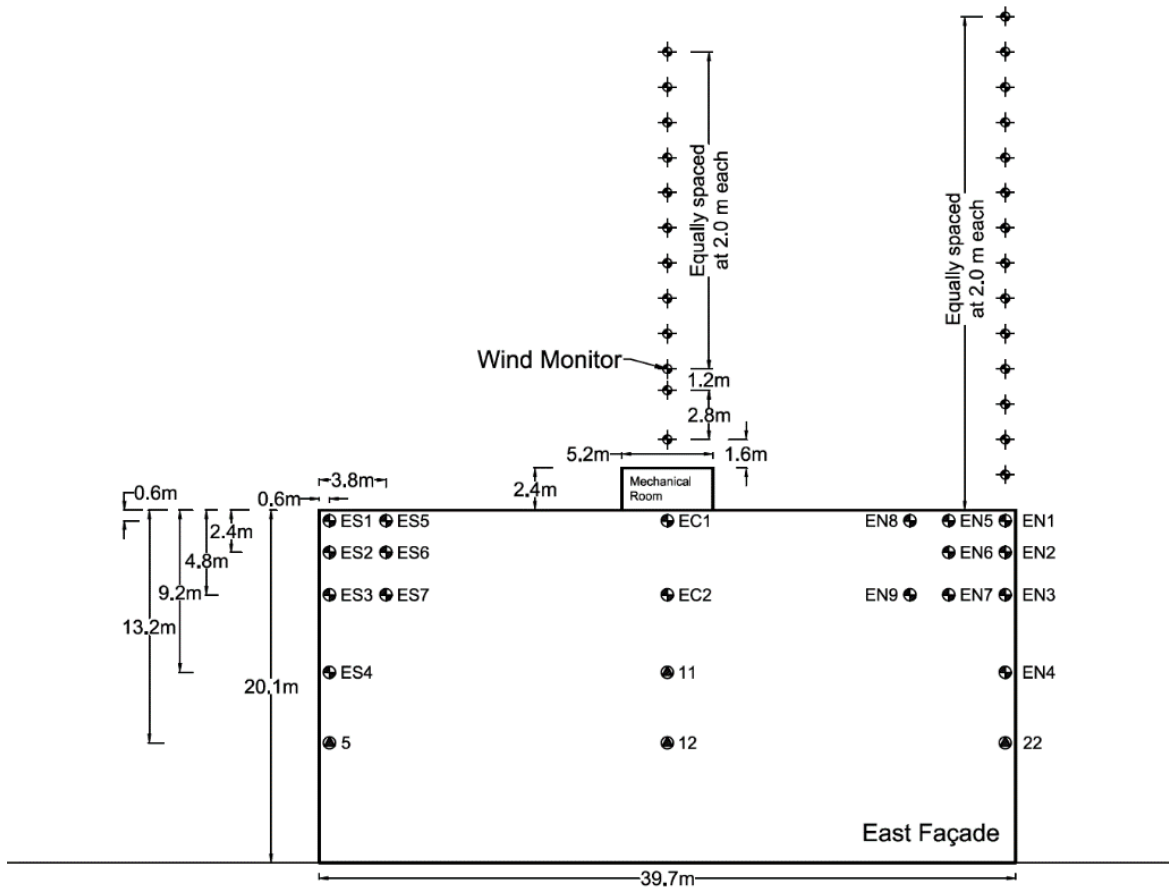


Figure D.1 - Contour of velocity magnitude on a plane 0.5 m upstream of the east façade, with surrounded building unprotected and protected with façade covering overhang

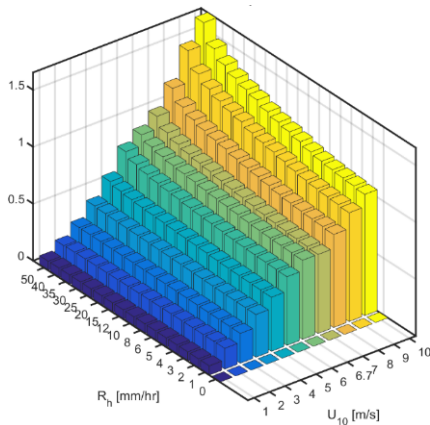
Appendix E - Catch Ratio Parametric Study

For reference, Figure 2.3.13b is presented here again.

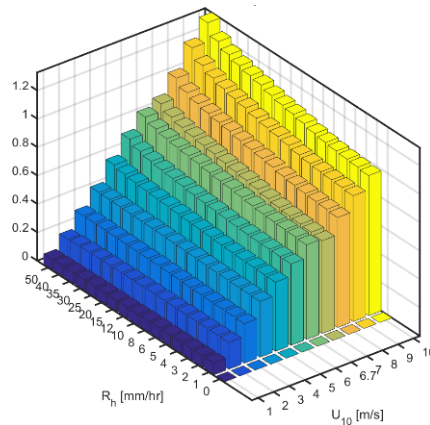


- b - Measurement locations in front of the east façade and above the mechanical room

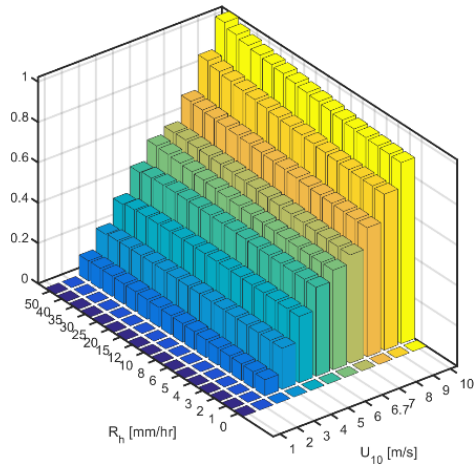
Figure 2.3.13 - Location of wind velocity measurements around the test building



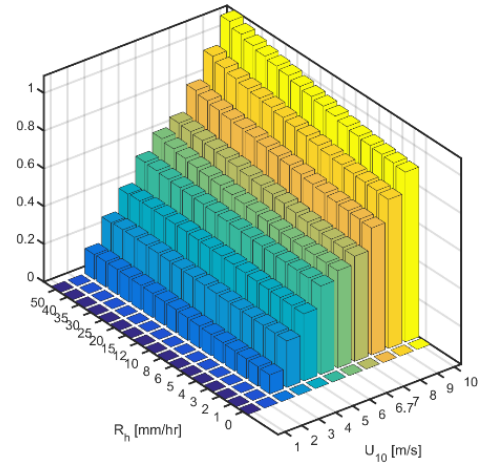
- a - ES2, unprotected façade



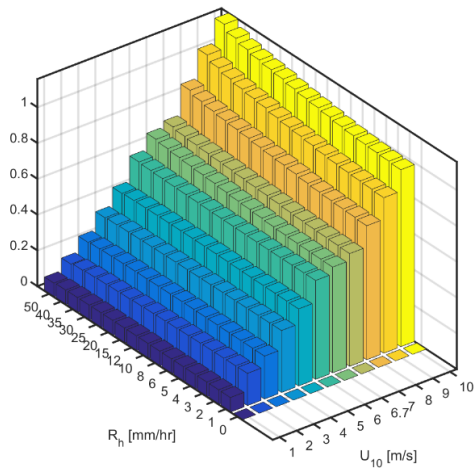
- b - EN2, unprotected façade



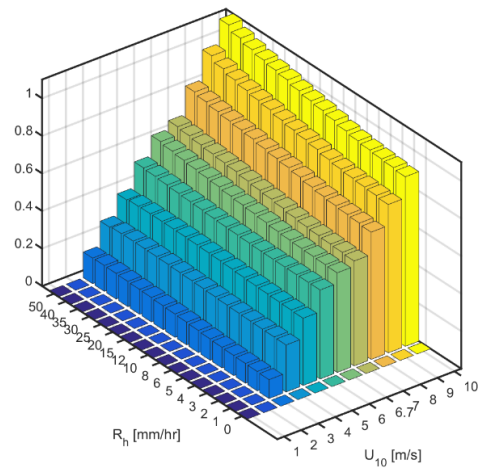
- c - ES2, protected façade with 3' façade-covering overhang



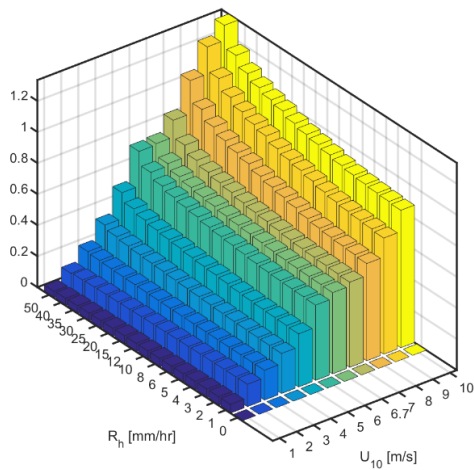
- d - EN2, protected façade with 3' façade-covering overhang



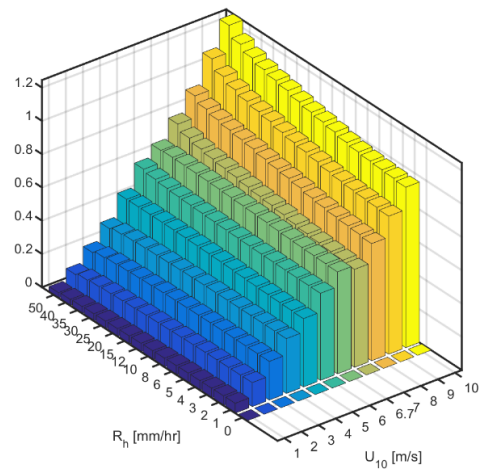
- e - ES2, protected façade with 3' on-site overhang



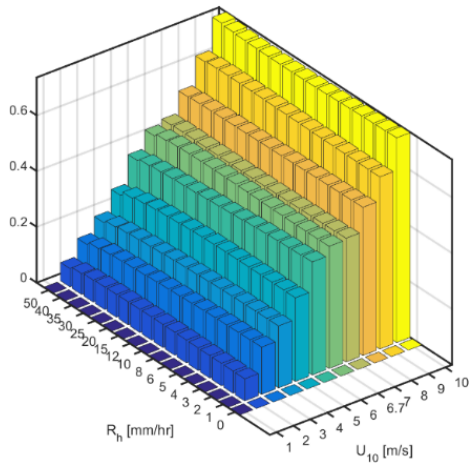
- f - EN2, protected façade with 3' on-site overhang



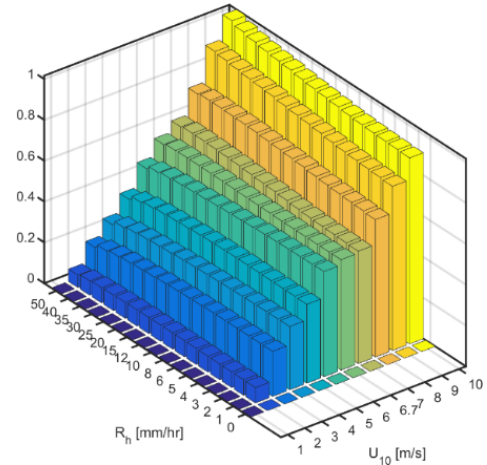
- g - ES3, unprotected façade



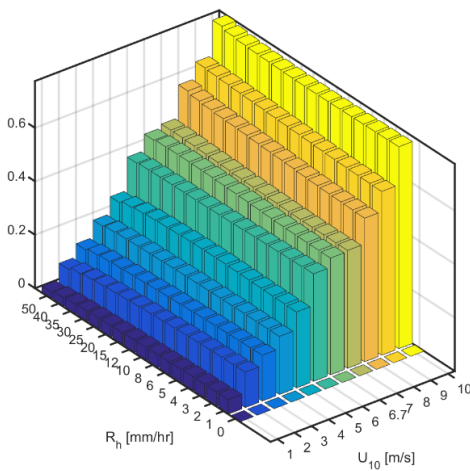
- h - EN3, unprotected façade



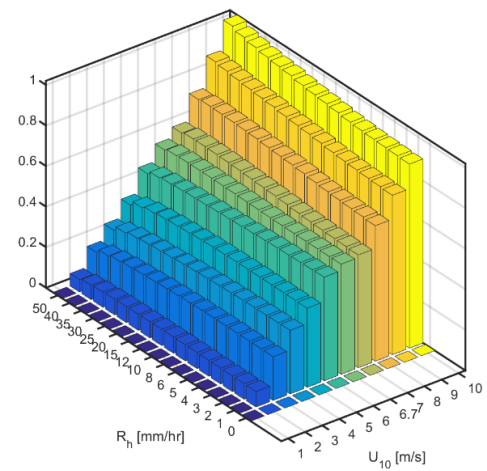
- i - ES3, protected façade with 3' façade-covering overhang



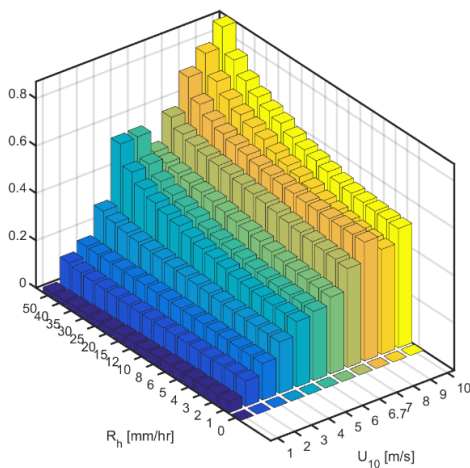
- j - EN3, protected façade with 3' façade-covering overhang



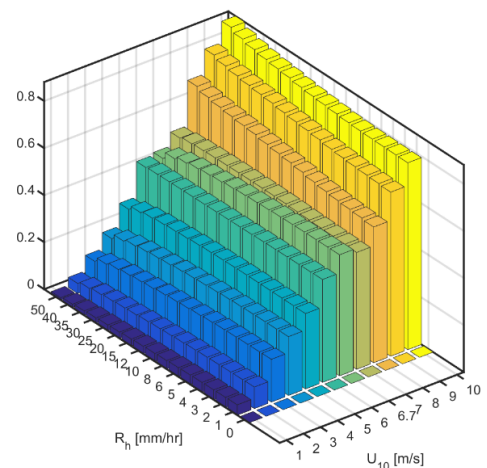
- k - ES3, protected façade with 3' on-site overhang



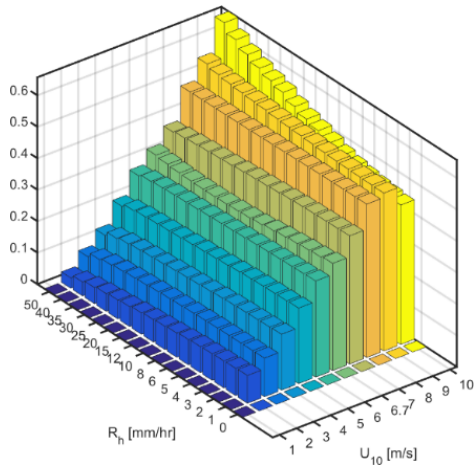
- l - EN3, protected façade with 3' on-site overhang



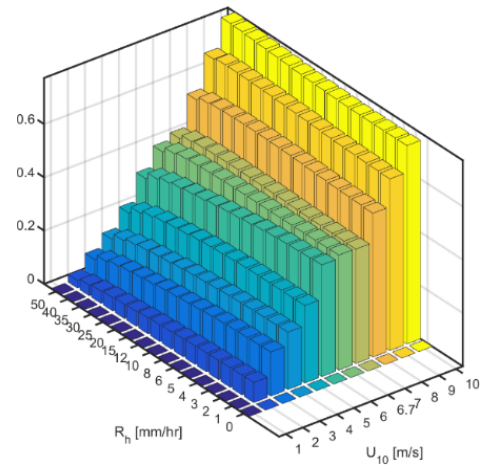
- m - ES4, unprotected façade



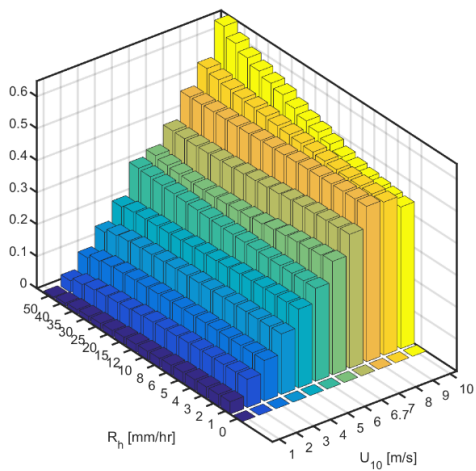
- n - EN4, unprotected façade



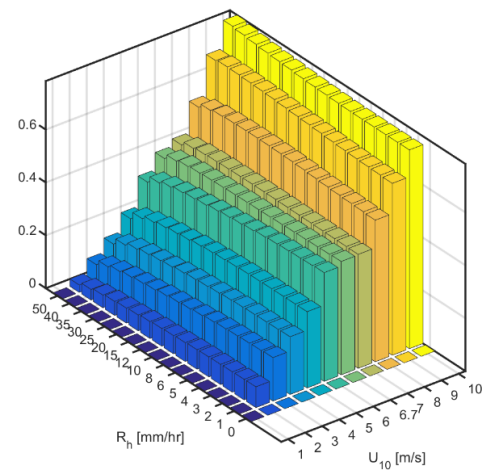
- o - ES4, protected façade with 3' façade-covering overhang



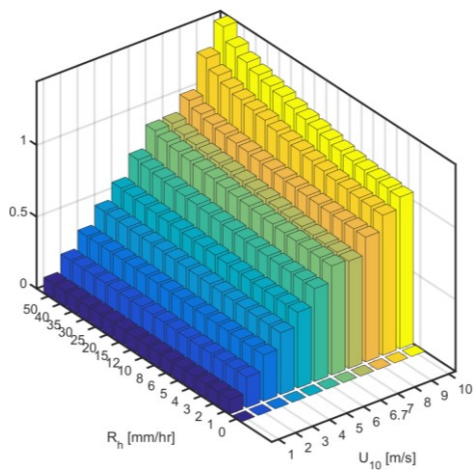
- p - EN4, protected façade with 3' façade-covering overhang



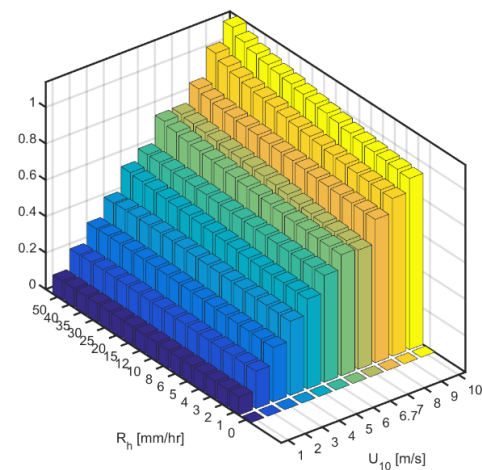
- q - ES4, protected façade with 3' on-site overhang



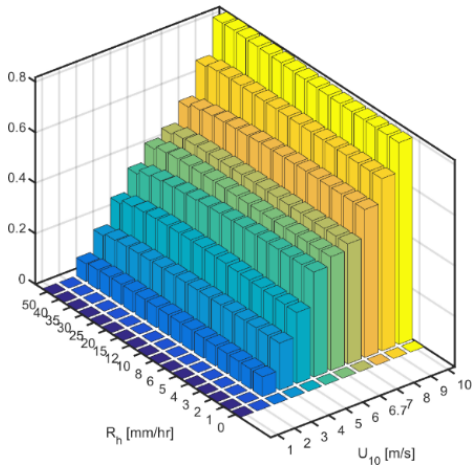
- r - EN4, protected façade with 3' on-site overhang



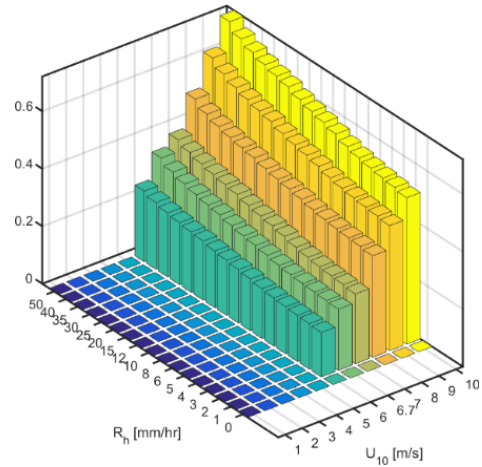
- s - ES5, unprotected façade



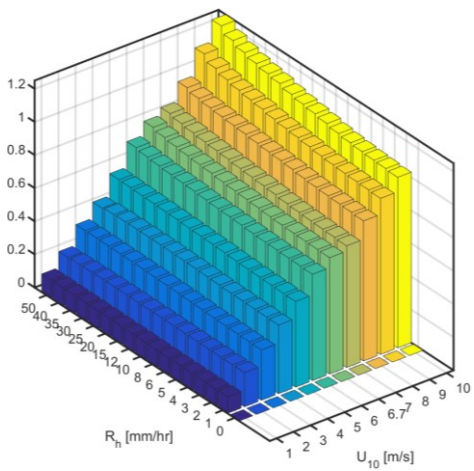
- t - EN5, unprotected façade



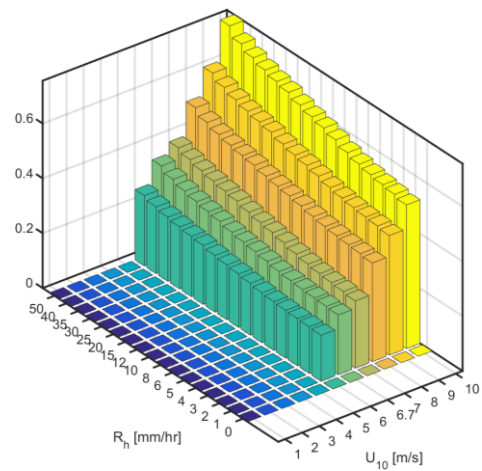
- u - ES5, protected façade with 3' façade-covering overhang



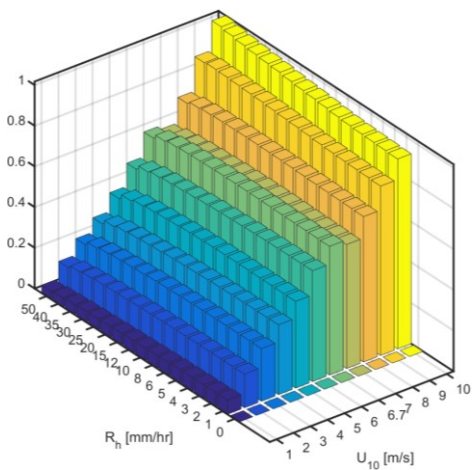
- v - EN5, protected façade with 3' façade-covering overhang



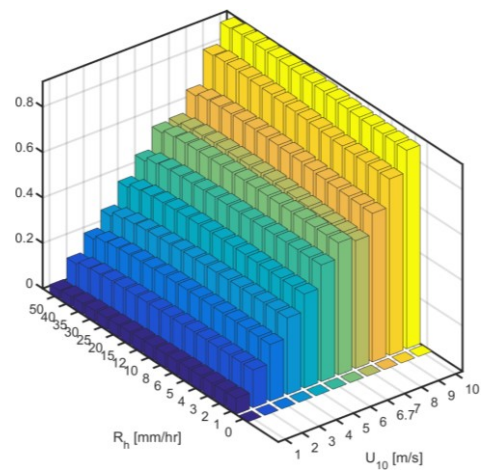
- w - ES5, protected façade with 3' on-site overhang



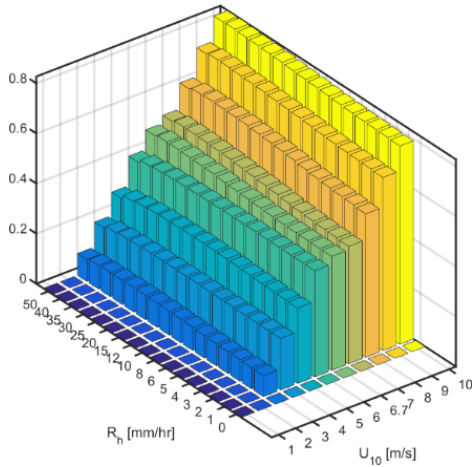
- x - EN5, protected façade with 3' on-site overhang



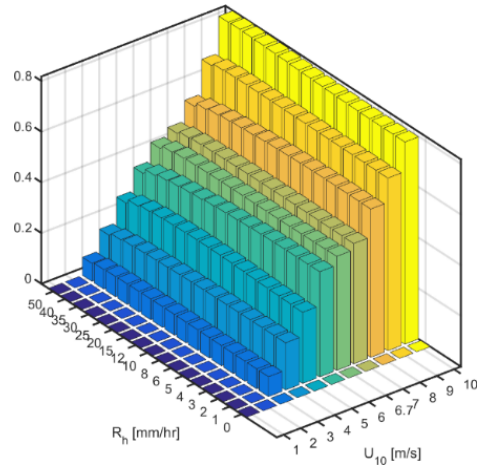
- y - ES6, unprotected façade



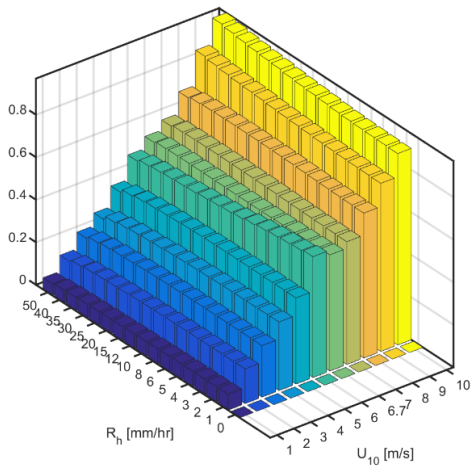
- z - EN6, unprotected façade



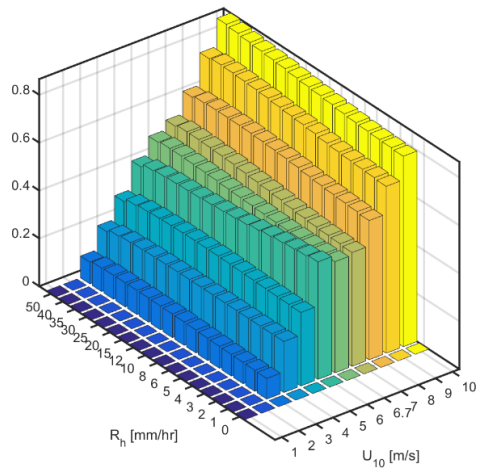
- aa - ES6, protected façade with 3' façade-covering overhang



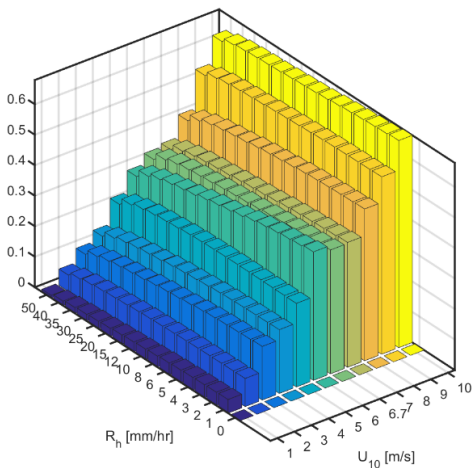
- ab - EN6, protected façade with 3' façade-covering overhang



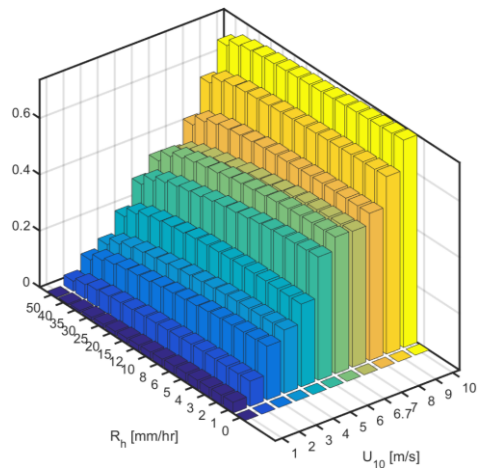
- ac - ES6, protected façade with 3' on-site overhang



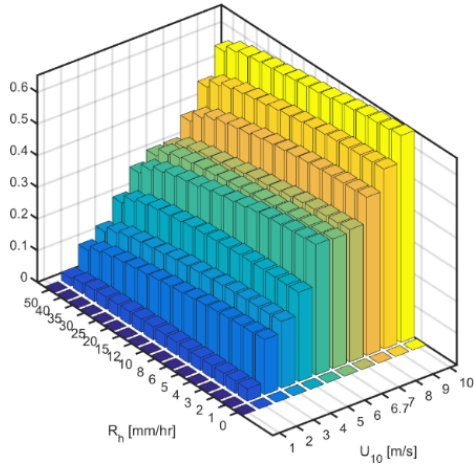
- ad - EN6, protected façade with 3' on-site overhang



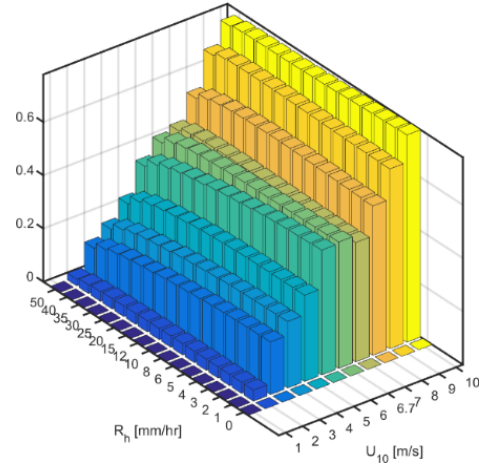
- ae - ES7, unprotected façade



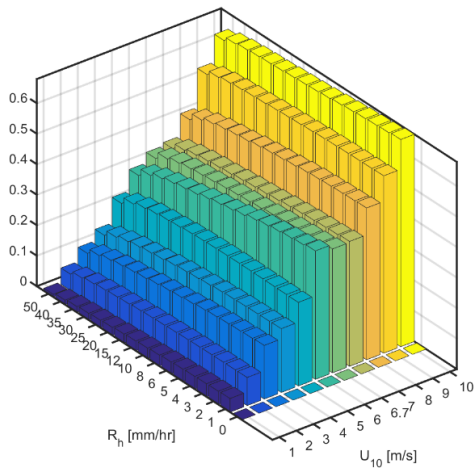
- af - EN7, unprotected façade



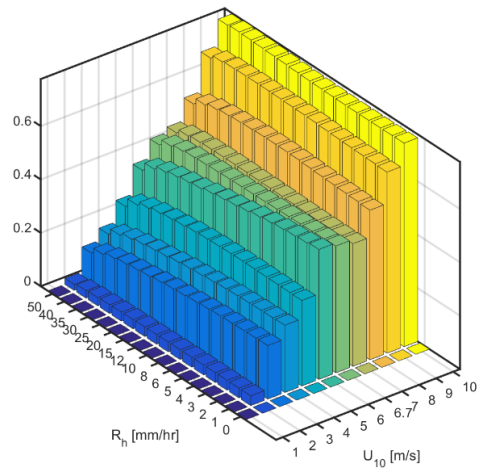
- ag - ES7, protected façade with 3' façade-covering overhang



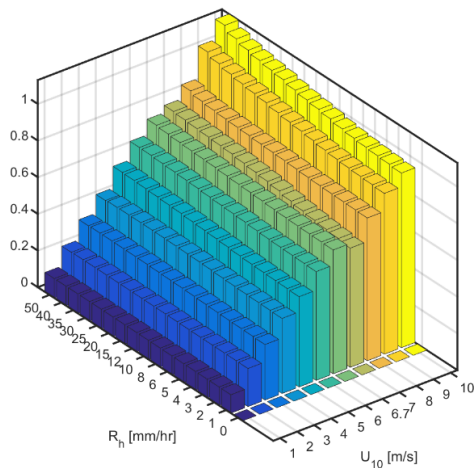
- ah - EN7, protected façade with 3' façade-covering overhang



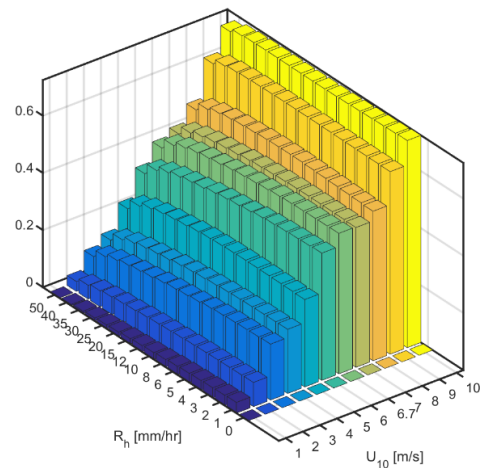
- ai - ES7, protected façade with 3' on-site overhang



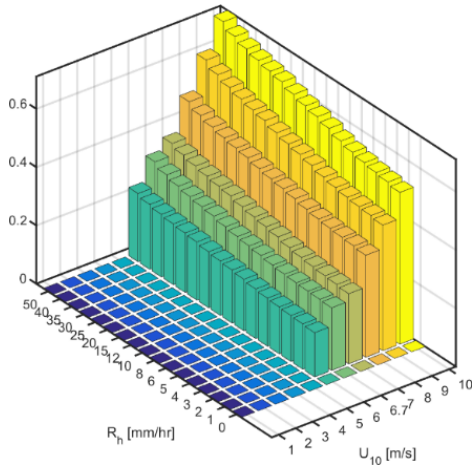
- aj - EN7, protected façade with 3' on-site overhang



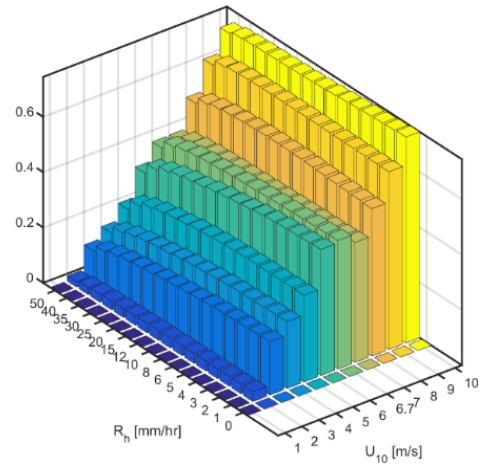
- ak - EN8, unprotected façade



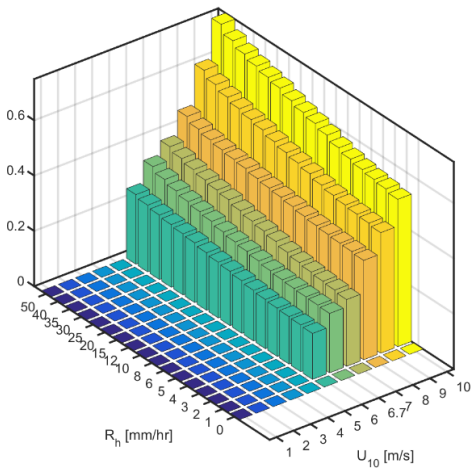
- al - EN9, unprotected façade



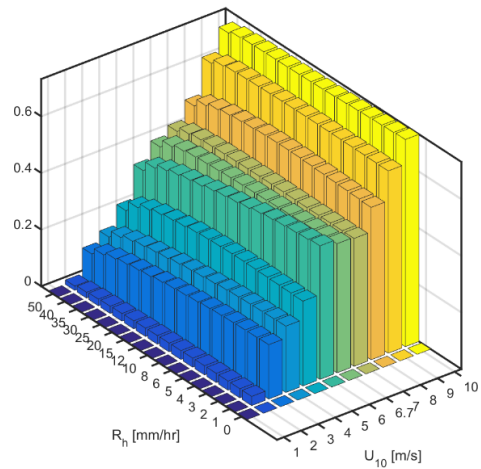
- am - EN8, protected façade with 3' façade-covering overhang



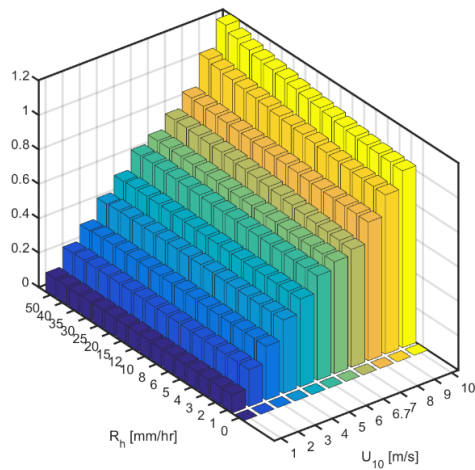
- an - EN9, protected façade with 3' façade-covering overhang



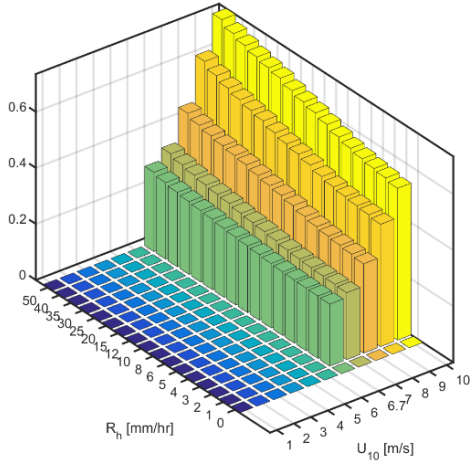
- ao - EN8, protected façade with 3' on-site overhang



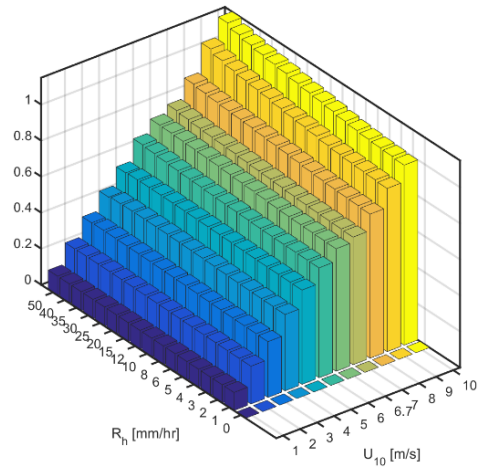
- ap - EN9, protected façade with 3' on-site overhang



- aq - EC1, unprotected façade



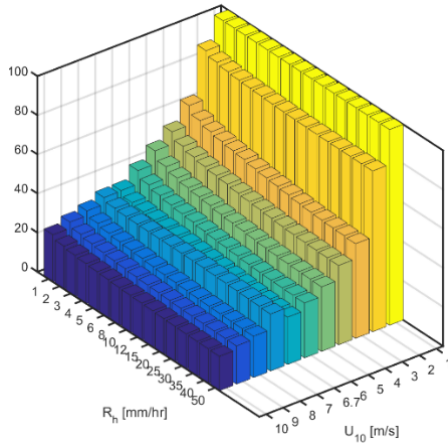
- ar - ECI, protected façade with 3' façade-covering overhang



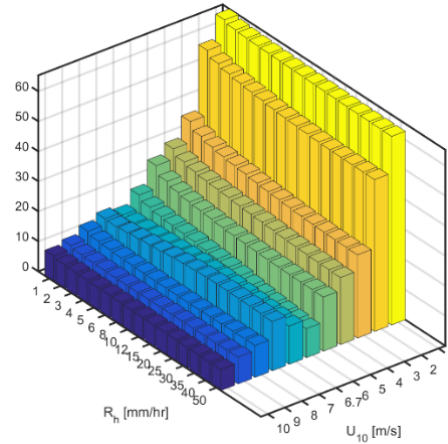
- as - ECI, protected façade with 3' on-site overhang

Figure E.1 - Catch ratio parametric study for protected and unprotected windward façade, the east façade, exposed to normal wind at different rates, at ESI and ENI

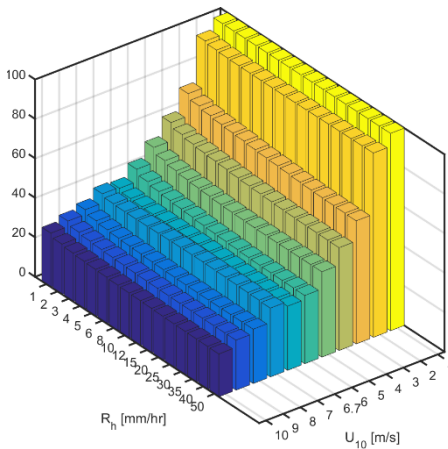
Appendix F - Effectiveness Charts



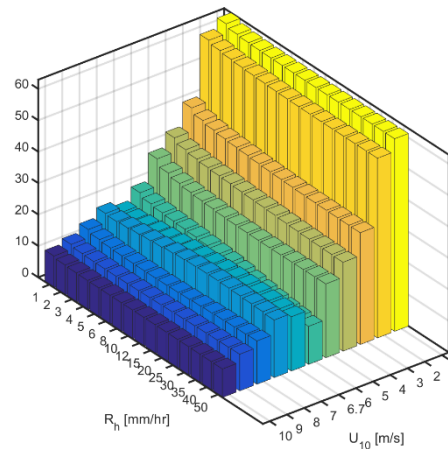
- a - 3' façade-covering overhang, A2



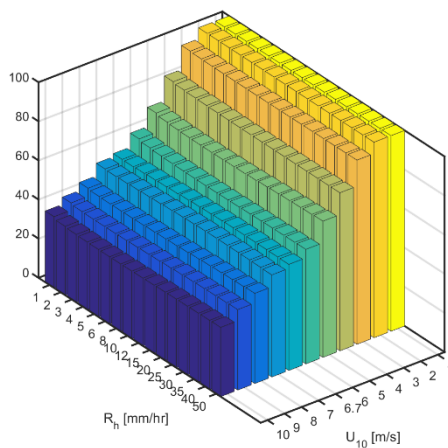
- b - 3' on-site overhang, protected portion, A2



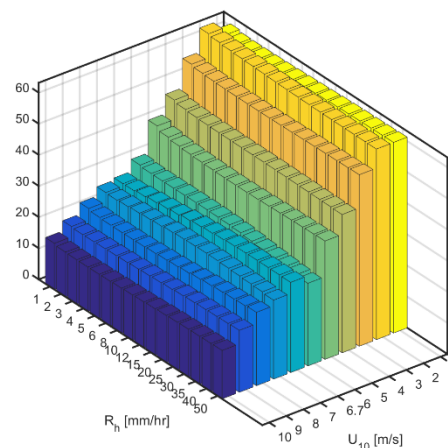
- c - 3' façade-covering overhang, A3



- d - 3' on-site overhang, protected portion, A3



- e - 3' façade-covering overhang, A4



- f - 3' on-site overhang, protected portion, A4

Figure F.1 - Effectiveness of overhang on windward façade, exposed to normal wind at different rates, and rain in different intensities